

FLUIDS ENGINEERING DIVISION
Technical Editor
FRANK M. WHITE (1989)
Executive Secretary
L. T. BROWN (1989)
Calendar Editor
M. F. ACKERSON

Associate Editors
Fluid Machinery
WIDEN TABAKOFF (1988)
Fluid Measurements
UPENDRA S. ROHATGI (1990)
Fluid Mechanics
JOHN F. FOSS (1990)
Fluid Transients
J. CRAIG DUTTON (1990)
DANIEL C. REDA (1990)
DEMETRI P. TELIONIS (1989)
WILLIAM W. DURGIN (1988)
Numerical Methods
FREDERICK J. MOODY (1989)
Multiphase Flow
PATRICK J. ROACHE (1988)
M. C. ROCO (1988)
Review Articles
GEORGES L. CHAHINE (1990)
K. N. GHIA (1988)

BOARD ON COMMUNICATIONS
Chairman and Vice President
K. N. REID, Jr.

Members-at-Large
J. T. COKONIS
M. FRANKE
M. KUTZ
F. LANDIS
J. R. LLOYD
T. C. MIN
R. E. NICKELL
R. E. REDER
R. ROCKE
F. W. SCHMIDT
W. O. WINER

President, **R. ROSENBERG**
Executive Director
D. L. BELDEN
Treasurer,
ROBERT A. BENNETT

PUBLISHING STAFF
Mng. Dir., Publ.,
JOS. SANSONE
Managing Editor,
CORNELIA MONAHAN
Editorial Production Assistant,
MARISOL ANDINO

Transactions of the ASME, The Journal of Fluids Engineering (ISSN 0098-2202) is published quarterly (Mar., June, Sept., Dec.) for \$95 per year by The American Society of Mechanical Engineers, 345 East 47th Street, New York, NY 10017. Second class postage paid at New York, NY and additional mailing offices. POSTMASTER: Send address changes to The Journal of Fluids Engineering, c/o THE AMERICAN SOCIETY OF MECHANICAL ENGINEERS, 22 Law Drive, Box 2300, Fairfield, NJ 07007-2300. CHANGES OF ADDRESS must be received at Society headquarters seven weeks before they are to be effective. Please send old label and new address.

PRICES: To members, \$27.00, annually; to nonmembers, \$95. Add \$12.00 for postage to countries outside the United States and Canada. STATEMENT from By-Laws. The Society shall not be responsible for statements or opinions advanced in papers or ... printed in its publications (B7.1, Par. 3).

COPYRIGHT © 1988 by The American Society of Mechanical Engineers. Reprints from this publication may be made on condition that full credit be given THE TRANSACTIONS OF THE ASME, JOURNAL OF FLUIDS ENGINEERING and the author, and date of publication be stated.

INDEXED by Applied Mechanics Reviews and Engineering Information, Inc.

Published Quarterly by The American Society of Mechanical Engineers

VOLUME 110 • NUMBER 1 • MARCH 1988

- 1 Fluids Engineering Calendar
- 4 Fluids Engineering Education: Current Status and Future Directions
C. Dalton and J. P. Lamb
- 9 Basic Elements in a Fluid Mechanics Laboratory Experience: An Engineering Science Approach
J. F. Foss
- 16 Performance of Butterfly Valves as a Flow Controller
K. Eom
- 20 Analyses of Hydrodynamic Radial Forces on Centrifugal Pump Impellers
D. R. Adkins and C. E. Brennen
- 29 Navier-Stokes Computation of Radial Inflow Turbine Distributor
T. C. Vu and W. Shyy
- 33 Effect of Particle Characteristics on Trajectories and Blade Impact Patterns
A. Hamed
- 38 A Reynolds-Stress Model for Near-Wall and Low-Reynolds-Number Regions
Nobuyuki Shima
- 45 Experimental Investigation of More's Method for Wind Tunnel Contractions
E. G. Tulapurkara and V. V. K. Bhalla
- 48 Experimental and Computational Investigation of the Two-Dimensional Channel Flow Over Two Fences in Tandem
F. Durst, M. Founti, and S. Obi
- 55 Noise and Vibration Related to the Patterns of Supersonic Annular Flow in a Pressure Reducing Gas Valve
Masami Nakano, Eisuke Outa, and Kiyohiro Tajima
- 62 Supercomputing of Supersonic Flows Using Upwind Relaxation and MacCormack Schemes
Oktay Baysal
- 69 Solution Procedure for Unsteady Two-Dimensional Boundary Layers
O. Key Kwon, R. H. Pletcher, and R. A. Delaney
- 76 Some Observations of Flow Patterns and Statistical Properties of Three Component Flows
H. K. Kytömaa and C. E. Brennen
- 85 Modelling Collisional Stresses in a Dense Fluid-Solid Mixture
H. H. Shen, M. A. Hopkins, and N. L. Ackerman

Technical Briefs

- 91 Limitation of Ejector Performance Due to Exit Choking
J. C. Dutton and B. F. Carroll
- 93 Incremental Pressure Drop Number in Parallel-Plate Heat Exchangers
T. V. Nguyen and I. L. MacLaine-cross
- 96 Theoretical Calculations of the Flow Around a Rotating Circular Cylinder Placed in a Uniform Flow
Taha K. Aldoss and Awad Mansour
- 98 Eddy Viscosity Distributions Through the Transition of an Incompressible Free Jet
S. Emami, G. Morrison, and G. Tatterson
- 101 Discussion on Previously Published Papers
- 103 List of Reviewers

Announcements and Special Notices

- 3 Call for Papers—3rd Joint ASCE/ASME Mechanics Conference
- 37 Transactions Change of Address Form
- 44 Call for Papers—Symposium on Turbulent Shear Flows

(Contents continued on page 8)

Contents (Continued)

- 84 Call for Papers—1989 Fluids Engineering Conference
- 100 Announcement—50th Annual Forum on Unsteady Flow
- 105 ASME Prior Publication Notice
- 105 Submission of Papers
- 105 Statement of Experimental Uncertainty

C. Dalton

Professor of Mechanical Engineering,
Associate Dean of Engineering,
University of Houston,
Houston, Texas.
Fellow ASME

J. P. Lamb

Ernest Cockrell Professor of Engineering,
Chairman, Department of Aerospace
Engineering and Engineering Mechanics,
University of Texas at Austin,
Austin, Texas.
Fellow ASME

Fluids Engineering Education: Current Status and Future Directions

This paper presents a summary of panel presentations at the 1986 ASME Winter Annual Meeting. A total of eleven panelists from university, industry, and governmental organizations participated in the program. The authors have also included a number of editorial and interpretative comments to enhance the breadth of coverage.

EDITOR'S NOTE:

The two papers which follow arose from the Panel on Fluid Mechanics Education at the 1986 Winter Annual Meeting in Anaheim, CA. The paper by C. Dalton and P. Lamb gives the highlights of the presentations of the various panelists. The paper by J. F. Foss was especially solicited as a discussion of the author's undergraduate fluids laboratory program. These two papers fulfill the request of the Fluids Engineering Division to review fluid mechanics education in the Journal every ten years.

Background

At the 1986 ASME Winter Annual Meeting the Fluids Engineering Division sponsored two sessions covering educational issues relating to fluids engineering education. The panel format was used for these sessions to accommodate a broad range of viewpoints representing the three primary sectors: academic, government and industry. Names and affiliations of the eleven panelists are listed at the end of the paper (under Acknowledgments). The authors, as organizers of the two sessions, have attempted to summarize in this paper the highlights of each panelist's remarks within a coherent and logical framework of important issues.

The session began with a historical review of fluid mechanics by W. R. Sears. A summary of his remarks is given in the Appendix.

Major Issues in Fluids Engineering

The present discussion encompasses both *fluid mechanics*, which is interpreted as the body of knowledge relating to the physics of fluid flow, and *fluids engineering*, which is interpreted as the application of fluid mechanics to the design and development of new processes and devices. Some of the major

questions to which the panelist's remarks were directed are as follows:

- What is the current status of textbook usage and subject matter in undergraduate fluids courses in U.S. engineering schools?
- What are the educational objectives of undergraduate fluids courses?
- Should the specific objectives of fluids courses differ if a majority of the students were preparing for professional careers immediately after graduation rather than anticipating advanced study for the MS or PhD degree?
- What is the relative importance of laboratory experiences? Should such experiences encompass demonstrations, films and other visual media, as well as hands-on experiments? Should the laboratory experience be highly correlated with lecture material?
- Should the undergraduate fluids curriculum include some coverage of contemporary computational methods, i.e., numerical solution of discretized forms of governing equations?

Major questions relating to graduate-level fluids education include the following:

- Inasmuch as some students seeking advanced degrees will not become principal or associate investigators but rather will become R&D managers, should some graduate courses be broad in scope, emphasizing the interrelation between fluid phenomena and other technologies (such as structures or controls), or should all courses be narrow in scope, emphasizing detailed physical processes?
- Should there be some emphasis on emerging areas of fluids engineering technology which are anticipated to be more important in the future than the past?
- What relative weight should be given to traditional, analytical approaches as compared with contemporary methods of measurement and computer simulation (CFD)?

Survey of Course Offerings

Professor Frank White presented results of a recent survey of undergraduate fluids courses and compared the data with

Contributed by the Fluids Engineering Division for publication in the JOURNAL OF FLUIDS ENGINEERING. Manuscript reviewed by the Fluids Engineering Division July 27, 1987.

that presented by Lamb and Swim [1] in 1976. White's survey included 93 institutions in the continental U.S. and Hawaii distributed by region as follows: northeast 24, southeast 16, midwest 18, southwest 16, and far west 19. Seventeen percent of the responding institutions operated on the quarter system; of this group 44 percent required a single fluids course, 38 percent required two courses while only 12 percent required three courses (equivalent to one academic year) and 6 percent required four courses. The vast majority (83 percent) of the responding institutions operated on the semester system; 61 percent of these schools required one course, 30 percent required two courses (one year), while 8 percent required three courses. Surprisingly, one of the semester schools required no fluids courses for undergraduate engineering students. In addition to the required fluids courses, 72 percent of the responding schools offer additional (elective) fluids courses.

Shown in Table 1 is a comparison of information from the current and previous surveys; this tabulation indicates which departments have the responsibility for teaching the first fluids course to undergraduate ME students. The current level of 76 percent ME departments compares favorably with 71 percent from the 1976 survey. Furthermore, the percentage of civil engineering departments represented in the table is identical in the two surveys, while engineering mechanics decreased from 9 percent to 1 percent in the current survey and chemical engineering participation increased from zero to 5 percent in the current survey.

The present survey indicates that the most often used textbooks for basic fluids courses were as follows (authors' names are in alphabetical order): Fox and McDonald [2], Gerhart and Gross [3], Roberson and Crowe [4], Shames [5] and White [6].

In the 1976 survey both Fox and McDonald and Shames had been mentioned along with Olsen [7] and Streeter [8]. As in the 1976 results, the current survey indicated that many other texts see some use; 16 additional texts were mentioned at least occasionally in White's survey.

Table 2 indicates the subject coverage of various advanced undergraduate courses reported in the present survey. Slightly more than half of the respondents indicated that such courses contained a variety of topics while 45 percent indicated compressible flow as the second course. In addition to those topics shown in Table 2, the current survey indicated isolated course offerings in other subjects such as acoustics, geophysical flows, meteorology, sedimentation, fluid transients, and multi-phase flow.

For courses in compressible flow, the texts most often used included the following: Anderson [9], John [10], Shapiro [11] and Zucker [12] while five additional texts were used occasionally.

White's survey also included questions concerning use of various supplementary materials. The major results are shown in Table 3, where it is seen that 74 percent of the respondents reported the use of films while slightly less than half reported significant laboratory experience. It is also seen that the use of commercially produced computer software has not yet become widespread in undergraduate fluids courses. In the authors' opinion, increased activity in this area would result in significant improvements in teaching effectiveness as well as in greater student enthusiasm for fluid mechanics as a subject. Indeed, White's oral presentation included personal experiences with student use of software for PC-level machines.

Perspectives From Universities

The consensus of the speakers was that an understanding of basic fluid mechanics is still important. A sound knowledge of fundamentals remains the key to mastering specific applications as well as to facilitating further learning. Several

Table 1 Departments teaching the first fluids course to mechanical engineers

	1986 White	1976 Lamb and Swim
Mechanical Engineering	76%	71%
Civil Engineering	14%	14%
Chemical Engineering	5%	0%
Undesignated	3%	6%
Engineering Mechanics	1%	9%
Aerospace Engineering	1%	0%

Table 2 Advanced undergraduate courses after the first fluids course

Survey of advanced topics	52%
Compressible flow	45%
Aerodynamics	17%
Turbomachinery	14%
Viscous flow	4%
Computational fluid flow	2%

Table 3 Use of supplementary material in fluid mechanics courses

Use of Professionally Produced Films

None	Some	Many
26%	58%	16%

Use of Commercially Produced Software

None	Some	Many
75%	20%	5%

Fluid Mechanics Laboratories

None	Some	Many
6%	48%	46%

speakers emphasized that both lecture and laboratory experiences are necessary to gain a proper physical understanding of the subject.

Professor John Foss noted that the purpose of undergraduate education could serve either of two goals:

1. to serve the technological purposes addressed by mechanical engineers (in concert with heat transfer, thermodynamics, flow-induced vibrations, etc.) with a level of sophistication characterized by the EIT examination, or
2. to build the foundation for fluid mechanics as one of the engineering sciences and, with the intent as explicated in the Grinter Report, "to provide the fundamental basis for a lifetime technical career."

The fundamentals to be covered in the undergraduate fluids curriculum are represented by these goals which could be considered as the two limiting conditions of fluid mechanics instruction. Foss, noting that fluid mechanics is an experimental science, emphasized that laboratory work must be an integral part of basic courses. He pointed out that a properly structured course should have a closely integrated lecture and laboratory. Foss presented the outline of a set of experiments which allows the instructor to correlate lecture and laboratory properly. Further details of Foss' presentation are given in an accompanying paper [13].

In his presentation Professor Allan Acosta listed overall goals for engineering courses, especially introductory ones, as follows:

1. to develop competence in fundamentals, enabling the student to begin reading technical literature.

2. to establish some connections between engineering and science, to understand "scale" of engineering projects and the necessity of making engineering decisions without full scientific understanding of a subject.

3. to lay a basis for the student to *become proficient* in the practice of engineering in subsequent employment and self-study.

Computers have a major role in both experimental fluid mechanics and computational fluid mechanics. Professor Alan McDonald noted that the computer revolution was applying new pressure for change within the undergraduate curriculum. Industry is expecting the new graduate to be computer literate. Universities, and engineering colleges in particular, should make better use of the computer in order to make their instructional activities more cost effective. McDonald noted that, while computer literacy was important, he did not think it represented as overriding a concern as sound engineering fundamentals.

Professor Dale Anderson addressed the role of computational fluid mechanics (CFD) for undergraduate education. His approach is to teach the necessary numerical analysis as well as computational methods (including an introduction to finite elements) and interpretation skills. Anderson believes that the goal for an undergraduate is to gain limited code-development experience and to learn to run simple programs. An outcome of this goal is to understand the power of numerical approaches and their limitations as well. The philosophy suggested by Anderson is to introduce CFD as an independent area to complement experimental and analytical fluid mechanics. The idea is to incorporate CFD into the undergraduate student's problem-solving abilities through the use of existing codes and to intersperse the material throughout existing fluid mechanics courses.

Anderson suggests a different philosophy for graduate students studying CFD. He thinks that the student should be taught to have some skepticism about existing codes; code limitations should be understood. The student must learn to discern realistic from unrealistic solutions and to interpret the flow physics from the numeric anomalies. Anderson also believes that both graduate and undergraduate students should develop their skill and confidence by solving model problems or model equations. Also, he suggests that the numerical skills should be developed before application is made to fluid dynamics problems. He reminded the audience that the computer is also used extensively as a basic laboratory instrument, for experiment control and for data acquisition.

Professor A. L. Addy discussed the content of fluid mechanics within the undergraduate curriculum and noted the ever present challenge of balancing the depth of coverage with the breadth of coverage while recognizing that it is extremely difficult to cover all of the necessary material with any degree of depth. He suggested ten major topic areas which should be covered:

1. Fluid statics
2. Control volume analysis
3. Differential equation analysis
4. Dimensional analysis and similarity
5. Viscous flows
6. Inviscid, incompressible flows
7. Open channel flows
8. Compressible flows
9. Turbomachinery
10. Computational analysis

Addy also noted the objectives of laboratory instruction should be the following:

1. to improve understanding

2. to stimulate interest

3. to confirm theory

4. to demonstrate "real world" problems

5. to provide "hands-on" experiences.

He reminded his listeners that the "laboratory aspect" of fluid mechanics should be interpreted broadly to include various approaches:

1. Demonstrations (in both class and laboratory)

2. Films and videotapes

3. Simplified experiments integrated with lectures to demonstrate and illustrate phenomena under discussion

4. More complex experiments on systems and/or isolated phenomena.

Addy also suggested that our fluid-mechanics teaching effectiveness could be improved by offering a course with an integrated lecture and laboratory which would include weekly experiments, relevant videotape and movies, computer-based data acquisition procedures, and emphasis on physical phenomena and understanding. A means of providing this integrated instruction could involve a national effort to design, develop and evaluate a set of experiments appropriate for fluid mechanics instruction. He suggested that there should be close cooperation among universities, government and industries in experiment selection and design. In addition, there should be a regular review and evaluation of these experiments.

Some aspects of graduate study in fluid dynamics were discussed by Prof. Thomas J. Mueller who, recognizing that first-year graduate students come from a variety of backgrounds, recommends a common, intermediate-level fluid mechanics course to bring them all to the same level. Furthermore, he recommends that students pursuing graduate study in fluids engineering should be required to take courses in all three major areas of fluid dynamics, i.e., theoretical, experimental, and computational, regardless of their ultimate goal. Mueller also addressed what he considers to be the major and most important difference between undergraduate and graduate degrees, i.e., the research experience. He thinks that all M.S. students should be required to do research and write a thesis. (This opinion was also shared by one other panelist and several discussers.) The combined experience of writing and research was judged by Mueller to be invaluable whether the student terminates with the master's degree or continues to the Ph.D. level. (*Authors' note: there is an alternative belief in certain sectors of the University community that the M.S. thesis should be required only for those students committed to R&D careers. For others an M.S. program involving advanced courses, which require some writing experience, appears to be desirable.*)

Perspectives From Industry and Government

The general consensus among industry and government agency participants was that, while a sound understanding of the fundamentals of fluid mechanics is very important, it should be accomplished without the elegance frequently used by engineering educators. Dr. Kenneth Hickman noted that many companies with "engineered products" do not have large engineering staffs nor many fluids specialists. These companies often have broad technology applications. Most of their engineers tend to be "generalists" who increase their value to the firm through experience, aided by a few "specialists" who serve as mentors and consultants. Fluids engineering often is not a separate discipline in these companies, but instead is imbedded in the design function. The design or project engineer in these smaller firms needs to be aware of his knowledge limitations and recognize when to seek help from others such as the specialists. In large companies where fluids engineering is important, as in the aerospace,

automotive, or petroleum industries, staffs of specialists in fluid mechanics are necessary and can be accommodated easily. Nevertheless, each industry has a different set of specialized requirements from the others. Thus, a general undergraduate preparation is desirable to provide flexibility of choice even for engineers pursuing large company or institutional careers.

Speaking to educators, Hickman emphasized that new fluids engineers need a solid grounding in fluid mechanics without a large measure of elegance. The beginning fluids engineer should have developed problem-solving skills and should have been taught to recognize the existence of experimental uncertainty and analytical modeling limitations as well as the inexact nature of many design tools. With respect to textbooks, he suggested that they be written primarily to promote learning and not to serve as comprehensive reference books, that they contain a minimum of mathematics and a large number of practical examples, and that they include challenging homework problems designed to reinforce the lecture material. He suggested that emphasis in lectures be put on teaching students to formulate problems from given data, making such assumptions as are dictated by the desired level of sophistication of the solution. He was especially interested in the use of films, flow visualization albums, and visits to advanced laboratories in the community or local industries as "interest builders" for undergraduates, i.e., methods of highlighting fluid flow processes and equipment which would stimulate the beginning student's interest in pursuing further study in fluids engineering. He also stressed the importance of "hands-on" laboratories rather than purely demonstrational activity. Moreover, he thought that some experimental work should include a challenging "open-ended" project (in contrast to a preplanned standard experiment).

Presenting the view of a manager in a larger company, Mr. Roger Hanson noted that teamwork and cooperation are very important and that a fluids specialist must frequently interact with specialists from other areas. Large company goals are product-driven, just as in a small company, but multi-technology products are more common. The fluids specialist, or any other for that matter, needs to understand design concept synthesis with input from many technologies. Hanson views research as the creation of analysis methods/tools to effect design. He believes that nonfocused research in a product-driven profit-making company is not desirable; research must produce implementable results. (*Authors' note: This is clearly a debatable issue for numerous examples of significant discoveries illustrate that pure research is indeed an important part of science and engineering.*) Hanson also noted that research and design go hand-in-hand for an engineer practicing in industry while in a university the application of the research is often of secondary importance. (*Additional note: While the authors agree with Hanson on this last point, we note that the major functions of a university can be described as the "development and transmission of knowledge." A university does not exist primarily to effect technology transfer, although this type of activity is becoming more common in many institutions.*)

Dr. Paul Kutler discussed fluid mechanics from the viewpoint of NASA research centers. He observed that the Ames Research Center is currently developing the National Numerical Aerodynamic Simulation Facility or "computational wind tunnel." This effort involves two major thrusts, the first of which is theoretical, i.e., the development of numerical techniques (solution methodologies and algorithms) as well as fundamental work on turbulence physics. The second aspect is developmental in nature, with applications to hypersonic flow, turbulence and transition modeling, and control-surface heating.

Kutler noted that NASA will continue to rely heavily on

universities for research and innovation in fluid mechanics as well as for graduates motivated toward research careers. He reminded the audience that NASA is also involved in experimental fluid mechanics as well as CFD; extensive experimental work is required to calibrate codes and to improve the understanding of flow physics. Kutler also emphasized the National Aeronautical R&D goals which encompass substantial improvements in subsonic flight technology as well as entirely new capabilities for civilian transportation at supersonic speeds and for sustained trans-atmospheric flight with aircraft configurations.

Dr. Michael Reischman spoke on the needs of government funding agencies regarding the technical content of fluid mechanics curricula. He reiterated the need on the undergraduate level for strength in fundamentals with additional skills in both instrumentation and communication. More specifically, Reischman noted the following critical areas where significant advances in fluids engineering capability are needed for the near-term: three-dimensional and non-equilibrium flows, turbulent flow simulation, remote sensing of fluid surfaces, unsteady flow phenomena, and recirculating flows. Corresponding critical areas for the far-term include hypersonic flows, reacting flows, flow management and control, and flow/structure interaction.

Both Kutler and Reischman, representing agencies which focus on emerging technical areas, stressed the importance of producing engineers with graduate degrees who are capable of addressing new national technological thrusts. They urged schools to continually introduce new graduate courses in emerging areas. (*The authors note that it would be difficult for a university to continually introduce complete courses in new subject areas. In order for proper background in fundamentals to be developed, the graduate student must take a certain number of relatively uniform courses. Exposure to new subject areas can be done effectively through occasional special topics courses, exposure to the research of other graduate students, and research seminars given by faculty members and outside speakers.*)

Concluding Remarks

The positions expressed by university speakers and their industry/agency counterparts were hardly surprising. It appears that long-standing attitudes about fluids education continue to be prevalent. For example, the university community continues to believe that fundamentals are important so that the practicing engineer will have the breadth and understanding to handle a large variety of problems. Laboratory experiments and movies are still quite important in aiding physical understanding. The computer now plays a significant role in undergraduate (and graduate) education, assisting not only in simple problem solving, but also in data acquisition and analysis, and in numerical solutions of complicated problems.

Industry and agency representatives expect the practicing engineer to be able to readily solve practical problems as well as to understand hardware and economic constraints. Their position is that mathematical elegance is often overemphasized and does not contribute to the understanding of fluid mechanics. It was also noted that industry/agency engineers must be "team players" who are dedicated to the goals of their organization and not "free wheelers" who have their own professional agenda. (*Authors' note: A certain amount of personal entrepreneurship is required if one is to be successful as a faculty member.*)

The authors, while sympathetic to both positions, do not believe that there is any easily definable "middle ground." Indeed, it may be that the present degree of pluralism in fluids engineering education (being highly dependent on local institutional goals and faculty philosophies) does, in fact, produce the appropriate variety of backgrounds required to sup-

port national technological progress. Thus, it is incumbent on employers to select carefully those institutions which are most likely to produce the types of beginning engineers needed to accomplish their mission.

At the conclusion of the panelists' presentations, there ensued a lively discussion from the audience, thus confirming that the topic of fluids engineering education remains an important concern to the Mechanical Engineering profession. A recurring emphasis from the audience was that fluid mechanics should not be perceived by the typical undergraduate student as a subset of applied mathematics or computer programming; rather that the physics of fluid flow must be emphasized. Courses must illuminate to the greatest extent possible the ultimate use of fluid mechanics in the design of devices and systems. In particular undergraduate students must learn to formulate problem statements from realistic input data and not be satisfied with learning only how to solve contrived "homework" problems.

While the field of computational fluid dynamics continues to flourish at the graduate level there needs to be much more effort in introducing user friendly CFD codes into the undergraduate domain while, at the same time, reminding the users to be aware of the types of fluid flow models which are embedded within the code. Indeed, this caution applies even more seriously to the graduate student domain where students are often more interested in the numerics than the physics. In addition, the introduction of computer-based data acquisition systems and computer-driven experiments should be accelerated.

For educators, financial constraints are often an overriding concern. Laboratory equipment and computer software are high cost items as are the salaries of technicians required to maintain them. Keeping undergraduate fluids courses at the leading edge requires a group of highly dedicated faculty at each institution. Otherwise, only the highly visible research programs will receive the funding necessary to sustain growth and development.

Acknowledgment

The authors express their appreciation for the assistance of panelists in providing summaries of their comments. Panelists included Professors Allan Acosta (Cal Tech), A. L. Addy (University of Illinois), Dale Anderson (University of Texas at Arlington), John Foss (Michigan State University), Alan McDonald (Purdue University), Thomas J. Mueller (Notre Dame University), and Frank White (University of Rhode Island); Mr. Roger Hanson (Boeing Aerospace Company, Seattle), Dr. Kenneth Hickman (York Corporation, Pennsylvania), Dr. Paul Kutler (NASA-Ames Research Center), Dr. Michael Reischman (Office of Naval Research) and Dr. William R. Sears (University of Arizona).

References

- 1 Lamb, J. P., and Swim, W. B., "A Survey of Fluid Mechanics Education of Mechanical Engineers," ASME JOURNAL OF FLUIDS ENGINEERING, Vol. 99, No. 3, 1977, pp. 446-455.
- 2 Fox, R. W., and McDonald, A. T., *Introduction to Fluid Mechanics*, Wiley, New York, 2nd Ed., 1973.

3 Gerhart, P. M., and Gross, R. J., *Fundamentals of Fluid Mechanics*, Addison-Wesley, New York, 1985.

4 Roberson, J. A., and Crowe, C. T., *Engineering Fluid Mechanics*, Houghton Mifflin, Boston, 2nd Ed., 1975.

5 Shames, I. H., *Mechanics of Fluids*, McGraw-Hill, New York, 2nd Ed., 1982.

6 White, F. M., *Fluid Mechanics*, McGraw-Hill, New York, 1979.

7 Olsen, R. M., *Essentials of Fluid Mechanics*, International Textbook, Scranton, Pa., 1961.

8 Streeter, V. L., *Fluid Dynamics*, McGraw-Hill, New York, 3rd Ed., 1962.

9 Anderson, J. D., *Modern Compressible Flow*, McGraw-Hill, New York, 1982.

10 John, J. E. A., *Gas Dynamics*, Allyn and Bacon, Boston, 1969.

11 Shapiro, A. H., *Dynamics and Thermodynamics of Compressible Fluid Flow*, Vol. 1, Ronald, New York, 1953.

12 Zucker, R. D., *Fundamentals of Gas Dynamics*, Matrix, Champaign, Ill., 1977.

13 Foss, J. F., "Basic Elements in a Fluid Mechanics Laboratory Experience: An Engineering Science Approach," ASME JOURNAL OF FLUIDS ENGINEERING, published in this issue, pp. 9-15.

APPENDIX

Introductory Remarks by Professor William R. Sears

Although fluid mechanics is really a very old subject, for most of us its history begins with Prandtl, Joukowski, "and that crowd" at about the beginning of this century. Before that, it seems, the theory of fluid motions was a beautiful mathematical discipline with little relevance to engineering.

Prandtl seems to have been first to see that the whole mathematical discipline could be related to reality if the gross phenomena due to viscosity—vortices, circulation, separation, wakes, jets, shock waves, etc.—were admitted while the viscosity itself was neglected.

We entered an era when the teaching of fluid mechanics meant, indeed required, teaching about partial differential equations, including mappings, transforms, singularity distributions, boundary conditions, etc.

It is easy to argue that the pendulum swung too far; surely many students lost sight of the forest because of the trees. The worst examples occurred in research; the only requirement for a research topic seemed to be "do-ability". Students were led to believe that there really *are* frictionless fluids, one- and two-dimensional flows, steady flows, infinite domains, and singularities! They were not taught that fluid mechanics is a phenomenological subject, and that the great power and utility of mathematic models is remarkable!

Somehow, the result wasn't catastrophic. Look at the accomplishments of the students of that epoch—probably because students are more impervious to bad teaching than we think.

And now we are into a newer era, that of the high-speed computer—which "can solve any problem"! However, I am concerned with these questions: Is it being made clear to students that computers do *not* solve partial differential equations? What is going to become of all the powerful approximations that have been so useful to practicing engineers? Are we regressing into another age of empiricism, characterized by the statement, "The answer must be right because the code says so. The code must be right because it worked once, for someone?"

Basic Elements in a Fluid Mechanics Laboratory Experience: An Engineering Science Approach

J. F. Foss

Professor,
Department of Mechanical Engineering,
Michigan State University,
East Lansing, Mich. 48824

Experiments for a first fluid mechanics course are described. The basic concepts of pressure and velocity as the primitive variables, the control volume equations and the field equations with Reynolds number dependent properties are reinforced in these experiments. The use of such experiments, as the experimental background for future lecture instruction, is emphasized.

1 Introduction

Fluid mechanics instruction, in a Mechanical Engineering Curriculum, can be presented over a wide range of topics and levels of sophistication. Its focus can range from preparation for the EIT exam to considering the engineering science elements of this discipline subject area. The latter approach was recommended in the historically important Grinter Report [1] and it has been reinforced in the recent communication by Tadmor et al. [2].

The foundational elements for a first engineering science based fluid mechanics course are considered to be:

- (i) pressure and velocity as continuously distributed field variables in space and time,
- (ii) the conservation relationships for mass, momentum, and energy that describe these variables in control volume form, and
- (iii) the differential forms of the mass and momentum conservation equations.

Laboratory experiments, which have been developed to reinforce and to extend the students understanding of these foundational elements, are described below. They have been developed over a substantial period (ca 20 years) in the first of two required courses at MSU. The purpose of this communication is to provide a sufficient description of the experiments (and their motivating spirit) that similar courses, which are being revised or developed, can benefit from the MSU experience.

The importance of the laboratory in fluid mechanics instruction has been addressed by Shapiro [3] (paraphrased): "Fluid Mechanics is an experimental science; having a fluid mechanics course without a laboratory is like having a music appreciation course and never listening to music." It is proposed that this importance is represented in a well recognized and explicit form: "laboratory efforts that build upon and extend the topical material presented in the lecture section," and in a less widely recognized and implicit form: "experiences which serve as the observational bases for future lecture presentations." As an example of the latter form, the lecture instructor could, in the sixth week, make reference to a

specific laboratory observation or experience from the second week. Specific examples of this information flow from the laboratory to the lecture are identified with the phrase: "feed forward" in the following descriptions.

The following experiments also provide an opportunity to introduce the students to a wide range of instruments and data acquisition devices. For the MSU laboratory, manometers, pressure transducers, hot-wire anemometry, and various analog recording devices in addition to a PDP 11-73 microcomputer with A/D, D/A and graphics terminals are used by the students. A conventional instructional style is employed: one TA with 12 students, albeit an "open laboratory" format [4] could be employed. Interested parties are invited to correspond with the author for an exchange of ideas and for additional information regarding the MSU program.

2 The "Universal" Flow System

The laboratory experiments to be described are executed using a single (C.W.) flow system.¹ This facility is shown in Fig. 1 and it has the property of permitting various experiments to be attached to the 6 pressure-side segments of the octagonal chamber. The contoured inlet delivers flow to the two segments that, in turn, deliver the inlet flow to a centrifugal fan at the center of the octagon. The down draft is passed between the floor and a raised plate (i.e., in a radial diffuser passage); it then "fills" the interior space which serves as a common plenum for the "pressure-side" experiments.

3 Elementary Concepts

3.1 Pressure. Thermodynamics provides the student with a basic understanding of pressure as a state variable in a static or a bulk flow condition. Fluid statics extends this basic understanding to include the concept of a pressure distribution on a submerged surface. Given this limited formal background, it is important to recognize that the concept of a continuously variable pressure field (within a fluid and on the

¹Contributed by the Fluids Engineering Division for publication in the JOURNAL OF FLUIDS ENGINEERING. Manuscript received by the Fluids Engineering Division July 27, 1987.

¹The designation: "C.W.," is in recognition of the senior year design project by Candace Wark which was used as the basis for the construction of the facility.

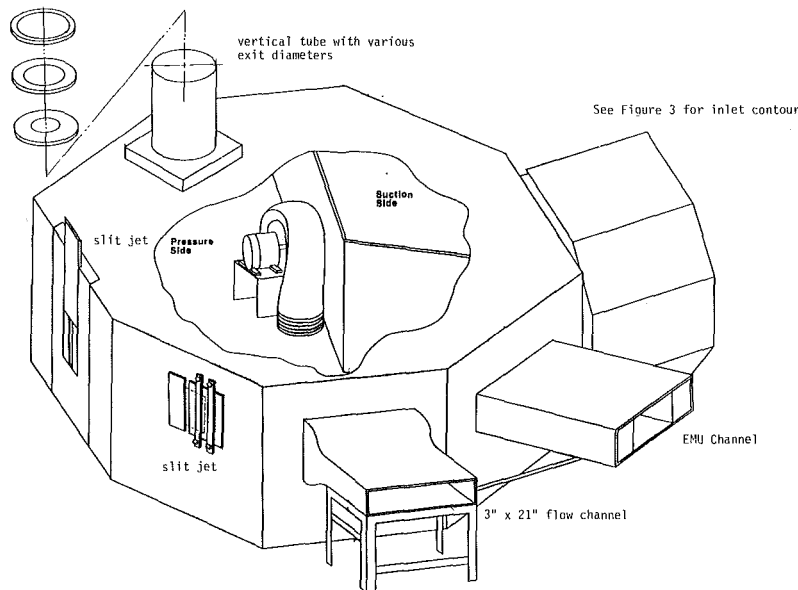


Fig. 1 The C. W. flow system

bounding surfaces of a flow field) requires a substantial increase in the student's perceptual sophistication. Clearly, properly posed experiments can help to build this deeper understanding. Examples of such experiments are described following a brief statement of the salient concepts that should accompany the introduction of pressure as one of the primitive fluid dynamic variables.

The thermodynamic pressure concept can be directly transferred to fluid mechanics if one restricts the scale to that of a fluid dynamic particle.² Since the student can readily imagine an observer in a pressurized volume (eg., $3 \times 3 \times 3 \text{ m}^3$) with a pressure gage to measure the volume's pressure, one need only contract the scale of observation (to, for example, $0.3 \times 0.3 \times 0.3 \mu\text{m}^3$) to identify the pressure of a particle. Since a fluid particle can move, one can further imagine a tracking device which permits a probe and sensor to follow such a particle. This can be identified as an "in-principle" measurement technique. The operational difficulties of such a probe are apparent! However, the imagined device provides the context in which to appreciate our conventional techniques to measure the pressure in a flowing fluid.

The channel flow past a cylinder, which will be used as a principal flow field for this laboratory session, provides an instructive flow field for the relationship of the "in-principle" and "in-practice" pressure measurements; see Fig. 2. Consider a fluid particle which enters the channel to the immediate left of the central streamline. Consider further the particular time when the particle is adjacent to a pressure tap at the cylinder's surface. The scalar character of the pressure shows that the in-principle measurement and the wall tap will provide the same reading (given a sufficiently fast transducer for the in-principle measurement). If the flow is steady, it is noted that all particles on this trajectory experience the same pressure at the tap and a "slow acting" transducer is seen to be quite adequate for this pressure measurement. (A liquid manometer can be introduced as a "very slow" transducer.)

The essential concepts of a Lagrangian and an Eulerian

²Defining pressure in terms of the stress tensor is expected to be a later development in the fluids course. It is expected that the concept of a fluid dynamic particle will have been established in a previous lecture. The following are noted here for completeness. The particle's volume is very small with respect to the mechanical dimensions of the flow but large enough to contain a statistically reliable (e.g., 10^8) number of molecular elements. The particle's velocity: $\mathbf{V}(x_0, y_0, z_0, t)$, is, of course, equal to the net drift velocity of the molecular elements surrounding its centroid.

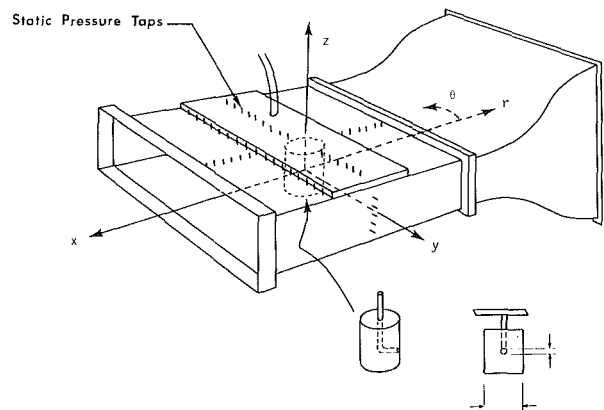


Fig. 2 Schematic representation of cylinder and static taps in the 3×21 " channel. Note: The cylinder can be removed from the channel which permits multipurpose use of this part of the flow system.

description are contained in this example problem. It is clearly advantageous to have these concepts established before the above discussion is presented to the students in the laboratory session.

The measurement of the pressure *in* a flowing stream is clearly a more delicate matter. A probe, whose relatively small cross sectional area and whose streamlined shape provides a negligible disturbance to the flow must be postulated. At this early stage in the students' fluid mechanics experience, it is (perhaps) satisfactory to note that the conventional "L-head" probe provides a balance between the accelerative effect associated with the "nose" of the probe and the decelerative effect of the probe's stem in order to provide a pressure value that would exist in the absence of the probe. Given these considerations, it will be apparent that the cylinder and the L-head probe provide, in practice, the same measurement technique. The cylinder however is the subject of the flow field; the L-head probe is, in principle, a physical device that does not alter the fluid pressure in its neighborhood.

An explicit identification of the errors which can exist with up-or-downwind burrs at a wall tap, as well as the identification of tap-size errors,³ is considered to be appropriate. If the student would, at some future time, be responsible for direc-

³See, for example, Wallace[5].

ting a technician's efforts to place taps in a test model, these factors represent errors to be avoided.

The experimental facility of Fig. 2 provides several quite instructive pressure distributions. The single tap in the cylinder's surface can be positioned to any θ value; $p(D/2, \theta, 0)$ readily follows. The forward ($\theta=0$) and lateral ($\theta=\pi/2$) upper-surface pressure taps that extend beyond the cylinder, can be used to provide pressure distributions which show, respectively, the deceleration of the approach flow and the pressure increase across curved streamlines. For this early lab, the instructor can note that the pressure does not vary laterally (i.e., in the z direction) if the streamlines are parallel. Hence, the pressures at the upper wall represent the pressure for all z values. The agreement between the extrapolated pressure from the ceiling taps and the measured values at $\theta=0$ and $\pi/2$, respectively, help demonstrate this point. The variation of $p(r>D/2, \pi/2, h/2)$ also helps to make this point by contrast.

One of the obvious benefits of such a lab is to provide the conceptual basis for a pressure field: $p[r \geq D/2, \theta]$, from which discrete segments have been examined. Prepared graphical representations of such a field provide a good supplement to this lab. The lecture instructor could use such graphical materials after the students' laboratory experience as an example of the pressure surface $p[r, \theta]$ and its level contours (isobars) which are associated with this flow field. This "feed forward" function is especially effective in the discussion of the pressure gradient term in the differential momentum equation.

3.2 Total Pressure. An accurate concept of "total pressure" is not easily gained; at a minimum it is important to recognize that it is *not* a pressure. That is, a quantity that is dependent upon the choice of a coordinate system⁴ for its value cannot be a scalar quantity. It is recommended that the theoretical bases for "total pressure" be well established before its experimental observations are considered. Namely, the student should understand that the limiting conditions of an (i) inviscid, (ii) incompressible, and (iii) steady flow⁵ will permit the differential (or field) momentum equation to be integrated along a streamline to provide:

$$p_T = p + \rho gh + \rho \frac{V^2}{2}. \quad (1)$$

(The streamline constraint can, of course, be relaxed for irrotational flows but this point is appropriately reserved for later instruction. Also, the incompressible flow condition is required for (1) but not p_T . This more general understanding can also be reserved for later instruction.)

With this foundation, the student can be invited to reconsider the prior experiment and to focus on the equality:

$$p_{\text{plenum}} = p[r = D/2, 0, 0].$$

That is, equal pressures are observed at two locations on a streamline in a portion of the flow that satisfies the conditions: (i), (ii), and (iii). In this sense, the cylinder serves as a "total pressure probe". Since p_T has been shown to be a constant along the trajectory: r and $\theta=0$, the previously acquired $p[r, 0, h/2]$ data can be directly converted to velocity data for:

⁴As an example, one can cite the p_T value of a fluid particle that is located 3m in front of a bicyclist travelling at U_0 . The cyclist, and a stationary observer, would "record" the same p value but would differ on the value of $\rho V^2/2$. Of course, neither p_T nor the "so-called" "dynamic pressure" should be confused with the quantity: "pressure", noted above. The "universal" use of the "total" and "dynamic pressure" require, however, that these terms be defined and clarified for the students.

⁵The first two conditions literally apply, of course, to the fluid of which there aren't any. Functionally, if the flow condition permits, we may speak of the hybrid condition: "inviscid or incompressible flow". See, e.g., Potter and Foss[6], pp. 352 and 55.

$V[r, 0, 0]$. Published examples of flow visualization results for such a flow (e.g., Van Dyke [7]) can be used to complement the quantitative distribution and a presentation of the data in the form $\{V[r, 0, 0]/V_{\text{channel inlet}}\}$ for two different V_{ci} values provides an early experience with a non dimensional representation of experimental data.

With this background, the students can utilize an x - y traverse device and place a Pitot (or a Pitot-static) probe at various locations in the channel flow. The locations, for which the streamlines have experienced shear effects will, of course, show p_T values that are less than p_{plenum} and the magnitude of the reduction can be related to the intensity and the duration of the shear. This flow, like many others that the students will experience in the laboratory, will be turbulent at the Reynolds numbers of a typical laboratory device. Consequently, the output of a pressure transducer, that is attached to the Pitot probe, will show the irregular (and low-pass filtered) fluctuations of such a flow. This laboratory observation may substantially (in time) precede the formal introduction of the Reynolds decomposition (e.g., $u(t) = \bar{u} + \hat{u}$). However, since the fluctuations are an inherent attribute of the flow, the concept of turbulent fluctuations can be noted by the laboratory instructor. This represents another example of the "feed forward" interaction between the student's laboratory and lecture experiences.

The total pressure measurements behind a cylinder provide a natural introduction for the "local" use of the Bernoulli equation and the evaluation of local velocity magnitudes. Since $p_T < p_{pl}$ near the walls and in the wake, one can introduce the concept of "frictional effects" in a flowing fluid and how they can degrade the p_T value along a streamline. However, to apply the Bernoulli equation, the "frictionless" assumption need only apply in the local neighborhood of the stagnation point on the Pitot probe. In their first experience, it is relatively easy for the students to confuse the "global" and the "local" variations in the total pressure. A recognition of their difference is, of course, important for an accurate interpretation of the stagnation probe data. (It is also of interest to note that the increasing p_T value, along the streamline of initially ambient fluid that is accelerated in an ejector flow, provides an example where shear effects increase p_T . Experimentally, this can be demonstrated downstream of the channel exit.)

Another experiment that clarifies that: " p_T need not be a constant along the complete streamline but only in the local neighborhood of the probe" is shown in Fig. 3. This inlet flow is supplied from the atmosphere and, consequently, the interior streamlines exhibit $p_T=0$. The p_T distribution is therefore "flat topped" and $p_T \rightarrow p_w$ as the stagnation probe is moved toward the inlet's surface. The essential point is that the local deceleration (in the neighborhood of the probe tip)

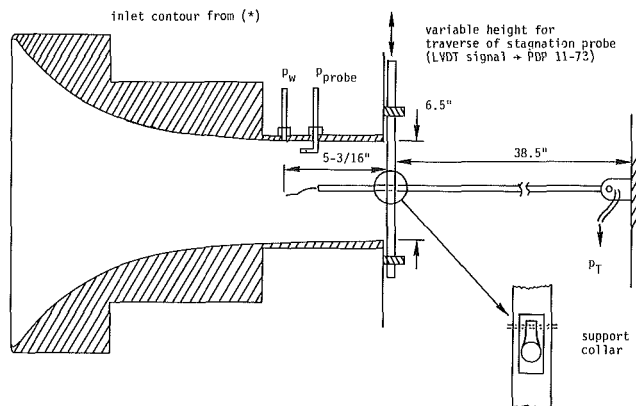


Fig. 3 Total pressure survey at the inlet to the C. W. flow system.* Smith and Wang, *Jour. Aero. Sci.*, Vol. 11, No. 4, 1944, pp. 356-361.

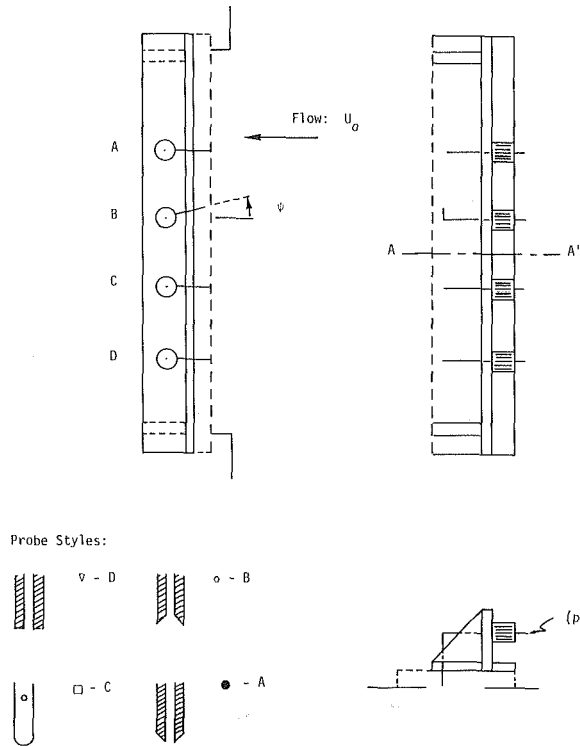


Fig. 4 Yaw angle (ψ) probe response facility. (The slit jet at $\psi=w$ is used to provide U_0 , see Fig. 7.)

must be “inviscid” for the use of the pitot probe to infer the local p_T value whereas globally $p_T < 0$ because of viscous effects. Since the exiting streamlines are adequately straight, a single p_w measurement, in addition to $p_T(r)$, permits $u_x(r)$ to be evaluated.

The experiment of Fig. 3 provides an excellent example of an early (i.e., distant) feed forward for our instruction at MSU. We refer to the decreased velocity region as a “boundary layer”, and we use this phrase at other opportune times as well, even though we will not formally consider boundary layers until the second course.

In an attempt to clarify the difference between the *name* of the probe and the quantity that is measured, a set of probes (with various opening shapes) are positioned at various inclinations (ψ) in a uniform jet flow at atmospheric pressure. The $\psi=0$ data will show zero for the static probe and uniform values for the three pitot probes. The $p_T(\psi)$ and $p_S(\psi)$ results clearly show the results of misalignment and why an apparent increase in flow speed would be recorded with a Prandtl probe. (The latter observation is in agreement with the more rapid decrease in the “ p_S ” reading as compared with that of the “ p_T ” values.)

4 Control Volume Considerations

The conservation laws: Mass, Momentum and Energy (and Moment-of-Momentum as time permits) clearly “deserve” explicit experiments for their elucidation. Some of the experiments that are used at MSU are described in the following sections.

4.1 Conservation of Mass. The slit-jet that was used for the probe angular response evaluation can be used to calibrate the discharge coefficient: $(c_D)_i$, of the inlet contour if all other passages are closed in the C.W. flow system; see Fig. 1. Specifically, since $c_D = 0.611$ for the slit jet (a result of inviscid flow calculations that can be treated as given information for this lab), the exiting flow rate is known if p_T is known. Hence, the additional p_i measurement allows $(c_D)_i$ to be defined as

$$(c_D)_i \equiv \frac{q_i}{A_i U_i} \quad (2a)$$

where

$$A_i = \pi d_i^2 / 4 \text{ and } U_i = \sqrt{\frac{2(p_{\text{atm}} - p_i)}{\rho}} \quad (2b)$$

and

$$q_i = q_e = 0.611 \sqrt{\frac{2(p_{pl} - p_{\text{atm}})}{\rho}} (w L). \quad (2c)$$

The results for the MSU flow system show that $(c_D)_i$ varies as $0.7 \leq (c_D)_i \leq 0.98$ for $0.05 \leq -p_i \leq 0.7$ in. H_2O for the Smith and Wang [8] style of inlet nozzle. This experiment also serves as a good example of the feed forward process. The $p_T(r)$ data from Session 2 can be used to show that $u(r_i)$ is not constant and that the velocity decrease near the wall requires $(c_D)_i$ to be less than 1.0. Since $(c_D)_i$ decreases as the magnitude of the subatmospheric pressure: p_i , decreases, it is also possible to associate thicker boundary layers with lower Reynolds numbers.

The students can be required to reason through the logic of obtaining $(c_D)_i$ from measurements of p_i and p_{pl} using an appropriate control volume and to then experimentally determine $(c_D)_e$ for a set of nozzle plates whose flows are fed from the same plenum; see the nozzle plates of Fig. 1. The measurements are quite simple: $|p_i, p_{pl}|$, but the exercise provides good experience in control volume selection and it introduces discharge coefficients.

4.2 Conservation of Energy. The energy equation stands as the basis for the characteristic curve of a given fan, blower or pump. In the present context, it is useful to define a characteristic curve for the flow system from the atmosphere to the plenum. That is, a given inlet flow rate (q_i) is associated with a given plenum pressure (p_{pl}). The prior data from the conservation of mass experiment can be used to define this: $p_{pl} = f(q_i)$, relationship and this relationship is identified as the flow system’s characteristic curve, see Fig. 5. The concept of a “system load curve,” i.e., the required plenum pressure to deliver a given flow rate through a flow system such as: (i) the channel flow with cylinder, (ii) the slit jet, or (iii) the stack and nozzle plates combination, can likewise be established from the prior experiments; see also Fig. 5. (Note that these earlier data provide a natural “feed-forward” of the information to define a characteristic and a system load curve.)

These prior data allow the prediction of the stable operating point for new combinations of system loads: e.g., channel flow with cylinder and stack flow with a given nozzle plate. The students can easily evaluate their predictions (by direct observations) once they have configured the flow system to conform with the outlet flow geometries of their calculations.

The energy equation is also used as the basis for a flow system description which associates a $p(s)$ value with the streamwise position: s , through the system. The particle paths start in the atmosphere: $p(0)=0$, and return to the atmosphere. The minimum pressure at the fan’s inlet and the maximum pressure at the radial diffuser’s outlet can be noted. The natural diffuser effect for the channel flow past a cylinder⁶ is also used to introduce the concept that a flow can proceed “up the pressure hill.”

4.3 Conservation of Momentum. The previously established $p_T(y)$ and $p_S(y)$ data as well as $p_S(y)$ data for the channel inlet (Fig. 2) can be used as a good example of the conservation of momentum equation. Specifically, various control volumes, e.g., Fig. 6, can be defined which serve to

⁶The $p(r \geq D/2, \theta = \pi/2, h/2)$ measurements show these values to be less than zero. Hence, a “natural diffuser” is present in the channel as the fluid returns to $p=0$ at the channel exit.

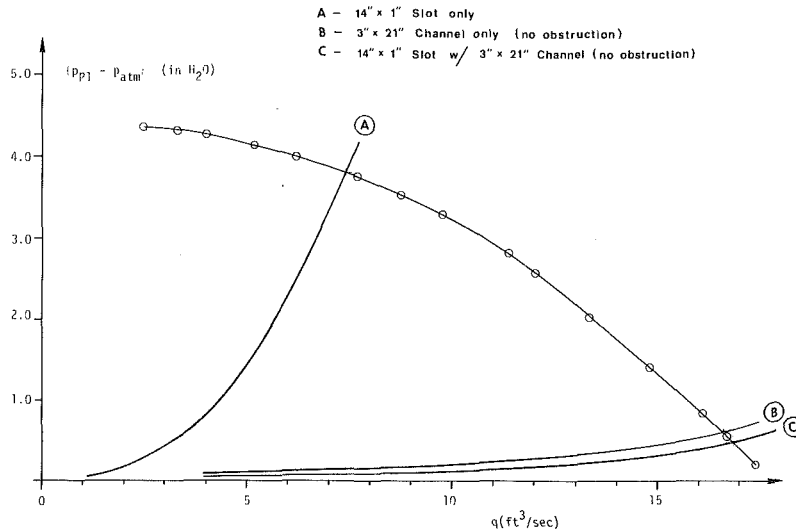


Fig. 5 Characteristic curve for the C. W. flow system

identify various force and momentum flux values for this relatively simple flow field. The generic control volume shown in Fig. 6 could be configured such that x_1 and x_3 were quite far up-and-downstream from the cylinder. In this configuration, the boundary "3" would not be joined to "4" and an external force at some z location(s) would be required to support the cylinder. For the control volume shown, only a portion of the cylinder contributes to the force on the control volume through a pressure and a shear integral. The selection and analysis of different control volumes in this physical problem can strongly contribute to the student's understanding of the terms in the control volume momentum equation. A force transducer, attached to the cylinder via an appropriate sting, could also be used to directly measure the total force on the cylinder. In our laboratory, this force is estimated from the $p(D/2, \theta)$ measurements as recorded in Session No. 1.

A cup anemometer, as used in meteorological wind measurements, provides a quite instructive exemplar problem for the momentum (i.e., for an individual cup) and for the moment-of-momentum (i.e., the complete anemometer) equations. For example, the larger net momentum flux of the open face cup orientation as compared with that of the streamlined configuration is easily demonstrated. A total pressure survey downstream of the complete anemometer (in a stationary orientation) can be used to demonstrate the net moment-of-momentum flux. (Also, torque measurements on the central shaft for various rotational speeds can be used as an excellent example of the shaft work output that is one term in the control volume energy equation.)

5 Field Equations

The acquisition of the basic concepts, that are central to an understanding of the field equations, is greatly assisted by properly posed experiments. Three such experiments are described below. The first experiment also provides a convenient medium for the introduction of the hot-wire anemometer as a tool for the measurement of one or more components of $V(x, y, z, t)$.

5.1 The Accelerating Flow Through a Slit-Jet. Following a description of its basic operating principles, a hot-wire probe can be calibrated at $(x = 3w, y = z = 0)$ in the slit-jet flow field of Figs. 1 and 7. That is, E_{HW} and p_{p1} are jointly measured and the A, B, n coefficients in the expression:

$$E^2 = A + BV^n, \quad (3)$$

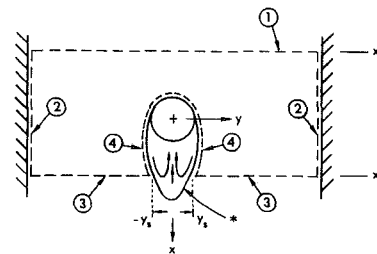


Fig. 6 Control volume surfaces and separation stream surface (y_s) designations for conservation of momentum considerations

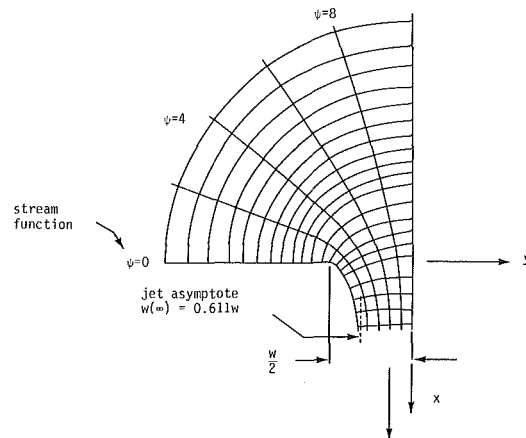


Fig. 7 Slit jet streamline pattern from Berkhoff and Zaratello, *Jets, Wakes and Cavities*, Academic Press, N. Y., Vol. 2. Note: A hot-wire probe located in the neighborhood of $\psi/w = 3$ can be calibrated by simply noting the plenum pressure for various flow rates.

can be evaluated for several velocity values. The hot-wire probe can then be moved laterally and an oscilloscope can be used to show the decrease in \bar{E}_{HW} and the increase in the fluctuation level in the turbulent shear layers. This demonstration is to show the inherent use of the hot-wire device as a tool for following a rapidly varying velocity and to establish a conceptual basis for the subsequent Reynolds decomposition: $u = \bar{u} + u'$, to be introduced in subsequent lectures. These peripheral elements can be accomplished in a short segment of the instructional session.

The probe, once calibrated, can then be used to plot

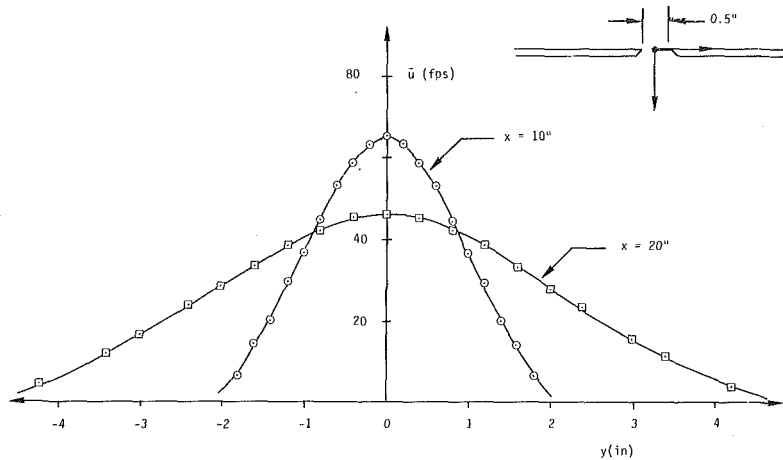


Fig. 8 Dimensional velocity profiles in the slit-jet flow field

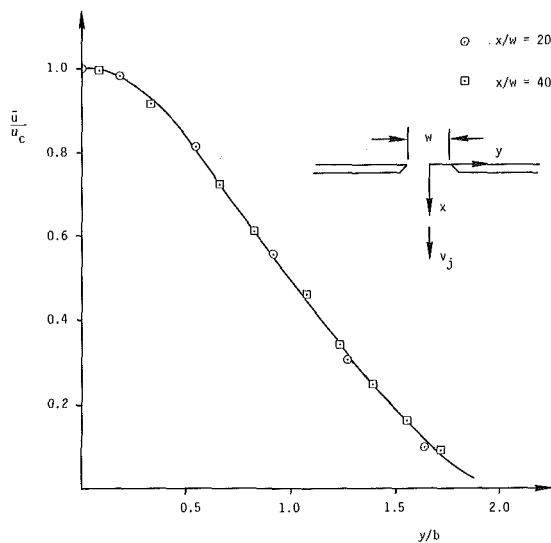


Fig. 9 Self-preserving velocity distribution in a planar jet (b is velocity field "half-width")

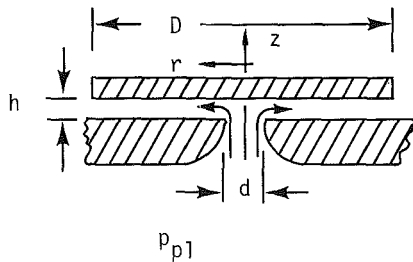


Fig. 10 Radial flow between parallel plates

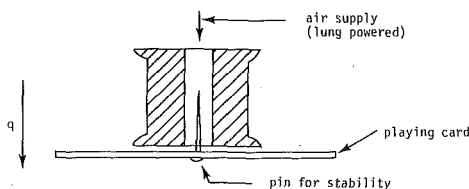


Fig. 11 A high Reynolds number lifting device

$u(x,0,0) (= u_c(x))$ as the observation point is moved into the plenum; see Fig. 1. This $u_c(x)$ distribution can be compared with the irrotational flow solution (viscous effects are confined to thin boundary layers on the nozzle walls) that was used to provide the discharge coefficient of the conservation of mass experiment.

The $u_c(x)$ data so obtained can be used to evaluate $v(x_0, \delta y, 0)$ using the conservation of mass equation in a differential form as:

$$\frac{\partial u}{\partial x} + \frac{\partial v}{\partial y} = 0 \quad (4)$$

and

$$\begin{aligned} v(x_0, \delta y, 0) &= \int_0^{\delta y} \left. \frac{\partial v}{\partial y} \right|_{x_0, y, 0} dy \\ &\approx \left. \frac{\partial v}{\partial y} \right|_{x_0, 0, 0} \delta y \\ &= - \left. \frac{\partial u}{\partial x} \right|_{x_0, 0, 0} \delta y, \end{aligned} \quad (5)$$

where this mathematical formulation is given quantitative expression using the experimental values for $u_c(x)$ and it is supplemented by a graphical representation of the $u_c(x)$, $u_c(x + \delta x)$, $v(y=0) = 0$ and $v(\delta y) < 0$ values that represent the volume fluxes into an Eulerian cube centered at $(x_0, \delta y/2, 0)$. Similarly, a numerical value can be placed on the acceleration of a fluid element that occupies $(x_0, 0, 0)$ at time t :

$$\frac{Du}{Dt} = u \frac{\partial u}{\partial x}, \quad (6)$$

and the pressure gradient that balances this acceleration: $(\partial p / \partial x)$, can also be computed and expressed as a pressure difference (Δp) over the length (δx) of a small cube of fluid. An acceleration of order 50 g's is readily obtained and this helps to establish representative magnitudes for the student's intuitive reference.

A driving motivation for these considerations is to emphasize the Lagrangian character of "acceleration," as directly represented by the left side of (6), and its Eulerian representation on the right side of this equation. With good fortune, the students understand that the fluid particle accelerates (Du/Dt) whereas the region of space is stationary and that $u_c(x)$ is a mapping function between the particle's velocity and its time dependent location.

5.2 A Plane-Jet Flow Field. The flow downstream of the slit-jet opening provides an excellent example of a momentum

preserving (and a self-preserving) flow field. This flow can be examined using a Pitot probe;⁷ see Fig. 8.

The master data of Fig. 8 can be distributed and their source explained. The students can then execute a traverse at $x/w = 30$ and add their processed data to Figs. 8 and 9. The agreement of all data sets for Fig. 9 makes a strong impression and elementary arguments for a self-preserving form of the equations of motion can be given.

This experiment cannot, of course, be completely explained without more advanced concepts but it provides an excellent example of a mass flux increase (entrainment), a zero net momentum flux (uniform pressure and no shear forces for $y \rightarrow \pm \infty$), and a decreasing energy flux (dissipation) that reinforce the previous control volume concepts. It also provides a feed-forward effect that supports the future discussion of modeling a turbulent flow using the Reynolds decomposition: $\bar{u} + \bar{u}'$, and the Reynolds shear stress.

5.3 The Radial Outflow Between Parallel Disks. The appropriately normalized Navier-Stokes equations:

$$\frac{D\mathbf{V}}{Dt} = -\nabla p + \frac{1}{Re} \nabla^2 \mathbf{V} \quad (7)$$

can be thought of as a statement of the balance between the fluid particle's acceleration and the net pressure and viscous forces acting on the particle. In non dimensional form, the Reynolds number provides a guide to the relative importance of the inertial and viscous effects. A graphic demonstration of these concepts is provided by the radial outflow between parallel disks; see Foss [9].

Briefly stated, for the given geometry of Fig. 10 and for the limiting conditions of a large Re value, the radial pressure gradient must decelerate the fluid motion from the region of the entry tube to the outer diameter: D . Conversely for small Re values, the pressure is required to drive the fluid between the same limits. Hence, the "parlor trick" of lifting a playing card while blowing through a spool (high Re) or the operation of an air-hockey table (low Re) are seen as examples of the limiting conditions; see Figs. 11 and 12, respectively. Engineering examples: e.g., a transfer device or an air supported pallet, are easily provided as "real life" motivational problems to the students. Experimental data, from the laboratory device used by the students, is shown in Fig. 13. See Wark and Foss [10], Fig. 1, for a description of the flow system used in this experiment.

6 Summary

A student's undergraduate fluid mechanics course can serve as an introduction to the discipline of fluid mechanics; the laboratory experience is a vital element of this introduction. The effective use of the laboratory requires that theoretical concepts from the lecture are reinforced via experience and that foundational observations, for future concepts, are incorporated into the current experiments.

The examples described above suggest how this can be accomplished, using a common flow system, for (i) the basic variables of fluid mechanics: $\{p(x,y,z,t), \mathbf{V}(x,y,z,t) \text{ and } p_T\}$, (ii) the control volume equations and (iii) the field equations.

⁷The hot-wire probe of the previous experiment could be used for this experiment; it would, of course, offer some advantages in the evaluation of the desired mean velocity magnitude. The ease of hot-wire repair will, it is expected, influence this choice of experimental techniques.

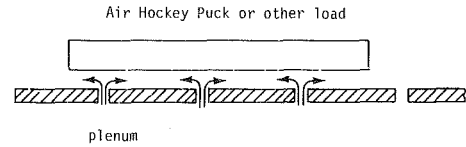


Fig. 12 A low Reynolds number supporting device

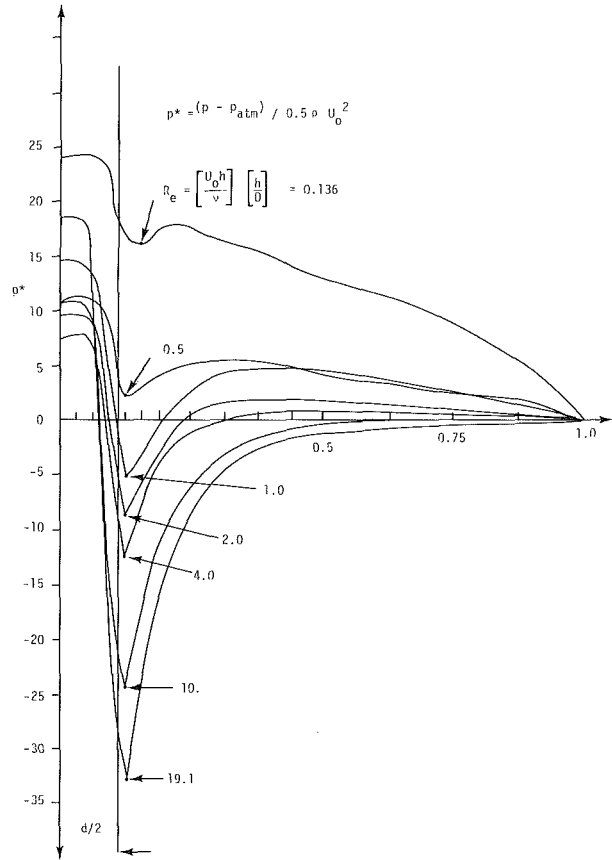


Fig. 13 Nondimensional representation of the pressures on the impact disk of the radial outflow experiment

References

- 1 Grinter, L., "Report on Evaluation of Engineering Education: 1952-1955," *Am. Soc. for Engr. Ed.*, 1955.
- 2 Tadmor, Z., Kohavi, Z., Libai, A., Singer, P., and Kohn, D., "Engineering Education 2001," *Engineering Education*, Nov. 1987, pp. 106-124.
- 3 Shapiro, A. H., "Educational Films in Fluid Mechanics," Nominated Lecture No. L8/64, Institution of Mechanical Engineers, 8 Apr. 1964.
- 4 Thompson, H. D., "An Open Laboratory in Fluid Mechanics," ASEE and IEEE, *3rd Ann. Frontiers in Education*, Purdue University, 9-11, Apr. 1973. (contact the author c/o ME at Purdue University).
- 5 Wallace, J. M., "Absolute Measurements of Static-Hole Error Using Flush Transducers," *Journal of Fluids Mech.*, Vol. 42, 1970, pp. 33-48.
- 6 Potter, M. C., and Foss, J. F., *Fluid Mechanics*, Ronald Press Co., 1975 (Now available from authors at MSU: Great Lakes Press).
- 7 Van Dyke, M., *An Album of Fluid Motion*, The Parabolic Press, Calif. 1982.
- 8 Smith, R. H., and Wang, C. T., *Journal of the Aerospace Sciences*, Vol. 11, No. 4, 1944, pp. 356-361.
- 9 Foss, J. F., "Radial Flow Between Parallel Disks," *Experiments in Fluid Mechanics*, Ed. R. Granger, Holt Rinehart and Winston Book Co., New York, 1988, Exp. 23, pp. 151-156.
- 10 Wark, C. E., and Foss, J. F., "Forces Caused by the Radial Outflow Between Parallel Disks," *ASME JOURNAL OF FLUIDS ENGINEERING*, Vol. 106, 1984, pp. 292-297.

Performance of Butterfly Valves as a Flow Controller

K. Eom

University of Toronto
Institute for Aerospace Studies,
Downsview, Ontario, Canada
M3H 5T6

Butterfly valves have been used for shut-off and throttling-control application. It is found that the information available on loss coefficients of butterfly valves for good throttling control is limited at present. This report investigates the performance of two different configurations of butterfly valve: perforated blades and different diameter of solid blades that allow partial opening of the valve at closed position. The experimental results support the suitability of a butterfly valve for good flow control.

1 Introduction

Butterfly valves are advantageous over gate, globe, plug, and ball valves in a variety of installations, particularly in the larger sizes. The most obvious advantages are savings in weight, space and cost. They are suitable for shut-off and throttling-control applications; they are especially suited for handling large flows of liquids or gases at relatively low pressures and for handling slurries or liquid with large amounts of suspended solids (Schweitzer, 1972). Operation of a butterfly valve is quick and easy because a 90-degree rotation of the spindle moves the flow control element from the fully closed to the fully opened position.

Butterfly valves are one of the oldest known types of control valves. When a valve is required for control purposes, a predetermined partial opening of the valve will be required in order to have good control characteristics. Furthermore, in order to afford good stable control, a smooth control curve with no hysteresis is required and the valve should not be overly sensitive in any region.

The first attempt at collecting and collating published data was made by Cohn (1951). Based on a flow formula adopted by Cohn, a study of butterfly valve flow characteristics was conducted by McPherson et al. (1951). But the information available on loss coefficients of butterfly valves for good throttling control is limited at present.

The objective of this work is to measure and to present the results obtained by using perforated blades and different diameters of solid blade that allow partial opening of the valve at the closed position (blockage ratio, $R = \text{area of disk}/\text{area of pipe or duct}$).

2 Test Configuration and Methods

The test configuration consists of a butterfly valve, orifice, blower, Helipot industrial servo system, piezoresistive pressure transducers, instrumentation amplifier, analog filter (4th order Chebyshev), Keithly data acquisition system, and an IBM-PC (see Fig. 1). The total pressure loss, ΔP_1 , across the valve is measured as shown in Fig. 2, and a constant

diameter, $D = 4''$, is maintained between station 1 and station 2. In order for hydraulic grade lines to be unaffected by the valve, a distance of $2D$ upstream and $4D$ downstream is allowed for the measurements of ΔP_1 (see Fig. 2). Two pressure transducers are used to measure pressure loss across the orifice and butterfly valve. Data from these units are conditioned by an ENDEVCO® Model 4423 signal conditioner. Signal filtering is provided by 4th order Chebyshev filters. Data is fed via an A/D converter into an IBM personal computer for analysis. In order to study the effects of closing angle, and partial opening of the valve at closed position, two different types of valve configuration are used in this work: (1) per-

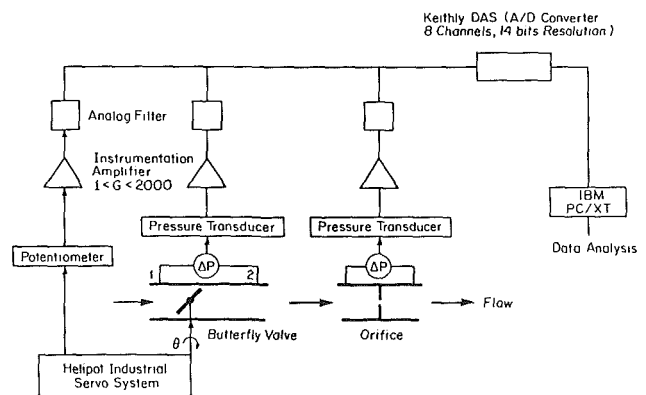


Fig. 1 Test configuration

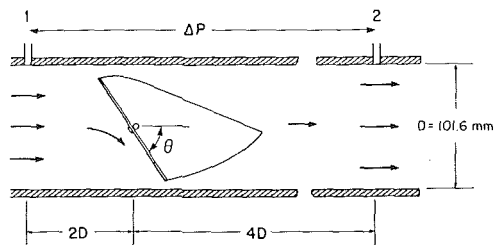


Fig. 2 Flow across butterfly valve

Contributed by the Fluids Engineering Division for publication in the JOURNAL OF FLUIDS ENGINEERING. Manuscript received by the Fluids Engineering Division October 2, 1986.

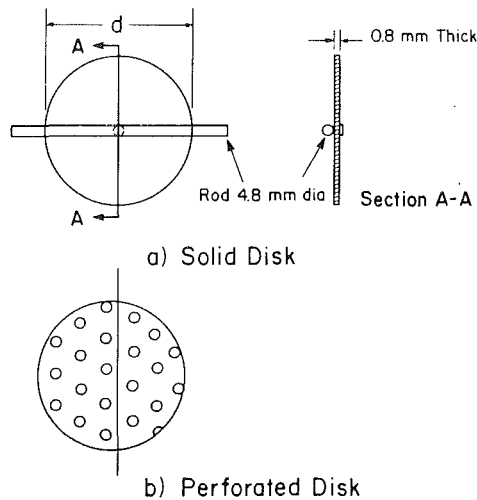


Fig. 3 Blade configuration

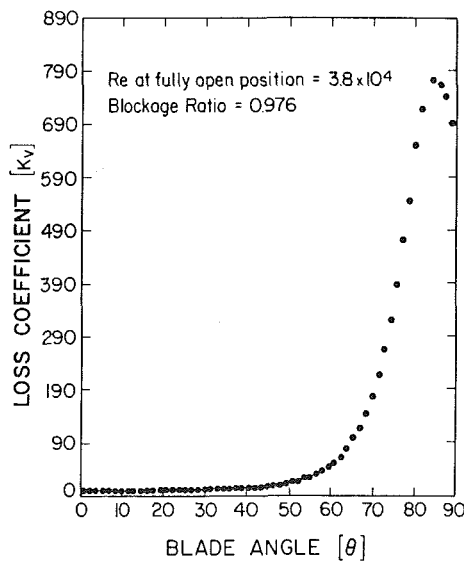


Fig. 4 Loss coefficients of butterfly valve versus blade angle. (Uncertainty in $K_v = \pm 2$ percent and in $\theta = \pm 5$ percent.)

forated disk (screen type), and (2) solid disk (see Fig. 2). Each disk (blade) allows partial opening of the valve at closed position (percent opening of valve) and its solidity is listed in Table 1.

3 Loss Coefficients

In order to study particular aspects of internal flow, there are considerable advantages in adopting one performance parameter, the system loss coefficients, for all system components.

A loss coefficient is defined as the nondimensional difference in total pressure between the extreme ends of two long

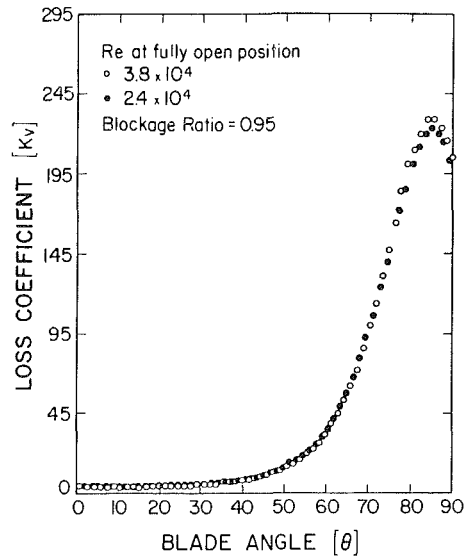


Fig. 5 Loss coefficients of butterfly valve versus blade angle. (Uncertainty in $K_v = \pm 2$ percent and in $\theta = \pm 5$ percent.)

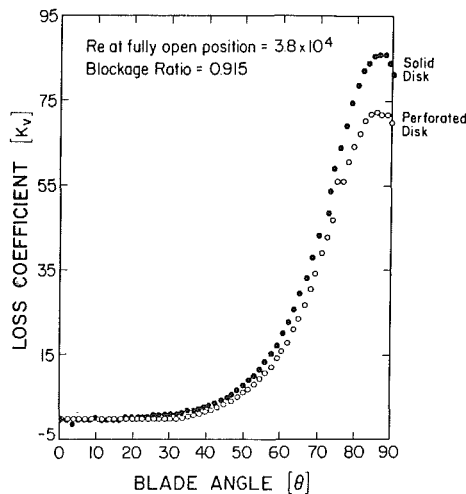


Fig. 6 Loss coefficients of butterfly valve versus blade angle. (Uncertainty in $K_v = \pm 2$ percent and in $\theta = \pm 5$ percent.)

pipes or passages. In nondimensionalizing the pressure loss, the convention is to use the component's inlet velocity pressure, except when the component is an inlet from a large space when the pipe or passage velocity pressure is used. The long pipe or passage before the component ensures a developed flow at inlet, and the long pipe or passage at outlet from the component ensures that losses caused by flow redevelopment after the component are debited to the component. The inlet and outlet developed friction gradients are projected to component and the difference between them established. The loss coefficient, K , is given by (Miller, 1978):

Nomenclature

D = diameter of pipe
 C_Q = flow coefficient
 g = gravity
 ΔH = total head loss
 K = loss coefficient
 ΔP = total pressure loss

R = blockage ratio (= area of disk/area of pipe or duct)
 U = mean velocity
 $\Delta\theta$ = controllable blade angle
 $L = \theta(0.95 K_{\max}) - \theta(0.05 K_{\max})$
 θ = blade angle

Subscripts

1, 2 = flowfield locations
max = maximum
v = valve

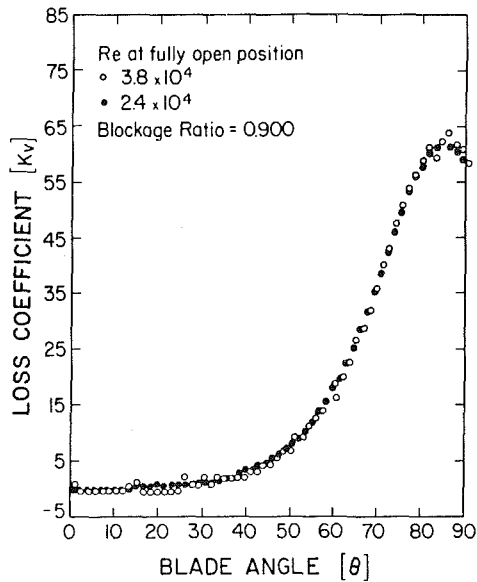


Fig. 7 Loss coefficients of butterfly valve versus blade angle. (Uncertainty in $K_v = \pm 2$ percent and in $\theta = \pm 5$ percent.)

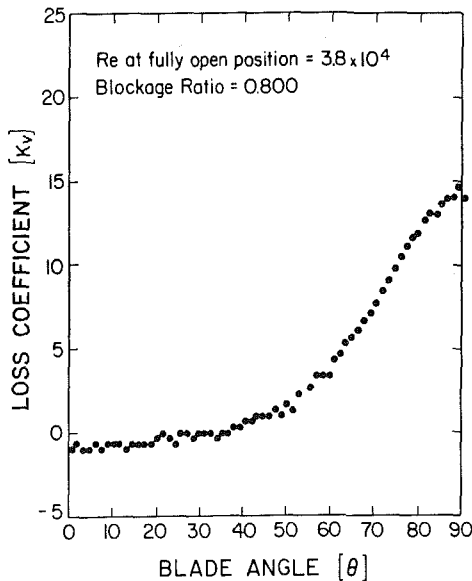


Fig. 8 Loss coefficients of butterfly valve versus blade angle. (Uncertainty in $K_v = \pm 2$ percent and in $\theta = \pm 5$ percent.)

$$K = \frac{\Delta H}{\frac{U^2}{2g}} = \frac{\Delta P}{\frac{\rho U^2}{2}}$$

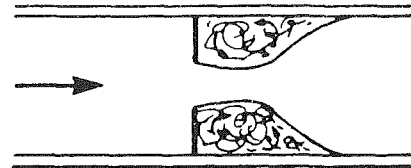
where ΔH is the total head loss, m of fluid; ΔP is the total pressure loss, in N/m^2 ; U is the mean velocity, m/s

The relation between loss coefficient, K , and flow coefficient, C_Q , adopted by Cohn (1951) is

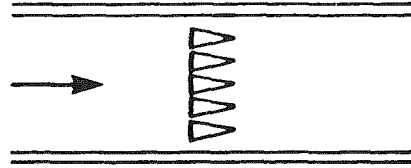
$$C_Q = (2K/\pi)^{1/2}$$

4 Results and Discussion

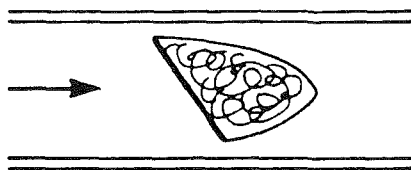
In order to test the performance of butterfly valves intended to produce good throttling control, the percentage opening of the valve at closed position is varied systematically. Based on mean pipe velocity head, the loss coefficients of solid disks at blockage ratio of 0.976, 0.950, 0.915, 0.900, and 0.800 were



a) Orifice Plate



b) Screen



c) Butterfly Valve

Fig. 9 Flow separation generated by system component

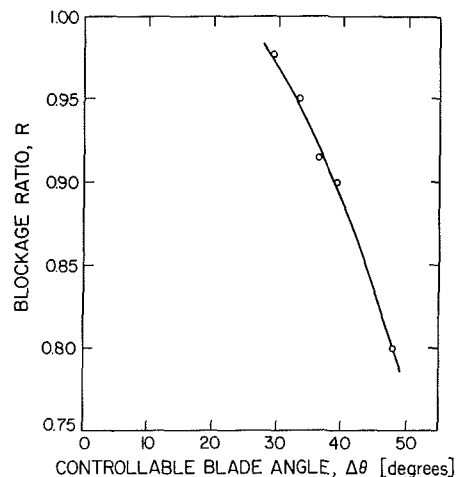


Fig. 10 Blockage ratio, R , versus controllable blade angle, $\Delta\theta$. (Uncertainty in $\Delta\theta = \pm 1$ percent and in $R = \pm 1$ percent.)

obtained at Reynolds number of 10^4 . From experimental data, the loss coefficient is plotted against closing angle for each disk and the effect of blockage ratio on loss coefficients are shown in Figs. 4 to 8. It is presumed that the very slight negative values of loss coefficients, K_v , in Figs. 5 to 8 result from a change in calibration of the pressure transducer due to sensitivity of the temperature. In addition, the peak values of

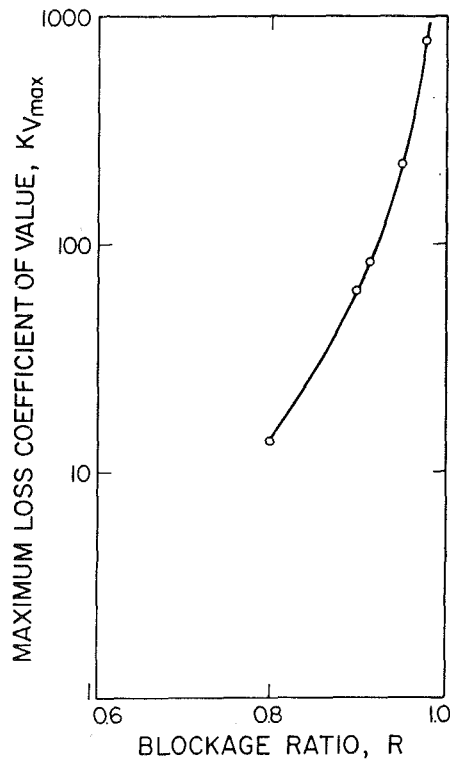


Fig. 11 K_{vmax} versus blockage ratio, R . (Uncertainty in $K_{vmax} = \pm 2$ percent and in $R = \pm 1$ percent.)

K_v occurring in the vicinity of the 90 deg blade angle instead of at the 90 deg blade angle are due to the calibration inaccuracy of the potentiometer. According to results obtained from predetermined percentage opening of the valves, the curves are smooth and have reasonably good slopes for good throttling control when the solid disk allows 0.950, 0.915 blockage ratio, and no hysteresis was found. Tests were performed at Reynolds numbers of 3.8×10^4 and 2.4×10^4 for 5 and 10 percent opening of the valve, respectively. These Re were obtained when $\theta = 0$ deg. Within this limited range of Reynolds number, the loss coefficient appears to be virtually independent of Reynolds number. With a view to investigating the effect of a screen type of blade on loss coefficients, both perforated disk and solid disk at blockage ratio of 0.915 were tested and the results are given in Fig. 6. As an illustration, Fig. 9 shows flow separation, followed by intense mixing and flow reattachment, generated by system components used in this work. As shown in Fig. 6, the maximum loss coefficient of a solid disk is a little larger than that of a perforated disk when the valve approaches the closed position. However, the difference between values of loss coefficients of the solid disk and of the perforated disk is not large. As shown in Fig. 10, good correlation was obtained between controllable blade angle, $\Delta\theta$, and percentage opening of the valve (blockage ratio). On the other hand, blockage ratio is plotted against maximum loss coefficient of valve, K_{vmax} , in Fig. 11. In an in-

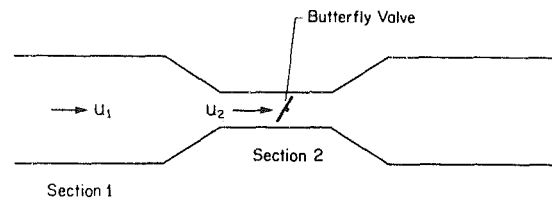


Fig. 12 Venturi-type butterfly valve installation.

Table 1 Percent opening of valve used by different types of valves

Type of valve	Blockage ratio, R
Perforated disk	0.915
Solid disk	0.976, 0.950, 0.915, 0.900, 0.800

$$R = \frac{\text{area of disk}}{\text{area of pipe or duct}}$$

dustrial application, when the controllable K_v is determined from the specification of air flow system, the controllable blade angle, depending upon the accuracy of throttling control, can be chosen. Then, the corresponding blockage ratio can be found in Fig. 10 and the resulting K_{vmax} is also determined from Fig. 11. Furthermore, venturi-type butterfly valve installation, as shown in Fig. 12, can be employed to get amplified or attenuated K by simply exploiting the fact that $K_1 = K_2 \times (U_2/U_1)^2$.

5 Conclusions

The systematic investigation of the performance of the butterfly valve by varying the blockage ratio allows to perceive the capability of a butterfly valve for throttling control purposes. As the position of the valve changes, fairly good correlation is obtained for each valve given the fixed blockage ratio in the values of loss coefficients.

Acknowledgment

Grateful acknowledgment is made to N. Milligan who assisted in the preparation of experimental setup, and to Prof. B. Etkin, who suggested and supervised this research.

Financial support was provided by NSERC Operating Grant No. A0339.

References

- Cohn, S. D., 1951, "Performance Analysis of Butterfly Valves," *Instruments*, Vol. 24, pp. 880-884.
- McPherson, M. D., Strausser, H. S., and Williams, J. C., 1951, "Butterfly Valve Flow Characteristics," *J. Hydraulic Division*, ASCE, Vol. 83, pp. 1167.1-1167.27.
- Miller, D. S., 1978, "Internal Flow System," *BHRA Fluid Engineering Series*, Vol. 5, pp. 7-16.
- Schweitzer, P. A., 1972, *Handbook of Valves*, Industrial Press Inc., pp. 93-103.

Analyses of Hydrodynamic Radial Forces on Centrifugal Pump Impellers

D. R. Adkins*

C. E. Brennen

California Institute of Technology,
Pasadena, CA 91125

Hydrodynamic interactions that occur between a centrifugal pump impeller and a volute are experimentally and theoretically investigated. The theoretical analysis considers the inability of the blades to perfectly guide the flow through the impeller, and also includes a quasi-one dimensional treatment of flow in the volute. Flow disturbances at the impeller discharge and the resulting forces are determined by the theoretical model. The model is then extended to obtain the hydrodynamic force perturbations that are caused by the impeller whirling eccentrically in the volute. Under many operating conditions, these force perturbations were found to be destabilizing. Comparisons are made between the theoretical model and the experimental measurements of pressure distributions and radial forces on the impeller. The theoretical model yields fairly accurate predictions of the radial forces caused by the flow through the impeller. However, it was found that the pressure acting on the front shroud of the impeller has a substantial effect on the destabilizing hydrodynamic forces.

Introduction

This study investigates the forces that result from the hydrodynamic interaction between the impeller and the volute in a centrifugal pump. Figure 1 shows a common type of centrifugal pump with a few of the key components identified. Volutees are usually constructed to provide a uniform impeller discharge when the pump operates at design conditions. However, the discharge flow pattern will no longer be uniform at off-design conditions. Once the flowrate changes, the discharge conditions around the impeller become asymmetric for any given volute. Even at the volute design flowrate, the discharge conditions could still become asymmetric if the impeller is displaced from the "design" center of the volute by shaft deflection, bearing wear, etc. In either case, a net radial force on the impeller will result from the asymmetric discharge conditions.

It is customary in rotordynamic analyses to linearize the radial forces acting on the rotor in terms of a steady portion acting on the centered impeller, and a time dependent part caused by the impeller whirling. Here it will be assumed that the impeller whirls in a small circular orbit. Referring to Fig. 1, these terms may be expressed as,

$$\begin{Bmatrix} F_x^* \\ F_y^* \end{Bmatrix} = \begin{Bmatrix} \bar{F}_x \\ \bar{F}_y \end{Bmatrix} + \begin{bmatrix} A_{xx}^* & A_{xy}^* \\ A_{yx}^* & A_{yy}^* \end{bmatrix} \begin{Bmatrix} \epsilon^* \cos \omega t \\ \epsilon^* \sin \omega t \end{Bmatrix}, \quad (1)$$

where \bar{F}_x and \bar{F}_y result from the interaction of the centered impeller with the volute, and the matrix $[A]$ relates the perturbed

force to the eccentric position of the impeller. The $[A]$ matrix will be a function of the whirl speed, ω , and is often expressed as a quadratic in ω so that the system resembles a simple stiffness, damping, and mass model.

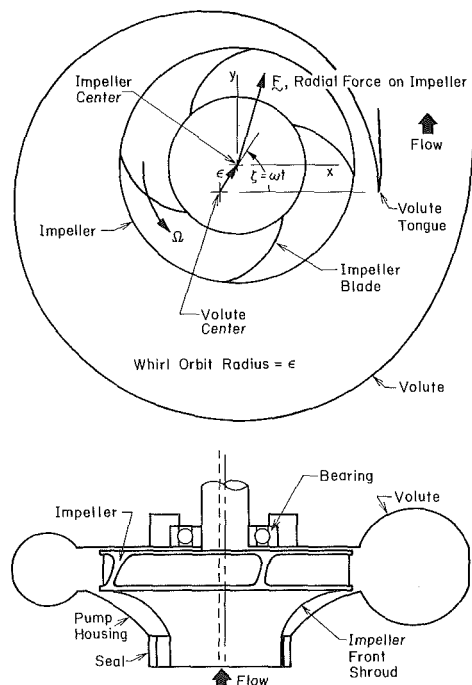


Fig. 1 Description of a centrifugal pump

*Now at Sandia National Laboratories, Albuquerque, NM 87185.

Contributed by the Fluids Engineering Division for publication in the JOURNAL OF FLUIDS ENGINEERING. Manuscript received by the Fluids Engineering Division September 29, 1986.

The steady or mean forces, \bar{F}_x and \bar{F}_y , have been examined in several studies and an understanding of them has been greatly enhanced through papers by Iversen et al. (1960), Csanady (1962), and Agostinelli et al. (1960) to name a few. All of these authors have shown that there is a particular flow-rate where forces on the impeller will be minimized for a given volute. Previous experimental (Chamieh et al., 1982, and Jery et al., 1984) and theoretical (Colding-Jorgensen, 1980) investigations have also shown that the components of $[A]$ are such that a whirling motion of the impeller would be encouraged rather than dissipated by the hydrodynamic effects. This finding has generated concern that the rotor assembly may whirl at one of its natural frequencies even though the shaft may be rotating well above this speed. If the impeller whirls at a subsynchronous speed, the shaft will be subjected to alternating flexural stresses that can cause metal fatigue (see Ehrich and Childs, 1984).

In the current study, a theoretical model of the volute and impeller flows will be developed and compared to experimental results. Previously, a potential flow model for the steady forces on a centered impeller was given by Csanady (1962) and this work was later extended by Colding-Jorgensen (1980) to include the effects of the impeller whirling within the volute. Two dimensional potential flow models for whirling impellers have also been developed by Shoji and Ohashi [1980] and [1987]. In potential flow models, however, problems arise in relating the two dimensional theoretical volute profiles to the three dimensional geometries of real volutes. To avoid this problem, the model developed in this paper uses a bulk flow description of the volute flow which can use measured volute geometries directly. A similar treatment of the volute flow was presented by Iversen et al. (1960), but the influence of this flow on the impeller discharge conditions was largely ignored and only the non-whirling impeller was considered. The impeller/volute interaction will be included along with the effects of impeller whirl in the present analysis.

Theoretical Analysis

In developing the current theoretical model, the problem is broken into its two natural parts; models are constructed for the flow through the impeller and in the volute. The equations that are generated in these two parts are then combined by matching the pressures and velocities at the impeller discharge to those at the volute inlet. A full development of this model is given by Adkins (1985) and only a brief summary will be presented here.

Nomenclature

b = width of impeller discharge passage
 h = total head ($h^* = 2h/\rho\Omega^2 R_2^2$)
 $j = \sqrt{-1}$
 k = impeller phase coefficient = $\cos(\tan \gamma \ln(R)) + j \sin(\tan \gamma \ln(R))$
 r, θ = polar coordinate system
 s = length in tangential direction
 t = time
 v = relative velocity in impeller
 w = width in volute
 x, y, z = rectangular coordinate system
 $\frac{A}{\ln rA}, \frac{rA}{\ln rA}$ = moments of volute cross-sectional area (defined in equations (14a-e))
 A_{ij} = ($i = x, y, j = x, y$) components of generalized hydrodynamic force matrix $[A]$ ($A_{ij}^* = A_{ij}/\rho\pi b\Omega^2 R_2^3$)
 C_{ij} = ($i = x, y, j = x, y$) components of damping force matrix $[C]$ ($C_{ij}^* = C_{ij}/\rho\pi b\Omega R_2^2$)

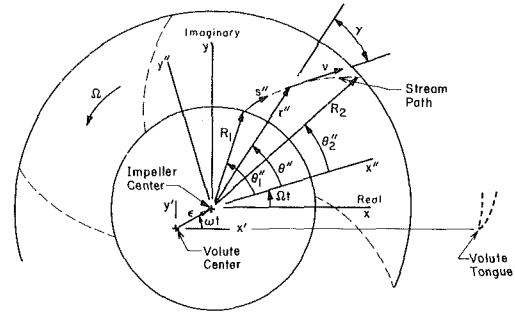


Fig. 2 Geometry of a centrifugal pump impeller

Governing Equations for the Impeller. Figure 2 illustrates the geometries used in developing the impeller model. To relate the pressure between the inlet and discharge of the impeller, a simplified unsteady form of Bernoulli's equation is written as,

$$\frac{P_i}{\rho} + \frac{v^2}{2} - \frac{\Omega^2 r''^2}{2} + \int_{s''} \frac{\partial v}{\partial t} ds'' - \omega^2 \epsilon \int_{s''} \cos(\omega t - \Omega t - \theta'') dr'' - \omega^2 \epsilon \int_{s''} \sin(\omega t - \Omega t - \theta'') r'' d\theta'' = F(t), \quad (2)$$

Here the flow is assumed to be two dimensional and the impeller whirl speed constant.

To simplify the model, certain assumptions must be made about the velocity field within the impeller. Specifically, the flow in the impeller is assumed to follow a spiral path with inclination angle, γ , which is fixed relative to the impeller for a given flowrate and head rise so that,

$$\theta_2'' = \theta'' + \tan \gamma \ln(r''/R_2). \quad (3)$$

Here (r'', θ'') and (R_2, θ_2'') are the coordinates of a general point on a streamline within the impeller and at the position of discharge respectively. The flow path angle, γ , of the streamlines is permitted to deviate from the impeller blade angle and it is found by equating theoretical and experimental head/flowrate characteristics (see Closure Conditions). To account for the impeller flow asymmetry caused by the volute, a circumferential perturbation is superimposed on the mean impeller flow. This flow perturbation is assumed to be stationary

D_p = pressure coefficient at volute inlet = $2(P_v(R_2', \theta') - h_1)/\rho\Omega^2 R_2^2$
 F = force acting on impeller ($F^* = F/\rho\pi b\Omega^2 R_2^3$)
 $F(t)$ = integration constant in Bernoulli's equation
 J_{ij} = ($i = x, y, j = x, y$) coefficients of the jerk force matrix $[J]$ ($J_{ij}^* = J_{ij}/\rho\pi bR_2^2/\Omega$)
 K_{ij} = ($i = x, y, j = x, y$) components of stiffness force matrix $[K]$ ($K_{ij}^* = K_{ij}/\rho\pi b\Omega^2 R_2^2$)
 M_{ij} = ($i = x, y, j = x, y$) components of inertia force matrix $[M]$ ($M_{ij}^* = M_{ij}/\rho\pi bR_2^3$)
 P_i = pressure in impeller ($P_i^* = 2P_i/\rho\Omega^2 R_2^2$)
 P_v = pressure in volute ($P_v^* = 2P_v/\rho\Omega^2 R_2^2$)
 R = impeller radius (with no subscript, $R = R_2/R_1$)
 R_t = radius of pressure tap ring
 V = velocity in volute (with no subscript, $V^* = V_{\theta'}/\Omega R_2$)
 W_i = external width of impeller at R_2 ($W_i^* = W_i/b$)
 β = perturbation function for impeller flow

in the volute reference frame. Together, these stipulations require that,

$$v = (v_r^2 + v_\theta^2)^{1/2} = \phi \Omega R_2^2 \beta(\theta'', r'', \Omega t, \omega t, \epsilon) \sec \gamma / r'' \quad (4)$$

From continuity considerations, the perturbation function, β , must be constant along a streamline. For whirl motions with small eccentric orbits, β may be linearized as,

$$\beta(\theta'', r'', \Omega t, \omega t, \epsilon) = \bar{\beta}(\theta_2) + \epsilon^* \{ \beta_c(\theta_2) \cos \omega t + \beta_s(\theta_2) \sin \omega t \} \quad (5)$$

Equations (4) and (5) can now be substituted into equation (2). The pressure at the impeller discharge is then given as a function of β and the inlet pressure. If it is assumed that the total head is circumferentially constant at the impeller inlet and there is no inlet pre-swirl, the inlet pressure can be written as,

$$P_i^*(R_1, \theta_1) \cong h_1^* - \phi R \bar{\beta}(\theta_2) \left\{ \phi R \bar{\beta}(\theta_2) + 2\epsilon^* \frac{\omega}{\Omega} \sin(\theta_1 - \omega t) \right\} - 2\epsilon^* \phi^2 R^2 \bar{\beta}(\theta_2) \{ \beta_c(\theta_2) \cos \omega t + \beta_s(\theta_2) \sin \omega t \}, \quad (6)$$

for small eccentric displacements. By utilizing equations (4) through (6), and neglecting terms of order ϵ^2 and higher, Bernoulli's equation can now be separated into harmonics with steady, $\epsilon \cos \omega t$, and $\epsilon \sin \omega t$ dependence as,

$$\phi \sec^2 \gamma \left[2 \ln(R) \frac{d\bar{\beta}}{d\theta_2} + \phi \bar{\beta}^2 \right] + \bar{D}_p - 1 = 0, \quad (7a)$$

$$2\phi \sec^2 \gamma \left[\ln(R) \frac{d\beta_c}{d\theta_2} + \phi \bar{\beta} \beta_c + \frac{\omega}{\Omega} \ln(R) \beta_s \right] + D_{pc} - \sin \theta_2 \frac{d\bar{D}_p}{d\theta_2} + 2 \frac{\omega}{\Omega} [\phi R \bar{\beta} \sin(\theta_2 + \tan \gamma \ln(R))] - \cos(\theta_2 + \tan \gamma \ln(R)) / R - 2 \frac{\omega^2}{\Omega^2} [\cos \theta_2 - \cos(\theta_2 + \tan \gamma \ln(R)) / R] / \tan^2 \gamma = 0, \quad (7b)$$

$$2\phi \sec^2 \gamma \left[\ln(R) \frac{d\beta_s}{d\theta_2} + \phi \bar{\beta} \beta_s - \frac{\omega}{\Omega} \ln(R) \beta_c \right] + D_{ps} + \cos \theta_2 \frac{d\bar{D}_p}{d\theta_2} - 2 \frac{\omega}{\Omega} [\phi R \bar{\beta} \cos(\theta_2 + \tan \gamma \ln(R))] + \sin(\theta_2 + \tan \gamma \ln(R)) / R - 2 \frac{\omega^2}{\Omega^2} [\sin \theta_2 - \sin(\theta_2 + \tan \gamma \ln(R)) / R] / \tan^2 \gamma = 0, \quad (7c)$$

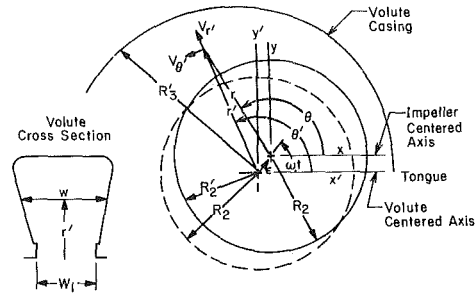


Fig. 3 Geometry of a volute

where,

$$D_p(\theta') = \bar{D}_p(\theta') + \epsilon^* [D_{pc}(\theta') \cos \omega t + D_{ps}(\theta') \sin \omega t] \quad (8)$$

In equations (7a-c) the volute inlet pressure coefficient, $D_p(\theta')$, has been transformed into the impeller reference frame by the approximation, $\theta_2 = \theta' + \epsilon^* \sin(\theta' - \omega t)$. This will prove convenient in the future, because the impeller discharge pressure will be equated with the volute inlet pressure.

Governing Equations for the Volute. The geometries used in developing the volute model are shown in Fig. 3. The volute flow will be described by a continuity equation, a moment of momentum equation, and an equation of motion in the radial direction. Each of these three equations can be written respectively as,

$$\frac{\partial(wV_{\theta'})}{\partial\theta'} + \frac{\partial(wr'V_{r'})}{\partial r'} = 0, \quad (9)$$

$$\frac{\partial(wr'V_{\theta'}V_{\theta'})}{\partial\theta'} + \frac{\partial(wr'r'V_{\theta'}V_{r'})}{\partial r'} + wr'r' \frac{\partial V_{\theta'}}{\partial t} = -\frac{wr'}{\rho} \frac{\partial P_v}{\partial\theta'}, \quad (10)$$

and,

$$\frac{\partial P_v}{\partial r'} = \frac{\rho V_{\theta'} V_{\theta'}}{r'} \quad (11)$$

Here it has been estimated that $V_{r'}$ and $V_{z'}$ (and their gradients) are much smaller than $V_{\theta'}$, except at the inlet of the volute.

Nomenclature (cont.)

ζ = angular location of the impeller center
(= ωt = constant)
 γ = angle of flow path through impeller
 ϵ = distance between impeller and volute centers ($\epsilon^* = \epsilon/R_2$)
 ρ = fluid density
 ϕ = flow coefficient = flowrate through pump / $2\pi b \Omega R_2^2$
 ψ = total head rise coefficient = $(h_d - h_1) / \rho \Omega^2 R_2^2$
 ω = orbit speed of impeller center (whirl speed)
 Ω = rotational speed of impeller (shaft speed)

Subscripts

c, s = $\cos \omega t$ and $\sin \omega t$ components (nondimensional)
 d = downstream of pump
exp = experimental result
 m = force component due to momentum exchange

p = force component due to pressure
 r, θ = radial or angular component
 x, y = components in rectangular directions (real = x and imaginary = y)
1, 2 = impeller inlet and discharge

Superscripts

' = measurement made in volute reference frame
" = measurement made from frame fixed to rotating impeller
* = nondimensionalized quantity

Special Notation

F = bold type denotes vector quantity
 \bar{V} = overbar denotes centered impeller value (nondimensional)
[A] = square brackets denote a matrix quantity
 \dot{x} = dot represents a time derivative

Flow within the volute is considered to be primarily in the θ' direction and the velocity profile is assumed to be flat. This treatment will allow equations (9), (10), and (11) to be integrated over the volute cross-section. When these equations are combined with equations (4) and (5), the pressure and velocity distributions in the volute will be given in terms of moments of the volute cross-sectional area and the perturbation function, β . Both equations (9) and (10) can then be separated into three parts (steady, $\epsilon \cos \omega t$, and $\epsilon \sin \omega t$) as follows:

Continuity:

$$\frac{d(\bar{V}\bar{A})}{d\theta'} = \phi\bar{\beta}, \quad (12a)$$

$$\frac{d(V_c\bar{A})}{d\theta'} = W_i^* \frac{d(\bar{V} \cos \theta')}{d\theta'} + \frac{\omega}{\Omega} \sin \theta' + \phi \left[\beta_c + \frac{d(\bar{\beta} \sin \theta')}{d\theta'} \right], \quad (12b)$$

$$\frac{d(V_s\bar{A})}{d\theta'} = W_i^* \frac{d(\bar{V} \sin \theta')}{d\theta'} - \frac{\omega}{\Omega} \cos \theta' + \phi \left[\beta_s - \frac{d(\bar{\beta} \cos \theta')}{d\theta'} \right], \quad (12c)$$

Moment of momentum:

$$\frac{\bar{r}\bar{A}}{2} \frac{d\bar{D}_p}{d\theta'} = - \frac{d(\bar{r}\bar{A}\bar{V}^2)}{d\theta'} - \overline{r\ln rA} \frac{d(\bar{V}^2)}{d\theta'} + \phi(1 - \phi \tan \gamma \bar{\beta}) \bar{\beta}, \quad (13a)$$

$$\begin{aligned} \frac{\bar{r}\bar{A}}{2} \frac{dD_{pc}}{d\theta'} = & -2 \frac{d(\bar{r}\bar{A}\bar{V}V_c)}{d\theta'} + \frac{\omega}{\Omega} (W_i^* \sin \theta' \bar{V} - \overline{r\bar{A}V_s}) \\ & + (W_i^* + \bar{r}\bar{A}) \frac{d(\bar{V}^2 \cos \theta')}{d\theta'} - 2\overline{r\ln rA} \frac{d(\bar{V}V_c)}{d\theta'} \\ & + \phi^2 \sin \theta' \bar{\beta}^2 + \phi \cos \theta' \left(\frac{\omega}{\Omega} + 2 - 2\phi \tan \gamma \bar{\beta} \right) \bar{\beta} \\ & + \phi(1 - 2\phi \tan \gamma \bar{\beta}) \left(\beta_c + \sin \theta' \frac{d\bar{\beta}}{d\theta'} \right) + \frac{W_i^*}{2} \cos \theta' \frac{d\bar{D}_p}{d\theta'}, \end{aligned} \quad (13b)$$

$$\begin{aligned} \frac{\bar{r}\bar{A}}{2} \frac{dD_{ps}}{d\theta'} = & -2 \frac{d(\bar{r}\bar{A}\bar{V}V_s)}{d\theta'} - \frac{\omega}{\Omega} (W_i^* \cos \theta' \bar{V} - \overline{r\bar{A}V_c}) \\ & + (W_i^* + \bar{r}\bar{A}) \frac{d(\bar{V}^2 \sin \theta')}{d\theta'} - 2\overline{r\ln rA} \frac{d(\bar{V}V_s)}{d\theta'} \\ & - \phi^2 \cos \theta' \bar{\beta}^2 + \phi \sin \theta' \left(\frac{\omega}{\Omega} + 2 - 2\phi \tan \gamma \bar{\beta} \right) \bar{\beta} \\ & + \phi(1 - 2\phi \tan \gamma \bar{\beta}) \left(\beta_s - \cos \theta' \frac{d\bar{\beta}}{d\theta'} \right) + \frac{W_i^*}{2} \sin \theta' \frac{d\bar{D}_p}{d\theta'}, \end{aligned} \quad (13c)$$

where,

$$\bar{A}(\theta') = \int_{R_2}^{R_3'} w dr' / bR_2,$$

$$\overline{\ln rA}(\theta') = \int_{R_2}^{R_3'} \ln(r'/R_2) w dr' / bR_2,$$

$$\overline{rA}(\theta') = \int_{R_2}^{R_3'} r' w dr' / bR_2^2,$$

$$\overline{rrA}(\theta') = \int_{R_2}^{R_3'} r' r' w dr' / bR_2^3,$$

$$\overline{r\ln rA}(\theta') = \int_{R_2}^{R_3'} r' \ln(r'/R_2) w dr' / bR_2^2, \quad (14a-e)$$

and,

$$V^*(\theta') = \bar{V}(\theta') + \epsilon^* [V_c(\theta') \cos \omega t + V_s(\theta') \sin \omega t] \equiv \frac{V'_\theta}{\Omega R_2}. \quad (15)$$

In equations (12a-c) and (13a-c) the perturbation function, β , has been transformed into the volute reference frame for convenience in obtaining a solution.

To complete the basic equations for the volute problem, equation (11) may be integrated to give the radial pressure variation in the volute as,

$$\begin{aligned} P_v^* = & \bar{D}_p + 2\bar{V}^2 [\ln(r'/R_2) - \epsilon^* \cos(\theta' - \omega t)] \\ & + \epsilon^* [D_{pc} + 4\bar{V}V_c \ln(r'/R_2)] \cos \omega t \\ & + \epsilon^* [D_{ps} + 4\bar{V}V_s \ln(r'/R_2)] \sin \omega t. \end{aligned} \quad (16)$$

Closure Conditions. Equations (7), (12), (13), and (16) will describe the flow in the impeller and the volute after certain boundary conditions are satisfied. Even though β is referred to as the perturbation function, it was never assumed to be small. However, from the definition of the flow coefficient, β is required to have an average of one. The flow perturbation is further assumed to possess at least zeroth order continuity around the periphery of the impeller. This restriction on β can be met by satisfying the condition,

$$\beta(R_2, 0) = \beta(R_2, 2\pi), \quad (17)$$

At the tongue of the volute, it is assumed that the average total head of the recirculated flow will be constant across the tongue, so that,

$$\begin{aligned} \int_{R_2'(0)}^{R_3'(0)} (P_v + \rho V_\theta^2 / 2) |_{\theta' = 2\pi} w dr' \\ = \int_{R_2'(0)}^{R_3'(0)} (P_v + \rho V_\theta^2 / 2) |_{\theta' = 0} w dr', \end{aligned} \quad (18)$$

From the remaining flow that is discharged, the flow path angle, γ , will be determined. This angle will vary with flowrate and total head and it can be found by equating the predicted and experimental total head rise across the pump as,

$$\psi_{\text{exp}} = \psi = [\bar{D}_p(2\pi) + C_v \bar{V}^2(2\pi)] / 2, \quad (19)$$

where,

$$C_v = 1 + 2[\overline{\ln rA}(2\pi) - \overline{\ln rA}(0)] / [\bar{A}(2\pi) - \bar{A}(0)].$$

Admittedly, using an experimental result does limit the preliminary design applications of this model. However, the "H/Q" curve (in dimensionless form the function $\psi_{\text{exp}}(\phi)$) is normally available for any pump and it is important that this fundamental characteristic is properly represented in the model.

This completes the development of equations necessary to determine the flow properties, β , D_p , \bar{V} , and γ . However,

some guidance on obtaining a solution is needed. Volute properties specified in equation (14a-e) are introduced as second order spline curve-fits of measured volute dimensions. The nine ordinary differential equations (7), (12), and (13) are written in a centered difference form and solved in an iterative manner. Steady flow properties are obtained as follows:

- Assume $\bar{\beta}(\theta_2) = 1$ and choose $\bar{D}_p(2\pi) - \bar{D}_p(0)$ and γ .
- Calculate $\bar{V}(0)$ using the steady part equation (16) combined with equation (18). Solve equation (12a) for $\bar{V}(\theta')$.
- Solve equation (13a) for $\bar{D}_p(\theta')$. $\bar{D}_p(0)$ is chosen so that the 0 to 2π integral of equation (7a) is satisfied.
- If $\bar{D}_p(2\pi) - \bar{D}_p(0)$ does not match the original estimate, update the estimate and return to step (b).
- Solve for $\bar{\beta}(\theta_2)$ using equation (7a) and the closure condition in equation (17).
- If $\bar{\beta}(\theta_2)$ does not match the original estimate, update the estimate on $\bar{\beta}(\theta_2)$ and return to step (c). (Note, the average of $\bar{\beta}$ must equal one.)
- When $\bar{\beta}(\theta_2)$ has converged, check that equation (19) is satisfied. If this condition is not met, return to step (b) with a new estimate of γ .
- After equation (19) is satisfied, the solution has converged and $\bar{\beta}$, \bar{D}_p , \bar{V} , and γ are known.

The numerical solution was tested using exact solutions for sinusoidal $\bar{\beta}$ distributions. Flow properties for an off-centered impeller were obtained with a similar iterative procedure except γ is assumed to be fixed by the steady flow computations. For a whirling impeller, the $\cos\omega t$ and $\sin\omega t$ terms become coupled and parts (b) and (c) of equations (7), (12), and (13) must be solved simultaneously.

Hydrodynamic Forces on the Impeller. Basically, there are two sources that contribute to the radial hydrodynamic forces on an impeller. One part is due to an asymmetric pressure distribution around the impeller and the other part is caused by the asymmetric momentum fluxes at the impeller inlet and discharge. The first contribution is evaluated by integrating the pressure around the inlet and discharge of the impeller:

$$\mathbf{F}_p = (F_x + jF_y)_p = b \int_0^{2\pi} P_i(R_1, \theta_1) R_1 e^{j\theta_1} d\theta_1 - W_i \int_0^{2\pi} P_i(R_2, \theta_2) R_2 e^{j\theta_2} d\theta_2, \quad (20)$$

where j denotes the imaginary part that corresponds to the y direction (see Fig. 2). The second contribution is found by applying the momentum equation to obtain,

$$\frac{\mathbf{F}_m}{\rho b} = \frac{(F_x + jF_y)_m}{\rho b} = -e^{j\Omega t} \frac{\partial}{\partial t} \int_0^{2\pi} \int_{R_1}^{R_2} (v_r'' + jv_\theta'') e^{j\theta} r'' dr'' d\theta'' - e^{j\Omega t} \left[\int_0^{2\pi} (v_r'' + jv_\theta'') v_r'' e^{j\theta} r'' d\theta'' \right] \Big|_{R_1}^{R_2} - e^{j\Omega t} 2\Omega \int_0^{2\pi} \int_{R_1}^{R_2} (jv_r'' - v_\theta'') e^{j\theta} r'' dr'' d\theta'' + \omega^2 \epsilon \pi (R_2^2 - R_1^2) e^{j\omega t}. \quad (21)$$

When the pressure distributions of equations (6) and (7), and the velocity profiles described by equations (3)–(5) are applied to equations (20) and (21), the resulting force on the impeller is,

$$\mathbf{F}^* = \mathbf{F}_p^* + \mathbf{F}_m^* = \bar{\mathbf{F}} + \epsilon^* (\mathbf{F}_c \cos \omega t + \mathbf{F}_s \sin \omega t), \quad (22)$$

where,

$$\bar{\mathbf{F}} = \phi^2 [W_i^* \sec^2 \gamma + \mathbf{k}R - 2 + 2j \tan \gamma] \int_0^{2\pi} \bar{\beta}^2(\theta_2) e^{j\theta_2} d\theta_2 / 2\pi - j\phi [W_i^* \sec^2 \gamma \ln(R) + 1] \int_0^{2\pi} \bar{\beta}(\theta_2) e^{j\theta_2} d\theta_2 / \pi, \quad (23a)$$

$$\mathbf{F}_c = \phi^2 [W_i^* \sec^2 \gamma + \mathbf{k}R - 2 + 2j \tan \gamma] \int_0^{2\pi} \bar{\beta}(\theta_2) \beta_c(\theta_2) e^{j\theta_2} d\theta_2 / \pi - j\phi [W_i^* \sec^2 \gamma \ln(R) + 1] \int_0^{2\pi} \beta_c(\theta_2) e^{j\theta_2} d\theta_2 / \pi + \frac{\omega}{\Omega} \phi [W_i^* \sec^2 \gamma \ln(R) + \mathbf{k}/R - 1] \int_0^{2\pi} \beta_s(\theta_2) e^{j\theta_2} d\theta_2 / \pi + \frac{\omega}{\Omega} \left[\phi R W_i^* \int_0^{2\pi} \bar{\beta}(\theta_2) \sin(\theta_2 + \tan \gamma \ln(R)) e^{j\theta_2} d\theta_2 / \pi \right] - \frac{\omega}{\Omega} [2j\phi + W_i^* / (\mathbf{k}R)] - \frac{\omega^2}{\Omega^2} \{ W_i^* [1 - 1/(\mathbf{k}R)] / \tan^2 \gamma - 1 + 1/R^2 \}, \quad (23b)$$

$$\mathbf{F}_s = \phi^2 [W_i^* \sec^2 \gamma + \mathbf{k}R - 2 + 2j \tan \gamma] \int_0^{2\pi} \bar{\beta}(\theta_2) \beta_s(\theta_2) e^{j\theta_2} d\theta_2 / \pi - j\phi [W_i^* \sec^2 \gamma \ln(R) + 1] \int_0^{2\pi} \beta_s(\theta_2) e^{j\theta_2} d\theta_2 / \pi - \frac{\omega}{\Omega} \phi [W_i^* \sec^2 \gamma \ln(R) + \mathbf{k}/R - 1] \int_0^{2\pi} \beta_c(\theta_2) e^{j\theta_2} d\theta_2 / \pi - \frac{\omega}{\Omega} \left[\phi R W_i^* \int_0^{2\pi} \bar{\beta}(\theta_2) \cos(\theta_2 + \tan \gamma \ln(R)) e^{j\theta_2} d\theta_2 / \pi \right] - \frac{\omega}{\Omega} j [2j\phi + W_i^* / (\mathbf{k}R)] - \frac{\omega^2}{\Omega^2} j \{ W_i^* [1 - 1/(\mathbf{k}R)] / \tan^2 \gamma - 1 + 1/R^2 \}, \quad (23c)$$

and, $\mathbf{k} = \cos(\tan \gamma \ln(R)) + j \sin(\tan \gamma \ln(R))$. Expressed in the terms used in equation (1), these components are,

$$\bar{\mathbf{F}} = \bar{F}_x + j\bar{F}_y, \quad \mathbf{F}_c = A_{xx}^* + jA_{yy}^*, \quad \text{and} \quad \mathbf{F}_s = A_{xy}^* + jA_{yy}^*. \quad (24a-c)$$

Presentation of the calculated results will be postponed so that the experimental and theoretical results can be discussed together.

Test Facility

The experimental results presented in this paper were obtained using the Rotor Force Test Facility at the California Institute of Technology, Pasadena. Details of the equipment have been given in previous papers (Brennen et al., 1980, Chamieh, 1983, and Jery et al., 1984), so only a brief description will be presented here. Figure 4 shows the test section where the centrifugal pump being examined is located. The impeller is mounted on the internal balance and the entire assembly is turned by the main shaft. The main shaft passes through an eccentrically drilled cylinder, which when rotated, causes the impeller to whirl in a 2.51 mm diameter circular orbit. Forces on the impeller are sensed through strain gauges on four posts located in the internal balance. The relationships between the strains and forces were found by static calibration tests.

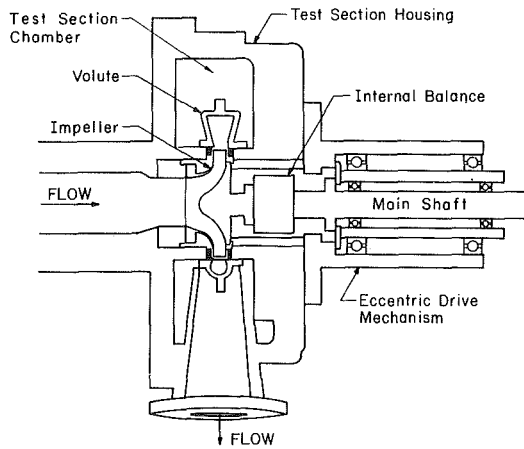


Fig. 4 Schematic of the test section

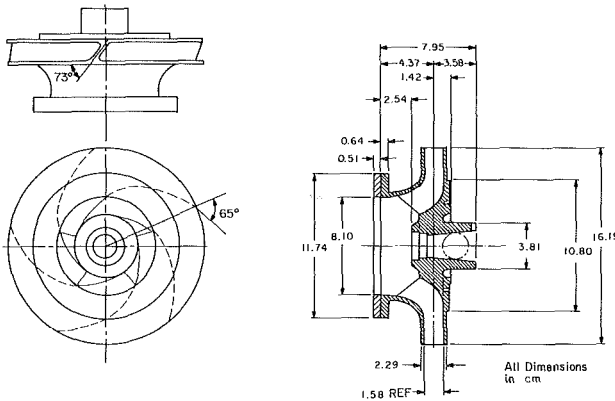


Fig. 5 Dimensions of Impeller X

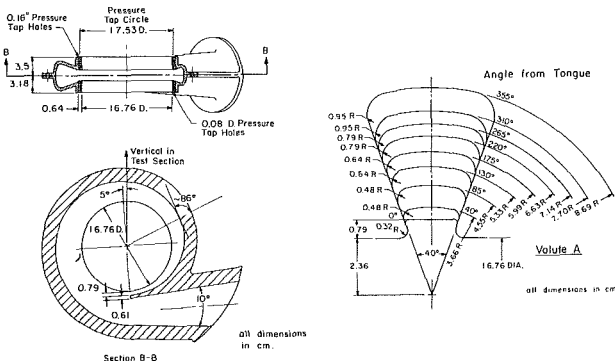


Fig. 6 Dimensions of Volute A

Descriptions of the test impeller and volute are given in Figs. 5 and 6. The impeller (referred to as Impeller X) is a five bladed cast bronze impeller with a specific speed of 0.57 and blade angle of 65 deg. The 86 deg spiral volute (Volute A) is constructed of fiberglass and designed to be "well matched" with Impeller X at a flow coefficient of 0.092. The dimensions of the volute cross-sections, shown in Fig. 6, were used in evaluating the integrals of equations (14a-e).

For this study, the test facility has been modified slightly from the configuration used by Chamieh [1983] and Jery et al. [1984]. The modifications shown in Fig. 7 were considered necessary in order to isolate the interaction between the impeller and the volute from external influences. To separate the flow in the volute from the annular gap region, rings were in-

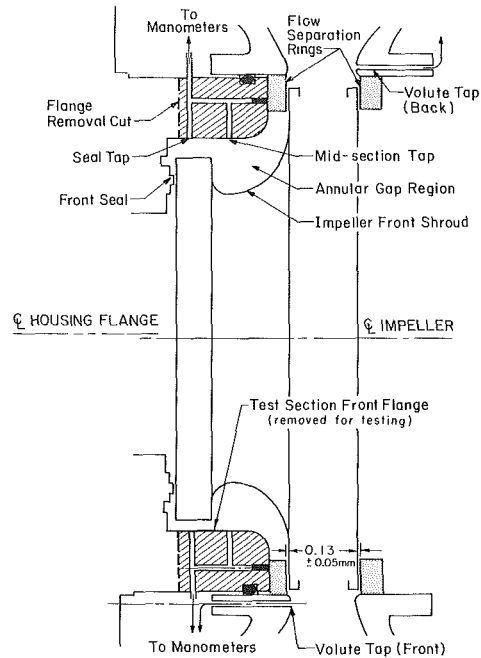


Fig. 7 Modifications of the test facility

stalled 0.13 mm from the edge of the impeller. In addition, the front flange of the test section was removed so that the front shroud of the impeller was exposed to the "reservoir-like" conditions of the test chamber (see Fig. 4).

The removal of the front flange of the test section was judged to be essential after pressure measurements were made in the annular gap region with the flange in place and the rings removed. The measurements indicated that the fluid trapped in this region was responsible for a hydrodynamic stiffness (see equation (26)) given approximately by,

$$\begin{bmatrix} K_{xx} & K_{xy} \\ K_{yx} & K_{yy} \end{bmatrix} = \begin{bmatrix} -1.6 & 0.3 \\ -0.3 & -1.6 \end{bmatrix}$$

When compared with Chamieh's (1982) direct measurements of the total hydrodynamic stiffness on the impeller (annular gap plus volute) given approximately by,

$$\begin{bmatrix} K_{xx} & K_{xy} \\ K_{yx} & K_{yy} \end{bmatrix} = \begin{bmatrix} -2.0 & 0.9 \\ -0.9 & -2.0 \end{bmatrix}$$

it is seen that the contribution from the annular gap is significant. Impeller shroud forces also had a dominant influence on the hydrodynamic stiffnesses measured by Jery et al. [1984]. With the flange removed, the fluid forces on the front shroud of the impeller were largely eliminated.

Comparisons Between Experimental and Theoretical Results

The numerical results in this paper can be duplicated using Impeller X properties given in Fig. 5, the Volute A properties in Fig. 6, and the pump performance curves in Fig. 8. A preliminary step in the theoretical calculations is to obtain the impeller flow path angle, γ (see Closure Conditions). By setting $\psi = \psi_{exp}$, the flow path angle, γ , shown in Fig. 9 was obtained. Note that the typical magnitude of γ is about 80 deg while the blade angle of Impeller X is 65 deg.

Measurements of the static pressure at the discharge from the impeller were made using holes drilled at the inlet to the volute (see Figs. 6 and 7). The circumferential pressure distributions are compared with the theoretical results in Figs.

10 and 11. The pressure taps are alternately located in the front and back of the volute, resulting in the slight oscillation of the data. The results were obtained for a range of shaft speeds from $\Omega = 800$ to 1200 rpm, but the nondimensionalized pressures were found to be independent of the speed. Figure 10 shows that the theory gives a good approximation of the pressure distributions over a moderate range of flow coefficients. However, for flow coefficients below this range, the

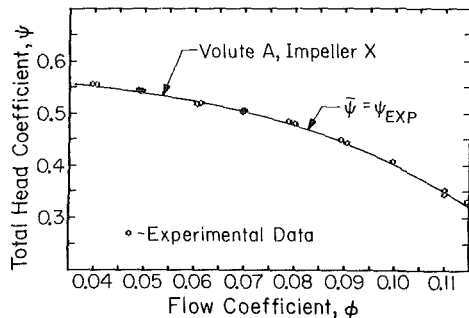


Fig. 8 Total head coefficient versus the flow coefficient for the Impeller X and Volute A pump. The solid line represents the average value of the experimental data. (Uncertainty in $\psi = \pm 1.5 \times 10^{-3}$, in $\phi = \pm 2 \times 10^{-3}$)

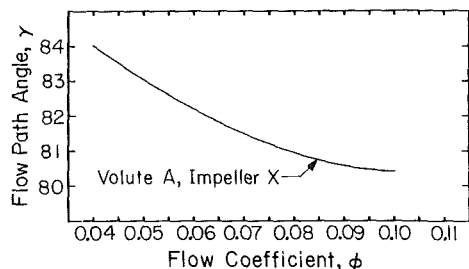


Fig. 9 The average angle the flow follows through the pump (measured with respect to the radial line) as a function of flowrate

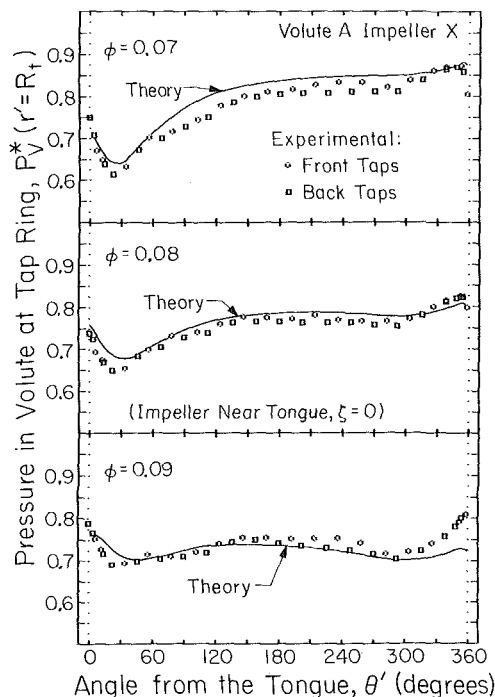


Fig. 10 Experimental and theoretical pressure distributions at the inlet of the volute for three different flowrates with the impeller placed near the tongue. Measurements were taken with $\Omega = 1000$ rpm. (Uncertainty in $P_V^* = \pm 3 \times 10^{-4}$, in $\phi = \pm 2 \times 10^{-3}$, in $\theta = \pm 0.25$ deg, in $\zeta = \pm 0.5$ deg)

pressure predictions begin to falter as shown in Fig. 11. The model's assumption of log spiral stream paths through the impeller probably fails at lower flowrates. For higher flow coefficients, it was concluded that the deviation was caused by the inadequacy of a one dimensional treatment of the flow near the tongue of the volute. At the higher flowrates, it has been suggested (Lazarkiewicz and Troskolanski, 1965) that there is a reversal of the direction of flow in the region just inside the tongue. The effect on the pressure distribution of displacing the impeller is also demonstrated in Fig. 11. The model appears to follow the changes that occur, even when the absolute pressure predictions are rather poor.

A comparison between the experimental and theoretical steady forces on the impeller is given in Fig. 12. One set of experimental results was obtained by placing the impeller in four equally spaced orbit positions and then averaging the internal balance force measurements. The second set of experimental results (for $\phi = 0.06$ and 0.10) was obtained by integrating the discharge pressure measurements. The theoretical model tends to overpredict the steady or average radial forces somewhat, but it does give reasonable results considering the crudeness of the model. Colding-Jorgensen's (1980) steady force calculations for a 67.5 deg blade angle impeller in an 86 deg spiral volute are also shown in Fig. 12. The present model appears to give a more accurate assessment of the measured steady forces. The agreement between the two sets of experimental data indicates that the primary cause of the radial forces is the asymmetric pressure distribution at the discharge of the impeller. Moreover, the theoretical model predicted that the discharge pressure was responsible for 99 percent of the total force on the impeller while the net momentum flux contribution was essentially negligible. It might also be of interest to note that over the entire range of flowrates for which theoretical results are presented, the predicted perturbation in the impeller discharge flow never exceeded 6 percent of the mean flow.

Figure 13 presents the components of the generalized hydrodynamic force matrix, $[A]$, that results when the impeller whirls in an eccentric orbit at the pump design flowrate

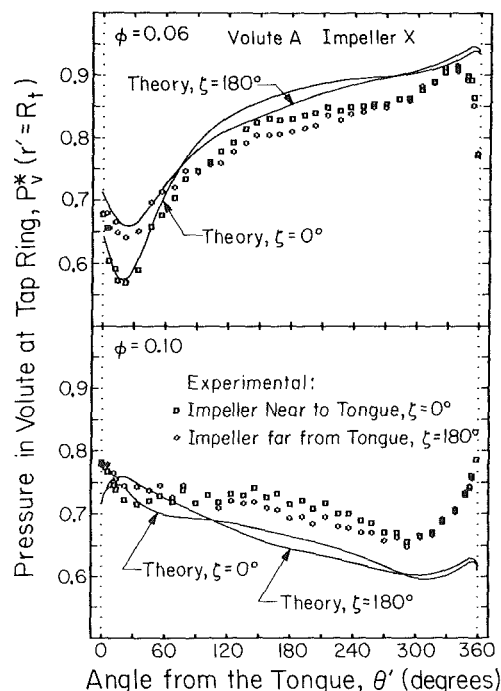


Fig. 11 Experimental and theoretical pressure distributions at the inlet of the volute for two different flowrates with the impeller placed near and far from the volute tongue. (Uncertainty in $P_V^* = \pm 3 \times 10^{-4}$, in $\phi = \pm 2 \times 10^{-3}$, in $\theta = \pm 0.25$ deg, in $\zeta = \pm 0.5$ deg)

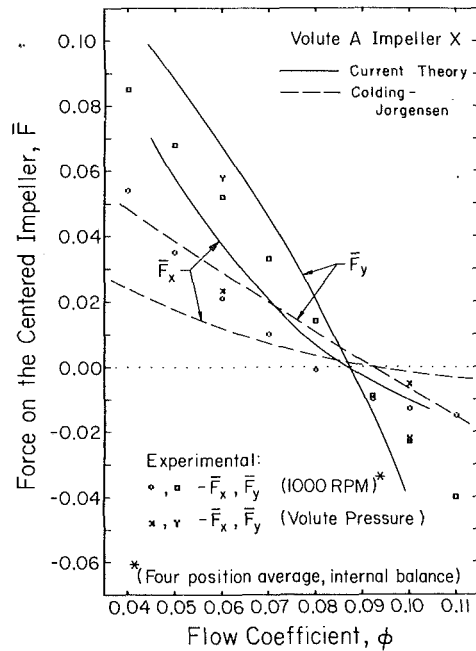


Fig. 12 Steady hydrodynamic forces acting upon Impeller X as function of flowrate. Experimental forces were obtained by both internal balance and discharge pressure measurements. Colding-Jorgensen's (1980) results are for an 86 deg spiral volute with a 67.5 deg blade angle impeller. (Uncertainty in $\bar{F} = \pm 3 \times 10^{-3}$, in $\phi = \pm 2 \times 10^{-3}$, in rpm = $\pm 10^{-3}$ rpm)

($\phi = 0.092$). Cross-coupled terms (i.e., A_{xy} , A_{yx}) in the experimental data suggest that forces act in the direction of the whirl orbit up to $\omega/\Omega = 0.10$. This destabilizing influence is predicted by the theoretical model to occur up to $\omega/\Omega = 0.14$. Due to the coupled nature of equations (7b) and (7c), it was not possible to calculate $[A]$ beyond the range of whirl ratios shown in Fig. 13. This problem is believed to result from current limitations of the iterative technique used in obtaining a numerical solution.

As was mentioned in the introduction, it is a standard practice to express the matrix elements of $[A]$ in powers of ω . By examining the A_{yx} term in Fig. 13, it is apparent that a quadratic in ω will not adequately describe the features of the matrix element. However, a cubic in ω can approximate all of the $[A]$ matrix element variations with ω . The coefficients of such an expansion can be written as,

$$\begin{bmatrix} A_{xx} & A_{xy} \\ A_{yx} & A_{yy} \end{bmatrix} = \begin{bmatrix} -K_{xx} - \omega C_{xy} + \omega^2 M_{xx} + \omega^3 J_{xy} & -K_{xy} + \omega C_{xx} + \omega^2 M_{xy} - \omega^3 J_{xx} \\ -K_{yx} - \omega C_{yy} + \omega^2 M_{yx} + \omega^3 J_{yy} & -K_{yy} + \omega C_{yx} + \omega^2 M_{yy} - \omega^3 J_{yy} \end{bmatrix} \quad (25)$$

or alternatively as,

$$[A(\omega/\Omega)] \begin{Bmatrix} x \\ y \end{Bmatrix} = -[K] \begin{Bmatrix} x \\ y \end{Bmatrix} - [C] \begin{Bmatrix} \dot{x} \\ \dot{y} \end{Bmatrix} - [M] \begin{Bmatrix} \ddot{x} \\ \ddot{y} \end{Bmatrix} - [J] \begin{Bmatrix} \dddot{x} \\ \dddot{y} \end{Bmatrix}, \quad (26)$$

where,

$$x = \epsilon \cos \omega t \quad \text{and} \quad y = \epsilon \sin \omega t.$$

The $[K]$, $[C]$, and $[M]$ matrices correspond to the stiffness, damping, and inertial components that are commonly

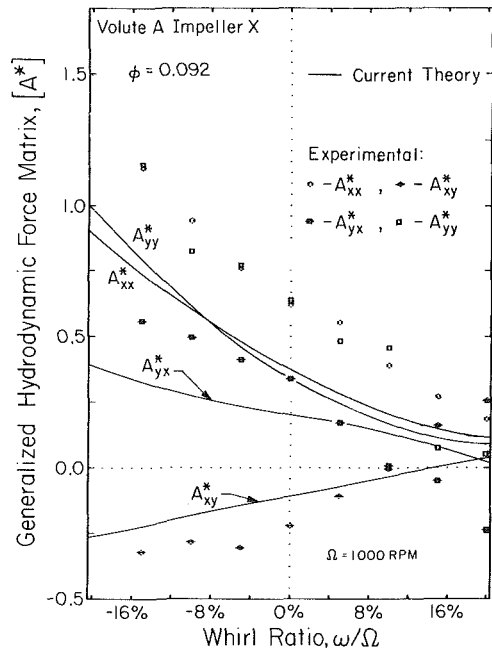


Fig. 13 The Generalized Hydrodynamic Force coefficients as functions of whirl speed at the volute design flow coefficient ($\phi = 0.092$). The experimental results were obtained from the direct force measurements of the internal balance. The radius of the whirl orbit for impeller X was $\epsilon = 2.51$ mm. (Uncertainty in $A^* = \pm 3 \times 10^{-3}$, in $\omega/\Omega = 10^{-2}$, in $\phi = \pm 2 \times 10^{-3}$)

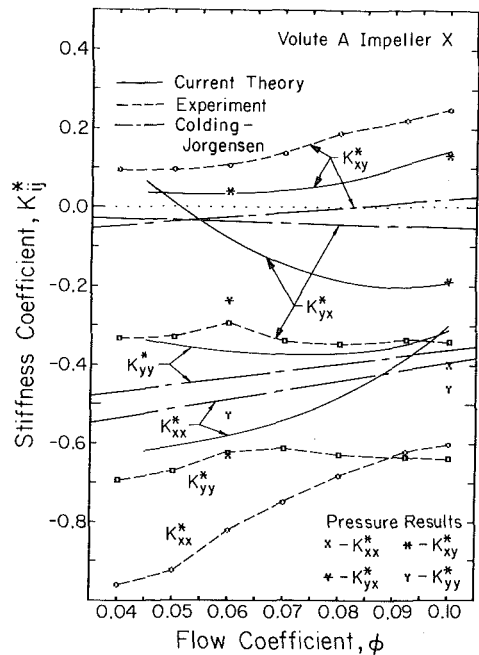


Fig. 14 Hydrodynamic stiffnesses as functions of the flowrate. Experimental results are from internal balance and pressure measurements. Colding-Jorgensen's (1980) results are for an 86 deg spiral volute with a 67.5 deg blade angle impeller. (Uncertainty in $K^* = \pm 3 \times 10^{-3}$, in $\phi = \pm 2 \times 10^{-3}$)

employed in rotordynamics. Since the $[J]$ matrix is related to the third order time derivative of the impeller displacement (which is conventionally known as the jerk), it will be referred to as the "jerk" matrix.

The resulting $[K]$ matrix elements of the cubic expansion are given in Fig. 14, and the $[C]$, $[M]$, and $[J]$ matrix elements are presented in Fig. 15. Included in Fig. 14 are the stiffnesses that were calculated using the force measurements (from the internal balance and the pressure distributions) taken at four impeller positions. Also shown in Fig. 14 are the stiffnesses

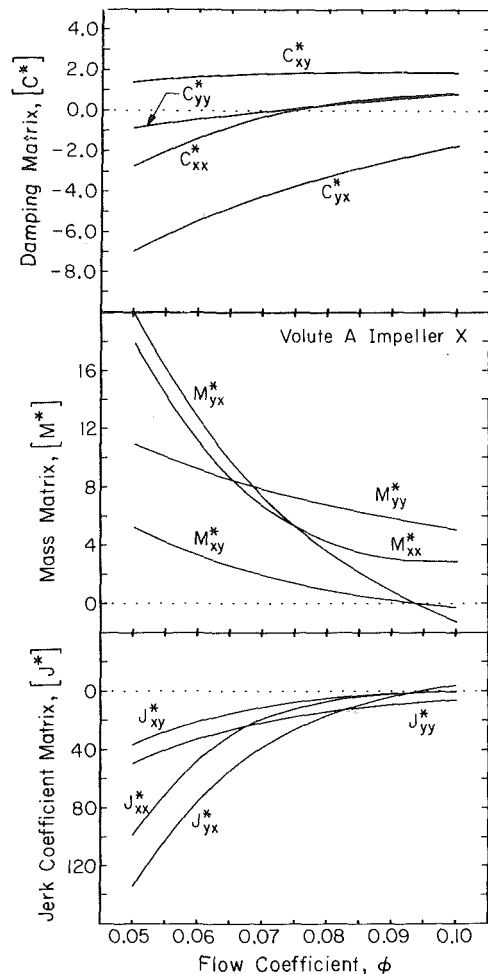


Fig. 15 Damping, mass, and jerk force coefficients of the flowrate as predicted by the current theoretical model

predicted by Colding-Jorgensen (1980) for an 86 deg spiral volute. With the exception of the K_{yx} term, the current model does a fair job of describing the variation of stiffness with flowrate. The magnitudes, however, tend to be underpredicted by the theory. Over most of the range of flow coefficients, the stiffness is such that it would encourage the whirling motion of the impeller. The same is also true of the damping when the flowrate drops below $\phi = 0.07$ as shown in Fig. 15. The magnitude of the damping components computed by Colding-Jorgensen (1980) were less than 10 percent of those predicted by the present model. In general, the inertial force would discourage an orbital motion of the impeller, but it will tend to drive the impeller in the direction of the displacement. The jerk force attains significant values only at the lower flow coefficients. However it must be emphasized that the damping, mass and jerk components have not been experimentally validated.

Closing Comments

A theoretical model has been developed to describe the flow in the impeller and the volute, along with the interactions that occur between them. This investigation was undertaken to provide a better understanding of the destabilizing hydrodynamic forces that have been observed by Chamieh et al. (1982) and Jery et al. (1984) on a whirling centrifugal pump impeller. To implement the model requires only a knowledge of the dimensions of the volute and impeller, and the total head rise across the entire pump. Comparisons between the predicted and experimental results are encouraging.

Experimentation with different volute geometries and over a wider range of operating conditions (flow coefficient and whirl ratio) would provide a more crucial test of the theoretical model. It might also be useful to incorporate the effects of inducers and diffuser vanes into the theoretical model. These devices are now commonly employed on many high performance centrifugal pumps.

Previous experimental results (Chamieh et al., 1982, and Jery et al., 1984) have tended to over-estimate the contribution of the volute/impeller interaction to the total stiffness force acting on the impeller. The over-estimation came about because of an asymmetric pressure distribution in the fluid trapped on the front shroud of the impeller. Since real pumps do have fluid in this region, it will be important in the future to perform a detailed study of this area. Some work is beginning to appear in this important area (Childs, 1986).

Acknowledgments

This research was funded by NASA George Marshal Space Flight Center, Huntsville, Alabama under contract NAS 8-33108. Both of the authors would like to express their gratitude to A. J. Acosta and T. K. Caughey for their helpful advice, and R. Franz and N. Arndt for their assistance with the experiments. One of the authors (D. R. Adkins) would also like to thank the Shell Companies Foundation for a fellowship that supported his graduate studies and Susan Berkley and Jan Patterson for their invaluable help in preparing this paper.

References

- Adkins, D. R., 1985, "Analyses of Hydrodynamic Forces on Centrifugal Pump Impellers," Ph.D. thesis, Division of Engineering and Applied Sciences, California Institute of Technology.
- Agostinelli, A., Nobles, D., and Mockridge, C. R., 1960, "An Experimental Investigation of Radial Thrust in Centrifugal Pumps," *ASME Journal of Engineering for Power*, Vol. 82, pp. 120-126.
- Brennen, C. E., Acosta, A. J., and Caughey, T. K., 1980, "A Test Program to Measure Fluid Mechanical Whirl-Excitation Forces in Centrifugal Pumps," *First Workshop on Rotordynamic Instability Problems in High Performance Turbomachinery*, Texas A&M University, NASA Conf. Pub. 2133, pp. 229-235.
- Chamieh, D. S., 1983, "Forces On A Whirling Centrifugal Pump-Impeller," Ph.D. thesis, Division of Engineering and Applied Sciences, California Institute of Technology.
- Chamieh, D. S., Acosta, A. J., Brennen, C. E., Caughey, T. K., and Franz, R., 1982, "Experimental Measurements of Hydrodynamic Stiffness Matrices for a Centrifugal Pump Impeller," *2nd Workshop on Rotordynamic Instability Problems in High Performance Turbomachinery*, Texas A&M University, NASA Conf. Pub. 2250, pp. 382-398.
- Childs, D. W., 1986, "Force and Moment Rotordynamic Coefficients for Pump-Impeller Shroud Surfaces," *Rotordynamic Instability Problems in High Performance Turbomachinery*, Texas A&M University, NASA Conf. Pub. 2443, pp. 503-529.
- Colding-Jorgensen, J., 1980, "The Effect of Fluid Forces on Rotor Stability of Centrifugal Compressors and Pumps," *First Workshop on Rotordynamic Instability Problems in High Performance Turbomachinery*, Texas A&M University, NASA Conf. Pub. 2133, pp. 249-266.
- Csanady, G. T., 1962, "Radial Forces in a Pump Caused by Volute Casing," *ASME Journal of Engineering for Power*, Vol. 84, pp. 337-340.
- Ehrich, F., and Childs, D., 1984, "Self-Excited Vibration in High Performance Turbomachinery," *Mechanical Engineering*, Vol. 106, No. 5, pp. 66-79.
- Iversen, H. W., Rolling, R. E., and Carlson, J. J., 1960, "Volute Pressure Distribution, Radial Force on the Impeller and Volute Mixing Losses of a Radial Flow Centrifugal Pump," *ASME Journal of Engineering for Power*, Vol. 82, pp. 136-144.
- Jery, B., Acosta, A. J., Brennen, C. E., and Caughey, T. K., 1984, "Hydrodynamic Impeller Stiffness, Damping and Inertia in the Rotordynamics of Centrifugal Flow Pumps," *Rotordynamic Instability Problems in High Performance Turbomachinery*, Texas A&M University, NASA Conf. Pub. 2338, pp. 137-160.
- Lazarkiewicz, S., and Trokolanski, A. T., 1965, *Impeller Pumps*, Pergamon Press, Translated by D. K. Rutter (Polish Ed. Title: *Pompy Wrowe*).
- Shoji, H., and Ohashi, H., 1980, "Fluid Forces on Rotating Centrifugal Impeller with Whirling Motion," NASA CP 2133, pp. 317-328.
- Shoji, H., and Ohashi, H., 1987, "Lateral Forces on Whirling Centrifugal Impeller (1st Report: Theory)," *ASME JOURNAL OF FLUIDS ENGINEERING*, Vol. 109, No. 2, pp. 94-99.

T. C. Vu

Dominion Engineering Works,
GE Canada, Lachine, Québec, Canada
H8S-2S8

W. Shyy

General Electric Corporate R&D,
Schenectady, NY 12301

Navier-Stokes Computation of Radial Inflow Turbine Distributor

A two-dimensional flow analysis of a radial inflow turbine distributor using full steady-state Reynolds-averaged Navier-Stokes equations is made. The numerical prediction of the total energy loss and the wicket gate torque is compared with experimental data. Also, a parametric study is carried out in order to evaluate the behavior of the numerical algorithm.

1 Introduction

The main functions of the distributor in a hydraulic turbine are to distribute the flow uniformly and to regulate the flow admission to the runner. In the distributor, the pivoting wicket gates control the flow rate and the flow direction whereas the fixed stay vanes contribute only to the structural integrity of the turbine.

Recently, intensive efforts have been devoted to develop a suitable numerical algorithm for computing the general Navier-Stokes flows bounded by complex geometries [1, 2]. The algorithm has been applied to solve various two- and three-dimensional flow problems, e.g., single cascade of turbine blades [3], annular dump diffuser [4], elbow draft tube [5], and gas turbine combustor [6].

In the present study, a two-dimensional flow analysis of a radial inflow turbine distributor is made. In order to validate the numerical algorithm, numerical results are compared with experimental data obtained from DEW hydraulic laboratory. Also, a parametric study is carried out in order to evaluate the influence of some important variables on the numerical prediction.

Two typical data relevant to the hydraulic performance of the distributor are used for both the parametric study and the validation: total energy loss and torque exerted on the wicket gate pivot. The total energy loss in the distributor is expressed as a percentage of the turbine net head. The wicket gate torque coefficient $T11$ is defined as:

$$T11 = \frac{\text{Torque}}{\text{Turbine Head} \times \text{Throat Diameter}^3}$$

2 Formulation and Numerical Algorithm

The two-dimensional radial cascade flow analysis is based on the full Reynolds-averaged Navier-Stokes equations. The standard $k-\epsilon$ two equation turbulence model [8] is adopted here as closure form. The numerical formulation comprises a linearized, semi-implicit, conservative finite volume algorithm implemented in a general curvilinear coordinate system.

As to the finite difference operators, the standard 2nd-order central difference approximation is applied to all the

derivatives except the convection terms. For the convection terms, both the commonly used hybrid scheme, i.e. combination of the 1st-order upwind and 2nd-order central differencing scheme, and the 2nd-order upwind scheme are used for discretization [4, 7]. The system of finite difference equations are solved using the successive line overrelaxation method. The grid system is generated using the combined elliptic generation method developed by Thompson et al. [9] and local interpolation procedures.

3 Boundary Conditions

Figure 2 illustrates the flow domain of a tandem radial cascade. The periodic boundaries are alternated with the solid walls representing respectively the stay vane and wicket gate surfaces. The periodic boundary conditions are imposed on the corresponding nodes in the free stream for the dependent variables and the contravariant velocity components. For radial cascade flow, due to the relative angle between two consecutive blades, the periodic conditions are applied with due consideration of the periodic angle. At the nodal position next to the solid wall, the so-called wall function treatment [8] is used, except for laminar flow.

At the inlet of the flow domain, a uniform flow distribution is assumed with a given flow angle. At the exit, a zero 1st-order derivative along the streamwise direction is adopted for all the dependent variables, except for the static pressure which does not require the numerical boundary conditions due to the nature of staggered grid system [1].

4 Parametric Study

Some important parameters are selected for the study in order to evaluate their influence on the convergence behavior and the accuracy of the numerical results. Those parameters comprise inlet flow angle, flow Reynolds number, grid size and finite difference operator.

The geometry of the distributor used for the investigation, as shown in Figs. 1 and 2, is described in section 5.1. Except otherwise stated, the following parameters are kept constant during the study. A fine grid system, 29×98 nodes, is used. The flow Reynolds number, based on the radial velocity at the distributor outlet and the throat diameter of the turbine, is specified at 10^6 which is similar to the operating conditions of

Contributed by the Fluids Engineering Division for publication in the JOURNAL OF FLUIDS ENGINEERING. Manuscript received by the Fluids Engineering Division, June 10, 1987.

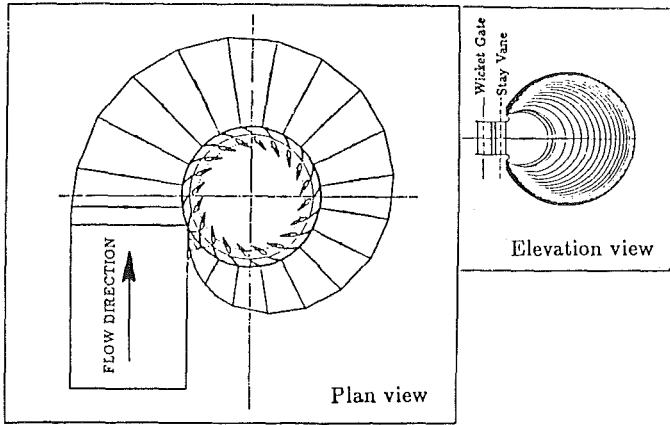


Fig. 1 Plan view and elevation view of the distributor and the spiral case

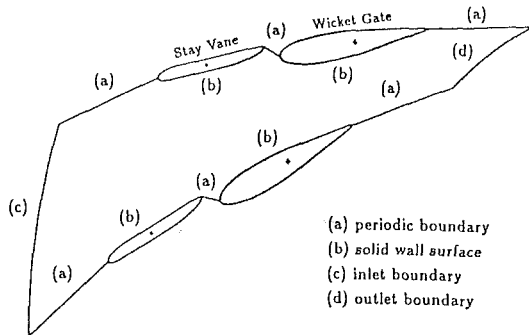


Fig. 2 Flow domain for a tandem radial cascade

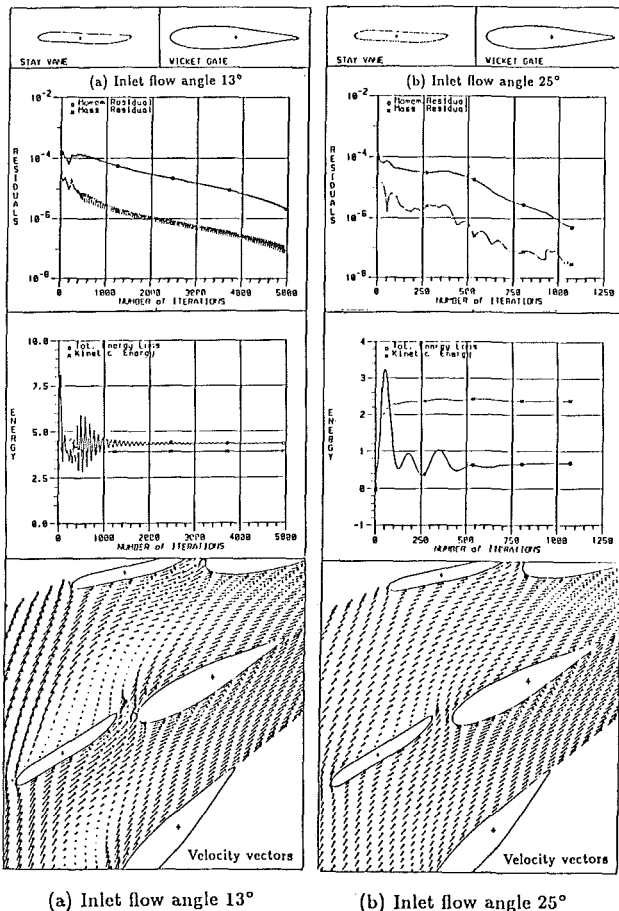


Fig. 3 Convergence behavior and velocity vectors for inlet flow angles 13 and 25 deg

Table 1 Effect of inlet flow angle – hybrid scheme

Inlet flow angle (deg)	Head loss (%)	Torque coeff. T11	Number of iteration	CPU time (hr)	Remarks
13	21.2	-.075	4950	8.1	Flow separ.
20	6.6	-.026	1562	2.3	Flow separ.
25	3.4	-.012	1076	1.6	
30	2.0	-.004	806	1.2	

Table 2 Effect of inlet flow angle – 2nd-order scheme

Inlet flow angle (deg)	Head loss (%)	Torque coeff. T11	Number of iteration	CPU time (hr)	Remarks
13	18.5	-.092	4950	8.2	Flow separ.
20	5.7	-.027	2905	4.5	Flow separ.
25	2.9	-.011	2046	3.2	
30	1.7	-.004	1378	2.1	

Table 3 Effect of the Reynolds number

Reynolds number	Head loss (%)	Torque coeff. T11	Remarks
10^7	2.5	-.018	Flow separ.
5×10^6	3.4	-.017	Flow separ.
2×10^6	3.2	-.014	Flow separ.
10^6	3.5	-.012	
10^5	4.2	-.009	
10^4 (turbulent)	6.5	-.002	
10^3 (laminar)	8.2	-.003	Flow separ.

the turbine model. The inlet flow angle, defined as an angle between the inlet velocity vector and the tangent, is 25 deg and the inlet turbulence level is 1 percent of the kinetic energy at the inlet. Various constants used in the turbulence model are specified as in [8]. The solution is considered to have converged when the sum of the momentum residuals divided by the total number of nodes is below 0.5×10^{-6} . All calculations were made on a VAX 8600 computer.

4.1 Effect of the Inlet Flow Angle. The inlet flow angle greatly influences the flow behavior of the distributor. As an example, flow analyses are performed for inlet flow angle specified respectively at 13, 20, 25, and 30 deg. At an unfavorable inlet flow angle 13 deg, the total energy loss is very high, 21.2 percent of the turbine head, due to a large flow separation zone occurring at the stay vane extrados (Fig. 3(a)). Reducing the severity of the inlet flow angle to 20 deg, the total energy loss is reduced to 6.6 percent of the head. At 25 deg angle which is considered as a favorable inlet flow condition, no flow separation is detected (Fig. 3(b)) and the total energy loss is 3.4 percent of the head. Figure 4 shows the influence of the inlet flow angle on the total energy loss in the distributor. The numerical solutions are obtained by both the hybrid and 2nd-order upwind schemes, and are shown here for comparison. Tables 1 and 2 summarize the numerical results for all the analyzed cases.

The numerical solution converges faster with a favorable inlet flow condition. The variation of mass and momentum residuals, total energy loss and kinetic energy of the flow domain as functions of the number of iterations, as shown in Fig. 3, indicates clearly this tendency.

4.2 Effect of the Reynolds Number. The Reynolds number influences significantly the flow behavior and the performance of the distributor. As shown in Table 3, as the Reynolds number increases by reducing the viscosity effect, the total energy loss in the distributor is also reduced. For more viscous flow where the Reynolds number is equal to 10^3 ,

Table 4 Effect of grid size – Favorable inlet flow 25 deg

Grid size	Head loss (%)	Torque coeff. T11	Number of iteration	CPU time (min)	Remarks
11×32	3.7	-.008	205	2	very coarse
15×47	3.5	-.009	3000	61	coarse grid
19×65	3.4	-.012	910	33	medium grid
29×98	3.4	-.012	1328	118	fine grid
45×165	3.2	-.014	1868	479	very fine

Table 5 Effect of grid size – Unfavorable inlet flow 13 deg

Grid size	Head loss (%)	Torque coeff. T11	Number of iteration	CPU time (min)	Remarks
11×32	21.9	-.039	762	9	Flow separ.
15×47	21.6	-.055	3000	59	Flow separ.
19×65	21.5	-.069	3000	116	Flow separ.
29×98	21.7	-.075	3000	303	Flow separ.
45×165	21.4	-.074	2745	744	Flow separ.

large flow separation zone occurs at the stay vane extrados. But no flow separation is detected when the Reynolds number is varied from 10^4 to 10^6 . Increasing the Reynolds number to 2×10^6 , a small recirculation bubble occurs again, and the bubble size continues to increase with higher Reynolds number.

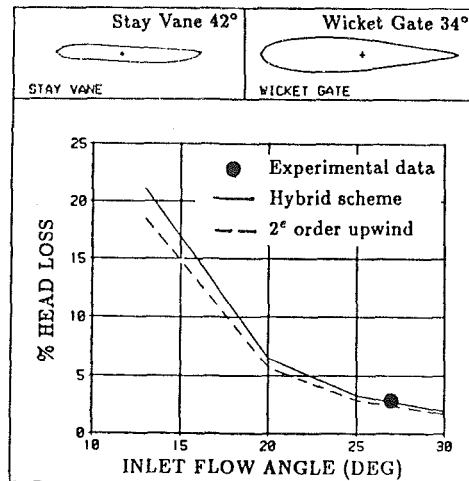
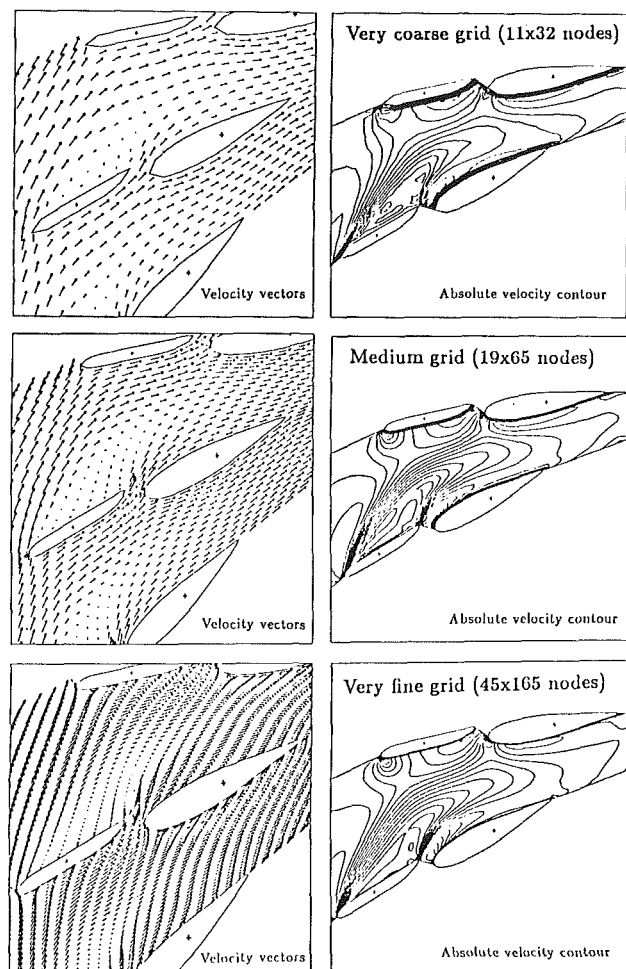
4.3 Effect of the Finite Difference Operator. As we mentioned above, both hybrid and 2nd-order upwind schemes are used in the study of the inlet flow angle. Under favorable and unfavorable inlet flow conditions, both schemes provide similar flow field information. The hybrid scheme converges faster but always overestimates the energy loss in the distributor by about 15 percent compared to the 2nd-order upwind scheme.

4.4 Effect of the Grid Size. The grid size affects the quality of the predicted flow field information and also the computation time. Flow analyses are performed for five grid sizes, varying from very coarse (11×32 nodes) to very fine (45×165 nodes), with two typical inlet flow angles 13 deg and 25 deg (Tables 4 and 5). Coarser grids over-estimate the energy loss and under-estimate the torque coefficient. Using the results obtained by the very fine grid as a reference base for comparison, the very coarse grid over-estimates the energy loss by about 15 percent and under-estimates the torque coefficient by about 46 percent, whereas the medium grid system over-estimates the energy loss by only 6 percent and under-estimates the torque coefficient by only 16 percent. The computation times required by the very coarse and medium grid systems are, respectively, 2 percent and 16 percent of the computation time required by the very fine grid.

5 Validation With Experimental Data

An experimental investigation of the energy losses in the distributor was carried out in order to validate the numerical results. Torque measurements were also made in the hydraulic laboratory with a different distributor geometry and are used to validate the torque calculation.

5.1 Experimental Investigation. Figure 1 shows the geometry of the distributor used for the experimental investigation. In order to determine an optimal position of the stay vane which provides a minimum energy loss, three different orientations of the stay vane were tested: 42, 37, and 32 deg. For each stay vane position, two wicket openings were specified: 34 and 39 deg. A particular cascade flow passage, located diametrically from the casing inlet, is selected for the

**Fig. 4 Effect of the inlet flow angle on total energy loss****Fig. 5 Velocity field obtained with 3 different grid sizes. Unfavorable inlet flow condition 13 deg.**

flow investigation. At the inlet and outlet of the flow passage, 8 pitot traverses were made with a 3 deg interval to cover a total angle of 21 deg. Three velocity components, total and static pressures were measured simultaneously with a 3-D five-hole probe. The precision on the measurement of the flow angle is ± 1 deg. The inlet flow angle is influenced by the stay vane orientation. At 34 deg wicket gate opening, the measured inlet flow angles are 26.6, 31.9 and 25 deg for the three stay vane orientations 42, 37, and 32 deg, respectively. At 39 deg

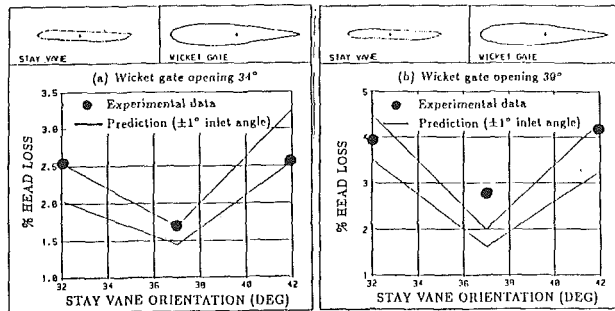


Fig. 6 Variation of the total energy loss as a function of the stay vane orientation

wicket gate opening, they change slightly to 25.2, 31.6 and 23 deg for the three stay vane orientations. The total energy loss is obtained by comparing the mass-weighted averaged total pressures at the distributor inlet and outlet, with a precision ± 0.4 percent of the turbine head. The flow Reynolds number during the test is about 0.75×10^6 .

5.2 Numerical Prediction of the Total Energy Loss. Flow analyses are performed for the six test cases. Fine grid system and hybrid scheme are used for the calculation. The inlet flow angles are specified according to the experimental data with a variation of ± 1 deg. Excellent agreement between the numerical results and experimental data is obtained in Fig. 6(a) showing the variation of the total energy loss as a function of the stay vane orientation for 34 deg wicket gate opening. In Fig. 6(b) for 39 deg wicket gate opening, the energy loss is somehow under-estimated at 37 deg stay vane position. But in all cases, both the numerical prediction and experimental data indicate clearly that the best position of the stay vane is at 37 deg. It should be mentioned that the prediction obtained from a 2-D flow analysis, without considering any secondary flow which could occur in a real 3-D flow passage, would be expected to slightly under-estimate the energy loss.

5.3 Numerical Prediction of the Wicket Gate Torque. The wicket gate torque measurements were carried out in another distributor with different geometries of the stay vane and wicket gate. Figure 7 illustrates the distributor geometry and the fine grid systems generated for wicket gate openings 16 and 52 deg. The flow Reynolds number is 10^6 . A hybrid scheme is used for calculation. The inlet flow angle was not measured, but a 3-D potential flow analysis of the spiral casing indicates that the inlet flow angle varies from 25 to 30 deg around the distributor. The torques were measured with two different configurations of the runner. In both cases, good agreement is obtained between the prediction and measurements as shown in Fig. 8.

6 Concluding Remarks

This paper discusses the application of a Navier-Stokes calculation procedure to a two-dimensional flow analysis in radial inflow turbine distributor. Although the flow in a turbine distributor is fully three-dimensional, we have demonstrated that the 2-D flow analysis could predict quite correctly the flow behavior and performance of the distributor for different operating flow conditions. It is an excellent and

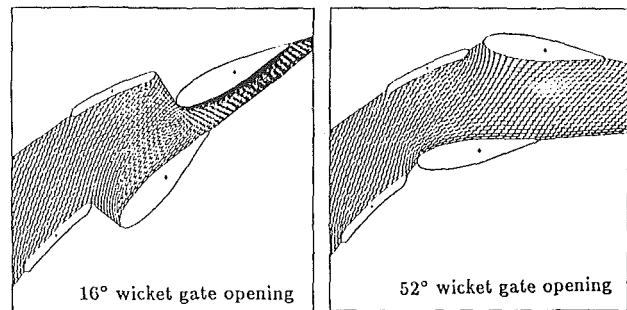


Fig. 7 Grid systems for 16 and 52 deg wicket gate openings

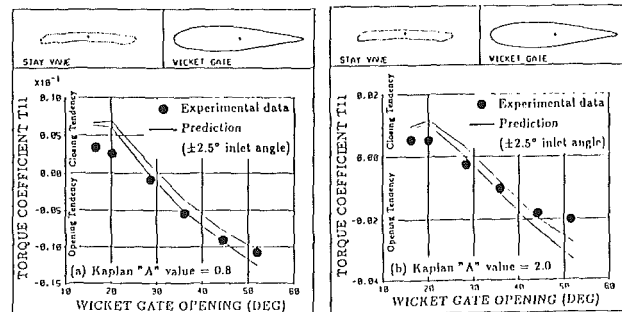


Fig. 8 Wicket gate torque coefficient as a function of the wicket gate opening

economical analytical tool and is being used regularly by our hydraulic turbine designers.

Acknowledgments

The authors gratefully acknowledge the helpful discussions with Dr. M. E. Braaten of General Electric Corporation Research and Development during the course of this study. Also thanks are due to Mr. E. Desbiens and the personnel of the Hydraulic Laboratory of Dominion Engineering Works for their cooperation during the experimental investigation.

References

- Shyy, W., Tong, S. S., and Correa, S. M., "Numerical Recirculating Flow Calculation Using a Body-fitted Coordinate System," *Numerical Heat Transfer*, Vol. 8, 1985, pp. 99-113.
- Braaten, M. E., and Shyy, W., "A Study of Recirculating Flow Computation Using Body-fitted Coordinates: Consistency Aspects and Skewness," *Numerical Heat Transfer*, Vol. 9, 1985, pp. 559-574.
- Shyy, W., and Vu, T. C., "A Numerical Study of Incompressible Navier-Stokes Flow Through Rectilinear and Radial Cascade of Turbine Blades," *Comp. Mech.*, Vol. 1, 1986, pp. 269-279.
- Shyy, W., "A Numerical Study of Annular Dump Diffuser Flows," *Comp. Meth. Appl. Mech. Eng.*, Vol. 53, 1985, pp. 47-65.
- Shyy, W., and Braaten, M. E., "Three-Dimensional Analysis of the Flow in a Curved Hydraulic Turbine Draft Tube," *Int. J. Num. Meth. Fluids*, in print.
- Shyy, W., Correa, S. M., and Braaten, M. E., "Computation Methods for Gas Turbine Combustor," ASME 104th Winter Meeting, 1986.
- Shyy, W., "A Study of Finite Difference Approximations to Steady State, Convection Dominated Flow Problems," *J. Comp. Physics*, Vol. 57, 1985, pp. 415-438.
- Lauder, B. E., Spalding, D. B., "The Numerical Calculation of Turbulence Flows," *Comp. Meth. Appl. Mech. Eng.*, Vol. 3, 1974, pp. 269-289.
- Thompson, J. F., Thames, F. C., and Mastin, C. W., "Automatic Numerical Generation of Body-fitted Curvilinear Coordinate System for Field Containing any Number of Arbitrary Two-Dimensional Bodies," *J. Comp. Physics*, Vol. 15, 1974, pp. 297-319.

Effect of Particle Characteristics on Trajectories and Blade Impact Patterns

A. Hamed

Professor,
Department of Aerospace Engineering and
Engineering Mechanics,
University of Cincinnati
Cincinnati, Ohio 45221

This work presents the results of a detailed study of the effect of particle characteristics on the particle dynamics and on the resulting pattern of blade impacts in a two stage axial flow gas turbine operating with particle laden flows. The particle dynamics computations combine the particle-blade impact characteristics, as determined from a three dimensional trajectory analysis with the particle rebound characteristics, which are obtained from experimental data. The results show the pattern of blade impacts in all stationary and rotating blade rows for fly ash and for sand particles. The results demonstrate that drastically different patterns of particle blade impacts are associated with the different particles.

Introduction

In many industrial, naval, and aeronautical applications, the flow in gas turbines is frequently laden with solid particles. This can be caused by the ingestion of particulate matter such as sand, dust or volcanic ash into the engine. The solid particles can also be byproducts of combustion in many advanced fuels. Depending on the particle size and weight, they tend not to follow the flow in the blade passage, and to impact the blade surface and the inner and outer annulus. If the particles are erosive, their impacts with the blade surfaces increase the blade surface roughness and cause a permanent loss of performance. In particular, the pitting and cutting of the blade leading and trailing edges has a detrimental effect on their aerodynamic performance. In case of severe erosion damage, the blade life can be adversely affected and structural failure of the blades might result.

The prediction of blade erosion in multistage turbomachines presents a very difficult problem. The blade erosion pattern is generally complex as it depends on many factors such as the blade row location, the blade geometry, the particle characteristics, the blade material, and the flow conditions [1, 2]. The erosion of metals by solid particle laden flow have been investigated experimentally [2, 3] to determine the parameters affecting the erosion rate. The results of these investigations indicate that the erosion rate is affected by the impacting velocity, impingement angle, the metal and gas temperatures and by the particle and target materials. These effects have been simulated experimentally, in especially designed erosion tunnels where the gas particle stream conditions can be controlled [4]. The experimental erosion data can be used to predict blade erosion if the particle impact locations as well as their impacting velocities and impingement angle relative to the blade surfaces are known.

Several factors affect the particle dynamics, including the blade passage geometry and the operating conditions [5, 6]. The particle blade impacts strongly influence the radial and circumferential particle distribution after each blade row. The effects of particle size and particle inlet slip velocity on the resulting particle trajectories in one turbine stage were presented by Hussein and Tabakoff [7]. However, the rebounding characteristics for nonerosive particles were used in the modeling. Clevenger and Tabakoff [8] determined the significant dimensionless parameters that affect the particle trajectories in radial turbines, and used them in correlating the trajectories in hot and cold flow fields. More recently, the restitution characteristics were determined experimentally for ash particles using LDV [9, 10]. These results and the rebound characteristics of sand particles which were determined experimentally using high speed photography [11] indicate that the rebound characteristics of these particles are quite different for the same target material and may consequently influence the particle trajectories.

In the present work, the dynamics of sand and ash particles are studied in a two stage gas turbine. These two types of particles represent the actual particle laden flow environment that would be encountered by the turbine engine. The larger 150 micron diameter sand particles are representative of the dust laden atmosphere in helicopter engines [5], while the 15 micron mean diameter ash particles are representative of the coal fired turbine particulate flow conditions. The particle size distribution for four types of ash particles were presented in reference [12] from which one can see that the 15 micron mean diameter is representative of the Cincinnati Gas and Electric fly ash particles. The particles whose material density is 162.3 lb/ft³ for sand and 104 lb/ft³ for ash particles exhibit different rebound characteristics according to the experimental measurements reported in references [9] and [11]. The three dimensional trajectories of the two types of solid particles are presented relative to the turbine blades. The results demonstrate large differences in the location and frequency of

Contributed by the Fluids Engineering Division of THE AMERICAN SOCIETY OF MECHANICAL ENGINEERS and presented at the AIAA/ASME Joint Fluid Mechanics Plasma/Laser Conference, Atlanta, Ga., May 1986. Manuscript received at ASME by the Fluids Engineering Conference January 28, 1987.

turbine blade impacts, by the two types of particles, which would significantly influence the resulting blade erosion damage.

Analysis

The equations governing the particle motion, in the turbomachinery flow field are expressed in a coordinate system relative to a frame of reference fixed with respect to the blades. The following equations are given for a rotating blade row:

$$\frac{d}{d\tau} \left(\frac{d\bar{x}_p}{d\tau} + r_p \omega \hat{e}_\theta \right) = \bar{F} \quad (1)$$

where \bar{x}_p define the particle location in the rotating frame of reference, ω the blade angular velocity, and \bar{F} the force of interaction between the two phases, per unit mass of particles. Under particulate flow conditions in turbomachines, the effect of the forces due to gravity and interparticle interactions are negligible compared to those due to aerodynamic and centrifugal forces. In addition, the force of interaction between the two phases is dominated by the drag due to the difference in velocity between the solid particles and the flow field. Therefore, the force of interaction is dependent on the relative velocity between the particles and the gas flow, as well as the particle size and shape, and is given by:

$$\bar{F} = \frac{3}{4} \frac{\rho}{\rho_p} \frac{C_D}{d} \left[\left(\bar{w}_g - \frac{d\bar{x}_p}{d\tau} \right) \cdot \left| \bar{w}_g - \frac{d\bar{x}_p}{d\tau} \right| \right] \quad (2)$$

where \bar{w}_g represents the relative gas velocity, ρ and ρ_p the gas and solid particle material densities, d the particle diameter, and C_D the particle drag coefficient. This coefficient is dependent on the Reynolds number, which is based on the relative velocity between the particle and the gas. Empirical relations are used to fit the drag curve over a wide range of Reynolds numbers. The same equations can be used in the stator by setting ω equal to zero and replacing the relative gas velocity \bar{w} by the absolute gas velocity \bar{V} .

The particle trajectory calculations consist of the numerical integration of the equations (1)–(2) in the flow field, up to the point of blade, hub or tip impact. The magnitude and direction of particle rebounding velocity after these impacts are dependent on the impacting particle conditions and on the impacted surface material. Figure 1 shows the combined results of references [10] and [12] for the rebound characteristics of ash and sand particles impacting 410 stainless steel. Empirical equations for the mean values of the velocity restitution ratios and the rebound directional coefficient are used in the trajectory computations to determine the rebounding particle conditions after each surface impact.

Blade Passage Flow Model. The large flow turning angles generally encountered in modern highly loaded axial flow turbine blading, produce large axial, pitchwise, as well as spanwise flow field variations. The flow field affects the particle

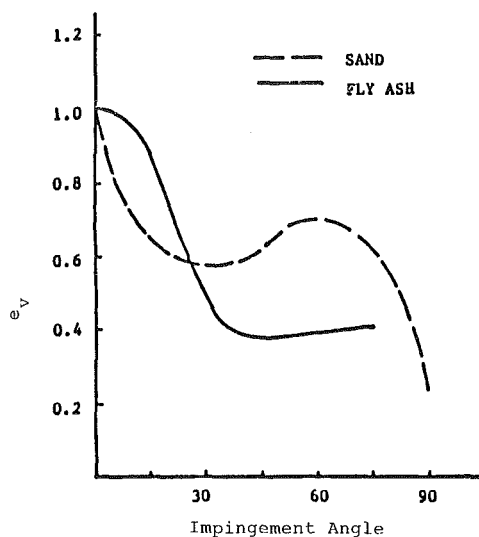


Fig. 1(a) Total velocity restitution ratio e_v

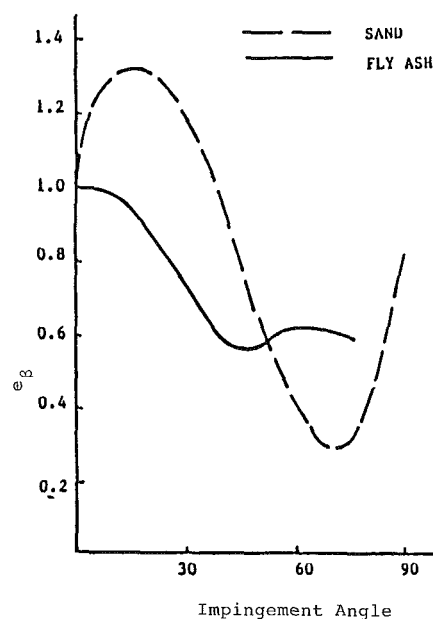


Fig. 1(b) Directional coefficient e_β

Fig. 1 Particle restitution coefficients for 410 stainless steel

trajectories, through the aerodynamic forces of interaction consisting mainly of the drag. It is important to represent the spanwise, pitchwise and chordwise variations in flow properties in the particle trajectory calculations, without excessive computer storage, and computer time for flow properties in-

Nomenclature

C_D = particle drag coefficient

d = particle diameter

e_v = total velocity restitution ratio (ratio of the particle rebound to impingement velocity)

e_β = directional coefficient (ratio of the particle rebound to impingement angle)

\hat{e}_θ = unit vector in the circumferential direction

\bar{F} = force of interaction between the gas and the particle

r = radial distance from the turbomachine axis

\bar{V} = absolute velocity

\bar{w} = relative velocity

\bar{x}_p = position vector

θ = angular coordinate

ρ = gas density

ω = rotor speed (radians/s)

τ = time

Subscripts

g = gas

I = impact

p = particle

R = rebound

Table 1 Blade design characteristics

Blade Row	Flow Channel Turning	Radius Ratio, r_h/r_t	Aspect Ratio, A	Solidity, $(c/s)_m$	Number of blades
Nozzle	70	0.823	0.85	1.57	43
First-stage rotor	134.7	0.789	2.26	1.63	98
Second-stage stator	130.1	0.746	2.78	1.62	97
Second-stage rotor	125.6	0.711	3.21	1.57	94

terpolations. The latter are required at each time step in the numerical integration of the particle equations of motion.

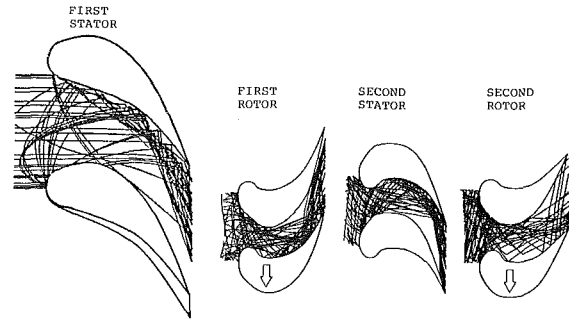
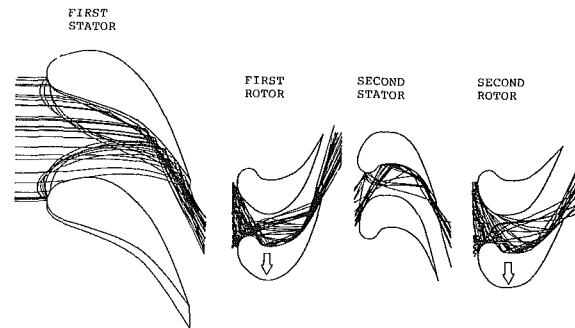
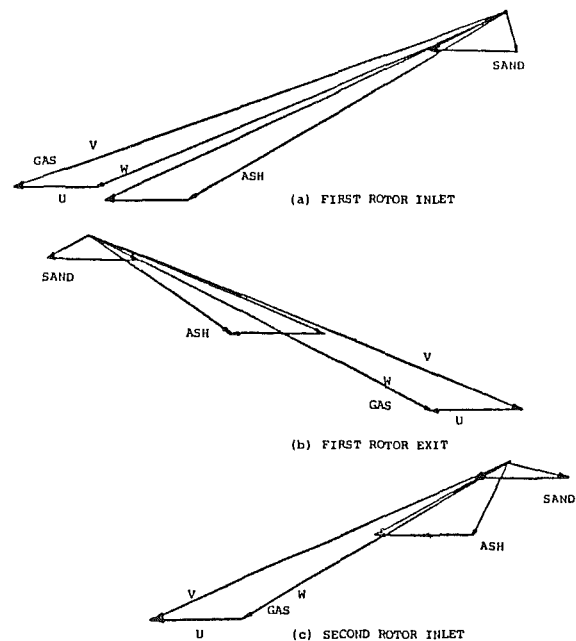
The flow field in a blade passage is synthesized from a number of blade-to-blade stream surface solutions [13]. Each flow field solution on a blade-to-blade stream surface [13] provides accurate description of the pitchwise and streamwise variation in the flow properties. The stream surface shapes and stream filament thickness as determined from a mid channel hub to tip stream surface solution [14], model the influence of the hub and tip contouring, and the hub to tip variation in the blade shapes. The details of the two dimensional inviscid compressible flow solutions on the blade-to-blade and hub-to-tip surfaces which are based on the stream function formulation, and use both matrix and velocity gradient methods in the numerical solution can be found in references [13] and [14].

The turbine blade shape must also be accurately represented in the trajectory analysis as it influences the predicted particle dynamics through blade, hub and tip impacts. The turbine blade leading edge geometry, in particular, strongly influences the computed trajectories since a large percentage of particles impact the blunt leading edges of the turbine blades. The blade surface coordinates at a number of sections between the hub and tip are used in the trajectory calculations to describe the radial variation in the blade shape. These data are used to identify the particle impact locations and to determine the blade surface orientation at each impact point.

Results and Discussion

The numerical computations for 15 micron fly-ash, and 150 micron sand particle dynamics were carried out through a 0.45 scale model, two stage axial flow oxidizer pump-drive turbine [15] for the standard inlet air equivalent conditions at 1893 rpm and 7.071 lb/s weight flow. The blade design parameters are summarized in Table 1. The distribution of both types of particles at the gas turbine inlet was statistically specified according to the mass flow. The small ash particles were assumed to be in equilibrium with the gas flow at the turbine inlet, while the larger ash particles had 50 percent slip velocity. The presented results show typical particle trajectories and blade impact patterns for the ash and sand particles.

Figures 2 and 3 present the computed trajectories for 25 sand and ash particles through the various blade rows of the two stage turbine. One can see from the particle trajectories in the first nozzle, that the main difference between the two sets of trajectories, is observed for those particles impacting the blunt leading edge. After rebounding, the larger sand particles deviate more from the flow streamlines and hence tend to impact the opposite surface further upstream. Comparing Figs. 2 and 3, one can observe a large difference between the ash and sand particle trajectories in the first rotor. The small ash particles impact only the blade pressure side, while many of the larger sand particles also impact the blade suction side. Similar, but less pronounced differences can be observed in the sand and ash particle trajectories through the second stator. The sand particle-blade suction surface impacts are observed over one third of the blade axial chord near the leading edge and over the last 10 percent of the axial chord near the trailing edge. On the other hand, very few ash par-

**Fig. 2 Sand particle trajectories****Fig. 3 Fly ash particle trajectories****Fig. 4 Velocity triangles for gas and particles**

ticles impact the leading edge of the blade suction side. One can see profoundly different trajectories for the sand and ash particles through the second rotor. The blade suction side is impacted by the sand particles much more frequently than the pressure surface. The opposite is true for the ash particles whose few impacts with the blade suction surface are limited to the leading edge region.

The main difference in the trajectories and blade impact patterns of the ash and sand particles is caused by their different directions at inlet relative to the blade rows. Although the direction of both particles as they leave the first stator is

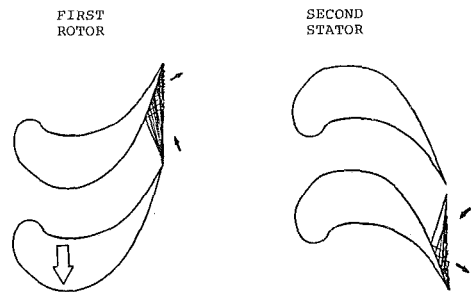


Fig. 5 Sand particle trajectories affected by intra-blade interaction

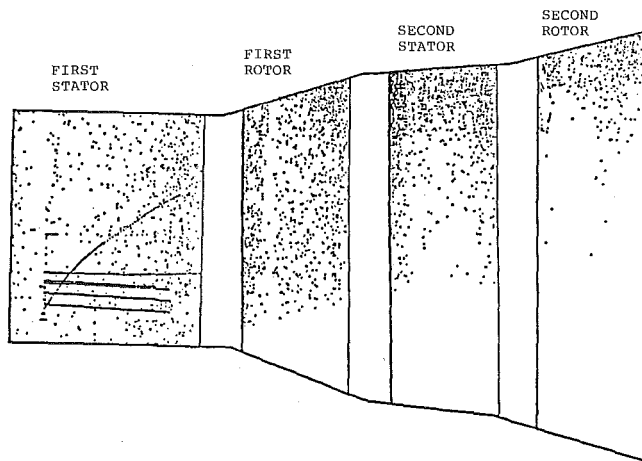


Fig. 6 Blade pressure side impact locations for sand particles

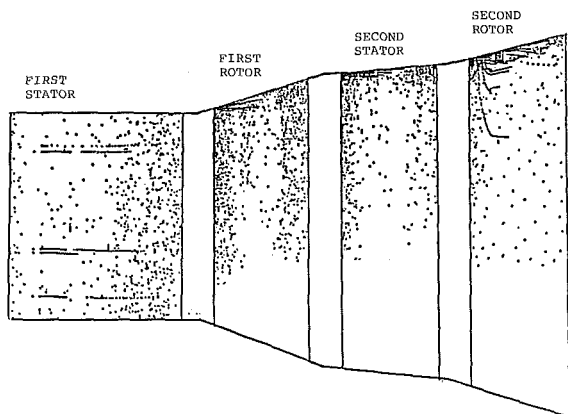


Fig. 7 Blade pressure side impact locations for fly ash particles

similar in the absolute frame of reference, their inlet velocity directions relative to the first rotor are very different since the sand particle absolute velocities are much lower. This is clearly illustrated in the gas, ash and sand velocity triangles of Fig. 4, which shows the gas and particle's mean velocities between the blade rows. It is clear that the mean inlet velocities for the sand and ash particles are different in both magnitude and direction relative to all the blade rows succeeding the first nozzle. One can see from Fig. 2 that the sand particles enter the first rotor with a large negative incidence angle, and continue to have increasing negative inlet incidence angles as they enter the second stator and the second rotor.

One additional significant difference characterized the large sand particle dynamics through the two stage turbine. Some of the sand particles return after impacting the leading edge of a given blade row to re-enter the preceding blade row and impact its blade suction surface very near the trailing edge as shown in Fig. 5. The percentage of particles with this intra-blade behavior are as follows: 26 percent between the first

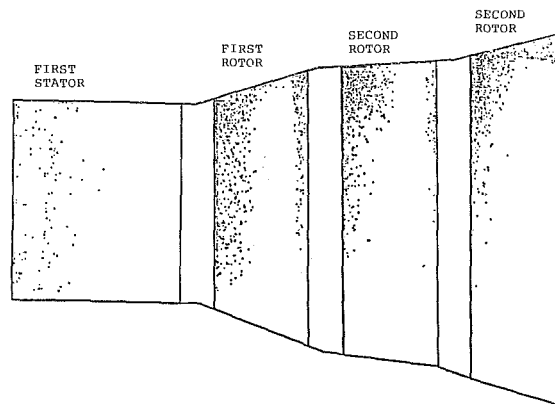


Fig. 8 Blade suction side impact location for sand particles

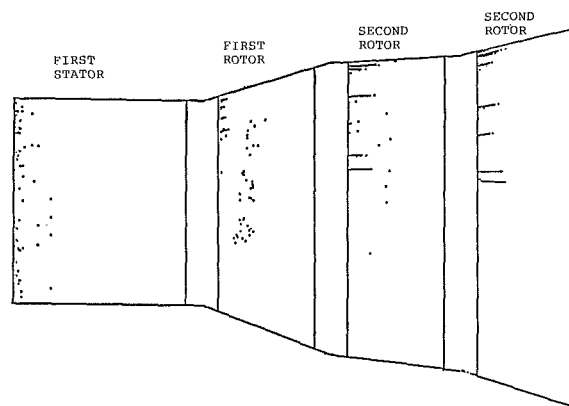


Fig. 9 Blade suction side impact location for fly ash particles

rotor and second stator, 22.2 percent between the second stator and second rotor, and only 0.5 percent of the particles re-entered the first stator after impacting the leading edge of the first rotor.

Figures 6 and 7 present the locations of blade pressure surface impact by 500 sand and ash particles respectively, while Figs. 8 and 9 present similar results for the blade suction surface. The first observation one can conclude from these figures is that both ash and sand particles start to centrifuge in the radial outward direction after their first rotor impact and continue through the rest of the turbine. Both particle pressure surface impacts (Figs. 6 and 7) are somewhat similar, but those for the larger sand particles tend to spread more evenly in the chordwise direction. On the other hand, very few ash particles impacts can be observed over the middle third of the blade axial chord, except very near the blade tip. The most obvious difference between the two impact patterns is over the blade suction surface (Figs. 8 and 9) where the impacts are more frequent for the sand particles compared to the insignificant number of ash particle impacts. Also, one can see some sand particle impacts with the first rotor and second stator blade suction sides near the trailing edge. These impacts are caused by intrablade interactions shown in Fig. 5. The concentration of these impacts near the blade trailing edge towards the tip, and their impingement angles which are close to that corresponding to maximum erosion (25°) for sand particles impacting 410 stainless steel can result in significant blade surface erosion.

Conclusions

The results of sand and ash particle trajectory computations are presented in a two stage turbine. The presented results show the difference between the trajectories and blade impact

patterns for the two types of particles. The differences are particularly obvious in the suction surfaces of the blade rows succeeding the first nozzle. The blade suction surfaces are impacted by the sand particles at the leading and trailing edges, but are practically not impacted by the fly ash particles. In addition, some of the sand particles return after impacting the leading edges of the following blade row to impact the blade suction surfaces of the first rotor and the second stator near the trailing edges. The erosion of the blade suction surface near the trailing edge by sand particles, in the intermediate blade rows, can adversely affect the turbine performance.

Acknowledgment

This research work was supported in part by the Department of Energy Contract No. 19X1-89628C, and in part by U.S. Army Research Office Durham under Contract No. DAAG29-82-K-0029. The author wishes to acknowledge Mr. M. Mansour's efforts in performing the numerical computations.

References

- 1 Hamed, A., and Fowler, S., "Erosion Pattern of Twisted Blades by Particle Laden Flows," *ASME Journal of Engineering for Power*, Vol. 105, Oct. 1983, pp. 839-843.
- 2 Grant, G., and Tabakoff, W., "Erosion Prediction in Turbomachinery Resulting from Environmental Solid Particles," *Journal of Aircraft*, Vol. 12, No. 5, 1975, pp. 471-478.
- 3 Tabakoff, W., Hamed, A. and Ramachandran, J., "Study of Metals Erosion in High Temperature Coal Gas Streams," *ASME Journal of Engineering for Power*, Vol. 102, Jan. 1980, pp. 148-152.
- 4 Tabakoff, W., and Hamed, A., "Investigation of Gas Particle Flow in Erosion Wind Tunnel," 7th Annual Conference on Materials for Coal Conversion and Utilization, National Bureau of Standards, Gaithersburg, MD, Nov. 16-18, 1982.
- 5 Tabakoff, W., and Hamed, A., "Installed Engine Performance in Dust Laden Atmosphere," AIAA Paper 84-2488, Nov. 1984.
- 6 Hamed, A., "Solid Particle dynamic Behavior through Twisted Blade Rows," *ASME JOURNAL OF FLUIDS ENGINEERING*, Vol. 106, No. 3, Sept. 1984, pp. 251-256.
- 7 Hussein, M. F., and Tabakoff, W., "Dynamic Behavior of Solid Particles Suspended by Polluted Flow in a Turbine Stage," *Journal of Aircraft*, Vol. 10, No. 7, pp. 434-440, July 1973.
- 8 Clevenger, W. B., and Tabakoff, W., "Similarity Parameters for Comparing Erosive Particle Trajectories in Hot-Air and Cold-Air Raidal Inflow Turbines," *ASME Journal of Engineering for Power*, pp. 358-364, Oct. 1974.
- 9 Tabakoff, W., and Malak, M. F., "Laser Measurements of Fly Ash Rebound Parameters for Use in Trajectory Calculations," ASME Paper No. 85-GT-161, 30th International Gas Turbine Conference and Exhibit, Houston, Texas, Mar. 17-21, 1985.
- 10 Tabakoff, W., Malak, M. F., and Hamed, A., "Laser Measurements of Solid Particles Rebound Parameters Impacting on 2024 Aluminum and 6A1-4V Titanium Alloys," AIAA Paper No. 85-1570, AIAA 18th Fluid Dynamics and Plasmadynamics and Lasers Conference, Cincinnati, Ohio, July 1985.
- 11 Tabakoff, W., Grant, G., and Ball, R., "An Experimental Investigation of Certain Aerodynamic Effects on Erosion," AIAA Paper 74-639, July 1974.
- 12 Kotwal, R., and Tabakoff, W., "A New Approach for Erosion Prediction Due to Fly Ash," *ASME Journal of Engineering for Power*, Vol. 3, pp. 265-270, April 1981.
- 13 Katsanis, T., "Fortran Program for Calculating Transonic Velocities on a Blade-to-Blade Stream Surface of a Turbomachine," NASA TND 2809, May 1965.
- 14 Katsanis, T., and McNally, W. D., "Revised Fortran Program for Calculating Velocities and Streamlines on the Hub-Shroud Mid Channel Stream Surface of an Axial, Raidal, or Mixed Flow Turbomachine or Annular Duct, Vols. 1 and 2," NASA TND 8430 and NASA TND 8431, 1977.
- 15 Roelke, R. J., Stabe, R. G., and Evans, D. G., "Cold-Air Performance Evaluation of Scale Model Oxidizer Pump-Drive Turbine for the M-1 Hydrogen-Oxygen Rocket Engine," II-Overall Two-Stage Performance, NASA TND-3368, 1966.

A Reynolds-Stress Model for Near-Wall and Low-Reynolds-Number Regions

Nobuyuki Shima

Associate Professor,
College of Engineering,
Shizuoka University,
Hamamatsu 432, Japan

The Reynolds stress model for high Reynolds numbers proposed by Launder et al. is extended to near-wall and low-Reynolds-number regions. In the development of the model, particular attention is given to the high anisotropy of turbulent stresses in the immediate vicinity of a wall and to the behavior of the exact stress equation at the wall. A transport model for the turbulence energy dissipation rate is also developed by taking into account its compatibility with the stress model at the wall. The model and the low-Reynolds-number model of Hanjalić and Launder are applied to fully-developed pipe flow. Comparison of the numerical results with Laufer's data shows that the present model gives significantly improved predictions. In particular, the present model is shown to reproduce the sharp peak in the distribution of the streamwise turbulence intensity in the immediate vicinity of the wall.

1 Introduction

Recently the modeled transport equation for Reynolds stresses has been used as a powerful tool for prediction of various turbulent flows. The applicability of such a model is usually limited to regions where the turbulence Reynolds number is high. Consequently, when the model is applied to wall-bounded flows boundary conditions are transferred to points removed from the wall on the basis of "universal laws." There are many circumstances, however, where "universal laws" are not applicable. It is desirable, therefore, to extend the model to near-wall and low-Reynolds-number regions so that boundary conditions can be specified just at the wall.

There are many such attempts for the so-called two-equation model, and Patel et al. (1981) evaluated the relative performance of the existing models. On the other hand, only a few studies have been made for the stress equation model so far. Hanjalić and Launder (1976) (hereafter referred to as HL) extended the high-Reynolds-number model of Launder et al. (1975) (hereafter referred to as LRR). However, when the model was applied to actual cases, it was reduced to a three-equation model for thin shear layers by introducing various assumptions. Therefore, the general performance of their model remains unknown. Prud'homme and Elghobashi (1983) proposed a model which largely modified the parent LRR model. However, their numerical result on turbulent normal stresses does not seem to reproduce the observed behavior well in the immediate vicinity of a wall. (They also reported the performance of the HL model for channel flow, but their treatment of the model was incorrect in that viscous transport term was dropped in the ϵ transport equation.) For a numerical simulation of buoyant turbulent flow, To and

Humphrey (1986) developed an algebraic stress model (and a k - ϵ model) for low Reynolds numbers, which partly adopted the HL model. It is clear that development of a reliable model at the full second-moment-closure level will also contribute to the closure at such levels.

The present study, like the studies mentioned above, is an attempt to extend the LRR model to near-wall and low-Reynolds-number regions. The model and the HL model are applied to fully-developed pipe flow and the numerical results are compared with Laufer's (1954) experimental data to clarify their performance.

After the present study was completed, a model which includes several improvements of the HL model has been proposed by Kebede et al. (1985). Some comments on the model will also be included.

2 Stress Transport Equation

2.1 Exact Equation. For incompressible flows the exact equation governing the Reynolds-stress transport may be written as

$$\begin{aligned} \frac{D}{Dt} \overline{u_i u_j} = & - \left(\overline{u_j u_k} \frac{\partial U_i}{\partial x_k} + \overline{u_i u_k} \frac{\partial U_j}{\partial x_k} \right) \\ & - 2\nu \frac{\partial u_i}{\partial x_k} \frac{\partial u_j}{\partial x_k} + \frac{1}{\rho} p \left(\frac{\partial u_i}{\partial x_j} + \frac{\partial u_j}{\partial x_i} \right) - \frac{\partial}{\partial x_k} \left\{ \overline{u_i u_j u_k} \right. \\ & \left. - \nu \frac{\partial}{\partial x_k} \overline{u_i u_j} + \frac{1}{\rho} \overline{p(u_j \delta_{ik} + u_i \delta_{jk})} \right\} \end{aligned} \quad (1)$$

where overbars imply the ensemble averaging and the summation convention is used for repeated suffices.

The terms on the right-hand side of the equation are identified as generation, dissipation, redistribution and diffusion.

Contributed by the Fluids Engineering Division for publication in THE JOURNAL OF FLUIDS ENGINEERING. Manuscript received by the Fluids Engineering Division, March 12, 1986.

Of these terms the generation and the viscous diffusion can be treated exactly on the present level of closure.

2.2 LRR Model. The dissipation term is modeled as

$$2\nu \frac{\partial u_i}{\partial x_k} \frac{\partial u_j}{\partial x_k} = \frac{2}{3} \delta_{ij} \epsilon \quad (2)$$

The redistribution term is modeled as

$$\frac{1}{\rho} p \left(\frac{\partial u_i}{\partial x_j} + \frac{\partial u_j}{\partial x_i} \right) = \phi_{ij,1} + \phi_{ij,2} + \phi_{ij,w} \quad (3)$$

where

$$\phi_{ij,1} = -C_1 \frac{\epsilon}{k} \left(\overline{u_i u_j} - \frac{2}{3} \delta_{ij} k \right) \quad (4)$$

$$\phi_{ij,2} = -\frac{C_2 + 8}{11} \left(P_{ij} - \frac{2}{3} \delta_{ij} P \right) - \frac{30C_2 - 2}{55} k \left(\frac{\partial U_i}{\partial x_j} + \frac{\partial U_j}{\partial x_i} \right) - \frac{8C_2 - 2}{11} \left(D_{ij} - \frac{2}{3} \delta_{ij} P \right) \quad (5)$$

$$\phi_{ij,w} = \left\{ 0.125 \frac{\epsilon}{k} \left(\overline{u_i u_j} - \frac{2}{3} \delta_{ij} k \right) + 0.015 (P_{ij} - D_{ij}) \right\} \frac{k^{3/2}}{\epsilon l} \quad (6)$$

The terms P_{ij} , D_{ij} , and P are defined by

$$P_{ij} = - \left(\overline{u_i u_k} \frac{\partial U_j}{\partial x_k} + \overline{u_j u_k} \frac{\partial U_i}{\partial x_k} \right) \quad (7)$$

$$D_{ij} = - \left(\overline{u_i u_k} \frac{\partial U_k}{\partial x_j} + \overline{u_j u_k} \frac{\partial U_k}{\partial x_i} \right) \quad (8)$$

$$P = - \overline{u_k u_l} \frac{\partial U_k}{\partial x_l} \quad (9)$$

The model constants C_1 and C_2 take the values 1.5 and 0.4 respectively. The symbol l denotes the distance from a wall when the flow is bounded by a single flat wall, and otherwise a generalization was suggested (see LRR).

Of the diffusion terms the pressure transport is neglected and the triple velocity correlation is approximated as

$$\overline{u_i u_j u_k} = -C_s \frac{k}{\epsilon} \left(\overline{u_i u_l} \frac{\partial}{\partial x_l} \overline{u_j u_k} + \overline{u_j u_l} \frac{\partial}{\partial x_l} \overline{u_i u_k} + \overline{u_k u_l} \frac{\partial}{\partial x_l} \overline{u_i u_j} \right) \quad (10)$$

with the model constant $C_s = 0.11$.

Although the viscous diffusion term is exact, it is neglected since its contribution is negligible for high Reynolds numbers.

2.3 HL Model. The model equation (2) for the dissipation is modified as

$$2\nu \frac{\partial u_i}{\partial x_k} \frac{\partial u_j}{\partial x_k} = \frac{2}{3} \epsilon \left\{ (1 - f_s) \delta_{ij} + \frac{\overline{u_i u_j}}{2k/3} f_s \right\} \quad (11)$$

where f_s is a function of the local turbulence Reynolds number R_T and given by

$$f_s = 1/(1 + R_T/10) \quad (12)$$

$$R_T = k^2/(\nu \epsilon) \quad (13)$$

For other terms the LRR model is adopted except that the viscous diffusion term is, of course, retained in this case.

2.4 Present Model. At a wall the dissipation term in the HL model is consistent with the term in the exact equation since the following equation holds there:

$$2\nu \frac{\partial u_i}{\partial x_k} \frac{\partial u_j}{\partial x_k} = \frac{\epsilon}{k} \overline{u_i u_j} \quad (14)$$

However, the redistribution term in the HL model is not consistent with the term in the exact equation. This is readily seen if the behavior of the equations at the wall is examined in Cartesian coordinates $O-x_1 x_2 x_3$ with $x_2 = 0$ on the plane wall. For the exact equation the redistribution term vanishes in u_1^2 , u_2^2 and u_3^2 equations, whereas the term generally takes a nonzero finite value in $u_1 u_2$ equation which counterbalances the pressure transport term. On the other hand, for the HL model the term takes a nonzero finite value in u_1^2 , u_2^2 and u_3^2 equations owing to the contribution of $\phi_{ij,1}$ ($\phi_{ij,2}$ and $\phi_{ij,w}$ being zero), whereas the term vanishes in $u_1 u_2$ equation.

To remove the defect we adopt Lumley's (1980) rearrangement of the dissipation and redistribution terms. According to the treatment, the terms in the exact equation are rearranged as

$$\begin{aligned} -2\nu \frac{\partial u_i}{\partial x_k} \frac{\partial u_j}{\partial x_k} + \frac{1}{\rho} p \left(\frac{\partial u_i}{\partial x_j} + \frac{\partial u_j}{\partial x_i} \right) &= -\frac{2}{3} \delta_{ij} \epsilon \\ + \left\{ \frac{1}{\rho} p_{(1)} \left(\frac{\partial u_i}{\partial x_j} + \frac{\partial u_j}{\partial x_i} \right) - 2\nu \frac{\partial u_i}{\partial x_k} \frac{\partial u_j}{\partial x_k} + \frac{2}{3} \delta_{ij} \epsilon \right\} \\ + \frac{1}{\rho} p_{(2)} \left(\frac{\partial u_j}{\partial x_i} + \frac{\partial u_i}{\partial x_j} \right) &\quad (15) \end{aligned}$$

Here p is decomposed into $P_{(1)}$ which is contributed only by fluctuations and $P_{(2)}$ which involves the mean velocity field. The first term on the right-hand side is the high-Reynolds-number form of the dissipation which no longer needs to be modeled. The second term is the redistribution which includes only fluctuations and the third is the redistribution which includes the mean velocity field. We, like LRR, neglect the pressure transport term in modeling. Accordingly we treat both of the redistribution terms to vanish at the wall in $u_1 u_2$ equation as well as in u_1^2 , u_2^2 , and u_3^2 equations. Thus, using equation (14), the second term at the wall reduces to $-(\epsilon/k)(u_i u_j - 2\delta_{ij} k/3)$. Moreover equation (4) may be considered as a model of the term for high Reynolds numbers. The second term is thus modeled as

$$\phi_{ij,1}^* = -C_1^* \frac{\epsilon}{k} \left(\overline{u_i u_j} - \frac{2}{3} \delta_{ij} k \right) \quad (16)$$

$$C_1^* = C_1 \{ 1 - (1 - 1/C_1) f_w \} \quad (17)$$

Nomenclature

k = turbulence energy
 p = fluctuation of pressure
 t = time
 u_i = fluctuation of velocity
 U_i = mean velocity
 U = axial mean velocity
 U_0 = axial mean velocity at pipe axis

U_τ = friction velocity
 uv = (kinematic) turbulent shear stress
 u' = axial turbulence intensity
 v' = radial turbulence intensity
 w' = tangential turbulence intensity

x_i = Cartesian coordinates
 y = distance from wall
 ϵ = isotropic turbulence energy dissipation rate
 ν = kinematic viscosity
 ρ = density

where f_w is a function which equals unity at a wall and zero for high Reynolds number regions remote from a wall. Although Lumley presented a more elaborate form, we here adopt rather simple expressions (16) and (17).

Launder and Reynolds (1983) pointed out that equation (14) is not asymptotically exact as a wall is approached. Accordingly Kebede et al. modified equation (11) into a more elaborate form. In the present study, however, equation (14) has been used to derive equations (16) and (17) since the equation exactly holds just at the wall and the interpolation function may largely affect the result.

With regard to the redistribution term involving the mean velocity field, we adopt equation (5) for $\phi_{ij,2}$. However, the term $\phi_{ij,w}$ is replaced by the expression:

$$\phi_{ij,w}^* = \left\{ \alpha \left(P_{ij} - \frac{2}{3} \delta_{ij} P \right) + \beta \left(D_{ij} - \frac{2}{3} \delta_{ij} P \right) + \gamma k \left(\frac{\partial U_i}{\partial x_j} + \frac{\partial U_j}{\partial x_i} \right) \right\} f_w \quad (18)$$

which, unlike $\phi_{ij,w}$, does not include the term related only to fluctuations and vanishes at a wall as well as in high Reynolds number regions. This replacement is based on the fact that the factor $k^{3/2}/\epsilon l$ vanishes at the wall and the term $\phi_{ij,w}$ has little effect in the immediate vicinity of the wall. Since the function f_w will be determined to depend explicitly on viscosity, the present model does not include the non-viscous wall-proximity effect. Although further addition of the effect is possible, it has been found that there is no overall advantage to be attained in this way.

The values of the model constants α , β , and γ are determined by starting with some probable values and refining them with trial computations to reproduce the observed stress levels in the immediate vicinity of a wall. The procedure, though not fundamental, is described below. If we assume $f_w = 1$, the Reynolds stress components in the logarithmic region may be evaluated, following the analysis of LRR, as

$$\overline{u_1^2}/k = 0.925 + 4(2\alpha - \beta)/9 \quad (19)$$

$$\overline{u_2^2}/k = 0.465 - 4(\alpha - 2\beta)/9 \quad (20)$$

$$\overline{u_3^2}/k = 0.610 - 4(\alpha + \beta)/9 \quad (21)$$

$$\begin{aligned} (-\overline{u_1 u_2}/k)^2 = & \{ (0.236 + \alpha) \overline{u_2^2}/k \\ & - (0.109 - \beta) \overline{u_1^2}/k + (0.182 - \gamma) \} / 1.5 \end{aligned} \quad (22)$$

where suffix 1 denotes the mean flow direction. Although these equations merely give imaginary levels in the logarithmic region, we here make use of them to produce the high anisotropy of stresses in the immediate vicinity of a wall (reasonable level in the actual logarithmic region being attained with the effect of the function f_w). We tentatively use the maximum values in the distributions of k , $\overline{u_2^2}$, $\overline{u_3^2}$ and $-\overline{u_1 u_2}$. Such values in Laufer's experiment (for the lower Reynolds-number case) are

$$k/U_\tau^2 \sim 4, \overline{u_2^2}/U_\tau^2 \sim 0.95, \overline{u_3^2}/U_\tau^2 \sim 1.7, -\overline{u_1 u_2}/U_\tau^2 \sim 0.9 \quad (23)$$

where U_τ denotes the friction velocity. Applying these values to equations (19)–(22), we obtain

$$\alpha = 0.45, \beta = -0.03, \gamma = 0.08$$

Starting with these values we finally assign the following values to the constants after trial computations:

$$\alpha = 0.45, \beta = 0, \gamma = 0.08 \quad (24)$$

The choice of the β value is based on the policy that the factors included should be as few as possible.

Kebede et al. used more elaborate wall-proximity terms which had been utilized by many authors. The term also include the multiplicative factor $k^{3/2}/\epsilon l$ and hence will affect little the turbulence levels in the immediate vicinity of a wall. In

fact their result does not seem to have reproduced the sharp peak in the streamwise turbulence intensity for flat plate boundary layer.

For the diffusion terms we, of course retain the viscous diffusion term and adopt equation (10) for $u_i u_j u_k$.

3 ϵ Transport Equation

3.1 LRR Model. The model is given by

$$\frac{D\epsilon}{Dt} = C_{\epsilon 1} \frac{\epsilon}{k} P - C_{\epsilon 2} \frac{\epsilon^2}{k} + \frac{\partial}{\partial x_m} \left(C_{\epsilon} \frac{k}{\epsilon} \overline{u_m u_l} \frac{\partial \epsilon}{\partial x_l} \right) \quad (25)$$

with $C_{\epsilon 1} = 1.44$, $C_{\epsilon 2} = 1.9$ and $C_{\epsilon} = 0.15$. The first two terms on the right-hand side represent generation and destruction of ϵ and the third approximates its diffusive transport.

3.2 HL Model. The second term $C_{\epsilon 2} \epsilon^2/k$ on the right-hand side of equation (25) is replaced by $C_{\epsilon 2} f_{\epsilon} \bar{\epsilon}/k$, where $\bar{\epsilon}$ are f_{ϵ} are given by

$$\bar{\epsilon} = \epsilon - 2\nu (\partial k^{1/2} / \partial x_l)^2 \quad (26)$$

$$f_{\epsilon} = 1.0 - (0.4/1.8) \exp\{- (R_T/6)^2\} \quad (27)$$

The viscous diffusion term $\nu \partial^2 \epsilon / \partial x_k \partial x_k$ is retained and an additional generation term related to the mean velocity field:

$$\psi = C_{\epsilon 3} \nu \frac{k}{\epsilon} \overline{u_j u_k} \frac{\partial^2 U_i}{\partial x_j \partial x_l} \frac{\partial^2 U_i}{\partial x_k \partial x_l} \quad (28)$$

is introduced. The model constants are somewhat modified as $C_{\epsilon} = 0.15$, $C_{\epsilon 2} = 1.8$ and $C_{\epsilon 1} = C_{\epsilon 2} - 3.5 C_{\epsilon} = 1.275$. The new constant $C_{\epsilon 3}$ is given the value 2.0.

3.3 Present Model. Deriving the transport equation for the turbulence energy k by a contraction of the stress equation and applying it to a wall, we obtain the following expression (for the exact equation, HL model and present model):

$$\epsilon = \nu \partial^2 k / \partial x_l \partial x_l \quad (29)$$

Further, deriving the transport equation for the right-hand side quantity of this equation and applying it to a wall, we obtain (for the HL and present models)

$$\frac{\partial}{\partial t} \left(\nu \frac{\partial^2 k}{\partial x_l \partial x_l} \right) = -\nu \frac{\partial^2 \epsilon}{\partial x_l \partial x_l} + \nu \frac{\partial^2}{\partial x_m \partial x_m} \left(\nu \frac{\partial^2 k}{\partial x_l \partial x_l} \right) \quad (30)$$

In the exact equations the coincidence of $\partial/\partial t (\nu \partial^2 k / \partial x_l \partial x_l)$ and $\partial \epsilon / \partial t$ at the wall is ensured by many additional correlation terms. Since, in modeling, such terms are absent, it is possible that k and ϵ are bound to each other in undesirable manner. We here try to arrange the ϵ transport equation to relax the possible binding.

Applying simple Taylor series expansion to u_1 , u_2 and u_3 in the vicinity of a wall and calculating k and $\epsilon = [\nu (\partial u_k / \partial x_l)^2]$, we obtain

$$k = ax_2^2 + bx_3^2 + cx_2^4 + \dots \quad (31)$$

$$\epsilon = \nu (2a + 4bx_2 + dx_2^2 + \dots) \quad (32)$$

where a , b , etc. are averaged quantities which are functions of x_1 , x_3 , and t . Since it is difficult to treat a general case, we below restrict ourselves to the case where the averaged quantities depend only on x_2 and t . If the right-hand side of equation (30) is calculated using equations (31) and (32), it reduces to $(-2\nu^2 d + 24\nu^2 c)$. However, $\partial \epsilon / \partial t$ of the HL model calculated similarly does not reduce to the same form at the wall. We here introduce an additional term:

$$\xi = \left\{ \left(-2 + \frac{7}{9} C_{\epsilon 2} \right) \frac{\epsilon \bar{\epsilon}}{k} - \frac{1}{2} \frac{\bar{\epsilon}^2}{k} \right\} f_w \quad (33)$$

where

$$\bar{\epsilon} = \epsilon - \nu \partial^2 k / \partial x_l \partial x_l \quad (34)$$

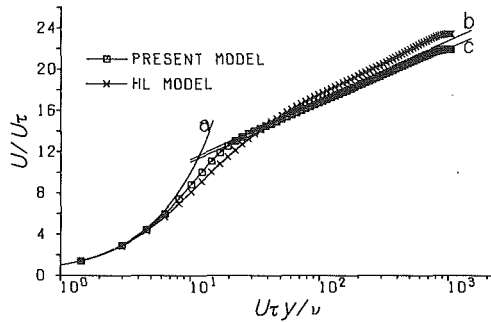


Fig. 1 Mean velocity, (a) $U/U_\tau = U_\tau y/\nu$; (b) $U/U_\tau = (1/0.4)\ln(U_\tau y/\nu) + 5.5$; (c) $U/U_\tau = (1/0.418)\ln(U_\tau y/\nu) + 5.5$

With this addition, as easily confirmed, $\partial\epsilon/\partial t$ becomes identical with $\partial/\partial t (\nu\partial^2 k/\partial x_i \partial x_i)$ at the wall.

We do not adopt the additional generation term ψ of HL. However, without the term the generation is too small in the immediate vicinity of a wall. Here we simply multiply the generation term $C_{e1} (\epsilon/k)P$ by a function as $C_{e1} (1 + C_{e4} f_w)$ ($\epsilon/k)P$.

The model constants are given the values as $C_e = 0.15$, $C_{e1} = 1.35$ and $C_{e2} = 1.8$. With regard to C_{e4} , we assign the value 1.0 on the basis of trial computations.

Kebede et al. arranged C_{e1} to vary from the high-Reynolds-number value to the wall value 2.0, and retained the term ψ with $C_{e3} = 0.3$. The present generation $C_{e1} (1 + C_{e4} f_w)$ ($\epsilon/k)P$ may be considered as the term which collectively represents the generation related to the mean velocity field by adjusting the C_{e4} value.

The argument of the function f_w is taken to be $\sqrt{k}x_2/\nu$ which explicitly includes the distance from a wall x_2 . The expression finally determined after trial computations is

$$f_w = \exp\{- (0.015\sqrt{k}x_2/\nu)^4\} \quad (35)$$

Of course the argument can be R_T or $U_\tau x_2/\nu$ instead of $\sqrt{k}x_2/\nu$. In fact such functions were tested and comparable results were obtained. Therefore, equation (35) is rather tentative until the model is tested for more complex flows.

4 Numerical Solution Procedure

The stress and ϵ transport equations together with the mean momentum equation are expressed in cylindrical coordinates for fully-developed pipe flow (with time-derivative terms retained). These equations are nondimensionalized with the friction velocity U_τ for the steady solution and the pipe radius R . Thus the governing parameter in computation is the Reynolds number $Re^* = U_\tau R/\nu$. Then the nondimensional radial coordinate r is transformed into σ by

$$r = (1/b)\tanh[\sigma \tanh^{-1}(b)] \quad (36)$$

($b = 0.98$) to yield increasingly fine mesh as the wall is approached with an equal-spacing discretization. Finally the equations are discretized with replacing the spatial-derivative by the central-difference and the time-derivative by the forward-difference.

An implicit unsteady approach is used for numerical solution. In this approach, as usual, the diffusion terms are evaluated at the next time step. For the turbulent diffusion terms in the stress equation, however, only the terms which result from $u^i u^j$ in $\{C_s (k/\epsilon)u^k u^l u^i u^j\}_{,k}$ (the superscript denotes the contravariant component and the comma denotes the covariant derivative) are evaluated at the next time step.

At the wall a finite difference analog of the equation:

$$\epsilon = 2\nu(\partial k^{1/2}/\partial x_i)^2 \quad (37)$$

, which exactly holds, is used as the boundary condition for ϵ . Other variables are set to zero at the wall. At the axis of the pipe the governing equations simplified on the basis of the symmetry are applied.

The value of the Reynolds number Re^* is set to 1050 which corresponds to (the lower Reynolds-number case of) Laufer's experiment.

The time step size is taken to be $2 \times 10^{-4} - 10^{-3}$ in the unit of nondimensional time tU_τ/R . The convergence criterion is that the ratio of the variation of each variable during time interval 10 to the final value of the variable should be smaller than 10^{-6} for every grid point.

Some test computations were made to obtain grid-independent solutions. Compared to the case of 71 grid points for the present model, the result with 61 grid points showed a decrease of 0.43 percent in the Reynolds number based on the bulk mean velocity and an increase of 0.86 percent in the pipe friction coefficient. The result with 81 grid points yielded respectively a decrease of 0.04 percent and an increase of 0.08 percent. From these results the computation with 71 grid points was judged to be sufficiently accurate and hence adopted.

The nondimensional governing equations in cylindrical coordinates and the discretized equations are given in the Appendix.

5 Comparison of Prediction With Experiment

Figure 1 shows profiles of the axial mean velocity in wall coordinates. In this and subsequent figures, the symbols are marked at locations of the grid points. It is seen that, in the logarithmic region, the result of the present model lies between two "laws" usually accepted while the result of the HL model shifts above appreciably. Corresponding to the profiles, in the pipe friction coefficient the HL model gives the value 7.0 percent lower than the Blasius formula, while the present model gives the value 1.6 percent higher than the formula. (In the U/U_0 versus y/R plot (not shown) both models give fuller shape than the data corresponding to the small (if not zero) "wake" component in Fig. 1. This suggests a problem of the parent LRR model.)

Profiles of the Reynolds shear stress and of the axial, radial and tangential turbulence intensities are shown in Figs. 2-5. It is seen from Fig. 3 that the HL model fails to reproduce the sharp peak in u' profile in the immediate vicinity of a wall. On the other hand, the present model yields the peak at nearly the same position as the data although the maximum value is still low. Figure 4 indicates a further defect of the HL model that the maximum in v' profile lies nearer to the wall than in u' profile. The present model seems favorable in this respect also. For w' profile, however, the present model shows a defect as seen from Fig. 5 that the profile has a flat part at $U_\tau y/\nu = 20 - 30$.

Figure 6 shows profiles of the energy dissipation rate ϵ . (Laufer's data in the figure are drawn from Hinze's (1975) book.) It is noticed that the HL model gives superior result in the maximum value of ϵ while the present model gives better result in the wall value of ϵ . However, the data on ϵ are usually subject to large errors and hence conclusive discussion is difficult to make.

As a whole the present model gives improved predictions. In particular, the improvement of u' distribution is significant. For other turbulent quantities, the improvement is relatively modest and perhaps the difference between the two models is not much larger than the experimental uncertainty of Laufer's data. However, the high anisotropy of turbulent stresses is a distinct feature of the turbulence structure in the immediate vicinity of a wall and there is sound evidence for the sharp

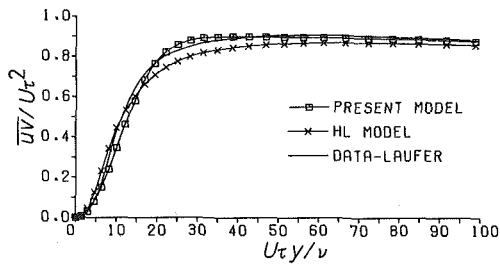


Fig. 2 Turbulent shear stress

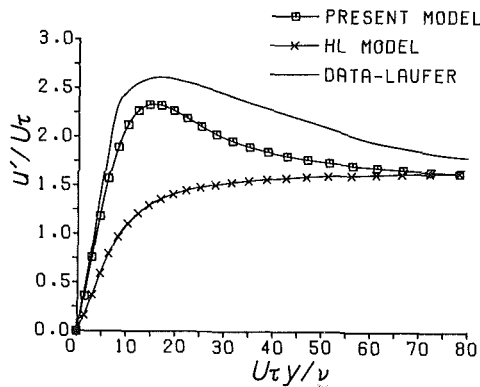


Fig. 3 Axial turbulence intensity

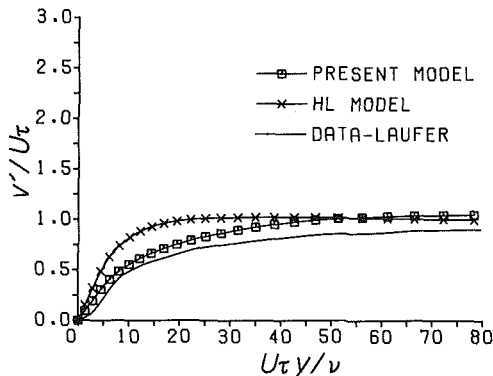


Fig. 4 Radial turbulence intensity

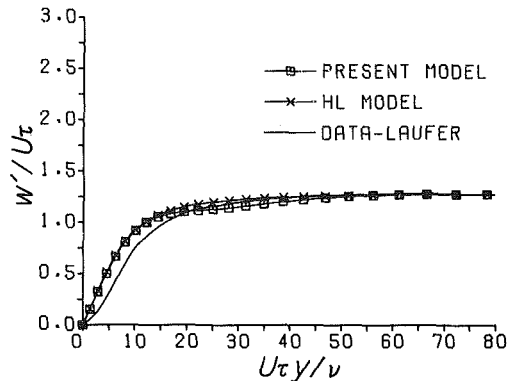


Fig. 5 Tangential turbulence intensity

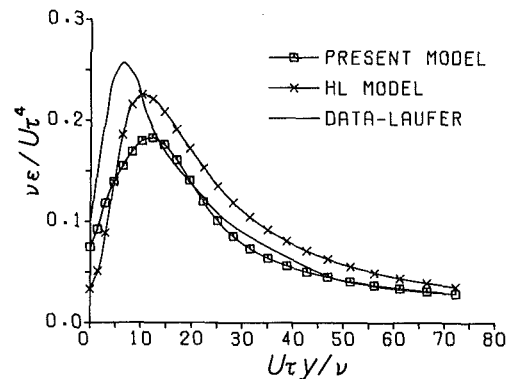


Fig. 6 Dissipation rate

peak in u' distribution from other experiments [e.g., Kreplin and Eckelmann (1979)].

The reason why the present model reproduces the high anisotropy may be traced to the redistribution terms. It should be remembered that the coefficient C_1^* of the return-to-isotropy term decreases as a wall is approached. Moreover, in the normal stress equations the net effect of the mean-strain part of the redistribution is considerably reduced by the term $\phi_{ij,w}^*$ with rather large value of α . (Note that the term with γ appears only in the shear stress equation and reduces the total effect of $\phi_{ij,w}^*$ in the equation.) These two effects (C_1^* and $\phi_{ij,w}^*$) strongly suppress the isotropization of stresses, thus producing the high anisotropy. In addition to the improvement of the redistribution, the present model augments the total turbulence energy to reproduce the experimental level (Figs. 3–5). The augmentation is related to the decrease in ϵ (Fig. 6) and perhaps due to a decrease in the generation of ϵ which results from the net effect of the term ξ and the term with $C_{\epsilon 4}$ in the ϵ transport equation.

6 Concluding Remarks

The Reynolds stress model of Launder et al. for high Reynolds numbers has been extended to near-wall and low-

Reynolds-number regions. The extended model has been successfully applied to fully-developed pipe flow.

If we restrict ourselves to a single simple flow, it is not very difficult to obtain a satisfactory prediction by adjusting the values of model constants. Moreover, in such simple flow the stress equation model is not largely superior to lower-order models. Therefore, the present model should be applied to more complex flows with success before it claims to be definitely useful. Thus the present study may be regarded as the presentation of a possible model and of its basic performance which suggests the promising nature of the model.

Finally it is acknowledged that the numerical computation was carried out on FACOM M382 at The Computer Center of Nagoya University.

References

- Hanjalić, K., and Launder, B. E., 1976, "Contribution towards a Reynolds-Stress Closure for Low-Reynolds-Number Turbulence," *Journal of Fluid Mechanics*, Vol. 74, pp. 593–610.
- Hinze, J. O., 1975, *Turbulence*, 2nd Ed., McGraw-Hill, p. 736.
- Kebede, W., Launder, B. E., and Younis, B. A., 1985, "Large-Amplitude Periodic Pipe Flow: A Second-Moment Closure Study," *Proceedings 5th Symposium on Turbulent Shear Flows*, Cornell University, New York, pp. 16.23–16.29.
- Kreplin, H. P., and Eckelmann, H., 1979, "Behaviour of the Three Fluctuating Velocity Components in the Wall Region of a Turbulent Channel Flow," *Physics of Fluids*, Vol. 22, pp. 1233–1239.
- Laufer, J., 1954, "The Structure of Turbulence in Fully Developed Pipe Flow," *NACA Report*, 1174, pp. 1–18.
- Launder, B. E., Reece, G. J., and Rodi, W., 1975, "Progress in the Development of a Reynolds-Stress Turbulence Closure," *Journal of Fluid Mechanics*, Vol. 68, pp. 537–566.
- Launder, B. E., and Reynolds, W. C., 1983, "Asymptotic Near-Wall Stress Dissipation Rates in a Turbulent Flow," *Physics of Fluids*, Vol. 26, pp. 1157–1158.
- Lumley, J. L., 1980, "Second Order Modeling of Turbulent Flows," *Prediction Methods for Turbulent Flows*, Kollmann, W., ed., Hemisphere, New York, pp. 1–31.
- Patel, V. C., Rodi, W., and Scheuerer, G., 1981, "Evaluation of Turbulence

APPENDIX

Governing Equations in Cylindrical Coordinates

The nondimensional equations for the present model can be expressed as

$$\frac{\partial \Phi}{\partial t} - \frac{1}{r} \frac{\partial}{\partial r} \left(r \Gamma_{\Phi} \frac{\partial \Phi}{\partial r} \right) + \frac{1}{r} \Lambda_{\Phi} \Phi = S_{\Phi}$$

where Φ stands for the dependent variables. The factors Γ_{Φ} and Λ_{Φ} are given for each Φ as follows:

Φ	Γ_{Φ}	Λ_{Φ}
U	$\frac{1}{\text{Re}^*}$	0
\overline{uv}	$C_s \frac{k}{\epsilon} \overline{v^2} + \frac{1}{\text{Re}^*}$	$C_s \frac{k}{\epsilon} \overline{w^2} + \frac{1}{\text{Re}^*}$
$\overline{u^2}$	$C_s \frac{k}{\epsilon} \overline{v^2} + \frac{1}{\text{Re}^*}$	0
$\overline{v^2} + \overline{w^2}$	$C_s \frac{k}{\epsilon} \overline{v^2} + \frac{1}{\text{Re}^*}$	0
$\overline{v^2} - \overline{w^2}$	$C_s \frac{k}{\epsilon} \overline{v^2} + \frac{1}{\text{Re}^*}$	$4 \left(C_s \frac{k}{\epsilon} \overline{w^2} + \frac{1}{\text{Re}^*} \right)$
ϵ	$C_{\epsilon} \frac{k}{\epsilon} \overline{v^2} + \frac{1}{\text{Re}^*}$	0

where u , v , and w denote axial, radial and tangential components of the velocity fluctuation respectively. Instead of v^2 and w^2 , $(\overline{v^2} + \overline{w^2})$ and $(\overline{v^2} - \overline{w^2})$ are adopted as the dependent variables for computational convenience. Note that all the variables here are nondimensional although the same symbols as the dimensional ones are used. The source terms are given as follows:

$$S_U = 2 - \frac{1}{r} \frac{\partial}{\partial r} (r \overline{uv})$$

$$S_{\overline{uv}} = -\overline{v^2} \frac{\partial U}{\partial r} - C_1^* \frac{\epsilon}{k} \overline{uv} + (C_{21} \overline{v^2} + C_{22} \overline{u^2} - C_{23} k) \frac{\partial U}{\partial r} + (-\alpha \overline{v^2} + \gamma k) \frac{\partial U}{\partial r} f_w$$

$$+ \frac{1}{r} \frac{\partial}{\partial r} \left[r C_s \frac{k}{\epsilon} \left(\overline{uv} \frac{\partial \overline{v^2}}{\partial r} + \overline{v^2} \frac{\partial \overline{uv}}{\partial r} \right) \right]$$

$$- \frac{1}{r} C_s \frac{k}{\epsilon} \left(\overline{uv} \frac{\partial \overline{w^2}}{\partial r} + \frac{1}{r} \overline{w^2} \overline{uv} \right)$$

$$S_{\overline{u^2}} = -2 \overline{uv} \frac{\partial U}{\partial r} - \frac{2}{3} \epsilon - C_1^* \frac{\epsilon}{k} \left(\overline{u^2} - \frac{2}{3} k \right)$$

$$+ \left(\frac{4}{3} C_{21} - \frac{2}{3} C_{22} \right) \overline{uv} \frac{\partial U}{\partial r} - \frac{4}{3} \alpha \overline{uv} \frac{\partial U}{\partial r} f_w$$

$$+ \frac{2}{r} \frac{\partial}{\partial r} \left(r C_s \frac{k}{\epsilon} \overline{uv} \frac{\partial \overline{uv}}{\partial r} \right)$$

$$S_{\overline{v^2} + \overline{w^2}} = -\frac{4}{3} \epsilon - C_1^* \frac{\epsilon}{k} \left(\overline{v^2} + \overline{w^2} - \frac{4}{3} k \right)$$

$$+ \left(-\frac{4}{3} C_{21} + \frac{2}{3} C_{22} \right) \overline{uv} \frac{\partial U}{\partial r} + \frac{4}{3} \alpha \overline{uv} \frac{\partial U}{\partial r} f_w$$

$$+ \frac{2}{r} \frac{\partial}{\partial r} \left(r C_s \frac{k}{\epsilon} \overline{v^2} \frac{\partial \overline{v^2}}{\partial r} \right)$$

$$+ \frac{2}{r} \frac{\partial}{\partial r} \left[C_s \frac{k}{\epsilon} \overline{w^2} (\overline{v^2} - \overline{w^2}) \right]$$

$$S_{\overline{v^2} - \overline{w^2}} = -C_1^* \frac{\epsilon}{k} (\overline{v^2} - \overline{w^2}) + 2 C_{22} \overline{uv} \frac{\partial U}{\partial r}$$

$$+ \frac{2}{r} \frac{\partial}{\partial r} \left(r C_s \frac{k}{\epsilon} \overline{v^2} \frac{\partial \overline{v^2}}{\partial r} \right)$$

$$- \frac{2}{r} \frac{\partial}{\partial r} \left[C_s \frac{k}{\epsilon} \overline{w^2} (\overline{v^2} - \overline{w^2}) \right]$$

$$- \frac{4}{r} C_s \frac{k}{\epsilon} \left[\overline{v^2} \frac{\partial \overline{w^2}}{\partial r} + \frac{1}{r} \overline{w^2} (\overline{v^2} - \overline{w^2}) \right]$$

$$S_{\epsilon} = -C_{\epsilon 1} (1 + C_{\epsilon 4} f_w) \frac{\epsilon}{k} \overline{uv} \frac{\partial U}{\partial r} - C_{\epsilon 2} f_{\epsilon} \frac{\epsilon \bar{\epsilon}}{k}$$

$$+ \left[(-2 + \frac{7}{9} C_{\epsilon 2}) \frac{\epsilon \bar{\epsilon}}{k} - \frac{1}{2} \frac{\bar{\epsilon}^2}{k} \right] f_w$$

$$C_{21} = (C_2 + 8)/11$$

$$C_{22} = (8C_2 - 2)/11$$

$$C_{23} = (30C_2 - 2)/55$$

When the coordinate transformation [equation (36)] is applied, the derivatives with respect to r are replaced by

$$\frac{\partial}{\partial r} = h_1 \frac{\partial}{\partial \sigma}$$

$$\frac{\partial^2}{\partial r^2} = h_1^2 \frac{\partial^2}{\partial \sigma^2} + h_2 \frac{\partial}{\partial \sigma}$$

where

$$h_1 = \frac{b}{\tanh^{-1}(b)} \frac{1}{1-s^2}$$

$$h_2 = \frac{2b^2}{\tanh^{-1}(b)} \frac{s}{(1-s^2)^2}$$

$$s = \tanh [\sigma \tanh^{-1}(b)]$$

Discretized Equations

The dependent variable Φ and its spatial derivatives are evaluated at the next time step $n+1$, the derivatives being replaced by the central difference. The time derivative is replaced by the forward difference between the time step $n+1$ and the current time step n . The discretized equation thus obtained is

$$A_{\Phi_i} \Phi_{i+1}^{n+1} + B_{\Phi_i} \Phi_i^{n+1} + C_{\Phi_i} \Phi_{i-1}^{n+1} = D_{\Phi_i}$$

where

$$A_{\Phi_i} = -\Delta t \left[\Gamma_{\Phi} \left(\frac{h_1^2}{\Delta\sigma^2} + \frac{h_2}{2\Delta\sigma} \right) + \frac{1}{r} \frac{\partial}{\partial r} (r\Gamma_{\Phi}) \frac{h_1}{2\Delta\sigma} \right]_i$$

$$B_{\Phi_i} = 1 + \Delta t \left(\Gamma_{\Phi} \frac{2h_1^2}{\Delta\sigma^2} + \frac{1}{r^2} \Lambda_{\Phi} \right)_i$$

$$C_{\Phi_i} = -\Delta t \left(\Gamma_{\Phi} \left(\frac{h_1^2}{\Delta\sigma^2} - \frac{h_2}{2\Delta\sigma} \right) - \frac{1}{r} \frac{\partial}{\partial r} (r\Gamma_{\Phi}) \frac{h_1}{2\Delta\sigma} \right)_i$$

$$D_{\Phi_i} = \Phi_i + \Delta t S_{\Phi_i}$$

In the expressions of the coefficients, the coordinate r is still used for conciseness. The symbols Δt and $\Delta\sigma$ are the increments in t and σ respectively. The subscript denotes the nodal position in the coordinate σ , while the superscript denotes the time step. The terms A , B , C and D are all evaluated at the time step n , the spatial derivatives included being replaced by the central difference again. (The superscript n are omitted in the equations for conciseness.)

In the solution procedure, the discretized equations are solved with the boundary conditions described in the section 4 by using a standard tri-diagonal matrix algorithm. This procedure is continued until the convergence criterion is satisfied.

E. G. Tulapurkara
Assistant Professor.

V. V. K. Bhalla
Graduate Student.

Department of Aeronautical Engineering,
Indian Institute of Technology,
Madras 600 036, India

Experimental Investigation of Morel's Method for Wind Tunnel Contractions

Based on a numerical study of the potential flow through contractions of chosen geometry, Morel (1975) has given a method to obtain the shape of contraction which gives small adverse pressure gradients and low nonuniformity in the velocity distribution at the exit. Two contractions with area ratios of 12 and 3.464 designed using this method are investigated experimentally. It is found that there is no separation of flow, the thickness of the boundary layer at the exit is small and the nonuniformity in velocity at the exit is smaller than the predicted value.

I Introduction

The contraction or the nozzle is an important component of a wind tunnel. As the flow passes through the contraction it accelerates and this results in a reduction of the nonuniformity and turbulence level of the stream. In practical contractions, which are of finite length, one finds that (i) adverse pressure gradients are present at the ends of the contraction (Bradshaw and Pankhurst, 1964), (ii) the axial velocity is higher than the velocity near the wall at the entry to the contraction and (iii) at the exit the velocity near the wall (i.e., outside the boundary layer) is higher than that on the axis. Thus for a good performance the nozzle contour should give low adverse pressure gradients at the ends of contraction so that no separation of flow takes place, the boundary layer thickness at the exit should be small and the nonuniformity in the velocity distribution at the exit (i.e. difference between velocity near the wall and that on the axis) must be small. A good contour should achieve these with a small length (L) to upstream diameter (D_1) ratio.

Nearly fifteen methods have been proposed to obtain the shape of contraction. Klein et al. (1973), Chmielewski (1974), and Morel (1975) give the bibliographic details of these methods. In a majority of these methods the governing equations for axisymmetric, incompressible potential flow are solved with an assumed axial velocity distribution (e.g., Tsien, 1943, Chmielewski, 1974). This gives a set of streamlines. The portion of a streamline which gives a monotonic velocity distribution and very nearly the desired contraction ratio is chosen as the contour of the contraction. In another type of theoretical approach (e.g., Thwaites 1946, Bossel, 1969) the ends of the contraction are taken as equipotential planes. Then assuming a variable-separable solution one gets an expression for the velocity potential in the form of a series. From this the streamlines are calculated. The coefficients in the series are evaluated such that a monotonic velocity distribu-

tion is obtained along the wall. On the other hand, Morel (1975) starts with a chosen geometry for the contraction and obtains a numerical solution for the flow inside the contraction along with suitable straight ducts at either ends of the contraction. The treatment of the contraction as having a finite length does give the adverse pressure gradients and nonuniform velocity distributions at the ends. Based on a criteria for boundary layer separation due to Stratford (1959), guidelines are obtained for getting a contour without separation. This provides a very quick method of obtaining a contour satisfying the requirements for good performance. A brief outline of Morel's method is given now.

The nozzle contour is obtained by two power-law curves matched at a point x_m and having their apexes at either ends of the contraction. During preliminary trials he finds that the cubic curves give the best results. Potential flow inside the contour is computed for values of contraction ratio (c) ranging from 2 to 25, the ratio L/D_1 from 0.75 to 1.25 and the ratio $X (=x_m/L)$ from 0.12 to 0.8. From the computed wall static pressure distributions the pressure coefficients at the inlet and the exit, C_{pi} and C_{pe} , defined as follows, are obtained.

$$C_{pe} = 1 - (V_i/U_{1,\infty})^2; C_{pi} = 1 - (U_{2,\infty}/V_e)^2$$

where V_i and V_e are, respectively, the minimum and maximum velocities near the inlet and the exit of contraction, $U_{1,\infty}$ and $U_{2,\infty}$ are the uniform velocities far upstream of the inlet and far downstream of the exit, respectively. Plots of C_{pi} and C_{pe} , with X and L/D_1 as parameters, are obtained for various contraction ratios. Cross plotting these, one gets X and L/D_1 for a given c and chosen values of C_{pi} and C_{pe} . It is further found that for $C_{pe} < .2$ the difference between the wall velocity and the axial velocity at the exit is proportional to C_{pe} . A value of 0.39 for C_{pi} is recommended so that separation near the inlet is avoided. For C_{pe} a value of 0.06 is suggested. This will ensure that the nonuniformity in the velocity distribution at the exit will not be more than 2 percent, which is considered to be a reasonable value. Incidentally this value of C_{pe} would

Contributed by the Fluids Engineering Division for publication in the JOURNAL OF FLUIDS ENGINEERING. Manuscript received by the Fluids Engineering Division June 8, 1987.

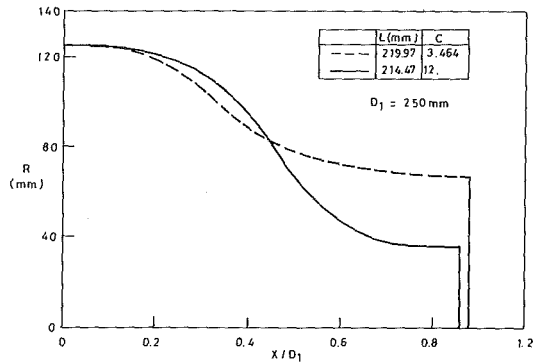
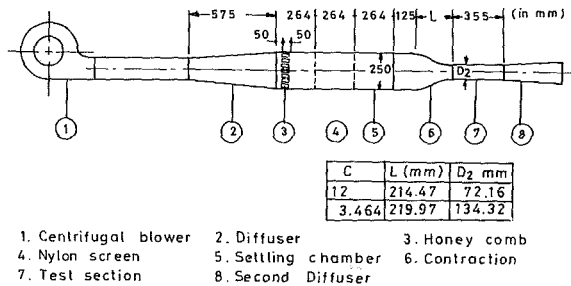


Fig. 1 Contraction shapes as obtained by Morel's method



1. Centrifugal blower
2. Diffuser
3. Honey comb
4. Nylon screen
5. Settling chamber
6. Contraction
7. Test section
8. Second Diffuser

Fig. 2 Experimental setup

also give separation free flow at exit. Once X and L/D_1 are known the contour is given by

$$\frac{D-D_2}{D_1-D_2} = 1 - \frac{1}{X^2} \left(\frac{x}{L} \right)^3 \quad \text{for } \frac{x}{L} \leq X$$

$$= \frac{1}{(1-X)^2} \left(1 - \frac{x}{L} \right)^3 \quad \text{for } \frac{x}{L} > X$$

where D is the diameter at a distance x from the inlet and D_2 is the exit diameter.

Though one would expect the conclusions based on the potential flow calculations to be valid in a contraction, it is felt that it would be interesting to verify them experimentally. Hence experiments are conducted on two contractions with $c=12$ and 3.464 and the parameters of interest like the axial and wall velocity distributions along the contraction, the velocity distributions at the ends and the exit boundary layer thickness are measured and the results are reported in this article. The contours studied are briefly described in section II. This is followed by a description of the experimental setup, experimental results and discussion.

II Contours Studied

Bradshaw and Pankhurst (1964) recommend a contraction ratio of 12 for a good low turbulence wind tunnel. However many wind tunnels in common use have smaller contraction ratios of the order of 4. Hence contractions with area ratios of 12 and $\sqrt{12}$ i.e., 3.464 are chosen for the present investigation. The diameter of the settling chamber ahead of the contraction is 250 mm. Velocity in the settling chamber is 4 m/s. Hence the value of C_{pi} which would not give separation, according to equation (12) of Morel (1975), is .323. A value of 0.35 is chosen for C_{pi} . Based on experience of Tulapurkara (1980) and the recommendation of Morel (1975) an acceptable value for the exit nonuniformity is chosen as 2 percent. This requires C_{pe} to be less than 0.057. A value of 0.05 for C_{pe} is chosen. These values of C_{pi} and C_{pe} give $X=0.537$ and $L/D_1=.858$ for $c=12$, and $X=0.332$ and $L/D_1=0.88$ for $c=3.464$. For D_1 of 250 mm we get D_2 equal to 72.17 mm and 134.32 mm

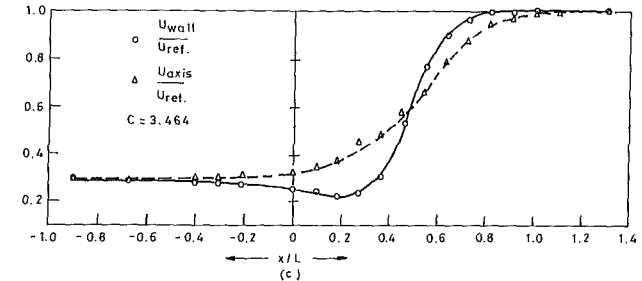
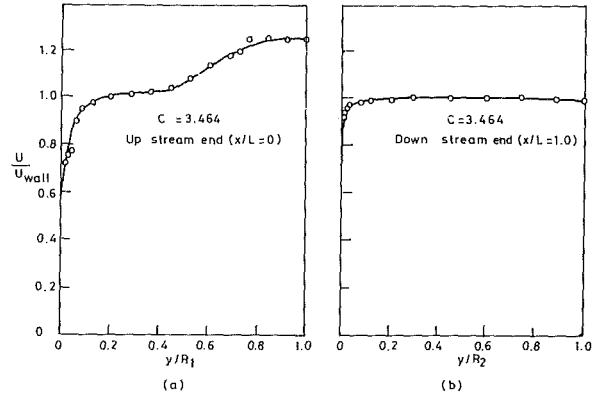


Fig. 3 Experimental velocity distribution for $c=3.464$. (a) Upstream end; (b) Downstream end; (c) Along the contraction. (Uncertainty in $U=2.5$ percent near upstream end = 0.1 percent near downstream end)

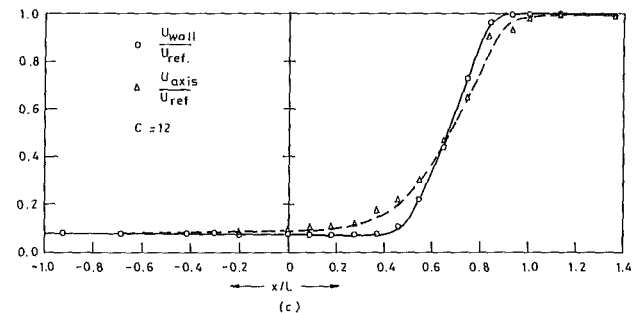
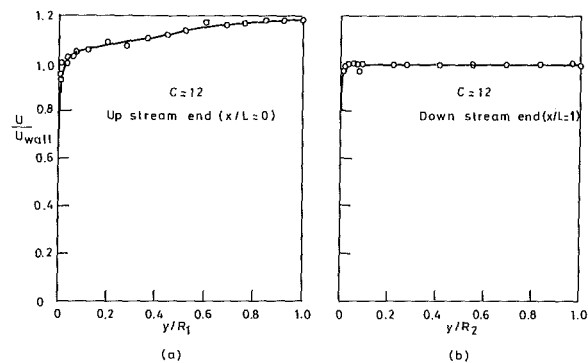


Fig. 4 Experimental velocity distribution for $c=12$. (a) Upstream end; (b) Downstream end; (c) Along the contraction. (Uncertainty in $U=2.5$ percent near upstream end = 0.1 percent near downstream end)

for $c=12$ and 3.464, respectively. The contours are shown in Fig. 1.

III Experimental Setup and Technique

The experimental setup is shown in Fig. 2. The centrifugal blower is driven by a 2 HP motor and delivers about 15 cubic meters of air per minute. The blower is connected to the dif-

fuser through a flexible hose. This prevents transmission of vibrations from the blower to other parts of the setup. The diffuser has an area ratio of 1:4 and a semiangle of 6 deg. The settling chamber which follows the diffuser has (i) a honeycomb of cell width 10 mm and depth 50 mm, (ii) nylon screens with wire diameter 0.36 mm and mesh width 1.25 mm and a settling length of 389 mm. The contraction is followed by a test section and a diffuser. The velocity in the settling chamber is 4 m/s. This would be nearly the settling chamber velocity in most of the wind tunnels with the test section speed between 50 to 60 m/s and the contraction ratio between 12 to 16.

The velocity distributions at the ends of the contraction and along the axis are obtained from measurements of the total pressure and static pressure using pitot and static pressure tubes. Micromanometers FC012 made by Furness Control Ltd. of U.K. are used for pressure measurements. The wall velocity distribution is obtained from the measurement of wall static pressure and the total pressure along the axis. Typical readings of the manometer during velocity measurements near the inlet and exit were $1.3 \pm .05$ and $190 \pm .5$ mm of water, respectively. This gives an accuracy of ± 2.5 percent near the inlet and ± 0.1 percent near the exit.

IV Results and Discussion

The velocity distributions at the ends and the distributions of axial velocity and wall velocity along the contraction are shown in Figs. 3 and 4 for $c=3.464$ and 12, respectively. R_1 and R_2 in these figures are the radii of contraction at the inlet and the exit. From Figs. 3(c) and 4(c) it is seen that the adverse pressure gradients near the inlet is small. In the experiments one does not notice any evidence of separation and the loss of total pressure along the contraction is less than one mm of water. The adverse pressure gradient near the exit is hardly noticeable. The velocity distribution at the inlet does show an appreciable difference between the axial velocity and the wall velocity (Figs. 3(a) and 4(a)), but this is not of much significance. The difference between the axial and wall velocities at the exit for both the contractions studied is only about 1 percent as compared to 2 percent assumed in the

design of their contours. The velocity distributions are seen to become almost uniform, (within ± 0.5 percent) at about $0.1 D_1$ from the exit of the contraction. The heights of the boundary layer at the exit are about 2 mm and 2.5 mm for $c=12$ and 3.464 respectively. It may be mentioned that the exit radii in the two cases are 36.1 mm and 67.2 mm and that the displacement thickness of the boundary layer would be only a small fraction of the boundary layer height.

V Conclusions

Two wind tunnel nozzles with contraction ratio of 12 and 3.464 are designed using Morel's method using $C_{pi}=0.35$ and $C_{pe}=0.05$, and are tested experimentally. It is found that (i) the adverse pressure gradient along the wall is small and there is no separation of flow. (ii) the nonuniformity in the exit velocity distribution is only 1 percent as compared to the design value of 2 percent, and (iii) the velocity distribution becomes practically uniform in $0.1 D_1$ behind the contraction exit.

References

- Bossel, H. H., 1969, "Computations of Axisymmetric Contractions," *AIAA Journal*, Vol. 7, No. 10, pp. 2017-2020.
- Bradshaw, P., and Pankhurst, R. C., 1964, "The Design of Low Speed Wind Tunnels," *Progress in Aeronautical Sciences*, Vol. 5, Kuchemann, D. and Sterne, L. H. G., Editors, Pergamon Press, pp. 1-69.
- Chmielewski, G. E., 1974, "Boundary Layer Considerations in the Design of Aerodynamic Contractions," *Journal of Aircraft*, Vol. 11, No. 8, pp. 435-438.
- Klein, A., Ramjee, V., and Venkataramani, K. S., 1973, "An Experimental Study of the Subsonic Flow in Axisymmetric Contractions," *ZFW*, Vol. 21, No. 9, pp. 312-320.
- Morel, T., 1975, "Comprehensive Design of Axisymmetric Wind Tunnel Contractions" *ASME JOURNAL OF FLUIDS ENGINEERING*, Vol. 97, No. 2, pp. 225-233.
- Stratford, B. S., 1959, "The Prediction of Separation of the Turbulent Boundary Layers," *Journal of Fluid Mechanics*, Vol. 5, Part 1, pp. 1-16.
- Thwaites, B., 1946, "On the Design of Contractions for Wind Tunnels," *Aeronautical Research Council*, London, R & M 2278.
- Tsien, H. S., 1943, "On Design of Contraction Cone for a Wind Tunnel," *Journal of Aeronautical Sciences*, Vol. 10, No. 2, pp. 68-70.
- Tulapurkara, E. G., 1980, "Studies on Thwaites' method for Wind Tunnel Contractions," *Aeronautical Journal*, Vol. 84, pp. 167-169.

Experimental and Computational Investigation of the Two-Dimensional Channel Flow Over Two Fences in Tandem

F. Durst

M. Founti

Institute of Fluid Mechanics,
University of Erlangen-Nuremberg,
8520-Erlangen, Federal Republic of Germany

S. Obi

Department of Mechanical Engineering,
Keio University, Yokohama 233, Japan

Measurements and computations of the mean streamwise velocity and its fluctuations are reported for an arrangement of two similar fences mounted in tandem in fully developed channel flow. The influence of Reynolds number and blockage ratio, in terms of the size and location of the primary and secondary recirculation zones, were investigated. The flow field around each fence was found to be similar to one another as well as to the corresponding single fence flow, for Reynolds numbers (based on the fence height) of up to 100. For higher Reynolds numbers, the shear layer developing from the first fence was significantly disturbed by the second fence resulting in earlier transition and higher turbulence intensities. This effect was most evident in the measured differences of the recirculation lengths downstream of each fence.

1 Introduction

Configurations involving arrangements of sequential baffles (ribs, thin obstacles, etc.) attached to a wall are commonly used for supporting and mixing purposes in heat exchangers, nuclear reactor cores, air-cooled solar collectors, some electronic circuit boards, internally cooled turbine blades, wastewater aeration tanks as well as chemical mixers and other chemical engineering applications. In some situations, turbulence generation and mixing associated with separation are desirable, whereas in others, separation is to be avoided as it causes a pressure loss. For example, while artificial obstructions mounted in heat exchanger pipes promote fluid mixing and heat transfer rates, these also augment drag; an overall improvement of the efficiency depends on the mutual balance of these counter acting factors. Recent investigations, e.g., Berner et al. [1], Founti et al. [2] indicate that the flow pattern in configurations involving multiple, sequential baffles cannot be readily anticipated from the known behavior of the flow over a single baffle. The position of each obstruction in the flow, in relation to that of its neighbors, determines the perturbation and alteration of the flow field upstream and downstream of the baffle. Understanding the flow over a single baffle is necessary before the relative influence between successive baffles can be defined.

The paper reports velocity measurements obtained with a laser-Doppler anemometer in a two-dimensional, fully developed channel flow where two thin fences have been vertically mounted on a channel wall (Fig. 1). The second fence was located slightly downstream of the expected reattachment region for a single fence. The flow over a single fence, in the

same channel and for the same fence sizes and Reynolds number range as presented in this report, has been investigated by Durst et al. [3] and Tropea and Gackstatter [4] allowing direct comparisons to be drawn between the single and double-fence flow with respect to the level of mixing as well as the size and location of primary and secondary recirculation zones.

The flow has been numerically simulated and the results compared to the experimental ones. The standard $k-\epsilon$ model, e.g., Launder and Spalding [5], has been used for cases involving higher Reynolds numbers. The modelled momentum, the turbulence energy, k , and dissipation rate, ϵ , transport equations were solved assuming a two-dimensional flow. For the lower Reynolds number flows ($Re_h < 100$) only the momentum equations were solved (i.e., flow was assumed non-turbulent).

An adapted version of the TEACH-code as described by Gosman and Pun [6] was used to solve the system of the partial differential equations governing the flow. The original code incorporated a HYBRID-scheme, e.g. see Spalding [7]. The QUICK-scheme, e.g. see Leonard [8] was alternatively applied for the treatment of the convective terms of the transport equations.

2 Previous Related Work

Past studies of the internal flow over a single fence or an obstacle helped establish the influence and effects of Reynolds number, blockage ratio, upstream conditions and, in the case

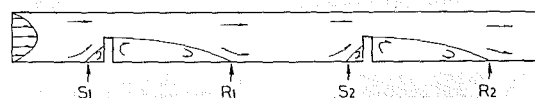


Fig. 1 Schematic view of the flow field

Contributed by the Fluids Engineering Division and presented at the 3rd International Symposium on Applications of Laser Anemometry to Fluid Mechanics, Lisbon, Portugal, July 1986. Manuscript received by the Fluids Engineering Division January 6, 1987.

of the obstacle, the length to height ratio. Reviews of wall-reattaching separated flows have been provided, among others, in references [3, 4, 9, and 10]. Particularly for the turbulent flow over a single thin fence, the following properties have been established:

(1) The oncoming flow separates at the upstream corner on top of the obstacle. The upstream influence, due to the streamline curvature before the fence, is carried and propagated downstream of separation. Depending on the geometry and Reynolds number, a third recirculation zone can occur on the top channel wall.

(2) The size and extent of the three characteristic separation regions are functions of the blockage ratio and Reynolds number. Figure 2 shows the dependence of R/h (the ratio of main reattachment length to obstacle height) to the value of Reynolds number and blockage ratio. It allows direct comparison with the present results.

(3) The developing shear layer after the downstream corner is thin enough not to be influenced by the walls. It curves sharply downwards in the reattachment region and impinges on the bottom channel wall.

There have been few experimental investigations of separated flows due to interacting neighboring bodies and none detailed enough to establish the physical characteristics and important parameters for this group of complex flows. Two recent contributions, where detailed velocity measurements have been obtained with the use of laser-Doppler anemometry, are those of Berner et al. [1] and Martin et al. [11] in two dimensional channel flows with multiple normal flat plates. In both cases, several flat plates have been used to model segmental baffles in heat exchanger geometries. The results can be useful in establishing certain characteristics of multiple-baffle flows; viz,

(1) There exists a minimum number of baffles (i.e., flat plates) required before the flow can attain streamwise-periodic characteristics. This necessarily implies that sufficient distance is required for the flow development.

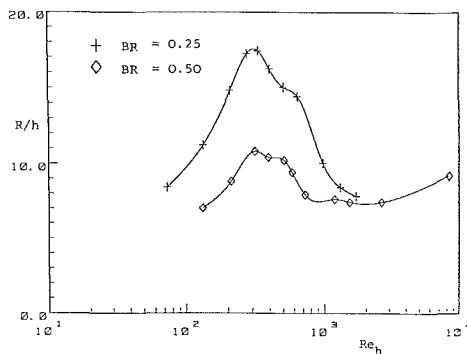


Fig. 2 Variation of reattachment length with Reynolds number for the flow over a single fence

(2) The development length (and consequently the number of required baffles) and the wake characteristics, for both laminar and turbulent flows, are functions of the Reynolds number, baffle spacing, and blockage ratio.

(3) A shorter development length is required at higher Reynolds numbers, due to the stronger mixing, in order to achieve spatial-periodicity of the flow.

In general, these flows are of great complexity and further experiments are required. It should also be noted that similar conclusions were reached for axisymmetric flows, see Founti et al. [2].

The above mentioned complexity and nonsimilarity characteristics of the plane flow over two or more obstacles imply that, from the numerical point of view, a special computational approach is required for each flow configuration. The extended zones of recirculation, the pressure gradients associated with the strong streamline curvature and the fact that peak velocities occur in the vicinity of the channel walls render the reproduction of experimental results a severe test for computational approaches.

3 Flow Configuration and Experimental Procedure

An air flow in an open cycle channel was used for this study (Fig. 3(a)). The experimental setup consisted of a blower, a light-scattering particle supply for the laser Doppler anemometer, a settling chamber which also served as a mixing chamber for the seeding particles, a nozzle to accelerate and streamline the flow as well as a two-dimensional test section with inlet identical to that used by Tropea and Gackstatter [4].

The test section was 1 m long, 10 mm high, and 180 mm

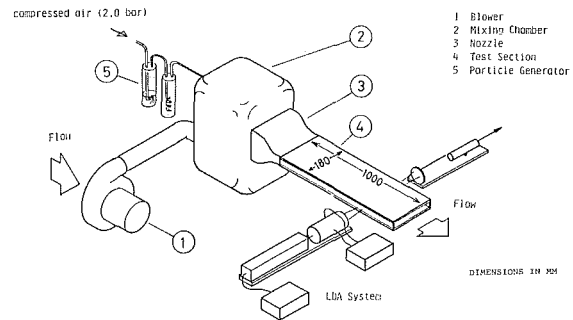


Fig. 3(a) Experimental setup

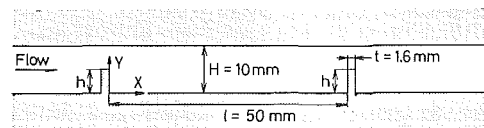


Fig. 3(b) The obstacle arrangement and definition of the coordinate system

Nomenclature

A = cross-sectional area of the channel = $H \times D$
 BR = Blockage Ratio = h/H
 D = channel span-width
 h = obstacle height
 H = channel height
 k = turbulence kinetic energy
 \dot{m} = mass flow rate
 R = reattachment point

downstream of a single obstacle
 R_1 = reattachment point downstream of first obstacle
 R_2 = reattachment point downstream of second obstacle
 Re_h = Reynolds number based on obstacle height = $U_b \cdot h/\nu$

S_1 = separation point upstream of first obstacle
 S_2 = separation point upstream of second obstacle
 U_b = bulk velocity = \dot{m}/A
 U_0 = maximum inlet velocity
 ϵ = dissipation rate of turbulence kinetic energy
 ν = kinematic viscosity

wide in the x , y , z -directions, respectively. The two obstacles (Fig. 3(b)) were manufactured out of a common block to avoid misalignment and were located on the bottom of the channel in the same manner as described in [4]. The first fence was located 700 mm downstream from the channel inlet, which corresponds to about 35 hydraulic diameters, and the second followed after 50 mm. The channel side-walls were made out of glass, whereas the top and bottom walls were constructed out of aluminum plates. The nomenclature used for the two reattachment points (R_1 , R_2) and the two separation points (S_1 , S_2) is shown in Fig. 1.

The two-dimensionality of the oncoming flow was confirmed in more than 85 percent of the spanwise direction. Flow stability in long time operations was within 1 percent, and was confirmed from the mass flow rates calculated by integrating each mean velocity profile.

A two beam, one-component LDA-system was used to obtain the streamwise velocity component and its rms values. The transmission optics comprised a 15 mW He-Ne laser, a beam splitter, dual Bragg-cells, a beam offset prism and a focusing lens of 120 mm focal length. The shift frequency ranged up to 2 MHz according to the magnitude of the reversed flow and the turbulence level. The beam offset prism translated one of the two beams and aligned it parallel to the optical axis, which was also parallel to the vertical obstacle faces. This arrangement enabled the control volume to be located close to the obstacle faces and avoided blocking the laser beam with the solid walls. The size of the control volume was approximately $\phi 220 \mu\text{m} \times 2.6 \text{ mm}$. The flow was seeded with $0.5 \mu\text{m} - 5 \mu\text{m}$ olive oil particles produced by a compressed-air atomiser.

The measuring point could be traversed in the three orthogonal directions by moving the channel itself while the LDA-system remained stationary. The control volume could be accurately located up to 0.1 mm from the channel side-walls. The reattachment length and velocity profile measurements were performed along the half-width line of the channel, i.e., at $z=0$.

The bandpassed signals from the photomultiplier were digitized by a transient recorder (Datalab 1080, 20 MHz) and directly transferred to a host computer (HP-1000), where the Doppler frequency was estimated. Mean and rms values were calculated from a statistically large enough number of sampled signals, ranging from 300 to 1500, depending on the flow conditions.

Initially, the dependence of the reattachment lengths to the value of Reynolds number was examined for the range of $20 \leq \text{Re}_h \leq 1100$. This approach was adopted in order to characterize the flow in laminar, transitional, and turbulent regimes analogous to the single fence flow. The reattachment point on the bottom of the channel was defined where the extrapolated line of zero mean velocity met the channel wall.

Detailed profiles of mean and rms axial velocities were obtained for the conditions shown in Table 1. Table 2 presents estimates of the maximum errors incurred in the measurements and, where percentage values are given, they are related to the maximum value of the property in the measurement plane.

4 Computational Procedure

Some examples of previous computations of the flow over a single wall-attached obstacle/fence are shown in Table 3.

The TEACH-code has been used for the solution of the system of partial differential equations and the computations have been performed on a CDC-4000 computer. The higher Reynolds number cases have been simulated using the standard version of the $k-\epsilon$ model of turbulence [5] which relates

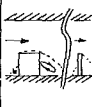
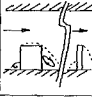
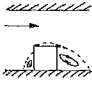
Table 1 Flow and geometric parameters investigated

BR	0.24			0.48		
Re_h	158	307	507	67	146	617

Table 2 Error estimates

Quantity	Max. Systematic	Possible Random
	Error	Error
x	$\pm 0.05 \text{ mm}$	$+ 0.02 \text{ mm}$
y	$\pm 0.005 \text{ mm}$	$+ 0.005 \text{ mm}$
z	$\pm 0.5 \text{ mm}$	$+ 0.05 \text{ mm}$
U	$\pm 0.015U$	$\pm 0.8\%$
$\overline{u'^2}$	$\pm 0.035\overline{u'^2}$	$\pm 1.5\%$
R_1, R_2	$\pm 1 \text{ mm}$	$\pm 0.5 \text{ mm}$
\dot{m}	$\pm 0.03\dot{m}$	1.5%

Table 3 Some previous related computational investigations

Author	Flow	Discretization scheme	T.M.	Grid size distrib.	Findings
Durst and Rastogi /12/		CUDS CSUDS and curvature modification	$k-\epsilon$	28x34 Non-uniform	-Recirculation zone length underpredicted -Discrepancies in the far wake due to poor calculation of rec.bub. -Need for more refined grid.
Benodekar Goddard and Gosman /13/		CUDS+SIMPLE CUDS+PISO BSUD+PISO and curvature modification	$k-\epsilon$	36x33 49x47 Non-uniform	-3.5% underprediction of recir. length with BSHD and PISO. -BSHD improves prediction of recir. length from 23.33% to 12.8%
Durao McGuirk and De Palma /14/		CUDS	$k-\epsilon$	60x43 Non-uniform	-Recir. length underpredicted by 13%. -Small recir. upstream and downstream not well represented. -Turbulence levels: correct but absolute values too low.

CUDS: Central-Upwind Differencing Scheme
 CSUDS:Hybrid Central / Skew-Upwind Differencing Scheme
 QUDS: Quadratic Differencing Scheme
 BSUD: Bounded Skew-Upwind Differencing Scheme
 T.M.: Turbulence Model

the Reynolds stress tensor to the mean rate of strain via a scalar turbulent viscosity hypothesis.

The inlet boundary conditions for the turbulence energy, and its dissipation rate, were estimated by the following relations:

$$k = \overline{u'^2}/1.1$$

$$\epsilon = k^{1.5}/H$$

where $\overline{u'^2}$ stands for the measured streamwise velocity fluctuations and H for the channel height. The normal velocity component was set equal to zero on the walls and the wall shear stresses were given as the boundary condition for the velocity component parallel to the wall. For the turbulent flow calculations, the standard wall-function treatment, which implicitly assumes a local equilibrium for k , was applied to the wall shear stresses [7]. Fully developed flow conditions were assumed at the outlet plane.

The SIMPLE-algorithm [15] was employed for the solution of the discretized momentum equations and the resulting matrix systems were solved with an iterative line-by-line procedure. The iterative cycle of the solution procedure was ter-

minated when the sum of the normalized residuals became less than 0.01 percent.

The required number of iterations was a function of the Reynolds number and the discretization scheme used. For example, laminar flow calculations with the HYBRID scheme needed 905 iterations, whereas 1554 iterations were required for turbulent flow calculations with the QUICK scheme.

The effect of grid spacing and density was determined by performing calculations with different grid arrangements. The grids were nonuniform, contracting at the two fences in both directions. Finer arrangements were required in the regions of steep gradients, whereas coarser grid distributions sufficed in the fully developed flow regions. The grid expansion ratio varied up to about 1.1 and 1.3 in the x - and y -directions, respectively. Typical distributions were, for laminar flow, 145×26 grid lines with the HYBRID scheme and 100×30 with the QUICK scheme. For the turbulent flow calculations 100×30 grid lines were used with both schemes.

The calculation domain extended from 30 mm ($=3H$) upstream of the first obstacle, where the flow was not influenced by the obstacle, to 150 mm ($=15H$) downstream of the second obstacle. This selection ensures that the domain spans at least 20 obstacle heights downstream of the reattachment point after the second obstacle, at which point the measured velocity profiles changed negligibly in the flow direction.

5 Experimental Results

For reasons of compactness, only a few of the experimental and computational results are presented here. A full account is given in reference [16].

5.1 Variation of Reattachment Length With Reynolds Number. Figures 4(a) and 4(b) show the measured reattachment points on the bottom of the channel versus Reynolds number, for both blockage ratios. The definitions of R_1 , R_2 , S_1 , and S_2 are schematically shown in Fig. 1. The size of the small recirculation zone upstream of each fence (S_1 , S_2) is not

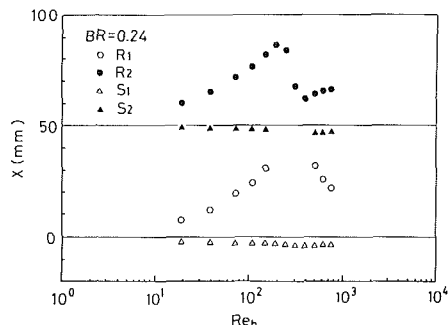


Fig. 4(a) BR = 0.24

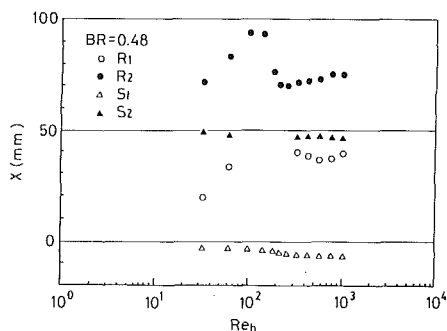


Fig. 4(b) BR = 0.48

Fig. 4 Variation of the location of the separation and reattachment points versus Reynolds number

significantly influenced by the value of the Reynolds number. The overall variation is between 0.4 and 1.2 fence heights for both blockages and S_2 is always shorter than S_1 . For $200 \leq Re_h \leq 400$ ($BR = 0.24$) and $70 \leq Re_h \leq 200$ ($BR = 0.48$) the separation zone upstream of the second fence merges with the one downstream of the first fence.

Comparison of the variation of the primary reattachment length behind a single (R) and a double fence (R_1 , R_2), shown in Figs. 2 and 5, respectively, confirmed the overall qualitative similarity between the two cases. Namely, in the laminar region the reattachment length increases with increasing Reynolds number and decreasing obstacle height. For Reynolds numbers up to about 100, Fig. 5, and for both blockage ratios, the presence of the second fence does not affect the reattachment lengths (R_1 , R_2) when compared to the single fence case. The slope of the curve remains the same as for the single fence case. The transitional flow regime is characterized by an abrupt decrease in the reattachment length and a subsequent increase to a constant level, which is characteristic of "turbulent-like" flow. However, for $Re_h \geq 500$ the constriction to the flow imposed by the second fence induces a longer recirculation zone after the first fence ($R_1 = 7.8h$) and a shorter one after the second fence ($R_2 = 4.9h$). Both are compared to the single fence case ($R = 7.0h$) and for the same Reynolds number. As for the single fence flow, increasing the blockage ratio reduces both R_1 and R_2 in relative terms (Fig. 5) but not in absolute terms (Fig. 4) and enhances an earlier transition to turbulence which, as expected, occurs earlier for the double fence flow ($Re_h \approx 100$) than for the single fence flow ($Re_h \approx 250$).

As shown in Fig. 4, no reattachment points could be measured between the two fences in the transitional regime for either blockage ratios. The corresponding velocity profiles (not shown here) show the merging of the two recirculation zones into one with diminishing width as the second fence is

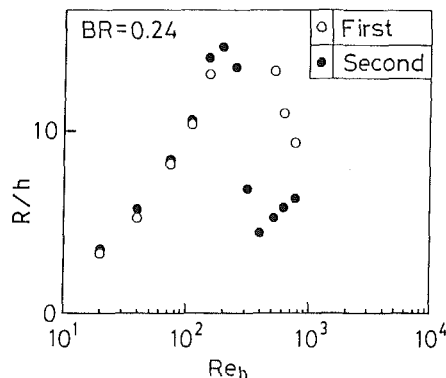


Fig. 5(a) BR = 0.24

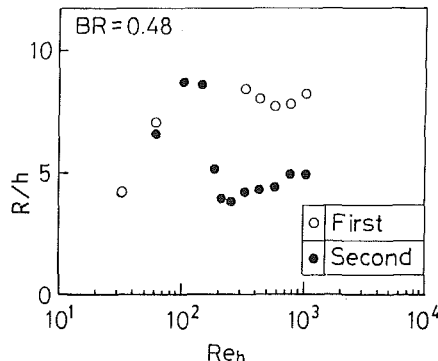


Fig. 5(b) BR = 0.48

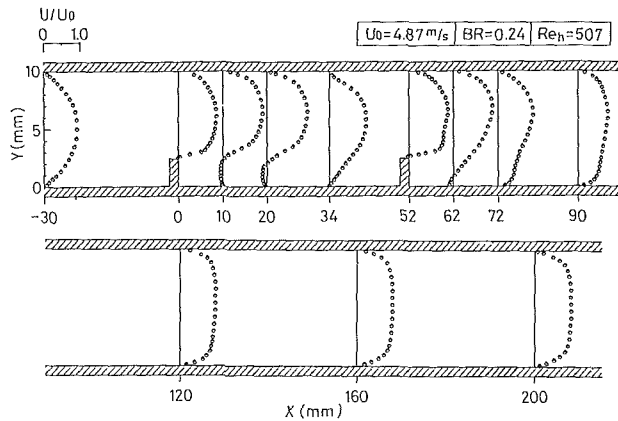
Fig. 5 Variation of primary reattachment lengths with Reynolds number

approached. Normal stresses remained small in this extended recirculation zone for both blockage ratios. Concurrently, the reattachment length after the second obstacle is abruptly reduced. At higher Re_h , the two recirculation zones between the obstacles reappear and the one after the second fence no longer displays sudden changes.

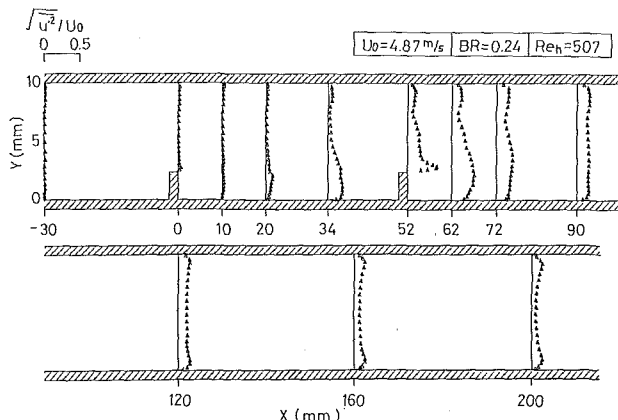
The observed variation of reattachment lengths with Reynolds number is associated with the momentum transfer mechanism, which is weaker for the lower values. As the Reynolds number is increased, the flow is accelerated above the first fence resulting in a reduced U -momentum transfer in the y -direction in order to overcome the pressure rise due to this fence; the net outcome being a shorter reattachment length. The momentum-transfer process is continued up to approximately half way between the two fences, where the existence of the second fence retards and finally inhibits the expected pressure recovery and, consequently, the momentum transfer. A reverse momentum transfer process is started which culminates with the acceleration of the flow over the second fence.

5.2 Mean and Fluctuating Velocity Profiles. Figures 6 and 7 present measured profiles for the two blockage ratios at various Reynolds numbers. It can be seen, Fig. 7(a), that the inlet flow conditions remain laminar as suggested by the parabolic mean velocity profiles at $X = -30$ mm, even for the highest Reynolds numbers examined here.

The mean velocity profiles at $X=0$ mm of Figs. 6(a) and 7(a) show negative velocities adjacent to the first obstacle, implying a flow separation at the upstream edge of the obstacle. The separated flow from the first obstacle reattaches between



(a) Mean velocity profiles



(b) Turbulence intensity distribution

Fig. 6 Measured profiles for $BR = 0.24$, $Re_h = 507$

the two obstacles, as can be inferred from the mean velocity profiles at $X=10, 20$ and 34 mm in Figure 6(a), which are more distorted than the corresponding profiles at low Reynolds numbers (not presented here).

At $X=52$ mm, both the mean velocity and the turbulence intensity profiles differ significantly from those at $X=0$ mm, confirming the existence of different characteristics for the two recirculating regions. At $X=72$ mm, which is 20 mm away from the second obstacle, the flow has already reattached and the reattachment length is much shorter than the first one. Downstream of the obstruction, at $X=120, 160, 200$ mm, the flow redevelops slowly.

The mean velocity profiles in Fig. 7(a) indicate that the channel area reduction due to the higher obstruction results in a greater flow rate above the obstacles. At $X=0$ and $X=52$ mm, the mean velocity profiles on top of the obstacles are asymmetric and imply a significant radial velocity component close to the fence, much steeper than at the top wall of the channel.

Figures 6(b) and 7(b) show the low turbulence intensities upstream and over the first fence and their increase between the two fences which also remains downstream of the second. For $BR = 0.24$, Fig. 6(a), the shear layer developing on top of the first fence experiences laminar separation but turbulent reattachment. The flow meeting the second fence is already turbulent at the separation point on top of the second fence. The higher turbulence levels in the second recirculation zone promote more efficient diffusion of momentum than in the first recirculation, which results in earlier reattachment.

Figure 7(b) shows the corresponding axial normal stresses. At $X=0$ mm, a small peak is present adjacent to the obstacle. The next profile at $X=19$ mm shows much higher values than in the case of the lower obstacle as seen in Fig. 6(b). For the region between the two obstacles, the turbulence characteristics for the two blockage ratios differ considerably.

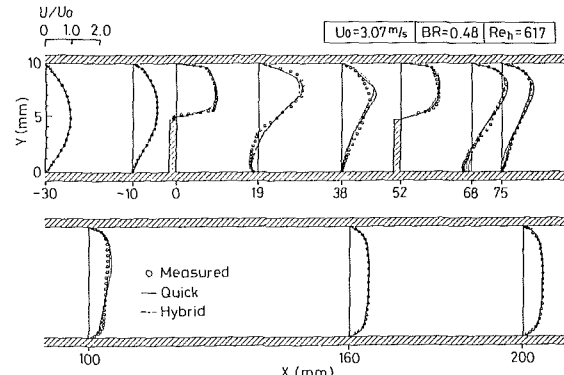


Fig. 7(a) Mean velocity profiles

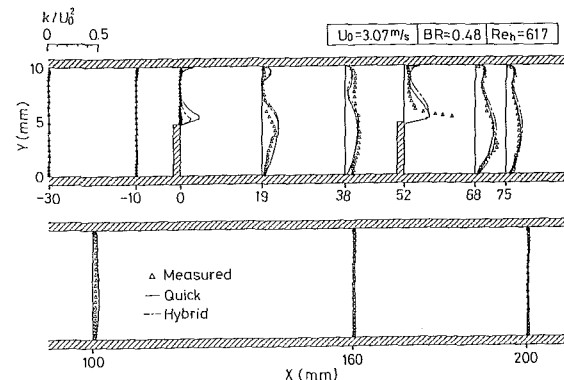


Fig. 7(b) Turbulent kinetic energy distributions

Fig. 7 Comparison of measured and calculated profiles, $BR = 0.48$, $Re_h = 617$

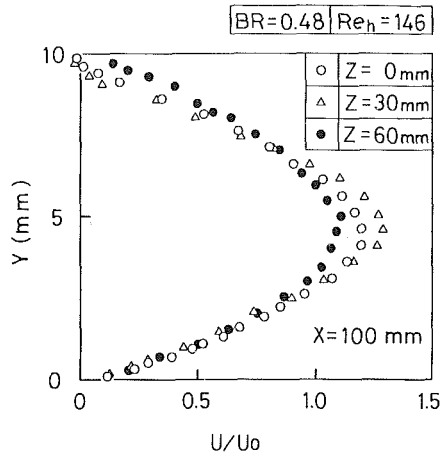


Fig. 8 Mean velocity profiles across the channel, $BR = 0.48$, $Re_h = 146$

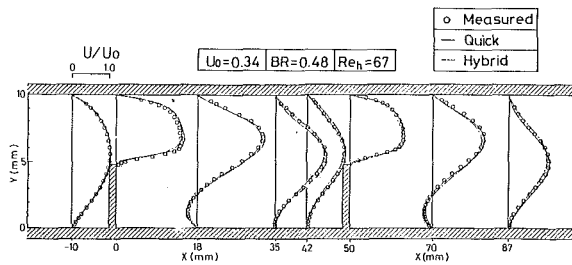


Fig. 9 Comparison of measured and calculated mean velocity profiles, $BR = 0.48$, $Re_h = 67$

Although in absolute terms, the reattachment lengths are nearly the same, turbulent mixing is much more active for $BR = 0.48$. Bimodal velocity probability distributions were measured above the second obstacle, and may indicate the existence of periodic characteristics in the separated flow.

Finally, a small-sized recirculation bubble was measured for transitional Reynolds numbers and $BR = 0.48$ on the top wall of the channel and downstream of the second obstacle. No such bubble was found downstream of the first fence, which can be due to the flow acceleration caused by the presence of the second fence. As is also observed in [3, 4], the bubble on the top channel wall induced a strong three dimensionality to the flow field downstream of the second obstacle. This observation was confirmed by velocity measurements, e.g., as in Fig. 8, at various cross-flow locations after the recirculation bubble. This bubble also contributed to the reduction of the reattachment length downstream of the second obstacle.

6 Computational Results

6.1 Laminar Flow. Figure 9 compares computed velocity profiles, obtained with the two different discretization schemes, to the experimental data for $BR = 0.48$ and $Re_h = 67$. The profiles were selected to lie in the recirculation region and they typify results obtained using the two discretization schemes. Upstream of the first obstacle, at $X = -10$ mm, both predicted profiles coincide with the experimental ones. Differences first appear in the subsequent profile at $X = 0$ mm. The QUICK scheme predicts a steeper velocity gradient than HYBRID, the latter suffers from false diffusion associated with the inclination of the streamlines against the numerical grid, see e.g., [15]. As shown at $X = 18$ and 35 mm, the flow predicted with the HYBRID scheme reattaches earlier than that with the QUICK scheme. The difference is a consequence of the upwind discretization embodied in the HYBRID scheme,

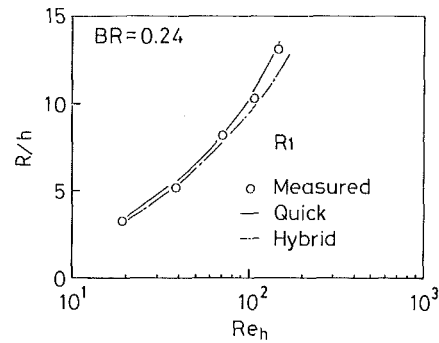


Fig. 10(a) Downstream of first obstacle

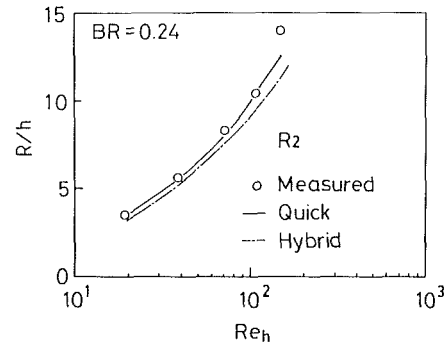


Fig. 10(b) Downstream of second obstacle

Fig. 10 Measured and computed reattachment lengths, laminar flow, $BR = 0.24$

that fails in the prediction of the recirculating flow. The influence remains downstream of the second obstacle.

Figure 10 shows the variation of predicted and measured reattachment lengths as a function of Reynolds number for $BR = 0.24$. As expected, in both recirculation regions the QUICK scheme provides much better agreement with the experimental data than does the HYBRID scheme. The extent of disagreement between the two schemes remains almost the same for the first and second reattachment points, and it increases with increasing Reynolds number and blockage ratio.

6.2 Turbulent Flow. Figure 7 is representative of the predicted mean velocity and turbulent kinetic energy profiles for the higher blockage ratio. Generally, and similarly to the laminar flow case, the QUICK scheme provides better agreement with the experiments than the HYBRID scheme for the mean quantities. Flow features such as the different reattachment lengths after the first and the second fences and the flow redevelopment in the far downstream region are apparently well reproduced by the present calculation method using the standard $k-\epsilon$ model. However, large discrepancies occur in the k -profiles, shown in Fig. 7(b), especially above the two obstacles. Turbulence energy is overpredicted above the first obstacle, suggesting the inadequacy of the turbulence model in this region. In contrast, the experiment shows a sharp peak above the second obstacle, which is not accurately predicted. It should be noted here that the measured turbulence energy was estimated only from the axial fluctuations, an assumption which is valid only for channel flows and makes it difficult to draw a general conclusion about the present results.

Finally, Fig. 11 shows the calculated and measured reattachment lengths versus Reynolds number for the turbulent cases. For the lower blockage ratio, the prediction hardly coincides with experiment. This discrepancy is, of course, caused by using the turbulence model without modification to account for the low Reynolds number nature of the flow. At the higher blockage ratio there is a better apparent agreement with the HYBRID scheme than with the QUICK scheme. However, the

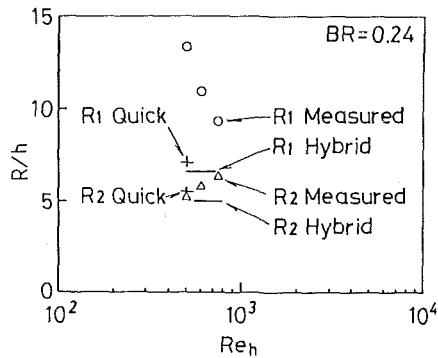


Fig. 11(a) Reattachment lengths for BR = 0.24

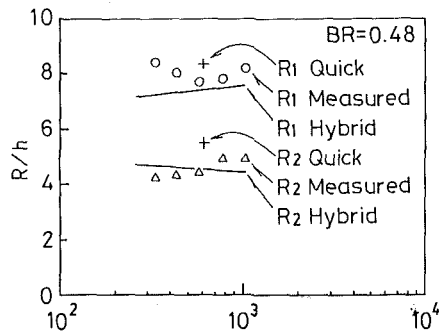


Fig. 11(b) Reattachment lengths for BR = 0.48

Fig. 11 Comparison of measured and calculated reattachment lengths for turbulent flow conditions

results with the HYBRID scheme include errors due to numerical diffusion. It is therefore anticipated that the apparently good agreement obtained with the HYBRID scheme is fortuitous. Nevertheless, the discrepancy due to the shortcomings of the turbulence model tends to be smaller with increasing blockage ratio and Reynolds number, which implicitly confirms that higher obstacles induce transition to turbulence earlier than the lower ones.

7 Summary

The flow over two surface-mounted obstacles in tandem has been investigated both experimentally and numerically.

In the laminar region, the reattachment lengths downstream of both obstacles increased with increasing Reynolds number. Their size and rate of increase was independent of the blockage ratio.

In the turbulent region the reattachment lengths changed slightly with Reynolds number. The first recirculation region was about twice the size of the second one. Normal stresses increased considerably above the first obstacle. The high values were retained within the separation zones and downstream of the second obstacle.

In the transitional region and reattachment lengths decreased rapidly with increasing Reynolds number. The recir-

culating region behind the second obstacle indicated earlier transition than the first one, and the critical Reynolds number was lower for the higher blockage ratio.

The flow details were reproduced with considerable accuracy by the computer code incorporating the QUICK scheme for the lower Reynolds numbers. For the higher Reynolds numbers examined in the present study, the flow field was a severe test case for a conventional turbulence model.

References

- 1 Berner, C., Durst, F., and McEligor, D. M., "Flow Around Baffles," ASME Winter Ann. Meet., Boston, Paper No. 83-WA/HT-9, 1983.
- 2 Founti, M., Vafidis, C., and Whitelaw, J. H., "Shell-side Distribution and the Influence of Inlet Conditions in a Model of a Disc-and-Doughnut Heat Exchanger," *Exp. in Fluids*, Vol. 3, 1985, pp. 293-300.
- 3 Durst, F., Founti, M., Gackstatter, R., Pereira, J. C. F., and Tropea, C., "The Wall-Reattaching Flow over Two-Dimensional Obstacles," *Proc. 2nd Intern. Sympos. on Applications of Laser Anemometry to Fluid Mechanics*, Lisbon, Portugal, 1984.
- 4 Tropea, C., and Gackstatter, R., "The Flow over Two-Dimensional Surface Mounted Obstacles at Low Reynolds Numbers," *ASME JOURNAL OF FLUIDS ENGINEERING*, Vol. 107, 1985, pp. 489-494.
- 5 Launder, B. E., and Spalding, D. B., "The Numerical Computation of Turbulent Flows," *Comp. Meth. in Appl. Mech. and Eng.*, Vol. 13, 1974, pp. 269-289.
- 6 Gosman, A. D., and Pun, W. M., "Calculation of Recirculating Flow," Heat Transfer Rep., HTS/74/2, Imperial College, London, 1974.
- 7 Spalding, D. B., "A Novel Finite-Difference Formulation for Differential Expressions Involving both First and Second Order Derivatives," *Int. J. Num. Methods Eng.*, Vol. 4, 1972, pp. 551-559.
- 8 Leonard, P. B., "A Stable and Accurate Convective Modelling Procedure Based on Quadratic Upstream Interpolation," *Comp. Meth. in Appl. Mech. and Eng.*, Vol. 19, 1979, pp. 59-98.
- 9 Eaton, J. K., and Johnston, J. P., "A Review on Subsonic Turbulent Flow Reattachment," *AIAA Journal*, Vol. 19, 1981, pp. 1093-1100.
- 10 Durst, F., and Founti, M., "Review: The Wall-Reattaching Flow over Two-Dimensional Obstacles and Preliminary Scanning of the Flowfield with Laser Doppler Anemometry," Technical Report, LSTM-Erlangen, 32/T/85, 1985.
- 11 Martin, W. W., Elphick, I. G., and Gollish, S., "Flow Distribution Measurement in a Model of a Heat-Exchanger," *Engineering Applications of Laser Velocimetry*, ASME Winter Ann. Meet., Phoenix, AZ, 1982, pp. 23-31.
- 12 Durst, F., and Rastogi, A. K., "Turbulent Flow over Two-Dimensional Fences," *In Turbulent Shear Flows 2*, (Ed. Bradbury et al.), Berlin, Springer-Verlag, 1980, pp. 218-231.
- 13 Benodekar, R. W., Goddard, A. J. H., and Gosman, A. D. and Issa, R. I., "Numerical Prediction of Turbulent Flow over Surface Mounted Ribs," *AIAA Journal*, Vol. 23, 1985, pp. 359-366.
- 14 Durao, D. F. G., McGuirk, J. J., and de Palma, J. M. L. M., "Measurements and Numerical Calculations of the Flow around a Two-Dimensional Rib," *EUROMECH 163*, Lisbon, Portugal, 1982.
- 15 Patankar, S. V., *Numerical Heat Transfer and Fluid Flow*, McGraw-Hill, New York, 1980.
- 16 Obi, S., "Flow Characteristics of Laminar and Turbulent Recirculating Regions and Numerical Analysis by High Order Discretization Scheme," M.Sc. thesis, Dept. of Mech. Eng., Keio University, Japan, 1986.

Acknowledgment

The work in the present paper received support through the Deutsche Forschungsgemeinschaft within the "Schwerpunktprogramm: Physik abgelöster Strömungen." This support is thankfully acknowledged.

Masami Nakano

Instructor.
Department of Precision Engineering,
Faculty of Engineering,
Yamagata University,
Yamagata, 992, Japan

Eisuke Ota

Professor.

Kiyohiro Tajima

Professor.

Department of Mechanical Engineering,
School of Science and Engineering,
Waseda University,
Tokyo, 160, Japan

Noise and Vibration Related to the Patterns of Supersonic Annular Flow in a Pressure Reducing Gas Valve

Cause of intense aerodynamic noise and vibration from a contoured type valve is revealed in close relation to the supersonic flow patterns. Simple conical plugs are used in the experiments, and the valve pressure ratio is up to twenty. Four typical patterns of the flow are observed by schlieren photography. In one of these patterns, the jet flow along the plug separates from the wall to form an annular jet impinging on the inner wall of the valve chest. Such flow oscillates significantly in resonance with the acoustic modes of the chest cavity. The radiated noise and the dynamic force acting on the valve stem reach intense levels, dominated by some discrete components of the corresponding frequencies. The mechanisms to generate or to suppress the flow oscillation, leading to the intense noise and vibration, are discussed.

Introduction

In fluid systems in various high power process plants, smooth control of the fluid energy has been one of the major techniques to insure the system against process runaway and structural failure and to keep the environment from heavy acoustic noise. However, the typical device of energy control, such as a control valve and a pressure relief valve, inevitably works to convert the kinetic energy not only to heat but to acoustic and vibration energy. The physical process involves turbulent mixing and very frequently resonance of a fluid- and structural system. Thus, the device itself is conflictingly a major source of various acoustical and mechanical disturbances.

Especially in gas flow control, the turbulent mixing of supersonic jets, arisen by the throttling, radiates extreme aerodynamic noise in the surroundings of the valve and the downstream piping. Furthermore, the high level noise contains, in most cases, intense discrete components with frequencies of more than several kilohertz [1]. Such components may be accompanied by oscillation of the jet in the valve and excitation of the flow in the piping, and fatigue failure may occur in the structural parts. The flow field can be separated into two regions. One is the source region, in which noise is generated aerodynamically and mechanical vibration is induced by the flow instability. The other is the propagation region where the noise and the dynamic disturbances are transmitted and excited. Many studies [2-5] concerning the acoustic characteristics of the propagation region have revealed that discrete tones, of particular modes inside the downstream pipe, are radiated from the valve-piping system.

In cases where the pressure drop across the valve exceeds the critical value a region of supersonic flow appears downstream of the valve restriction and the free layer with strong shear distribution interacts with several shock waves induced in the

flow. This mechanism of noise generation is quite different from the mechanism in subsonic shear flow [6]. Schmitt and Ziegert [7, 8] made an extensive study of the noise generated from valve trims of various types, and presented various schlieren pictures of the two-dimensional flow. In previous papers [9, 10] by the authors, the characteristics of noise and stem thrust were discussed in close relation to the supersonic flow patterns around a conical plug. However, the valve tested had no chest and the flow was directly diffused in the atmosphere so that effects of the inner wall of the chest could not be included in the discussions.

In a real valve, the supersonic jet from the contraction impinges on the inner wall of the valve chest before its diffusion is completed and, at some unstable flow patterns of the jet, the disturbance originated by the impingement will be fed back to excite an oscillation of the jet. The acoustic mode of the chest cavity will also control the resonance of the oscillation. Such oscillatory phenomena may be not only an additional source of an intense tone but also a cause of a flow-induced vibration of the valve components. Nevertheless, the interactions between the supersonic jet configuration in the vicinity of the contraction and the acoustic characteristics inside the valve chest have not been made clear; flow patterns under the resonance on the plug, such as configurations of the shock waves and a separated boundary layer, are of special interest.

The present investigation is intended to reveal the cause of intense discrete noise and flow-induced vibration of the valve stem under the condition of high pressure reduction. Since internal flows in real valves are too complicated to obtain fundamental understandings, only valve configurations with the most essential geometries are employed in this investigation. In addition to the noise and vibration measurements, schlieren photography is used. The flow patterns are divided into four types, and, to each of them, characteristic features in the noise, the vibration, in configurations of the shock wave and the separated boundary layer are assigned. Only one among

Contributed by the Fluids Engineering Division for publication in the JOURNAL OF FLUIDS ENGINEERING. Manuscript received by the Fluids Engineering Division March 19, 1985.

the patterns is found oscillatory in resonance with the acoustic mode inside the valve chest and with an exciting feedback loop by the jet impingement on the chest wall.

Experimental Apparatus and Procedure

Experiments were performed by using a blow-down facility. The main parts are a reservoir of 0.75 m³ in volume, a control valve of 1-1/2 in. nominal diameter, a diffuser of 15° vertex angle, a collecting chamber of 200 mm internal diameter, and a convergent nozzle with a contraction ratio of 400:1. The test valve is mounted at the nozzle exit of 10 mm diameter, as shown in Fig. 1(a). The test valve and the related devices are installed in an anechoic chamber with dimensions of 2.4 m in width, 6.8 m in length, and 2.3 m in height. The chamber is measured to be anechoic for frequencies higher than 500 Hz, which covers the usual range of supersonic aerodynamic noise.

The test valve is constructed as shown in Fig. 1(b). The diameter D_1 of the conical plug is 20 mm, and the vertex angle μ is varied between 60 and 180 degrees. The plane valve seat has a square edged circular port of 10 mm in diameter. The length of the chest l is 88 mm and the internal diameter D_2 is varied between 40 to 68 mm. In most cases, the chest is opened to the atmosphere in the direction of plug axis. A chest with a side opening is also used to compare the effect of skew in the flow. The plug and the stem are rigidly supported in the axis of discharging flow by a lift-adjusting device, which consists of two ball bushes and a stepping motor, as shown in Fig. 1(a). The natural frequencies of the plug-support system are measured to be 200 Hz and 3 kHz for bending and longitudinal vibration, respectively.

Area ratio of the valve opening β is calculated by the following expression,

$$\beta = \frac{[\text{The minimum cross-sectional area formed by the seat and the plug}]}{[\text{The cross-sectional area of nozzle exit}]} \quad (1)$$

and then, is expressed as a function of the valve lift h as follows,

$$\beta = \frac{1}{\cos(\mu/2)} \left\{ 1 - \left(1 - \frac{h}{d} \sin \mu \right)^2 \right\}. \quad (2)$$

The lift is adjusted with an accuracy of 1/100 mm.

Compressed dry air, 3 MPa in the reservoir at a pressure and a dew point of -70°C, is discharged through the test valve into the atmosphere. The blow-down operation is regulated by a control valve in such a manner that the stagnation pressure in the collecting chamber is slowly increased or

decreased with constant rate of change, i.e., 40 kPa/s. The flow field around the test valve is assumed quasi-steady. Precise measurements of steady flow are performed by keeping the stagnation pressure within an allowance of 2 percent.

The stagnation pressure P_0 and the stagnation temperature T_0 of the valve flow are measured at the collecting chamber and recorded on an electromagnetic oscillograph. The valve pressure ratio is defined as P_0/P_a , where P_a is the atmospheric pressure. The overall sound pressure level, i.e., O.A.SPL in dB, is measured at a distance of one meter from the valve using a 1/2-in. Brüel and Kjaer (B&K) condenser microphone and a B&K 2606 precision level meter. The rms value of stem thrust \bar{F}_{rms} is obtained by a Kistler piezotron load cell, mounted to the valve stem between the two ball bushes, using a B&K 2607 rms meter. It should be noted here that the dynamic thrust data, to some extent, are affected by stem bending due to the elastic character of the ball-supported bushes.

Both the noise and the thrust levels are continuously recorded versus the valve pressure ratio on an X-Y recorder. Fluctuations of the sound pressure and the stem thrust \bar{F} are recorded on a magnetic tape under steady flow condition. Ensemble-averaged spectra of these dynamic data are processed by a SD-330-20 spectral analyzer. During the measurements, the temperature T_b within the valve chest is kept at about 10°C. All of the transducers and instruments have an accuracy better than 0.1 percent over the frequency range from 20 Hz to 20 kHz; the frequency range of the microphone is between 4 Hz and 40 kHz, and the resonant frequency of the load cell is 70 kHz.

Instantaneous schlieren pictures of the flow pattern inside the valve chest are taken by using a chest equipped with optical

side windows. The cross-section is slightly different from circular, see Fig. 1(c). The frame of the picture is denoted by a dashed line rectangle in Fig. 1(b). Electric spark is used as a light source. The exposure time of the recording is less than 5 μ s.

Levels of Dynamic Thrust and Acoustic Noise, and Patterns of Throttled Flow

History of Dynamic Thrust and Noise Against Valve Pressure Ratio. In Fig. 2, the rms levels of the thrust fluctua-

Nomenclature

c = speed of sound	l = length of valve chest	SPL = sound pressure level in dB
d = diameter of valve port	$L_{im.}$ = characteristic length of annular impinging jet	T_b = air temperature in valve chest
D_1 = diameter of conical plug	\dot{m} = critical mass flow rate through valve throat	T_0 = stagnation temperature of valve flow
D_2 = internal diameter of valve chest	N_m = Neumann function of order m	V_a = isentropic flow velocity
f = resonant frequency of the chest cavity	O.A.SPL = overall sound pressure level in dB	z = axial distance from valve port
f_c = cut-off frequency of the chest cavity	p = acoustic pressure	β = area ratio of valve opening
\bar{F} = fluctuating fluid thrust acting on valve stem	P_a = atmospheric pressure	γ = isentropic exponent of air
\bar{F}_{rms} = rms value of \bar{F}	P_0 = stagnation pressure of valve flow	θ = circumferential coordinate around z -axis
h = valve lift	r = radial distance from z -axis	μ = vertex angle of conical plug
J_m = Bessel function of order m	R = gas constant	
k_z = axial wave number	S_t = Strouhal number	
K_{mn} = dimensionless radial wave number		

tion and the acoustic pressure are traced versus the pressure ratio during its increase. The alphabetic codes refer to the flow patterns which will appear in Fig. 3.

Several characteristics may be observed in these typical traces as follows:

1 Discontinuous changes in the levels appear at some particular pressure ratios, and the changes are accompanied by discontinuous switchings of the flow pattern. The most remarkable increases of the levels occur in the range of P_0/P_a from 10 to 12.5. The related flow pattern denoted by FP-B is

characterized by the annular jet diverging conically along the plug surface and by the boundary layer separating without reattachment on the plug. It will be made clear in Section 4 that the increase of the levels is due to a high frequency oscillation of the flow.

2 A considerable reduction occurs in the levels at a pressure ratio around 12.5. The flow pattern FP-B is abruptly switched to another pattern (FP-C), where the jet attaches to the valve seat. It should be noted that this pattern is one involving the lowest noise and vibration in the experiment.

3 At pressure ratios higher than 18.5 the jet, attached to the seat surface, separates again from the surface leading to the appearance of a flow pattern FP-D. The noise level increases again.

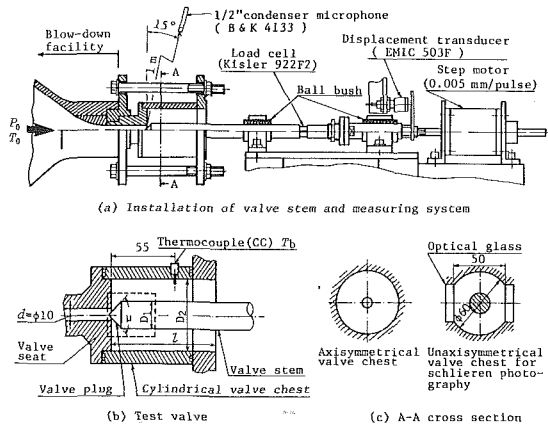


Fig. 1 Experimental apparatus

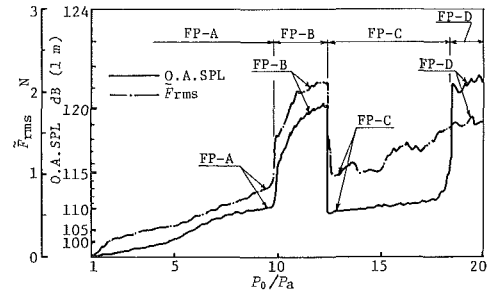


Fig. 2 Typical trace of levels of noise and dynamic thrust versus valve pressure ratios during the increase ($\mu = 100$ deg, $\beta = 0.3$, $D_1/d = 2$, $D_2/d = 6$)

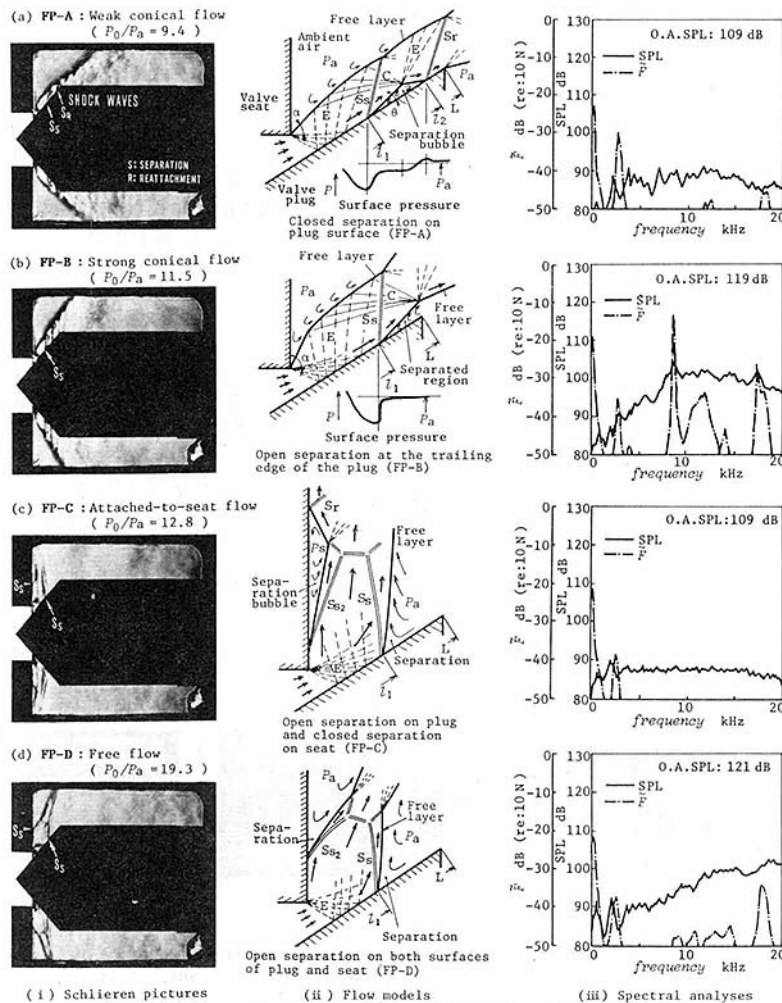


Fig. 3 Types of flow patterns on conical plug ($\mu = 100$ deg, $D_1/d = 2$, $D_2/d = 6$, $\beta = 0.3$)

Descriptions of Flow Patterns and the Transition. The levels of the aerodynamic noise and the fluid thrust fluctuations are found to have close relation to the patterns of the flow within the valve chest. In the present investigation, the patterns are classified into four different types according to their structures. The transition from one pattern to another takes place discontinuously at a pressure ratio particular to the pattern. In Fig. 3, the schlieren pictures are shown in order of appearance as the pressure ratio is increased. Configurations of the wave system and the separated boundary layer are deduced for the respective pictures. Clear differences are seen in the corresponding spectra of the radiated noise and the induced fluctuation of the thrust.

Each of the flow patterns and their transition have special features as follows:

[FP-A] Weak Conical Flow [Fig. 3(a)]: This supersonic pattern is observed in the lowest range of the pressure ratio. The wall jet from the throat diverges along the plug surface and leaves the trailing edge without separation from the surface. An expansion wave, issued from the leading edge of the seat, forms a compression wave C after reflections from the plug surface and the free layer, and the boundary layer on the plug is separated slightly due to the adverse pressure gradient across the wave C . A shock wave S_s is originated by the separation. Close to the trailing edge of the plug, the boundary layer reattaches and a second shock wave S_r is formed. This structure of the flow is also deduced from measurements of the pressure distribution and oil film profiles on the surface [9, 10].

The sound pressure shows an almost flat spectrum over the range higher than several kilohertz. The discrete components in the spectrum of the dynamic thrust are due to the resonance of supporting structure; i.e., 200 Hz for the lateral and 3 kHz for the longitudinal modes.

[FP-B] Strong Conical Flow [Fig. 3(b)]: This pattern is found to be oscillatory, and appears in a range of large valve lift. As the pressure ratio increases, the compression wave C becomes strong and the separation position of boundary layer is moved downstream. The separation bubble grows up and finally extends past the trailing edge of the plug. At this stage, this type of configuration is taking place: the jet flow is separated and deflected away from the plug surface, and diverges to impinge on the inner wall of the chest. The

pressure of the excess expansion is recovered almost to the atmospheric pressure by a single strong shock wave S_s .

The noise and the dynamic thrust associated with the pattern are at the highest level of all. The random components of noise increase in a frequency range higher than 5 kHz, and discrete components of about 8.7 kHz and the harmonics appear significantly in both of the spectra.

[FP-C] Attached-to-Seat Flow [Fig. 3(c)]: This pattern appears in a range of small valve lift. The flow is attached to the valve seat and is quite stable. Both the noise and the dynamic thrust are at the lowest levels, despite of the high pressure reduction.

The separated jet in the flow pattern FP-B may switch and be attached to the seat surface if the flow deflection α around the edge of the seat exceeds 90 deg across a sufficiently strong expansion. A closed separation bubble on the seat surface and an induced shock wave S_{s2} are observed in the schlieren picture. The shear stress distributed along the free layer may be less intense than the stress along the free layer in the pattern FP-B, since the layer in the present case is introduced by the boundary layer separation on the plug surface. Then, the noise emission from the free layer is considerably reduced.

[FP-D] Free Flow [Fig. 3(d)]: This highest pressure pattern appears with a valve of small opening, or with a chest of small inside diameter. The jet expanding from the valve throat is separated from both the plug and the seat surfaces.

As the pressure ratio is increased, the separation bubble on the seat surface, appearing in the pattern FP-C, is growing toward the inner wall of the valve chest. Eventually, the separated jet comes to impinge directly on the wall without reattachment to the seat surface, and the flow takes this new pattern. As in the case of the strong conical flow of type FP-B, the flow diverges conically downstream of separation and the turbulent noise takes a similar level at the very high frequency range. Nevertheless, discrete components are not significantly present in the spectra of the noise and the dynamic thrust.

Referring to numerical results [10] of the valve flow using the so-called Fluid-in-Cell method by the authors, it should be noted here that, in the pattern FP-B, the Mach number along the free layer is very high and the flow downstream of the shock wave still remains transonic, whereas the shock wave in the pattern FP-C makes the downstream, and consequently

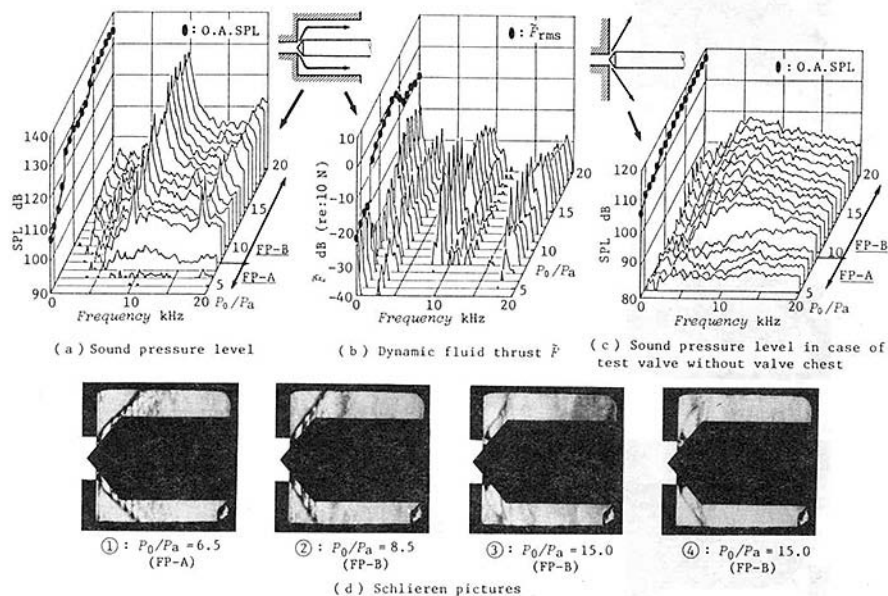


Fig. 4 Change in spectra of various dynamic data and appearance of discrete components induced by oscillating flow. The schlieren pictures show instantaneous pattern of the flow within respective pressure ranges where the dynamic characters are not altered ($\mu = 100$ deg, $D_1/d = 2$, $D_2/d = 6$, $\beta = 0.5$).

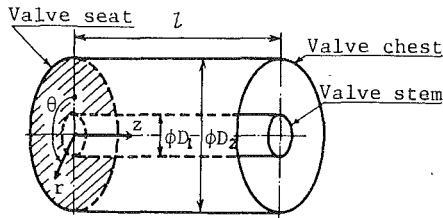


Fig. 5 Physical model inside valve chest; radial, axial and angular coordinates are denoted by r , z , and θ

the separated free layer, to be low subsonic. This is one of the reasons why the turbulent noise in high frequency range is reduced remarkably by the flow pattern FP-C.

Characteristics of Dynamic Thrust and Noise Induced by Oscillating Flow. Typical maps of the spectra of the various dynamic data versus pressure ratio are shown in Fig. 4. In this case of the valve opening, the patterns of type FP-A and type FP-B are observed. Instantaneous schlieren pictures are shown in the figure (d). The flow pattern switches at $P_0/P_a = 8$.

It is clearly seen in the spectra (c), that the discrete noise components which are quite intense in the spectra (a) are not present if the valve chest is removed. Also, several discrete components appear in the spectra (b) of the dynamic thrust. The two of the low frequencies are due to the resonance of the plug support.

The most remarkable increase in the levels of the noise and the dynamic thrust occurs at $P_0/P_a = 8$. This is associated with the switching of the flow pattern from the type FP-A to the type FP-B. A discrete component of 9 kHz and the harmonics become quite dominant in both of the spectra. These are caused by a self-sustained oscillation of the flow, and not by the superharmonics of the longitudinal fundamental of the plug support, since the components are induced only when the valve chest is installed, and since the frequencies vary with the inner diameter of the chest and with the pressure ratio. The flow may be oscillating in an axisymmetrical manner, as observed in the picture (2). The shock waves in the flow are observed oscillating back and forth along the plug, and fluctuations of large amplitudes are introduced in the pressure on the plug surface and, consequently, in the thrust force. Of course, such oscillation produces an intense tone noise.

As the pressure ratio is increased beyond 14, the frequency of the oscillation jumps to a higher value. This jump of the oscillation is triggered by the primary shock wave S_s reaching the trailing edge of the plug. The flow patterns in instantaneous pictures (3) and (4), which are taken by separate exposures, are observed asymmetric and reverse of each other. Therefore, the flow may be oscillating with a circumferential mode in addition to a radial mode. The level of the dynamic thrust is reduced by an amount of 10 dB, because the circumferential oscillation of the flow does not induce axial component of vibration.

Acoustic Resonant Frequencies in Valve Chest and Oscillation Frequency of Flow

Acoustic Modes in Valve Chest. The flow oscillation is likely excited by resonance with an acoustic field in the valve chest; i.e., the chest functions as a resonator. The resonant frequency is easily obtained, since the averaged flow velocity in the chest is very low compared with the sound velocity. Assuming the passage inside the chest as annular, as illustrated in Fig. 5, the resonant frequency f is given as;

$$f = \frac{c}{2\pi} \sqrt{k_z^2 + \left(\frac{2K_{mn}}{D_2}\right)^2} \quad (3)$$

where c is the sound velocity, and k_z is the axial wave number expressed as:

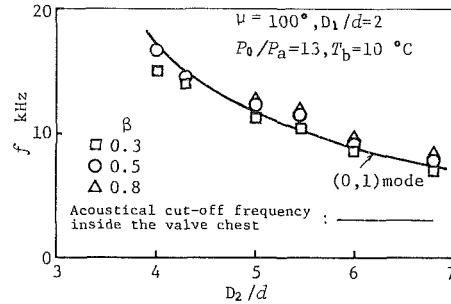


Fig. 6 Oscillation frequencies versus inner diameter D_2 of valve chest

$$k_z = (2i + 1)\pi/2l \quad (i = 0, 1, 2, \dots) \quad (4)$$

The dimensionless wave number K_{mn} is formed as an n th solution of the following eigen value equation of m th order for K_R :

$$\begin{aligned} \frac{\partial}{\partial R} J_m(K_R R) \Big|_{R=A} \cdot \frac{\partial}{\partial R} N_m(K_R R) \Big|_{R=1} \\ - \frac{\partial}{\partial R} J_m(K_R R) \Big|_{R=1} \cdot \frac{\partial}{\partial R} N_m(K_R R) \Big|_{R=A} = 0 \end{aligned} \quad (5)$$

where $R = r/(D_2/2)$ and $A = D_1/D_2$. J_m and N_m are Bessel and Neumann functions of order m , respectively.

A circumferential and radial wave mode, denoted as mode (m, n) , divides the cross section with m diametric and n circular nodes. It is found by a preliminary experiment that the oscillation frequency of the flow is independent of the length l of the chest, except in the case of extremely short length, so that the axial waves travelling in the z -direction are neglected; i.e., $k_z = 0$. Then the resonant frequency reduces to the cut-off frequency expressed as:

$$f_c = cK_{mn}/\pi D_2 \quad (6)$$

In the analysis, the following boundary conditions are applied:

$$\frac{\partial p}{\partial z} \Big|_{z=0} = 0, \quad p \Big|_{z=l} = 0, \quad \frac{\partial p}{\partial r} \Big|_{r=\frac{D_1}{2}, \frac{D_2}{2}} = 0 \quad (7)$$

where p is the acoustic pressure.

As seen in Fig. 6, the oscillation frequency of the flow decreases as the inner diameter D_2 of the valve chest is increased, and is slightly raised by an increase of area ratio β of the valve opening. The cut-off frequency of mode (0,1), which is calculated by equation (6), has a good agreement with the measured oscillation frequency. It may be concluded that the flow oscillation is in resonance with the radial acoustic mode in the valve chest.

Oscillation Mechanism of the Strong Conical Flow. An intense oscillation of the valve flow takes place when accompanied by the switching of the flow pattern to the strong conical flow of type FP-B. This fact suggests that the following two characteristics of the flow of type FP-B will be essential to the oscillation of the flow field;

Condition-1. The shock-induced separation of the boundary layer is not closed on the plug surface by the reattachment, so that the instability of the separation is directly excited by pressure disturbances arising in the ambient air.

Condition-2. The annular jet leaving the plug surface impinges on the inner wall of the valve chest, so that pressure disturbances are produced on the wall.

Now, for use in discussing the mechanism of the flow oscillation, a model as illustrated in Fig. 7 is proposed. The instability of the separated layer will cause fluctuation of the

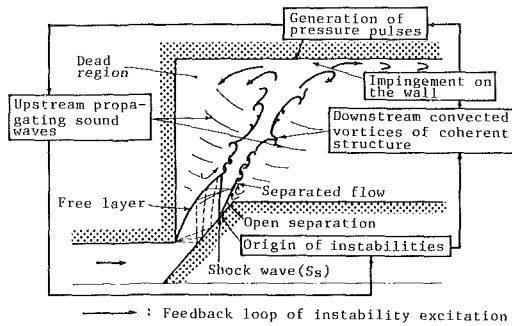


Fig. 7 Illustration of mechanism leading to the oscillation in the case of strong conical flow

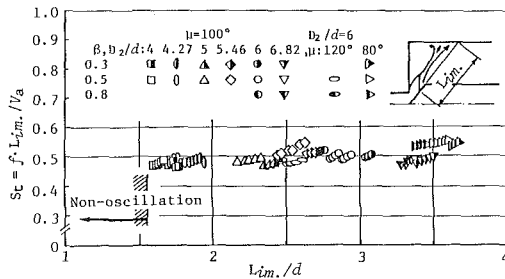


Fig. 8 Strouhal number of oscillation related to the flow of type FP - B. ($D_1/d = 2$, $l/d = 8.8$)

shock wave S_s , and will be modulated to generate turbulent vortices by its interactions with the free layer developed from the seat edge. These vortices convect downstream and grow to be coherent structures through the shear layers, and impinge on the inner wall of the valve chest. Thus, pressure pulses may be produced [condition-2]. The pressure waves propagate upstream through the ambient air as sound waves. Since the separation on the plug surface is opened to the ambient [condition-1], the sound waves control the instability of the separation. Thus, a feedback loop of the instability excitation is formed between two regions of the separation and the impingement of the flow. A standing wave pattern will be established and the oscillation of the flow is sustained if the superposition of the pressure field, induced by the downstream convected vortices and the upstream propagating sound wave, is in harmony with the acoustic mode in the valve chest.

The above consideration is concerned with the case where a radial mode of the oscillation dominates. However, when a circumferential mode comes to contribute, an additional mechanism must be introduced in the isentropic part of the flow upstream of the shock wave.

In the following subsections, several examples which support the oscillation mechanism will be introduced.

Characteristic Length and Strouhal Number of the Oscillating Flow. The present oscillation of flow may be characterized by the length L_{im} of a column of annular jet between the location of separation and the section of the impingement. The Strouhal number of the oscillation is defined as $St = f \cdot L_{im} / V_a$, and is presented versus the normalized length L_{im} / d in Fig. 8. The location of the separation is read from the schlieren picture as the location of the shock wave S_s . The isentropic flow velocity calculated from the valve pressure ratio is taken as the reference velocity V_a .

It is interesting that the Strouhal number is almost constant at a value of 0.5 for various geometries of the valve. The value is close to the Strouhal number which describes the oscillation of an impinging jet of high subsonic Mach number [11]. Note that the Mach number downstream of the shock wave S_s is around one as stated in Section 3 [10]. Also, the oscillation of

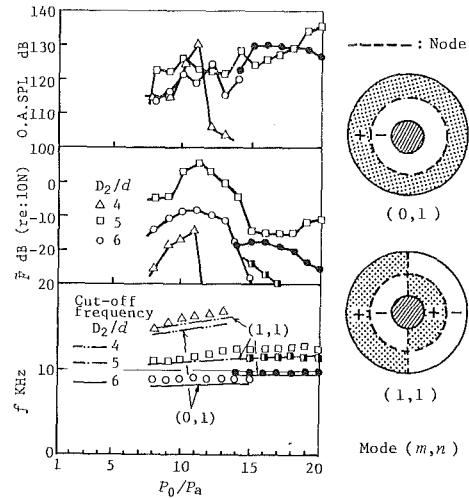


Fig. 9 Variation of oscillation frequencies and the component levels of dynamic thrust and noise versus pressure ratio. ($\mu = 100$ deg, $\beta = 0.5$)

flow does not occur at the impingement length L_{im} / d below 1.6. It may be so, because the length is so short that the downstream convected vortices cannot be fully amplified by the shear layer.

Oscillation Frequency Related to Valve Pressure Ratio. Figure 9 shows the variation of the oscillation frequencies and the component levels of the fluctuating thrust and noise versus the pressure ratio for different inner diameters D_2 of the chest.

As the pressure ratio is increased, the oscillation frequency gradually increases for every D_2 . However, beyond the pressure ratio at which the jump of the frequency is triggered by the primary shock wave reaching the plug trailing edge, no more increase of the frequency is noticed. In the same figure, the cut-off frequency in the passage is introduced, which is obtained by substituting the corresponding diameter of the shock wave position into D_1 of equation (5). The changing characteristics of oscillation frequency against pressure ratio show a good agreement with those of the theoretical cut-off frequency, so it can be said, macroscopically, that they are due to the movement of the separation point, i.e., the position of shock wave S_s where instability is imposed, along the plug surface depending on the pressure ratio.

It is also seen in Fig. 9 that the jump of oscillation frequency corresponds to an intermittent switching of the acoustic mode (0, 1) to the mode (1, 1) in the passage. Therefore, as observed in Fig. 4(d), in the middle range of pressure ratios the flow oscillates in an axisymmetrical manner since the mode induces only a radial pressure variation. As the pressure ratio increases, the shock wave reaches the trailing edge of the plug and a circumferential pressure variation comes to contribute to the mode. The flow oscillates in asymmetrical manner. Depending on the oscillation mode, the level of dynamic thrust becomes higher in the middle range of the pressure ratio and becomes lower in the range of relatively high pressure ratios. However, the noise level continues to increase with an increasing pressure ratio, irrespective to the mode difference.

Effect of Shapes of Plug, Seat and Chest on Oscillating Flow

Mechanisms of oscillation of the strong conical flow have been presented in Section 4. The oscillation can be suppressed or eliminated effectively by removing one of the factors inducing the flow oscillation. The rms values of thrust fluctuation normalized by the fluid momentum $\dot{m} \cdot V_a$ are compared in

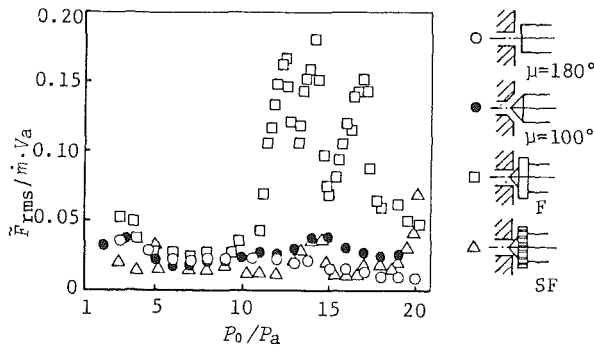


Fig. 10 Level of dynamic thrust generated by various shapes of seat and plug. ($D_1/d=2$, $D_2/d=6$, $\beta=0.5$, $l/d=8.8$)

Fig. 10 for several shapes of the plug and the seat. Here, \dot{m} is the critical mass flow rate through the valve throat expressed as:

$$\dot{m} = \frac{\pi}{4} d^2 \beta \left(\frac{2}{\gamma+1} \right)^{(\gamma+1)/(2(\gamma-1))} \times \sqrt{\frac{\gamma}{RT_0}} P_0 \quad (8)$$

and V_a is the isentropic flow velocity given by:

$$V_a = \sqrt{\gamma RT_0} \left(\frac{P_a}{P_0} \right)^{(\gamma-1)/2\gamma} \times \left\{ \frac{2}{\gamma-1} \left[\left(\frac{P_0}{P_a} \right)^{(\gamma-1)/\gamma} - 1 \right] \right\}^{1/2} \quad (9)$$

The level of a disk plug is significantly low over the entire range of the experimental pressure ratio because flow oscillation cannot occur due to the continuous appearance of the attached-to-seat flow. Arrangement of circumferential teeth on a conical plug, see type SF, is also effective in suppressing the fluctuation. The residual level in all of the cases is due to the longitudinal vibration of the plug support.

However, a conical plug with a circumferential bank, i.e., type F, leads to a remarkable rise of the level in the range of pressure ratio higher than 10 despite the flow being observed to remain always attached to the seat surface. The rise of the level, in this case, is associated with a growth of the discrete component of 3 kHz which is the frequency of the longitudinal fundamental of the plug support. This longitudinal vibration may be suppressed or stabilized by grooving the bank to form the plug of type SF.

The tapered seat is also effective in suppressing the flow oscillation and consequently the levels of the dynamic thrust are found to be low. In this case the seat directs the flow in the direction of the plug surface and the separation does not reach easily the trailing edge of the plug.

The dynamic thrust is significantly increased by mounting the exhaust port to the side wall of the chest, as illustrated in Fig. 11. In the lower range of the pressure ratio the bending vibration of the stem is dominant because the average flow is skewed and asymmetric. In the middle range of the pressure ratio, the oscillation of strong conical flow induces a vibration that is similar as in the case of the straight chest. Further analysis of the vibration is not made at this stage. However, it may be expected that the bend connected to the valve chest must be placed at a certain distance from the plug.

Conclusions

1 Four types of flow patterns are observed in the range of pressure ratio between 3 and 20; i.e., the weak conical flow, the strong conical flow, the attached-to-seat flow, and finally the free flow. These patterns form sequentially with increasing pressure ratio. The attached-to-seat flow is the pattern of lowest noise.

2 Due to the presence of the chest, intense noise and vibra-

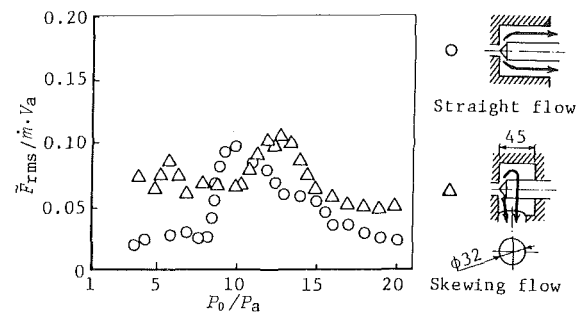


Fig. 11 Fluctuating thrust caused by side mounting of the exhaust port ($\mu=100$ deg, $D_1/d=2$, $D_2/d=6$, $\beta=0.5$, $l/d=8.8$)

tion is generated at the flow conditions where the strong conical flow takes place. The spectra of the noise and dynamic thrust are dominated by discrete components of high frequency and they are induced by oscillation of the flow.

3 This oscillation depends on the flow structure in the close vicinity of the plug and on acoustic modes in the passage formed by the plug and chest. The frequencies almost coincide with the resonant frequencies of circumferential and radial modes of the passage; the frequency of the axial mode is not effective. The length of the annular jet, which leaves the plug surface with the shock-induced separation and impinges on the inner wall of the chest, affects the frequency of the oscillation. However, the Strouhal number based on this length takes almost a constant value of 0.5 for various valve dimensions.

4 The oscillation is present when the following two conditions are reached; one, that the shock-induced separation of the plug boundary layer is not closed, so that the instability of the separation is directly excited by disturbances in the ambient air; and the other, that the annular jet leaving the plug surface impinges on the inner wall of the valve chest so that strong pressure pulses are produced by arrivals of large vortices convected by the jet.

5 Either a disk plug or a conical plug with circumferential teeth is preferable to a simple conical plug to reduce the noise and vibration, because the attached-to-seat flow can easily occur over a wide range of the pressure ratios and the flow oscillation is effectively suppressed or eliminated.

References

- Dear, T. A., "An Overview of the Present Valve Noise Scenario from the User's Viewpoint," *ISA Final Control Elements*, Vol. 3, 1977, pp. 85-93.
- Morfey, C. L., "Sound Transmission and Generation in Ducts with Flow," *J. Sound and Vib.*, Vol. 14, No. 1, 1971, pp. 37-55.
- Reed, C. L., "Sound Transmission Characteristics of Steel Piping," *ISA Paper*, 76-836, 1976.
- Kerschen, E. J., and Johnson, J. P., "Modal Content of Noise Generated by a Coaxial Jet in a Pipe," *J. Sound and Vib.*, Vol. 76, No. 1, 1981, pp. 95-115.
- Ramakrishnan, R., "A Note on the Reflection Coefficients of Higher Order Duct Modes," *J. Sound and Vib.*, Vol. 72, No. 4, 1980, pp. 554-558.
- Harper-Bourne, M., and Fisher, M. J., "The Noise from Shock Waves in Supersonic Jets," *AGARD CP-131*, 1973, pp. 1-13.
- Schmitt, Von M., and Ziegert, O., "Entwicklung geräuscharmer Stellglieder für Gase und Dämpfe," *Regelungstechnische Praxis*, Heft 7, 1978, pp. 207-214.
- Schmitt, Von M., and Ziegert, O., "Entwicklung geräuscharmer Stellglieder für Gase und Dämpfe," *Regelungstechnische Praxis*, Heft 8, 1978, pp. 233-240.
- Nakano, M., Outa, E., and Tajima, K., "Aerodynamic Study on Noise and Vibration Generated in High Pressure Gas Valves: Part 1," *Bull. JSME*, Vol. 22, No. 173, Nov. 1979, pp. 1578-1586.
- Nakano, M., Tajima, K., and Outa, E., "Aerodynamic Study on Noise and Vibration Generated in High Pressure Gas Valves: Part 2," *Bull. JSME*, Vol. 26, No. 213, Mar. 1983, pp. 372-379.
- Ho Chin-Ming, and Nossair, N. S., "Dynamics of Impinging Jet: Part 1," *J. Fluid Mech.*, Vol. 105, 1981, pp. 119-142.

Supercomputing of Supersonic Flows Using Upwind Relaxation and MacCormack Schemes

Oktay Baysal

Assistant Professor,
Mechanical Engineering
and Mechanics Department,
Old Dominion University,
Norfolk, Va. 23529

The impetus of this paper is the comparative applications of two numerical schemes for supersonic flows using computational algorithms tailored for a supercomputer. The mathematical model is the conservation form of Navier-Stokes equations with the effect of turbulence being modeled algebraically. The first scheme is an implicit, unfactored, upwind-biased, line-Gauss-Seidel relaxation scheme based on finite-volume discretization. The second scheme is the explicit-implicit MacCormack scheme based on finite-difference discretization. The best overall efficiencies are obtained using the upwind relaxation scheme. The integrity of the solutions obtained for the example cases is shown by comparisons with experimental and other computational results.

Introduction

Solving the full Navier-Stokes equations for complex single or multicomponent configurations exposed to high-Reynolds-number flows has become more efficient with the wide utilization of supercomputers. The ever-increasing quest for larger speeds and memories is being answered through architectural changes in the computers and new concepts for their software. These improvements, however, brought about strong dependence between the hardware architecture and the program algorithms. This nonuniformity necessitates the tailoring of the computer code to the hardware and the compiler to be used. The principal ways of introducing parallelism into the architecture of computers are through pipelining, array processing, and multiprocessing (reference [1]). A classification of parallelism and levels of parallelism may be given through Flynn's taxonomy: (a) single-instruction-stream/multiple-data-stream (SIMD), (b) multiple-instruction-stream/multiple-data-stream (MIMD). Pipelined computers and array processors are SIMD machines, and multiprocessor computers are MIMD machines. The conventional von Neumann scalar architectures operate on single-instruction-stream/single-data-stream (SISD) principle.

This paper reports the SIMD implementation and the results of two numerical schemes used in simulating two-dimensional supersonic flows. The effect of turbulence is incorporated through a zero-equation eddy viscosity model. Shocks are captured and treated by either special differences or artificial damping. The first scheme is an implicit upwind method solved by line-Gauss-Seidel relaxations. The effect of line-relaxations on convergence is accentuated through comparisons with the solutions obtained by the Beam-Warming

approximate factorization scheme. The second solution method uses the explicit-implicit MacCormack scheme. The effect of its implicit substeps is shown by comparisons with the solutions obtained by the explicit MacCormack scheme. The results indicate that the best convergence rates are obtained with the upwind line-relaxation scheme, and the significant speed-up achieved due to SIMD processing.

Mathematical Formulation

The strong conservation form of the Navier-Stokes equations is written in generalized curvilinear coordinates. The equations are nondimensionalized by a characteristic length, and freestream values of density (ρ_∞) and speed of sound (a_∞).

$$\frac{\partial U_1}{\partial t} + \frac{\partial F_1}{\partial \xi} + \frac{\partial G_1}{\partial \eta} = \frac{M}{\text{Re}} \left[\frac{\partial R_1}{\partial \xi} + \frac{\partial S_1}{\partial \eta} \right] \quad (1)$$

where

$$U_1 = U/J \quad (2a)$$

$$F_1 = (\xi_x F + \xi_y G)/J \quad (2b)$$

$$G_1 = (\eta_x F + \eta_y G)/J \quad (2c)$$

$$R_1 = (\xi_x R + \xi_y S)/J \quad (2d)$$

$$S_1 = (\eta_x R + \eta_y S)/J \quad (2e)$$

and

$$U = \begin{bmatrix} \rho \\ \rho u \\ \rho v \\ e \end{bmatrix} \quad F = \begin{bmatrix} \rho u \\ \rho u^2 + p \\ \rho uv \\ u(e+p) \end{bmatrix} \quad G = \begin{bmatrix} \rho v \\ \rho uv \\ \rho v^2 + p \\ v(e+p) \end{bmatrix} \quad (3a)$$

Contributed by the Fluids Engineering Division and presented at the Symposium on Parallel Processing in Fluids Mechanics, 1987 ASME Fluids Engineering Conference, June 14-18, 1987, Cincinnati, Ohio, of THE AMERICAN SOCIETY OF MECHANICAL ENGINEERS. Manuscript received by the Fluids Engineering Division February 5, 1987.

$$R = \begin{bmatrix} 0 \\ \tau_{xx} \\ \tau_{xy} \\ r \end{bmatrix} \quad S = \begin{bmatrix} 0 \\ \tau_{xy} \\ \tau_{yy} \\ s \end{bmatrix} \quad (3b)$$

Shear stress terms are given as follows:

$$\tau_{xx} = (\lambda + 2\mu)(u_\xi \xi_x + u_\eta \eta_x) + \lambda(v_\xi \xi_y + v_\eta \eta_y) \quad (4)$$

$$\tau_{xy} = \mu(u_\xi \xi_y + u_\eta \eta_y + v_\xi \xi_x + v_\eta \eta_x) \quad (5)$$

$$\tau_{yy} = (\lambda + 2\mu)(v_\xi \xi_y + v_\eta \eta_y) + \lambda(u_\xi \xi_x + u_\eta \eta_x) \quad (6)$$

$$r = u\tau_{xx} + v\tau_{xy} + \frac{\mu}{(\gamma - 1)Pr} \left(\xi_x \frac{\partial a^2}{\partial \xi} + \eta_x \frac{\partial a^2}{\partial \eta} \right) \quad (7)$$

$$s = u\tau_{xy} + v\tau_{yy} + \frac{\mu}{(\gamma - 1)Pr} \left(\xi_y \frac{\partial a^2}{\partial \xi} + \eta_y \frac{\partial a^2}{\partial \eta} \right) \quad (8)$$

The molecular viscosity is determined by the Sutherland law and the Stokes hypothesis is used for the bulk viscosity. The pressure is obtained by assuming air behaving as a perfect gas,

$$p = (\gamma - 1)[e - \rho(u^2 + v^2)/2] \quad (9)$$

The Cartesian coordinates (x, y) are defined with x being in the direction of the freestream and the generalized coordinates (ξ, η) are defined with ξ being along the body. The coordinate transformation Jacobian is given below.

$$J = \xi_x \eta_y - \xi_y \eta_x \quad (10)$$

One of the computationally least expensive methods of modeling the effect of turbulence is the algebraic method by Baldwin and Lomax [2]. The length and velocity scales of this model are specified based on the vorticity distribution, rather than the displacement thickness of the mean flow. Turbulence of the wall-shear flow is called the inner turbulence, and it is modeled using the Prandtl mixing length theory with the improvement of the Van Driest formulation. Turbulence of the outer region is based on the Clauser formulation using the Klebanoff approximation of the Gaussian error function that gives the intermittency factor. Further details of its formulation and implementation are given in reference [3].

Methods of Solution

Upwind Line-Gauss-Seidel Relaxation Scheme (ULR). This implicit finite-volume method employs upwind differencing for the convective and pressure terms, and central differencing for the diffusion terms. The accuracy is second-order in space and first-order in time. The upwind differencing used herein is based on Van Leer type flux vector splitting [4], which has the advantage of first derivative continuity at eigenvalue sign changes corresponding to sonic and stagnation

points, and it can represent normal shocks with at most two transition zones.

The solution is developed by implicit Euler time integration scheme applied to equation (1)

$$\frac{\Delta U_1}{\Delta t} = \text{Res}^{n+1} \quad (11)$$

where Res^{n+1} is the steady state residual evaluated at time level $(n + 1)$, and

$$\text{Res} = -\frac{\partial F_1}{\partial \xi} - \frac{\partial G_1}{\partial \eta} + \frac{M}{\text{Re}} \left(\frac{\partial R_1}{\partial \xi} + \frac{\partial S_1}{\partial \eta} \right) \quad (12)$$

The delta form of the vector-flux-split governing equation is as follows:

$$\left[\frac{I}{J\Delta t} + \nabla_\xi A^+ + \Delta_\xi A^- + \nabla_\eta B^+ + \Delta_\eta B^- - \frac{M}{\text{Re}} (\delta_\xi^2 P + \delta_\eta^2 Q) \right] \Delta U_1 = \text{Res}^n \quad (13)$$

where

$$\Delta U_1 = U_1^{n+1} - U_1^n \quad (14)$$

$$A = \frac{\partial F_1}{\partial U_1} = J \frac{\partial F_1}{\partial U} \quad (15)$$

$$B = \frac{\partial G_1}{\partial U_1} = J \frac{\partial G_1}{\partial U} \quad (16)$$

(+) and (-) superscripts indicate forward and backward flux split quantities, for forward and backward traveling information, respectively. (Δ) denotes a forward difference with its denominator being the corresponding spatial step. In a similar manner, (∇) denotes a backward difference. δ^2 denotes a central difference with its denominator being the square of the corresponding spatial step.

The flux Jacobian matrices P and Q are developed from the diffusion fluxes R_1 and S_1 , which are separated into functions that consist of ξ -derivatives only or η -derivatives only as given below.

$$R_1 = R_{11}(U_1, U_{1\xi}) + R_{12}(U_1, U_{1\eta}) \quad (17)$$

$$S_1 = S_{11}(U_1, U_{1\xi}) + S_{12}(U_1, U_{1\eta}) \quad (18)$$

where $U_{1\xi} = (\partial U_1 / \partial \xi)$ and $U_{1\eta} = (\partial U_1 / \partial \eta)$. The cross-derivative terms $(\partial R_{12} / \partial \xi)$ and $(\partial S_{11} / \partial \eta)$ are evaluated explicitly for simplicity. As shown in reference [5], the temporal linearizations of R_{11} and S_{12} lead to,

$$\Delta R_{11} = [(\partial R_{11} / \partial U_1) - \partial P / \partial \xi] \Delta U_1 + \partial (P \cdot \Delta U_1) / \partial \xi \quad (19)$$

$$\Delta S_{12} = [(\partial S_{12} / \partial U_1) - \partial Q / \partial \xi] \Delta U_1 + \partial (Q \cdot \Delta U_1) / \partial \eta \quad (20)$$

where $\Delta R_{11} = R_{11}^{n+1} - R_{11}^n$, $\Delta S_{12} = S_{12}^{n+1} - S_{12}^n$, $P = \partial R_{11} / \partial U_{1\xi}$, and $Q = (\partial S_{12} / \partial U_{1\eta})$. The first terms on the

Nomenclature

a = local speed of sound	Re = freestream Reynolds number	
c = chord length	t = time	
c_p = pressure coefficient	u, v = Cartesian velocity components	ρ = density
e = energy per unit volume	x, y = Cartesian coordinates	τ = viscous stress term
h = step height	γ = ratio of specific heats	
I = unit diagonal matrix	μ, λ = molecular and bulk viscosity coefficients	Subscripts and Superscripts
J = transformation Jacobian	μs = microseconds	i, j = spatial indices in ξ and η directions
M = freestream Mach number	ξ, η = generalized curvilinear coordinates	n = time level index
p = pressure		∞ = freestream
Pr = Prandtl number		$-$ = predictor value
R = specific gas constant		

right-hand sides of equations (19) and (20) can be omitted by assuming λ and μ to be locally constant and independent of U .

The direct solution of equation (13) is possible by, for example, Gaussian elimination; however, this method would require larger computer storage and have significantly larger round-off errors. The popular solution technique for equation (13) is through its approximate factorization resulting in block-tridiagonal inversions [5]. A point-relaxation method would require diagonal dominance, and possible, pivoting strategies for numerical stability. The line-Gauss-Seidel-relaxation method enhances the solution for all of these considerations, therefore, it is adapted herein from reference [6].

$$\begin{aligned} C\Delta U_{1,j-2} + D\Delta U_{1,j-1} + E\Delta U_1 + H\Delta U_{1,j+1} \\ + K\Delta U_{1,j+2} + L\Delta U_{1,i-2} + N\Delta U_{1,i-1} + W\Delta U_{1,i+1} \\ + Z\Delta U_{1,i+2} = \text{Res} \end{aligned} \quad (21)$$

The coefficient matrix consists of nine 4×4 block matrices ($C, D, E, H, K, L, N, W, Z$) which are solved by lower-upper (LU) decomposition [6]. The relaxation strategy is chosen to be sweeping in ξ -direction first left-to-right,

$$\begin{aligned} (C, D, E, H, K)\Delta U_1 = \text{Res} - N\Delta U_{1,i-1} \\ - L\Delta U_{1,i-2} \end{aligned} \quad (22)$$

then right-to-left,

$$(C, D, E, H, K)\Delta U_1 = \text{Res} - W\Delta U_{1,i+1} - Z\Delta U_{1,i+2} \quad (23)$$

where (C, D, E, H, K) represents the block pentadiagonal matrix which is solved in η -direction. The solution for ΔU_1 is updated after each sweep.

The spatial derivatives of convective and pressure terms are approximated by MUSCL (monotone upstream-centered scheme for conservation laws) type differencing as detailed in reference [4]. First nodal point values of U are extrapolated toward the cell interfaces and then already split flux-vectors are evaluated at the cell interfaces. The differencing of $(\partial B/\partial \eta)$, for example, is as given below.

$$\begin{aligned} \left(\frac{\partial B}{\partial \eta}\right) + 0[(\Delta \eta)^2] = \frac{1}{\Delta \eta} [B^+(U_{j+1/2}^-) - B^+(U_{j-1/2}^-) \\ + B^-(U_{j+1/2}^+) - B^-(U_{j-1/2}^+)] \end{aligned} \quad (24)$$

where $B(U)$ denotes B evaluated at U and

$$U_{j+1/2}^- = U_j + 0.5\phi_j^-(U_j - U_{j-1}) \quad (25)$$

$$U_{j+1/2}^+ = U_{j+1} - 0.5\phi_{j+1}^+(U_{j+2} - U_{j+1}) \quad (26)$$

The order of accuracy may be degraded to first order by setting $\phi^* = 0$ (second order corresponds to $\phi^* = 1$), which is required to eliminate oscillations in regions where the solution is discontinuous (shocks).

Explicit-Implicit MacCormack Scheme (EIM). Equation (1) is rewritten with the diffusion terms brought to the left-hand side.

$$\frac{\partial U_2}{\partial t} + \frac{\partial F_2}{\partial \xi} + \frac{\partial G_2}{\partial \eta} = 0 \quad (27)$$

where

$$U_1 = U_1 = U/J \quad (28a)$$

$$F_2 = [(F-R)\xi_x + (G-S)\xi_y]/J \quad (28b)$$

$$G_2 = [(F-R)\eta_x + (G-S)\eta_y]/J \quad (28c)$$

Since the flows being considered are supersonic, the MacCormack scheme [7], which is most suitable for predominant hyperbolic equations, is one of the methods adopted. The

method is second-order accurate both in time and space. Each step consists of an explicit and an implicit substep. The reasons of this substepping are: (i) when $\Delta t_{\text{implicit}} \leq \Delta t_{\text{explicit}}$, where $\Delta t_{\text{explicit}}$ is determined by the numerical stability criterion (equation (38)), the implicit calculations are bypassed resulting in the explicit scheme, (ii) the resulting differenced equations are either lower or upper block bidiagonal equations.

Explicit Predictor Step:

$$\Delta U_2^n = -\Delta t[\Delta_\xi F_2 + \Delta_\eta G_2] \quad (29)$$

Implicit Predictor Step:

$$[I - \Delta t(\Delta_\xi A_2)][I - \Delta t(\Delta_\eta B_2)]\overline{\Delta U}_2^{n+1} = \Delta U_2^n \quad (30)$$

which is solved for $\overline{\Delta U}_2^{n+1} = \overline{U}_2^{n+1} - U_2^n$, with $\Delta U_2^n = \overline{U}_2^{n+1} - U_2^n$ known from the explicit step (equation (29)), in two sweeps. A_2 and B_2 are related to the Jacobian matrices $\partial F_2/\partial U_2 = J(\partial F_2/\partial U)$ and $\partial G_2/\partial U_2 = J(\partial G_2/\partial U)$, respectively. Their construction includes $(\Lambda_A + \lambda_A I)$ and $(\Lambda_B + \lambda_B I)$, which are positive valued diagonal matrices, where

$$\lambda_A = \frac{2\nu}{\rho} [\xi_x^2 + \xi_y^2] - \frac{1}{2\Delta t} \quad (31)$$

$$\lambda_B = \frac{2\nu}{\rho} [\eta_x^2 + \eta_y^2] - \frac{1}{2\Delta t} \quad (32)$$

and

$$\nu = \max\left[(\lambda + 2\mu), \left(\frac{\gamma}{\gamma - 1}\right) \frac{\mu R}{Pr}\right] \quad (33)$$

which allows approximate inclusion of the viscous terms.

The corrector step is analogous to the predictor step with forward spatial differences replaced by backward differences. $\overline{\Delta U}_2^{n+1}$ is solved from the explicit corrector step and it is used as the right-hand side of the implicit corrector step which results in ΔU_2^{n+1} .

Explicit Corrector Step:

$$\overline{\Delta U}_2^{n+1} = -\Delta t(\nabla_\xi F_2 + \nabla_\eta G_2) \quad (34)$$

where

$$\overline{U}_2^{n+1} = \frac{1}{2} [U_2^n + \overline{U}_2^{n+1} + \overline{\Delta U}_2^{n+1}] \quad (35)$$

Implicit Corrector Step

$$[I + \Delta t(\nabla_\xi A_2)][I + \Delta t(\nabla_\eta B_2)]\Delta U_2^{n+1} = \overline{\Delta U}_2^{n+1} \quad (36)$$

and finally,

$$U_2^{n+1} = \frac{1}{2} [\overline{U}_2^n + \overline{U}_2^{n+1} + \Delta U_2^{n+1}] \quad (37)$$

When the time step, Δt , satisfies the CFL (Courant-Friedrichs-Lewy) stability conditions, modified in an approximate manner to account for the viscous terms,

$$\begin{aligned} \Delta t \leq \frac{1}{2} \left[|u\xi_x + v\xi_y| + a(\xi_x^2 + \xi_y^2)^{1/2} \right. \\ \left. + \frac{2\nu}{\rho} (\xi_x^2 + \xi_y^2) \right]^{-1} \end{aligned} \quad (38a)$$

$$\begin{aligned} \Delta t \leq \frac{1}{2} \left[|u\eta_x + v\eta_y| + a(\eta_x^2 + \eta_y^2)^{1/2} \right. \\ \left. + \frac{2\nu}{\rho} (\eta_x^2 + \eta_y^2) \right]^{-1} \end{aligned} \quad (38b)$$

then all the elements of $(\Lambda_A + \lambda_A I)$ and $(\Lambda_B + \lambda_B I)$ vanish, resulting in equations (30) and (36) being identically zero, i.e., explicit MacCormack Scheme (EM).

Table 1 Total CPU time in minutes to reduce the logarithm of Residual by four orders of magnitude

Flow & Grid Size	Computer Processing	Computational Scheme			
		EM	EIM	UAF	ULR
Laminar Flat Plate (89x101)	SISD	308.82	263.68	177.12	29.57
	SIMD	7.22	6.47	3.54	3.08
Laminar Step (150x89)	SIMD	16.17	12.82	7.61	5.35
Turbulent Corner (101x99)	SIMD	24.22	15.16	8.67	5.95
Turbulent Airfoil (191x55)	SIMD	27.52	19.65	11.61	6.54

Boundary Conditions. No-slip, impermeable, and adiabatic wall conditions are imposed on the solid walls. It is also assumed that $\partial p / \partial \eta = 0$ at the wall. Free-stream values of Mach number, Reynolds number, and total temperature are specified for the inflow boundary. Outflow boundary is predominantly supersonic, hence the gradients of conserved properties are extrapolated from the computation domain. The outer boundary conditions are specified after a flow direction check. When the sign of dot product of the velocity vector and the cell area vector is negative, i.e., inflow, the property values are set equal to free-stream values. When this product is positive, i.e., outflow, first degree extrapolation from the computational domain is used. The cells in front of the leading edges of open-geometry configurations are computed through symmetry about $\eta = 0$ line. Averaging is used along the wake cut of the C-mesh of NACA 0012 airfoil to provide continuous flow variables.

Results and Discussion

Remarks on Coding and SISD Processing. Present flow simulations were performed using single-instruction-single-data (SISD) processing on the CDC Cyber-170/855 computer and single-instruction-multiple-data (SIMD) processing on the CDC-Cyber 205 of NASA Langley Research Center (VPS-32). VPS-32 has a pipeline computer architecture with thirty-two million 64-bit-words memory [8]. A comparative performance test [9] show that 2-pipe Cyber-205 completes a test run (solving a system of linear equations of order 100 using Fortran and 64-bit arithmetic) at 70 percent of the CRAY-1S time for the same test.

Concurrent processing was achieved using explicit vectorization (as opposed to implicit vectorization which needs descriptor statements) as well as an automatic vectorizer/optimizer. A vector is a set of contiguous floating point operands defined by a location and length in the memory. When an identical operation was to be performed for each of the contiguous memory elements, a vector instruction was invoked using special vector syntax. This required the data base to be stored contiguously either by rows or by columns with the objective of constructing the longest possible vectors. The vectors longer than 8K-words (small page) were mapped on large pages (65K-words) since the data transfer rate from a large page was faster. In order to accommodate the second-order differences on the vector elements which corresponded to the cells adjacent to the upstream and lower boundaries of the computational domain, a ghost row and a ghost column were added. Among the methods to define a vector from scalars that are not contiguous in memory is the scatter-and-gather operation. This operation was found to be very efficient on this architecture and it was widely used herein. Another efficient capability of this architecture was the 32-bit (seven significant decimal places) arithmetic. Utilization of this option almost doubled the processing rate and cut the memory requirement to about one-half. The array indices were arrang-

ed in decreasing lengths and the nested D0 loops containing these indices were ordered likewise, so that the innermost loop corresponded to the longest dimension. DIMENSION statements, which did not invoke optimizers, were substituted by COMMON statements. Avoidable uses of expensive vector logical unit were eliminated.

Relaxation schemes pose an added complexity for vectorization due to their recursive nature. Therefore, total vectorization of these schemes require employing algorithms such as checkerboard successive-over-relaxation [1]. Although these algorithms were not used herein, speed-up improvements were still possible with partial vectorization. Most of the operations of the algorithm occurred in the LU decomposition for 4×4 block line inversions (equation (21)), which were computed simultaneously for all the η -lines before beginning the relaxation sweeps. A considerable amount of computation time was also saved by two additional steps implemented in the coding when time-accurate runs were not necessary (steady flows): (a) Courant number of the numerical stability condition (CFL), rather than the time step, was set constant for the computational domain (local time stepping), (b) the coefficient matrices were updated once every preset number of time steps, which was found to yield identical results to continuous updating.

Efficiencies. In an attempt to illustrate the comparative overall efficiencies (the sum of numerical efficiency which is due to the numerical scheme, and computational efficiency which is due to the coding and processing), total central-processing-unit (CPU) times to reduce the logarithm of the residuals by four orders of magnitude were tabulated (Table 1). The timing information presented here is not meant to evaluate the overall performance of a computer system. There exist too many variables to derive a conclusion as such, which would require a more exhaustive study. Each supersonic flow case was computed using the explicit-implicit MacCormack scheme (EIM) and the upwind line-relaxation scheme (ULR). Further computations were performed for the same cases using the explicit MacCormack scheme (EM) and the upwind approximate-factorization scheme (UAF). The latter of these schemes was obtained by the approximate factorization of the left hand side of equation (13), which resulted in the upwind-biased version of the centrally-differenced Beam-Warming scheme [5]. The case of supersonic flow over a flat plate with a leading edge was also run using SISD processing. The SISD run times allowed the comparisons of computational efficiencies due to SIMD processing and Fortran code optimizations. Since speed-up performance is also a function of data vector lengths, the grid sizes used for each case are also provided in this table.

The specific CPU times (CPU time per time step per grid point) were also computed for each scheme. The EM scheme had the lowest specific CPU time (around $10 \mu s$) since the number of operations performed was less than any implicit scheme. The specific CPU time for the UAF scheme was $20 \mu s$ which was lower than that of the EIM scheme, $28 \mu s$. This was chiefly attributed to the fact that the block-tridiagonal matrix inversions were totally, whereas the block-bidiagonal matrix inversions were partially vectorizable. Also, the substepping of the EIM scheme increases the number of operations per time step. The largest specific CPU time was found to be for the ULR scheme (approximately $85 \mu s$), which was due to three reasons; (a) this recursive scheme was only partially vectorized as explained above, (b) each time step required two to four iterations, (c) the block-pentadiagonal inversions required more operations than the other type of inversions. However, the CPU time needed to complete the job for a given case was the least for this scheme. This indicated that the unit CPU time was an insufficient indicator of the overall effi-

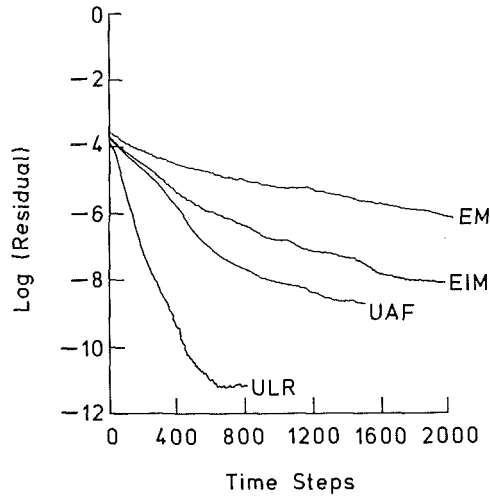


Fig. 1 Comparison of convergence histories for laminar flow over a flat plate with leading edge where $M=3$, $Re_L=1000$. ULR: upwind line-relaxation, UAF: upwind approximate-factorization, EIM: explicit-implicit MacCormack, EM: explicit MacCormack schemes.

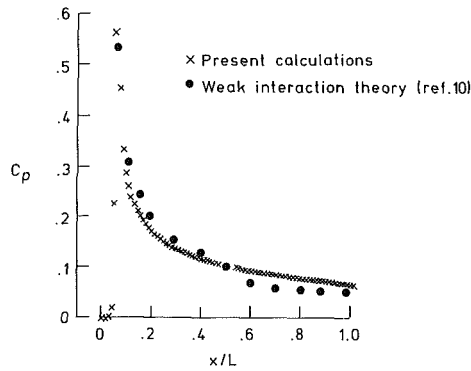


Fig. 2(a)

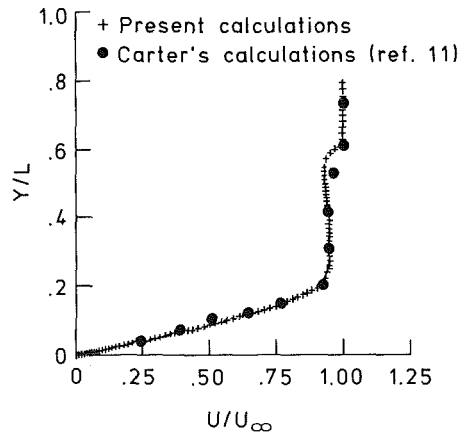


Fig. 2(b)

Fig. 2 Laminar flow over a flat plate with leading edge where $M=3$, $Re_L=1000$ and grid size of 89×101 . (a) Wall pressure coefficient distribution, (b) velocity profile at a fixed streamwise location.

ciency and the ULR scheme had the best numerical efficiency. This point was more accentuated when a comparison was made with the UAF scheme, which differed from the ULR scheme only in the method equation (13) was being solved. Major contributors to the faster convergence (Fig. 1) of the ULR scheme over UAF scheme were; (a) the approximation error due to the spatial factorization of the UAF scheme, (b) significantly lower truncation error of the iterative solver of the ULR scheme (that of the last iterate only) than the ac-

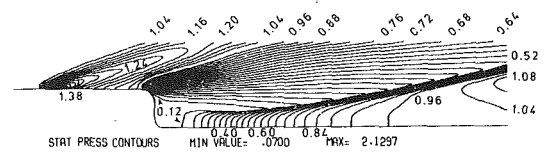


Fig. 3(a)

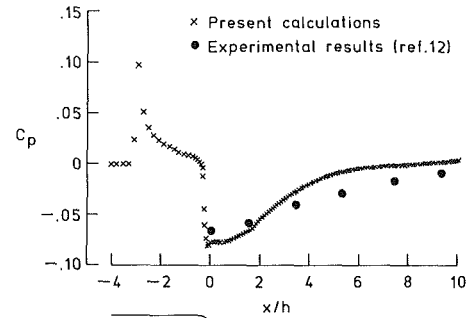


Fig. 3(b)

Fig. 3 Laminar flow over a rearward facing step with leading edge, where $M=4.08$, $Re_h=165,000$ and grid size of 150×89 . (a) Pressure contours, (b) wall pressure coefficient distribution.

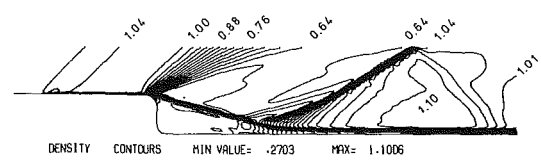


Fig. 4(a)

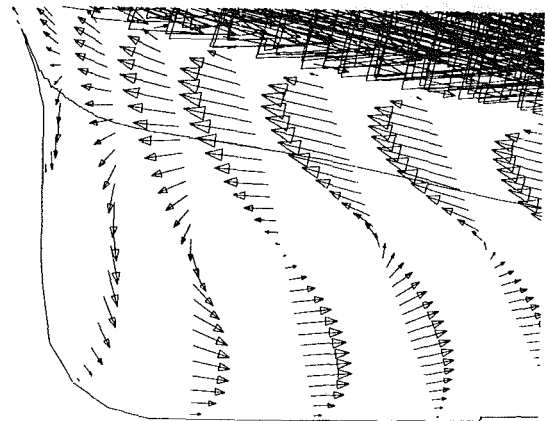


Fig. 4(b)



Fig. 4(c)

Fig. 4 Turbulent flow over a rearward facing step with leading edge where $M=1.5$, $Re_h=2 \times 10^6$, and grid size of 150×89 . (a) Density contours, (b) velocity vectors at the base, (c) velocity vectors downstream of the base.

cumulating round-off error of the noniterative solver of the UAF scheme. The computational times for the upwind implicit schemes (UAF and ULR) were better than the EIM scheme. This was attributed to the upwinding which increased the "robustness" of the schemes (diagonal dominance of the coefficient matrices were enhanced), thereby allowing the use of larger time steps.

Example Flow Cases. All of the four numerical schemes

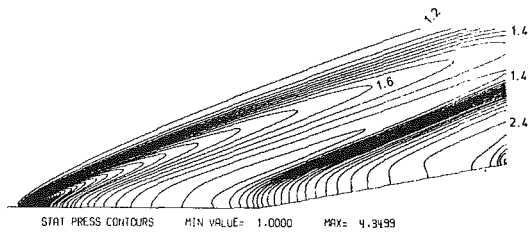


Fig. 5(a)

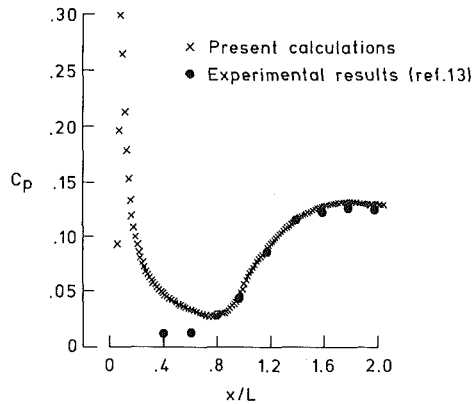


Fig. 5(b)

Fig. 5 Laminar flow over a 10°-compression corner with leading edge where $M=4$, $Re_L=68,000$ and grid size of 150×89 . (a) Pressure contours, (b) wall pressure coefficient distribution.

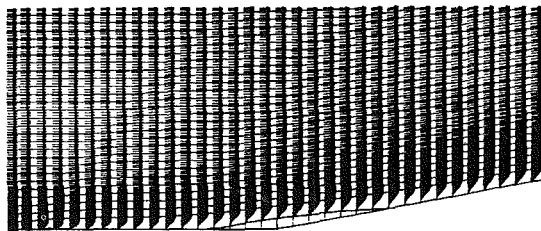


Fig. 6(a)

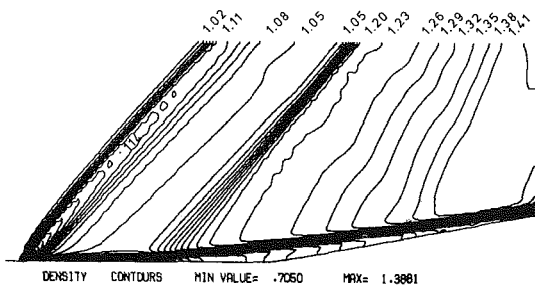


Fig. 6(b)

Fig. 6 Laminar flow over a 10°-compression corner with leading edge where $M=1.5$, $Re_L=2 \times 10^6$ and grid size of 150×89 . (a) Velocity vectors, (b) density contours.

(EM, EIM, UAF, ULR) predicted satisfactorily the salient features of the six illustrative cases chosen for two-dimensional simulations. The first case was the supersonic and laminar flow over a flat plate with a leading edge at $M=3.0$. Figure 2(a) shows the comparison of the computed wall pressure coefficient distribution with the weak interaction theory calculations of Kubota et al. [10]. Also shown (Fig. 2(b)) is the velocity profile at a location on the flat plate where $Re_L=1000$, and its comparison with Carter's calculations [11]. The computational results for the supersonic and laminar flow ($M=4.08$, $Re_h=165,000$) over a rearward facing step

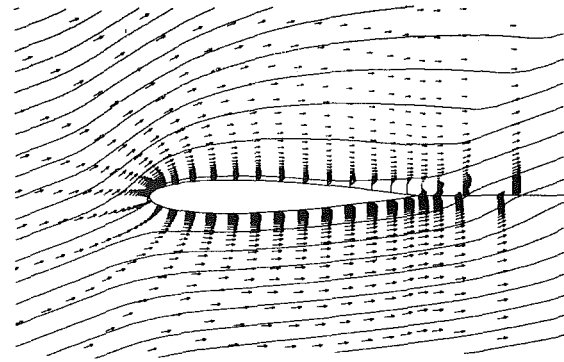


Fig. 7(a)

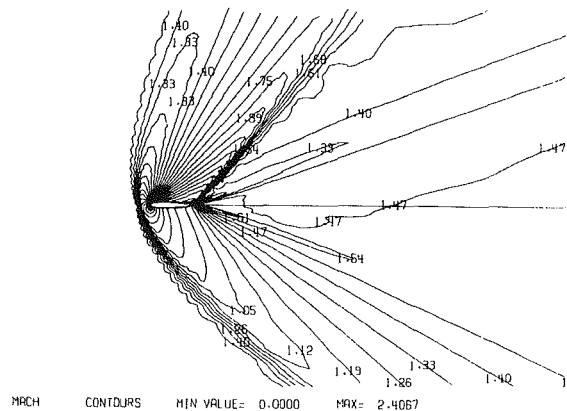


Fig. 7(b)

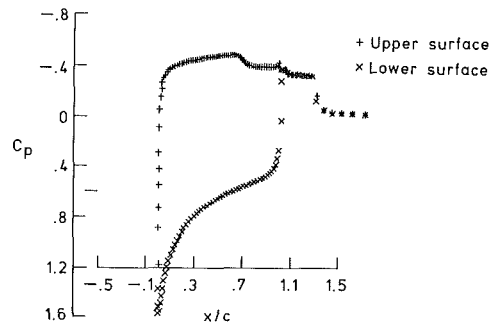


Fig. 7(c)

Fig. 7 Turbulent flow over NACA 0012 airfoil at 20° angle of attack with $M=1.5$, $Re_c=2 \times 10^6$ and grid size of 191×55 . (a) Velocity vectors, (b) Mach number contours, (c) wall pressure coefficient distributions.

with a leading edge are shown in Fig. 3. Figure 3(a) shows the pressure contours of this flow which includes a strong leading edge shock, a viscous expansion fan and a series of compression waves coalescing into a strong reattachment shock. Calculated wall pressure coefficient distribution was compared (Fig. 2(b)) with the experimental results of Jakubowski et al. [12]. Considering the complexity of the high Mach number shocks interacting with the separating boundary layers and the recirculation region, the agreement was very good. The effect of turbulence on this type of flow was shown through the next case where $M=1.5$ and $Re_h=2 \times 10^6$. Figure 4 shows the density contours and blow-ups of the velocity vector diagram for the recirculation region in front of the step.

Another classical example to show the computational capability of resolving the shock-boundary layer interaction is the supersonic flow over a ramp. The fourth case was chosen to be the laminar flow over a 10°-compression corner with a leading edge and $M_\infty=4.0$, $Re_L=68,000$. The comparison of

the computed wall pressure coefficient distribution with the experimental results of Lewis, et al. [13] is shown in Fig. 5. The calculations were then performed for the turbulent flow over a 10° -compression corner with $M=1.5$ and $Re_L=2 \times 10^6$. The separated and reversed flow in the corner can be observed in the velocity vectors diagram (Fig. 6(a)). Figure 6(b) is the density contours of this case demonstrating the detached corner shock as well as the weaker leading edge shock. The computational results for the turbulent flow over NACA 0012 airfoil at 20° angle of attack and with freestream conditions of $M=1.5$ and $Re_C=2 \times 10^6$ are shown in Fig. 7. The separation can be observed through the velocity vectors diagram (Fig. 7(a)) as well as the pressure coefficient distribution of the upper surface (Fig. 7(c)). The computational resolutions of the wake structure, the detached shock, and the trailing edge shock were very successful (Fig. 7(b)).

Conclusion

Supersonic flows were simulated computationally using the MacCormack scheme (EM and EIM) and an upwind relaxation scheme (ULR). The algorithms were computer coded for multiple-data processing (SIMD) to show the computational efficiencies obtained over sequential processing (SISD). The results indicated the superiority of the ULR scheme over not only the EM and EIM schemes but also the UAF scheme. Despite its ease of vectorizability, EM scheme showed the least overall efficiency. The implicit upwind schemes (UAF and ULR) proved to be more robust than EM and EIM schemes. Further study, however, is necessary to improve the type of flux splitting in order to control the numerical dissipation due to upwind differencing. Also, special line relaxation strategies need to be constructed to simulate unsteady flows.

Acknowledgment

This work was supported under NASA Grant No. NAG-1-664. The technical monitor was Wallace C. Sawyer.

References

- 1 Ortega, J. M., and Voigt, R. G., *Solution of PDE's on Vector and Parallel Computers*, SIAM Publications, Philadelphia, 1985, pp. 41-58.
- 2 Baldwin, B., and Lomax, H., "Thin Layer Approximation and Algebraic Model for Separated Flows," AIAA Paper No. 78-257, 1978.
- 3 Baysal, O., "Navier-Stokes Analysis of Muzzle-Blast-Type Waves," *AIAA J.*, Vol. 24, No. 5, 1986, pp. 800-806.
- 4 Van Leer, B., "Flux-Vector Splitting for the Euler Equations," ICASE Report No. 82-30, Sept. 1982. Also *Lecture Notes in Physics*, Vol. 170, 1982, pp. 507-512.
- 5 Beam, R. M., and Warming, R. F., "An Implicit Factored Scheme for the Compressible Navier-Stokes Equations," *AIAA J.*, Vol. 16, No. 5, Apr. 1978, pp. 393-402.
- 6 Thomas, J. L., and Walters, R. W., "Upwind Relaxation Algorithms for the Navier-Stokes Equations," AIAA Paper No. 85-1501 CP, 1985.
- 7 MacCormack, R. W., "A Numerical Method for Solving the Equations of Compressible Viscous Flow," AIAA Paper No. 81-0100, 1981.
- 8 CDC Cyber 205 Computer System Hardware Reference Manual, LaRC Series No. S-8, CDC Document No. 60256020B, NASA LaRC, Hampton, Virginia.
- 9 Dongarra, J. J., "Performance of Various Computers Using Standard Linear Equations Software in a Fortran Environment," Argonne National Laboratory, Technical Memorandum No. 23, May 1986.
- 10 Kubota, R., and Ko, D. R. S., "A Second Order Weak Interaction Expansion for Moderately Hypersonic Flow Past a Flat Plate," *AIAA J.*, Vol. 5, No. 10, p. 1915, Oct. 1967.
- 11 Carter, J. E., "Numerical Solutions of the Navier-Stokes Equations for the Supersonic Laminar Flow Over a Two-Dimensional Compression Corner," NASA-TR-R385, July 1972.
- 12 Jakubowski, A. K., and Lewis, C. H., "Experimental Study of Supersonic Laminar Base Flow With and Without Suction," *AIAA J.*, Vol. 11, No. 12, Dec. 1973, p. 1670.
- 13 Lewis, J. E., Kubota, T., Lees, L., "Experimental Investigation of Supersonic Laminar, 2-D Boundary Layer Separation in a Compression Corner With and Without Cooling," *AIAA J.*, Vol. 6, No. 1, Jan. 1968, p. 7.

O. Key Kwon

Senior Project Engineer,
Allison Gas Turbine Division,
General Motors Corporation,
Indianapolis, Ind.
Assoc. Mem. ASME

R. H. Pletcher

Professor,
Department of Mechanical Engineering
and
Computational Fluid Dynamics Center,
Iowa State University,
Ames, Iowa.
Fellow ASME

R. A. Delaney

Supervisor,
Allison Gas Turbine Division,
General Motors Corporation,
Indianapolis, Ind.
Mem. ASME

Solution Procedure for Unsteady Two-Dimensional Boundary Layers

An accurate and reliable solution procedure is presented for solving the two-dimensional, compressible, unsteady boundary layer equations. The procedure solves the governing equations in a coupled manner using a fully implicit finite-difference numerical algorithm. Several unsteady compressible and incompressible laminar flows are considered. Example results for two unsteady incompressible turbulent flows are also included. An algebraic mixing length closure model is used for the turbulent flow calculations. The computed results compare favorably with experimental data and available analytical/numerical solutions.

I Introduction

Many flows of practical importance are unsteady. These include flows over aircraft, rotorcraft, and in turbomachines. In many cases, these unsteady flows are also turbulent, compressible, three-dimensional, and recirculating. Because of these complicated flow characteristics and the lack of reliable experimental data and analyses, unsteady flows are among the least understood of the flows important in applications. However, the development of future high performance aircraft and rotorcraft requires accurate predictions of unsteady phenomena.

Following the early work of Moore [1], Lighthill [2], and Lin [3], numerous efforts have been made to develop quantitative and qualitative prediction procedures for unsteady viscous flows [4–8]. Most of these analytical efforts were limited to unsteady, incompressible, two-dimensional boundary layer flows in the absence of heat transfer [9].

For compressible flows, the analyses have been limited to relatively simple boundary layer and stagnation point flows. Most analytical methods for these studies are based on the unsteady, two-dimensional, compressible boundary layer equations written with transformed (similarity-type) variables in a manner that results in combining the continuity and momentum equations into a single third-order equation [10–13]. This choice of variables may have been made partly because the normal component of velocity, v , cannot easily be obtained by the direct time integration of the governing boundary layer equations. However, none of the schemes in

references 10–13 have been applied over a wide range of flow conditions. To date it appears that a general, reliable algorithm for unsteady, compressible boundary layers has not been identified.

In the present study, a new solution procedure for the general unsteady, compressible, two-dimensional boundary layer equations is presented. The governing equations are solved using the primitive variables, u , v , T , and ρ . A tightly coupled solution procedure that overcomes the problem associated with the time integration for the normal velocity component has been developed using an extension of the fully implicit numerical algorithm developed by Kwon and Pletcher [14]. With the solution procedure, the governing partial differential equations are discretized using a fully implicit numerical scheme. Application of Newton linearization to the finite-difference equations results in a linearized block-tridiagonal system with 3×3 blocks [14]. The system of equations is then solved using an efficient block solution procedure.

The solution procedure has been applied to several unsteady laminar and turbulent boundary layers. For laminar flow, various compressible and incompressible boundary layers have been computed; for turbulent flow, two incompressible, two-dimensional boundary layers were calculated using an algebraic mixing length model. The calculated results were compared with analytical/numerical solutions and/or measured data. The comparisons are presented in this paper along with details of the numerical procedure.

II Governing Equations

It is assumed that the flow is unsteady, two-dimensional,

Contributed by the Fluids Engineering Division of THE AMERICAN SOCIETY OF MECHANICAL ENGINEERS and presented at the AIAA/ASME 4th Mechanics Plasma Dynamics and Laser Conference, Atlanta, Ga., May 1986. Manuscript received by the Fluids Engineering Division May 18, 1987.

and compressible, and that the boundary layer approximation is valid. The governing boundary layer equations with the equation of state for an ideal gas can be written in Cartesian coordinates as

$$\frac{\partial \rho}{\partial t} + \frac{\partial}{\partial x}(\rho u) + \frac{\partial}{\partial y}(\rho v) = 0 \quad (1)$$

$$\rho \frac{\partial u}{\partial t} + \rho u \frac{\partial u}{\partial x} + \rho v \frac{\partial u}{\partial y} = -\frac{\partial p}{\partial x} + \frac{\partial}{\partial y}(\mu_{\text{eff}} \frac{\partial u}{\partial y}) \quad (2)$$

$$Cp\rho \frac{\partial T}{\partial t} + Cp\rho u \frac{\partial T}{\partial x} + Cp\rho v \frac{\partial T}{\partial y} = \frac{\partial}{\partial y} \left(k_{\text{eff}} \frac{\partial T}{\partial y} \right) + \mu_{\text{eff}} \left(\frac{\partial u}{\partial y} \right)^2 + \frac{\partial p}{\partial t} + u \frac{\partial p}{\partial x} \quad (3)$$

$$p = \rho RT \quad (4)$$

with

$$\mu_{\text{eff}} = \mu + \mu_t$$

$$k_{\text{eff}} = k + k_t = Cp \left(\frac{\mu}{Pr} + \frac{\mu_t}{Pr_t} \right)$$

where x and y are coordinates along and normal to the streamwise direction, respectively; t , the time; u and v , the velocity components in the x and y directions; p , the pressure; T , the temperature; ρ , Cp , μ , and k , the density, specific heat, viscosity, and thermal conductivity of the fluid, respectively; R , the gas constant; and Pr , the Prandtl number. The subscripts eff and t refer to the effective and turbulent quantities, respectively.

The boundary conditions are

$$\begin{aligned} \text{at } y=0, \quad u(x,0,t) &= u_w(x,t), \\ v(x,0,t) &= 0.0, \\ T(x,0,t) &= T_w(x,t) \end{aligned} \quad (5)$$

$$\text{as } y \rightarrow \infty, \quad u(x,y,t) = u_e(x,t), \quad (6)$$

and in the freestream where the normal gradients of velocity and temperature are zero, pressure, velocity, density, and

temperature must satisfy the following relations and the equation of state, equation (4),

$$\partial p / \partial x = -\rho_e (\partial u_e / \partial t + u_e \partial u_e / \partial x) \quad (7)$$

$$\partial p / \partial t = Cp\rho_e (\partial / \partial t + u_e \partial / \partial x) (T_e + u_e^2 / 2Cp) \quad (8)$$

Here, it is clear that one of the freestream variables of pressure, velocity, density, or temperature can be fixed by boundary conditions and the other three quantities should be determined using equations (4), (7), and (8). That is, with the prescribed freestream velocity u_e , pressure, density, and temperature in the freestream are, therefore, evaluated from equations (4), (7), and (8). It is noted that equation (8) indicates that, for unsteady flow, the total enthalpy is no longer constant but varies with time if the pressure varies with time.

The turbulent viscosity, μ_t , in the governing equations is evaluated using a simple mixing length model since the primary purpose of the present study is to develop a reliable numerical solution procedure for the unsteady boundary-layer equations. The evaluation of more complex models will be left for future work. According to the mixing length model, the turbulent viscosity, μ_t , is expressed by

$$\mu_t = \rho l^2 \left| \frac{\partial u}{\partial y} \right| \quad (9)$$

where l is the mixing length.

In the inner region of the boundary layer, the mixing length l is evaluated by the following formula:

$$l = 0.41y(1.0 - \exp[-y/A^+]) \quad (10)$$

where

$$A^+ = 26 \nu / u_\tau \sqrt{1 - 11.8(p_t^+ + p_x^+)}$$

$$u_\tau = \sqrt{\tau_w / \rho}$$

$$p_t^+ = (\nu / u_\tau^3) \partial u_e / \partial t$$

$$p_x^+ = (\nu u_e / u_\tau^3) \partial u_e / \partial x$$

Here y is the normal coordinate; ν , the kinematic viscosity; τ_w , the wall shear stress; u_e , the local freestream velocity; t , the time; x , the streamwise coordinate. The correction for A^+ was suggested by Cebeci [15].

In the outer region, the mixing length is evaluated by

Nomenclature

Cp = specific heat

c = constant

c_f = skin friction coefficient

g_c = gravitational constant

H = extent of computation domain in normal direction

J = proportionality factor between work and heat

k = thermal conductivity

L = reference length and extent of computation domain in streamwise direction

l = mixing length

P = nondimensional pressure defined in equation (12)

Pr = Prandtl number

p = pressure

q = heat flux rate

R = gas constant

Re = Reynolds number

St = Stanton number

T = temperature

t = time

U, V = nondimensional velocities defined in equation (12)

u, v = velocity component in x and y directions, respectively

u_τ = friction velocity

X, Y = nondimensional coordinates defined in equation (12)

x, y = Cartesian coordinates

θ = nondimensional temperature defined in equation (12)

δ = boundary layer thickness

μ = viscosity

ν = kinematic viscosity

ρ = density

τ = nondimensional time defined in equation (12)

τ_w = wall shear stress

ϕ = phase angle

ω = frequency

Δt = time increment

$\Delta X, \Delta Y$ = increments in X and Y directions, respectively

Subscripts and Superscripts

ad = adiabatic condition

e = boundary layer edge condition

eff = effective quantity

i, j = grid indices

n = time index

o = reference or freestream condition

R = reference quantity

s = shock

t = turbulent flow

w = wall

$(\)$ = nondimensional quantity defined in equation (12)

$(\)$ = average quantity

$[]^T$ = transpose of vector

$$l = 0.085\delta \quad (11)$$

Here δ is the boundary layer thickness defined as the y -location where the streamwise velocity component reaches 99 percent of the local freestream velocity. The switch from the inner to the outer model is made at the y -location where the mixing length, l , obtained from equation (9) becomes equal to or greater than l from equation (11). The turbulent Prandtl number, Pr_t , in the governing equations is set to a constant value of 0.9.

With known freestream conditions, equations (1) through (4) comprise a system of four equations for the four unknowns u , v , ρ , and T . In the present study, these governing equations are solved using an extension of the fully implicit coupling scheme developed by Kwon and Pletcher [14] without introducing similarity-type transformed variables [1]. This choice was made to overcome some of the disadvantages observed in the similarity variable approach in references 10-13, including the need to represent mixed derivatives.

III Numerical Algorithm

In terms of the nondimensional variables defined as follows

$$\begin{aligned} U &= u/u_R, & V &= v/u_R, & P &= g_c p / \rho_R u_R^2, \\ \theta &= g_c RT / u_R^2, & X &= x \rho_R u_R / \mu_R, & Y &= y \rho_R u_R / \mu_R, \\ \tau &= t \rho_R u_R^2 / \mu_R, & \hat{\mu} &= \mu / \mu_R, & \hat{\rho} &= \rho / \rho_R, \\ \hat{C}_p &= C_p / C_{pR}, & \hat{k} &= k / k_R, \end{aligned} \quad (12)$$

Equations (1) through (4) are discretized using a fully implicit finite-difference scheme as

$$\begin{aligned} & \frac{1}{4\Delta\tau} (\rho_{i,j}^{n+1} + \rho_{i,j-1}^{n+1} + \rho_{i-1,j}^{n+1} + \rho_{i-1,j-1}^{n+1} \\ & \quad - \rho_{i,j}^n - \rho_{i,j-1}^n - \rho_{i-1,j}^n - \rho_{i-1,j-1}^n) \\ & + \frac{1}{2\Delta X} [(\rho U)_{i,j}^{n+1} + (\rho U)_{i,j-1}^{n+1} - (\rho U)_{i-1,j}^{n+1} - (\rho U)_{i-1,j-1}^{n+1}] \\ & \quad + \frac{1}{\Delta Y} [(\rho V)_{i,j}^{n+1} - (\rho V)_{i,j-1}^{n+1}] = 0 \end{aligned} \quad (13)$$

$$\begin{aligned} & \rho_{i,j}^{n+1} \frac{U_{i,j}^{n+1} - U_{i,j}^n}{\Delta\tau} + (\rho U)_{i,j}^{n+1} \left[c \frac{U_{i,j}^{n+1} - U_{i-1,j}^{n+1}}{\Delta X} \right. \\ & \quad \left. + (1-c) \frac{U_{i+1,j}^{n+1} - U_{i,j}^{n+1}}{\Delta X_+} \right] + (\rho V)_{i,j}^{n+1} \frac{U_{i,j+1}^{n+1} - U_{i,j-1}^{n+1}}{\Delta Y_+ + \Delta Y} \\ & = - \frac{P_i^{n+1} - P_i^n}{\Delta X} + \frac{2}{\Delta Y_+ + \Delta Y} \left(\frac{\mu_{i,j+1}^{n+1} + \mu_{i,j}^{n+1} U_{i,j+1}^{n+1} - U_{i,j}^{n+1}}{2 \Delta Y_+} \right. \\ & \quad \left. - \frac{\mu_{i,j}^{n+1} + \mu_{i,j-1}^{n+1} U_{i,j}^{n+1} - U_{i,j-1}^{n+1}}{2 \Delta Y} \right) \end{aligned} \quad (14)$$

$$\begin{aligned} & (Cp\rho)_{i,j}^{n+1} \frac{\theta_{i,j}^{n+1} - \theta_{i,j}^n}{\Delta\tau} + (Cp\rho U)_{i,j}^{n+1} \left[c \frac{\theta_{i,j}^{n+1} - \theta_{i-1,j}^{n+1}}{\Delta X} \right. \\ & \quad \left. + (1-c) \frac{\theta_{i+1,j}^{n+1} - \theta_{i,j}^{n+1}}{\Delta X_+} \right] + (Cp\rho V)_{i,j}^{n+1} \frac{\theta_{i,j+1}^{n+1} - \theta_{i,j-1}^{n+1}}{\Delta Y_+ + \Delta Y} \\ & = \frac{2}{\Delta Y_+ + \Delta Y} \left(\frac{k_{i,j+1}^{n+1} + k_{i,j}^{n+1} \theta_{i,j+1}^{n+1} - \theta_{i,j}^{n+1}}{2 \Delta Y_+} \right. \\ & \quad \left. - \frac{k_{i,j}^{n+1} + k_{i,j-1}^{n+1} \theta_{i,j}^{n+1} - \theta_{i,j-1}^{n+1}}{2 \Delta Y} \right) + \mu_{i,j}^{n+1} \left(\frac{U_{i,j+1}^{n+1} - U_{i,j-1}^{n+1}}{\Delta Y_+ + \Delta Y} \right)^2 \\ & \quad + \frac{P_i^{n+1} - P_i^n}{\Delta\tau} + U_{i,j}^{n+1} \frac{P_i^{n+1} - P_{i-1}^{n+1}}{\Delta X} \end{aligned} \quad (15)$$

$$P_{i,j}^{n+1} = (\rho\theta)_{i,j}^{n+1} \quad (16)$$

where $c=0.0$ if $U < 0.0$; and $c=1.0$ if $U \geq 0.0$. For convenience, the caret defined in equation (12) and the subscripts eff to the effective viscosity and thermal conductivity are deleted in the finite-difference equations, equations (13) through (16).

The solution is to be advanced from the $(i-1)$ -th to the i th streamwise station. The finite-difference equations, equations (13) through (16), are algebraically nonlinear in the unknown dependent variables of U , V , ρ , and θ at the i th station of the $n+1$ time level. The linear representation of equations (13) through (16) is obtained through iterative application of the Newton linearization scheme to the nonlinear terms in the finite-difference equations (for details, one should refer to reference [14]). The linearized finite-difference equations are rearranged to obtain a block tridiagonal system for the unknown vector of $[U, V, \rho, \theta]^T$. The linear system of equations can be directly solved using a block tridiagonal matrix solver [16]. However, better solution efficiency can be achieved by reducing the size of the coefficient matrices from 4×4 to 3×3 since the inversion of a 3×3 element matrix takes significantly less time than required for a 4×4 matrix.

In the present study, this has been accomplished by eliminating the unknown densities $\rho_{i,j+1}^{n+1}$, $\rho_{i,j}^{n+1}$, and $\rho_{i,j-1}^{n+1}$ in the linearized finite-difference equations using the linearized equation of state. The reduced linearized system of finite-difference equations is now solved using the block tridiagonal matrix solver in reference [16] for the unknown U , V , and θ with the appropriate wall and freestream boundary conditions. The density is then calculated separately from equation (16).

It should be noted that since a linearization scheme has been used for the nonlinear terms during the present solution procedure, local iterations are necessary to obtain the solution that satisfies the governing equations simultaneously at each streamwise station. The local iterative procedure at a streamwise station starts with the solutions of U , V , θ , and ρ at the previous time level as the initial values. The fluid properties are updated after each local iteration. For air, a standard property table such as in reference [17] is used to evaluate the properties. Typically 4-5 iterations are required for the local iteration to achieve the convergence criterion that the maximum variation of U between two successive iterations be less than 0.01 percent of the U obtained at the latest iteration across the computation domain. As to the numerical stability, the present scheme is not constrained by the size of time step since the fully implicit algorithm is utilized for the discretization of the governing equations. However, relatively fine time steps were used for the solution to ensure computation accuracy.

IV Results and Discussion

Both compressible and incompressible flows are computed using the present unsteady solution procedure. Incompressible flow computations are included for demonstrating the capability and accuracy of the present scheme since most of the measured and computed unsteady flow results available in the open literature are for incompressible flow without heat transfer. For these incompressible flow computations, the present solution was modified as follows:

(a) The energy equation, equation (3), was replaced by the uniform temperature condition throughout the computation domain, e.g., $T = \text{constant}$, however, when heat transfer occurred, the energy equation was solved separately in an uncoupled manner.

(b) All of the properties, including the density, were set to constant values, and, thus, the procedure for updating properties was not required.

These modifications for incompressible flow resulted in

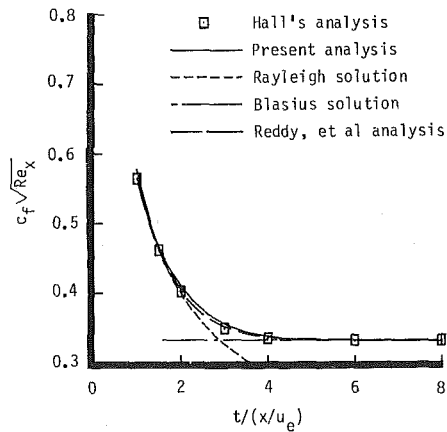


Fig. 1 Wall shear stress development for incompressible flow over an impulsively started semi-infinite flat plate

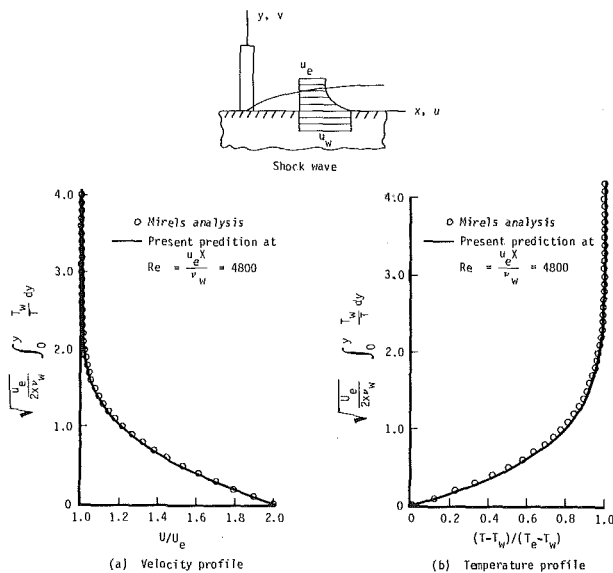


Fig. 2 Velocity and temperature profiles of the boundary layer developed behind a moving shock, $u_e/u_w = 0.5$

faster convergence (within 2–3 iterations) in the local Newton iteration loop.

Sudden Acceleration of a Semi-Infinite Flat Plate. The first test case is for the developing incompressible boundary layer on an impulsively started semi-infinite flat plate with a plate velocity of $-u_w$. The motion of the plate is parallel to itself, e.g., $v_w = 0.0$. The surrounding fluid is at rest. The boundary layer developing downstream of the leading edge is initially described by the Rayleigh solution [18] for an infinite plate and evolves eventually to the solution given by Blasius for a semi-infinite flat plate in a steady, uniform stream.

For the present analysis the coordinate system was fixed on the plate. The no-slip boundary condition was prescribed on the surface of the plate; the streamwise freestream velocity was set to the plate velocity but in the opposite direction ($u_e = u_w$). Figure 1 presents the development of the wall shear stress at a typical point located downstream from the leading edge. The present solution for wall shear stress initially follows the Rayleigh solution. As time increases, it starts to deviate from the Rayleigh solution and to approach to the Blasius exact solution. The present solution agrees well with other previous numerical solutions by Hall [19] and Reddy et al. [20] as shown in Fig. 1. The results were calculated using 81 unequally spaced grid points in the streamwise direction over

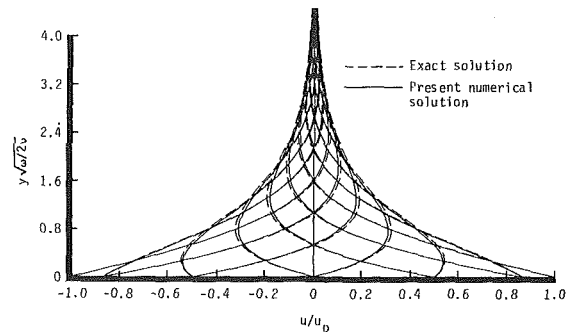


Fig. 3 Velocity profiles on an oscillating flat plate for each 30-deg increment of one cycle, $u_w = u_0 \cos \omega t$, $\omega = 2\pi$

$Re_L (=u_e L/\nu_e) = 2.6 \times 10^6$, where L is the extent of the computation domain in the streamwise direction. In the normal direction 71 grid points were used. The time increment, $\Delta t u_e/L$, was set to 0.0585.

Developing Boundary Layer Behind a Moving Shock. The developing compressible laminar boundary layer behind a moving shock that advances into a stationary fluid bounded by a wall was also analyzed using the present scheme. For the computation, the shock was assumed to have a zero thickness and to move with a constant velocity that is twice that of the developing flow behind the shock. The computational coordinate system was moving with the shock and, therefore, the solid wall was assumed to move at the shock speed, i.e., $u_w = -u_s$ (see Fig. 2). The computation started with the initial inviscid flow condition; that is, at $t=0$, zero boundary layer thickness was assumed. As time progressed, the wall boundary layer developed and the steady-state solution was eventually established.

The converged steady-state solutions at $Re_x (=u_e x/\nu_w) = 4800$ agree well with Mirels' analytical steady-state solutions [21] for both the velocity and temperature profiles, as shown in Fig. 2. The steady-state solutions were obtained after seven time steps using a time increment of $\Delta t u_e/L = 0.658$ over $Re_L (=u_e L/\nu_w) \times Re_H (=u_e H/\nu_w) = 4800 \times 450$, where L and H are the extent of the computation domain in the streamwise and normal directions. A 33×81 grid was used. The grid was stretched in the streamwise direction, whereas uniform grid spacing was used in the normal direction. The solution was assumed to be converged when the maximum change in U between two successive time steps was less than 5×10^{-5} .

Steady Oscillation of a Plate at $u_0 \cos \omega t$. This problem is one of the well-known problems of Stokes [18]. An infinitely long flat plate surrounded by a stationary incompressible fluid oscillates with the velocity $u_w(t) = u_0 \cos \omega t$, where u_0 is the reference velocity; ω , the frequency; and t , the time. The exact periodic oscillatory solutions for the velocities were given by Stokes [18] in the form

$$u/u_0 = \exp(-y\sqrt{\omega/2\nu})\cos(\omega t - y\sqrt{\omega/2\nu}) \quad (17)$$

Equation (17) represents a strongly damped oscillation.

Figure 3 compares the computed periodic velocity profiles with the exact solution given by equation (17). The computed solution is for $\omega/2\pi = 1.0$ Hz, and $Re = u_0 \rho L/\mu = 20.5$ with $L = 1.0$ m. The periodic solutions were established after six cycles with 60 time steps per cycle. The agreement between the present solution and the exact solution is excellent. The amplitude of both the computed velocity and the velocity obtained from the exact solution, equation (17), dropped to 1 percent of the maximum plate velocity u_0 at $y\sqrt{\omega/2\nu} \approx 4.6$. The small discrepancies between the computed and exact solutions noted in Fig. 3 are probably due to the difference between the infinitely long theoretical domain and the finite computational domain.

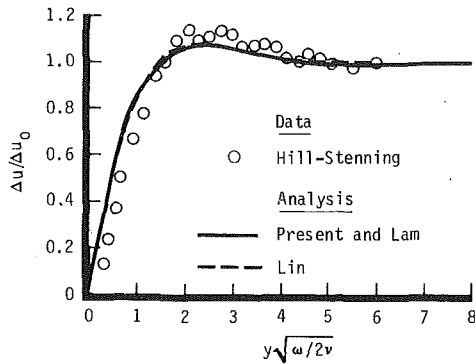


Fig. 4(a) Amplitude of oscillations in Blasius flow, $x\omega/u_0 = 4.98$, $\Delta u_0/u_0 = 0.10$

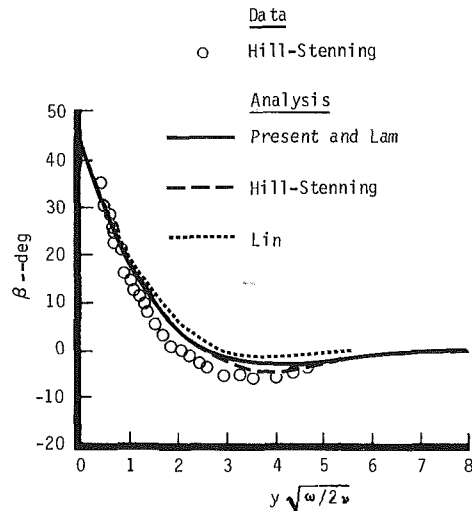


Fig. 4(b) Phase of oscillations in Blasius flow, $x\omega/u_0 = 4.98$, $\Delta u_0/u_0 = 0.10$

Oscillatory Flow Superimposed on Blasius Flow. The freestream velocity of the Blasius flow can be written in the following form when the free-stream harmonic oscillation is superimposed:

$$u_e = u_0 + \Delta u_0 \cos \omega t \quad (18)$$

where u_0 is the freestream mean velocity and Δu_0 is the maximum amplitude of freestream velocity oscillation. Hill and Stenning [22] measured this type of flow using a simple open-circuit suction type wind tunnel with the characteristic frequency parameter $x\omega/u_0$ ranging from 0.1 to 10.0. Harmonic oscillations of the flow were induced by moving a sliding throttle valve downstream of the test section. The amplitude of the measured oscillating free-stream velocity was approximately 10 percent of the mean free-stream velocity.

Figures 4(a) and 4(b) show the computed amplitude and phase of velocity oscillations across the boundary layer for $x\omega/u_0 = 4.98$. The free-stream amplitude was set to 0.10 of the free-stream mean velocity. The computed periodic solutions were obtained in the fourth cycle of the oscillations using 64 time steps per cycle. A 99×75 grid was used over $Re_L \times Re_H = 142,000 \times 7,400$, where L and H are the width and height of the computation domain, respectively. The Reynolds numbers were evaluated for the mean free-stream condition. The present solutions compare well with measurements although the predicted phase profile lies slightly above the measurements as shown in Fig. 4(b). The present solution is almost indistinguishable from the finite-difference solution obtained by Lam [23] and also compares well with Lin's shear wave solutions [3]. The computed maximum amplitude, max-

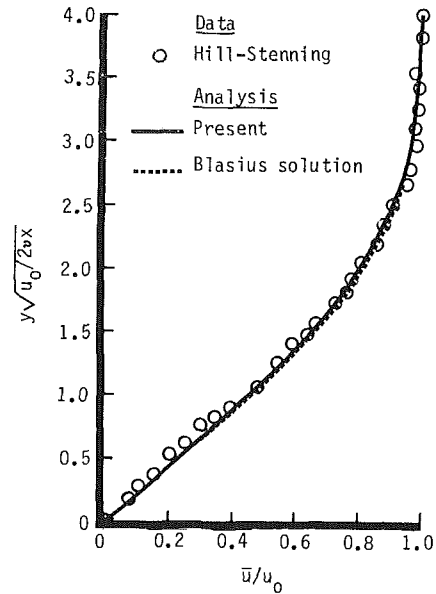


Fig. 5 Mean velocity profiles for oscillatory Blasius flow

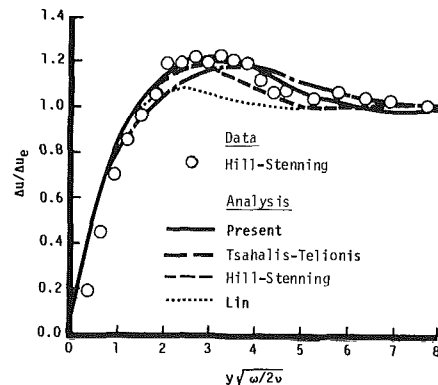


Fig. 6 Amplitude of oscillations in Howarth flow, $x\omega/\bar{u}_e = 3.16$, $bx/u_0 = 0.100$, $\Delta u_e/\bar{u}_e = 0.10$

imum phase lead, and maximum phase lag were 1.07 of the free-stream amplitude, 42.9 deg and 3.6 deg, respectively. Although the amplitude and phase shift inside the boundary layer vary significantly, the mean velocity seems to be unaffected by the oscillations as observed by Hill and Stenning [22]. Figure 5 shows excellent agreement between the computed mean velocity profile, the Blasius profile, and the measured data.

Oscillatory Flow Superimposed on Howarth Flow. The Howarth flow is a linearly retarded flow of the form

$$u_e(x) = u_0(1 - bx/u_0) \quad (19)$$

where u_0 is the free-stream mean velocity at the leading edge of the plate ($x = 0.0$); x , the distance along the plate; and b , a constant. Flow separation occurs at $bx/u_0 = 0.12$. When a small streamwise-uniform harmonic oscillation of free-stream velocity is superimposed on the mean flow, the velocity distribution on the boundary of a solid body has the form

$$u_e(x,t) = u_0(1 - bx/u_0) + \Delta u_0 \cos \omega t \quad (20)$$

Hill and Stenning [22] measured this type of laminar incompressible flow using the facility discussed previously.

Figure 6 shows the computed amplitude profiles at $bx/u_0 = 0.10$ for the characteristic frequency of $x\omega/u_e = 3.16$ compared with measured data by Hill and Stenning [22] and with available analytical/numerical solutions. The free-stream amplitude was set to 10 percent of the local mean free-stream

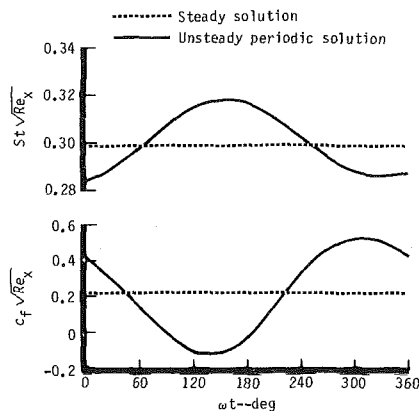


Fig. 7 Periodic variation of wall shear stress and Stanton number for incompressible oscillatory Howarth flow, $x\omega/\bar{u}_e = 3.16$, $bx/u_0 = 0.10$, $\Delta u_e/\bar{u}_e = 0.10$

velocity for the computation. The present solutions appear to agree more closely with the measured data than do the numerical or analytical solutions by Lin [3], Hill and Stenning [22], and Tsalhalis and Telionis [24]. Figure 7 shows the computed periodic solutions of wall shear stress and Stanton number, $St (= q_w/\rho_e C_p [T_e - T_w] u_e)$, at the same streamwise location. The wall shear stress indicates that a temporal flow reversal occurs periodically at $bx/u_0 = 0.10$ upstream of the steady separation point, $bx/u_0 = 0.12$. The Stanton number plotted in Fig. 7 is for incompressible flow. For the calculation, the wall temperature was arbitrarily set to 82.6 percent of the free-stream temperature. As can be seen in Fig. 7, the Reynolds analogy is no longer applicable to the unsteady flow. The phase of the wall shear leads the motion of the external stream while the wall heat transfer lags, in accordance with the analysis by Lighthill [2]. The computational grid used is 94×75 over $Re_L \times Re_H = 98,600 \times 6,600$, where the Reynolds numbers are evaluated for the mean free-stream condition; and L and H are the width and height of the computation domain, respectively. For each cycle of the oscillation 64 time steps were used.

Unsteady Incompressible Turbulent Boundary Layers. In this study, two unsteady incompressible turbulent flows, one measured by Karlsson [25] and another measured by Parikh et al. [26] were calculated. The flow measured by Karlsson is a uniform mean flow with a harmonic oscillation, while the flow studied by Parikh et al. is a linearly retarded mean flow with a harmonic oscillation. The characteristics of the freestream for these flows are:

(a) $\omega/2\pi = 0.33$ Hz, $\Delta u_e/\bar{u}_e = 0.14$ for the measurements by Karlsson [25]

(b) $\omega/2\pi = 0.25$ Hz, and $\Delta u_e/\bar{u}_e = 0.0$, $\partial(\bar{u}_e/u_0)/\partial x = 0.0$ if $x \leq 2.0$; and $\Delta u_e/\bar{u}_e = (x-2.0)/[12.0 - (x-2.0)]$, $\partial(\bar{u}_e/u_0)/\partial x = -1/12$ if $x > 2.0$ for the measurements by Parikh et al. [26].

Figures 8 and 9 compare the calculated amplitude profiles across the boundary layer for these flows with measured data as well as with other available solutions. The present solutions are found to agree very well with the experimental data. For Karlsson's measurements, the present solutions for both in- and out-of-phase components of amplitude also agree well with the numerical solution by Lam [23] and appear to be better than the solution obtained by Cebeci [15]. The present solutions are slightly below those obtained by Telionis and Romaniuk [27]. All the solutions shown in Fig. 8 except for those by Telionis and Romaniuk [27] utilized basically the same turbulence model. For the flow measured by Parikh et

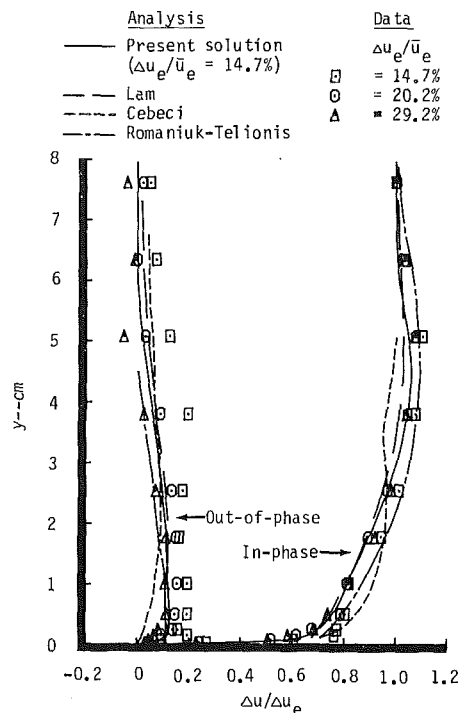


Fig. 8 Amplitude profiles for oscillating turbulent boundary layers with zero-streamwise mean pressure gradient; $\omega/2\pi = 0.33$ Hz

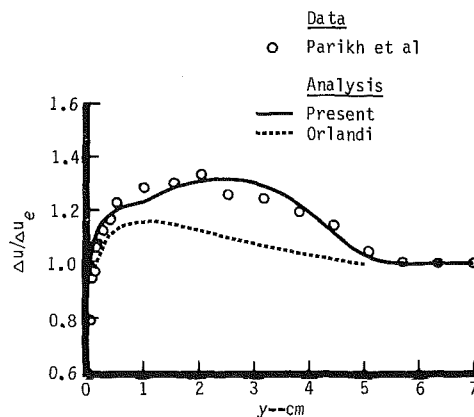


Fig. 9 Amplitude profiles for oscillating turbulent boundary layers with adverse streamwise pressure gradient; $\omega/2\pi = 0.25$ Hz

al. [26] the present results are found to be in much better agreement with the experimental results than the predictions of Orlandi [28] who used a higher-order turbulent kinetic energy transport equation model (see Fig. 9).

A 141×85 grid was used for the Karlsson case over $Re_L \times Re_H = (1.055 \times 10^6) \times (0.81 \times 10^5)$, where L and H are the width and height of the computation domain, and the Reynolds numbers are evaluated for the mean free-stream condition. The periodic solutions were achieved in four cycles using 128 time steps per cycle. For the Parikh et al. case, a 41×85 grid was used over $Re_L = 0.37 \times 10^6$ and $Re_H = 0.16 \times 10^6$, where L is the streamwise extent of the flow deceleration zone, H is the height of the computational domain, and the Reynolds numbers are evaluated for the free-stream condition at the leading edge. A 20 percent reduction of grid points in the normal direction was found to result in an insignificant change in the solution except for the region near the boundary-layer edge ($y = 3.5 \sim 5.0$ cm), where a relatively large grid spacing occurs. In that region, the maximum difference between the amplitudes computed with the original and a

coarser grids was approximately 1.68 percent. For the both cases, two cycles with 96 time steps per cycle were required to establish periodic solutions.

V Conclusion

An accurate finite-difference solution procedure has been developed for unsteady two-dimensional compressible boundary layer flow. The governing boundary layer equations for conservation of mass, momentum, and energy were written in primitive variables and solved in a fully coupled manner using a fully implicit finite-difference scheme. Such a coupled solution algorithm provides time accurate solutions and also overcomes the problem associated with obtaining a direct time-integration for the normal component velocity.

Several incompressible and compressible flows were computed with the present procedure. The computed results agreed very well with experimental data and other analytical/numerical solutions. In particular, for the flow with external harmonic oscillations, the mean flow was found to be generally unaffected by the free-stream fluctuations. For heat transfer, the Reynolds analogy is no longer applicable to flows with free-stream fluctuations. The temporal flow reversal was observed upstream of the steady separation point for the mean Howarth flow when harmonic oscillations were superimposed on the mean free-stream flow. For turbulent flow, a simple algebraic mixing length model was found to provide predictions in good agreement with experimental data for the cases considered in this study.

Acknowledgments

This research is sponsored by the Air Force Wright Aeronautical Laboratories/POTC, under Contract F33615-83-C-2339. The authors wish to express their gratitude to Dr. Charles MacAuthur (AFWAL/POTC), and Messrs. Donald Tipton and Stacy Thompson for their continued support and cooperation.

References

- 1 Moore, F. K., "Unsteady Laminar Boundary-Layer Flow," NACA TN 2471, 1951.
- 2 Lighthill, M. J., "The Response of Laminar Skin Friction and Heat Transfer to Fluctuations in the Stream Velocity," *Proc. Roy. Soc.*, Vol. 224A, 1954, pp. 1-23.
- 3 Lin, C. C., "Motion in the Boundary Layer with a Rapidly Oscillating External Flow," *Proc. 9th Int. Congr. Appl. Mech.*, Brussels, Vol. 4, 1956, pp. 155-169.
- 4 Stuart, J. T., "Unsteady Boundary Layers," in *Recent Research of Unsteady Boundary Layers*, ed. E. A. Eichelbrenner, Vol. 1, 1971, pp. 1-46.
- 5 Telionis, D. P., "Calculations of Time-Dependent Boundary Layers," in *Unsteady Aerodynamics*, ed. R. B. Kinney, Vol. 1, 1975, pp. 155-190.
- 6 Riley, N., "Unsteady Laminar Boundary Layers," *SIAM Review*, Vol. 17, 1975, pp. 274-297.
- 7 Wirz, H. J., "Computation of Unsteady Boundary Layers," *Lecture Notes in Physics, No. 41, Progress in Numerical Fluid Dynamics*, ed. H. J. Wirz, Springer-Verlag, Berlin, 1975, pp. 442-476.
- 8 Telionis, D. P., "REVIEW - Unsteady Boundary Layers Separated and Attached," *ASME JOURNAL OF FLUIDS ENGINEERING*, Vol. 101, 1979, pp. 29-43.
- 9 McCroskey, W. J., "Some Current Research in Unsteady Fluid Dynamics - the 1976 Freeman Scholar Lecture," *ASME JOURNAL OF FLUIDS ENGINEERING*, Vol. 99, 1977, pp. 8-38.
- 10 King, W. S., "Low-Frequency, Large-Amplitude Fluctuations of the Laminar Boundary Layer," *AIAA Journal*, Vol. 4, No. 6, 1966, pp. 994-1001.
- 11 Vimala, C. S., and Nath, G., "Unsteady Laminar Boundary Layers in a Compressible Stagnated Flow," *J. Fluid Mechanics*, Vol. 70, Part 3, 1975, pp. 561-572.
- 12 Telionis, D. P., and Gupta, T. R., "Compressible Oscillating Boundary Layers," *AIAA Journal*, Vol. 15, No. 7, 1977, pp. 974-983.
- 13 Kim, J. S., and Chang, K. S., "Calculation of Incompressible and Compressible Unsteady Boundary Layers by a Noniterative Finite Difference Method," AIAA paper No. 84-1639, 1984.
- 14 Kwon, O. K., and Pletcher, R. H., "Prediction of Sudden Expansion Flows Using the Boundary Layer Equations," paper presented at ASME Fluids Engineering Conference, Houston, Texas, June 20-23, 1983.
- 15 Cebeci, T., "Calculation of Unsteady Two-Dimensional Laminar and Turbulent Boundary Layers with Fluctuations in External Velocity," *Proc. Roy. Soc. London, A*, 355, 1977, pp. 225-238.
- 16 Anderson, D. A., Tannehill, J. C., and Pletcher, R. H., *Computation Fluid Mechanics and Heat Transfer*, Hemisphere Publishing Corporation, Washington, 1984.
- 17 Eckert, E. R. G., and Drake, R. M., *Analysis of Heat and Mass Transfer*, McGraw-Hill, New York, 1972.
- 18 White, F. M., *Viscous Fluid Flow*, McGraw-Hill, 1974.
- 19 Hall, M. G., "The Boundary Layer Over an Impulsively Started Flat Plate," *Proc. Roy. Soc.*, Vol. 310A, 1969, pp. 401-414.
- 20 Reddy, K. C., Sickles, W. L., and Yalamanchil, R., "Computation of Unsteady Boundary Layers," in *Unsteady Aerodynamics*, ed. R. B. Kinney, Vol. 1, 1975, pp. 221-244.
- 21 Mirels, H., "Boundary Layer Behind Shock or Thin Expansion Wave Moving into Stationary Fluid," NACA TN 3712, 1956.
- 22 Hill, P. G., and Stenning, A. H., "Laminar Boundary Layers in Oscillating Flow," *ASME Journal of Basic Engineering*, Vol. 82, 1960, pp. 593-608.
- 23 Lam, C. Y., "Unsteady Laminar and Turbulent Boundary Layer Computations using a Difference Method," Ph.D. thesis, University of London, London, 1983.
- 24 Tsahalis, D. T., and Telionis, D. P., "Oscillating Laminar Boundary Layers and Unsteady Separation," *AIAA Journal*, Vol. 12, No. 11, 1974, pp. 1469-1476.
- 25 Karlsson, S. K. F., "An Unsteady Turbulent Boundary Layer," *J. Fluid Mechanics*, Vol. 5, 1959, pp. 622-636.
- 26 Parikh, P. G., Reynolds, W. C., and Jayaraman, R., "On the Behavior of an Unsteady Turbulent Boundary Layer," paper presented at the Symposium on Numerical and Physical Aspects of Aerodynamic Flows, Long Beach, California, Jan. 19-21, 1981.
- 27 Telionis, D. P., and Romaniuk, M. S., "Turbulence Models for Oscillating Boundary Layers," AIAA paper 79-0069.
- 28 Orlandi, P., "Unsteady Adverse Pressure Gradient Turbulent Boundary Layers," *Unsteady Turbulent Shear Flows*, edited by R. Michel, J. Cousteix, and R. Houdeville, Springer-Verlag, New York, 1981, pp. 159-170.

Some Observations of Flow Patterns and Statistical Properties of Three Component Flows

H. K. Kytömaa¹

C. E. Brennen

Department of Mechanical Engineering,
California Institute of Technology,
Pasadena, Calif. 91125

Vertical air-water flows, solids-water flows and three component air-solids-water flows were investigated in a Three Component Flow Facility. Visual observations of the flow patterns show that three component flows undergo transition and can exhibit strong unsteady vortical motions. Measurements of the fluctuations in cross-sectionally averaged volume fraction measurements were made. The statistical properties of the fluctuations are presented in terms of their amplitude and coherent time scale in the form of the Signal To Noise Ratio (STNR) and the Time Constant (ξ), respectively. Remarkably, the solids-water flows and the dispersed bubbly air-water flows exhibit almost identical values of STNR for the same volume fraction. Equally remarkable in the linear relationship between the Time Constant and the mean bubble or particle velocity; this relationship is found to have the same constant of proportionality for both species in the well behaved disperse regime. In the two-component churn-turbulent and the three-component agitated vortical regimes, the variables ξ and STNR significantly deviate from their dispersed regime values. The onset of large coherent structures characteristic of these regimes is reflected by a rise in the amplitude of the fluctuations and a marked increase in their coherent time scale. The results of this study demonstrate the large information content in the fluctuations of the measured quantity, both as a flow regime indicator and as a measure of flow quantities in two- and three-component flows.

1 Introduction

The discrete nature of multi-component flows is well known to be the cause of fluctuations in measured flow quantities. The statistics of these fluctuations depend on the structure and spatial distribution of the discrete phase. A number of investigators have indeed demonstrated direct relationships between flow properties and the statistics in the measured "noise" that have allowed the extraction of information from the observed fluctuations. For example, the fluctuating component of the pressure drop in a two-phase flow through an orifice was used to derive the flow rates of the components by Ishagai et al. (1965). Jones and Zuber (1975) used the probability density function of X-ray attenuation volume fraction signals as a flow pattern discriminator for vertical bubbly, slug and annular flows. Bernier (1981) used the inherent noise of resistive volume fraction signals in his experimental analysis of kinematic wave propagation in bubbly flows. The significance of the statistical properties of volume fraction measurements depends entirely on the size of the influence volume of the measuring device. For example, hot wire anemometers, optical probes and other devices have been employed to make

point measurements of volume fraction. To obtain useful information, time averaging of the output is necessary. This limits the dynamic resolution of such a device. On the other hand, X-ray and Gamma-ray attenuation techniques inherently carry out line averages along the beam. Capacitive and resistive measuring techniques yield a volume average of concentration. The size and shape of the measuring volume is determined by the geometry of the electrodes. With a large averaging volume, good dynamic response is achieved at the cost of diminished spatial resolution.

In this study we exploit the fluctuation in the measured volume fraction signal to investigate the structure of two- and three-component flows as they undergo transition from a uniform to an agitated regime. We demonstrate that the fluctuations in the signal can be used to measure flow quantities. The flows considered consist of air bubbles (average diameter of 4 mm) and polyester particles (average diameter 3 mm) in a continuous medium of water. Real time volume fraction measurements were made using an Impedance Volume Fraction Meter (IVFM) (Bernier (1981), Kytömaa (1986)).

The fluctuations in the volume fraction signal are characterized by two properties of their auto-correlation function; its amplitude and "width" (coherent time scale). These two quantities are easily measured and are useful characterizations of the flow structure. The visual observations of the transition of two- and three-component flows are related to these statistics. The results suggest a non-intrusive method of

¹Present address: Department of Mechanical Engineering, Massachusetts Institute of Technology, Cambridge, Mass. 02139.

Contributed by the Fluids Engineering Division of the THE AMERICAN SOCIETY OF MECHANICAL ENGINEERS and presented at the International Symposium on Slurry Flows, ASME Winter Annual Meeting, Anaheim, Calif., December 7-12, 1987. Manuscript received by the Fluids Engineering Division June 13, 1986; revised manuscript received March 25, 1987.

measuring disperse flow quantities, namely the total volume fraction and velocity, for two- and three-component flows.

In the work presented here, Reynolds numbers of 1000 and 400 were measured for individual bubbles and particles respectively based on relative velocity. These values are significantly higher than the Reynolds numbers in other three-component flow studies by Fessas and Weiland (1981) and Batchelor (1986). Flow regime transitions were nevertheless observed in all these studies.

2 Experimental Facility and Instrumentation

The Three Component Flow Facility (TCFF) shown in Fig. 1 was used to study the statistical properties of volume fraction signals in bubbly, slurry and three component flows. The test section is a vertical clear acrylic pipe .1016 meters (4 in.) in diameter and 2.2 meters in length. The air-water flows are formed by introducing the gas through an injector situated inside the vertical pipe, .5 meters below the test section. The injector consists of an array of twelve 3.2 mm (1/8 in.) diameter brass tubes perforated with .4 mm (1/64 in.) holes. An 8 atm (120 psi) compressed air line supplies the injector through a regulator, an orifice plate flow meter (to monitor air mass flow), valves to control air flow and a manifold to distribute the air flow evenly among the brass tubes. The slurry flows studied consist of water and polyester particles. The polyester particles are of the type used for molding applications (specific gravity = 1.43). They are smooth and have a cylindrical shape with an equal mean height and diameter of 3 mm ($\pm .5$ mm). The most novel aspect of the facility is its ability to handle solids and to control their flow rate independently of the liquid without having to add or remove solids from the system. When at rest prior to an experiment the solids are trapped between a vertical 4 inch control cylinder and the storage hopper (see Fig. 1). As the control cylinder is raised from the reducer on top of which it sits, the gap created allows particles to enter the test section under the action of gravity. The vertical position of the control cylinder can be varied by means of a control rod attached to a worm gear mechanism and this permits the solids flow rate to be controlled by varying the gap between the cylinder and the reducer. To recycle the solids after an experiment the control cylinder is lowered to the closed position and sufficient upward water flow is generated to fluidize the solids in the lower tank and to carry them back to the upper tank where they settle into their original position.

The static pressure gradient in the test section is monitored using an inductive differential pressure transducer. The volume fraction of the dispersed medium is measured using an Impedance Volume Fraction Meter (IVFM). The IVFM was

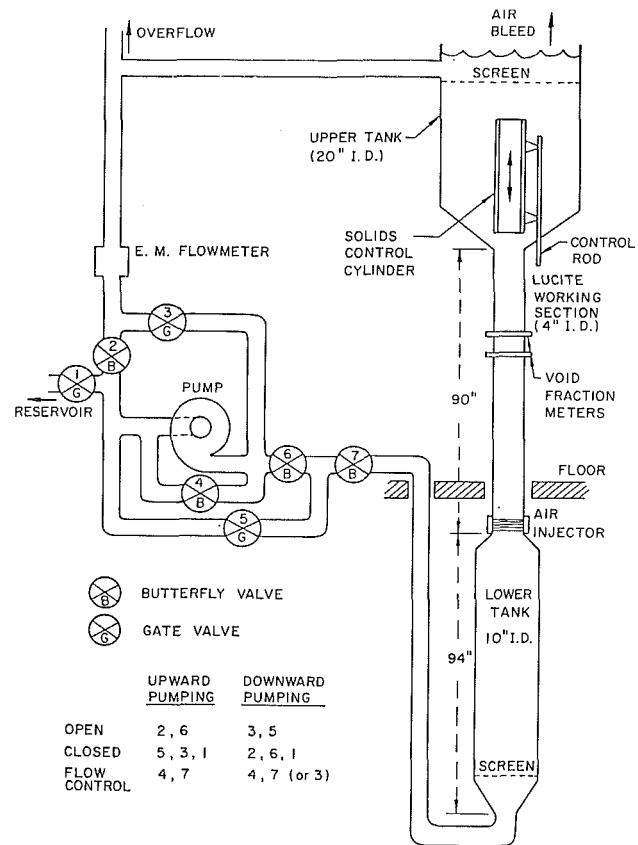


Fig. 1 Schematic of the Three Component Flow Facility

developed by Bernier (1981). It has been modified for temperature compensation and now has a shielded electrode configuration which decreases the axial extent of the influence volume over which the measurement is carried out. The active stainless steel electrodes which are flush mounted into a section of .1016 meter (4 in.) diameter non-conducting acrylic pipe are 6.4 mm in axial length and form diametrically opposed 90 degree arcs on the circumference of the pipe. The active electrodes are each sandwiched between two shielding electrodes. These are 9.5 mm in axial length and also form 90 degree arcs. Figure 2 shows the electrode configuration. The shielding electrodes duplicate the active electrode potential through a high input impedance voltage follower. The IVFM is excited at an amplitude of .3 volts r.m.s. and a frequency of

Nomenclature

ACF = Auto-Correlation Function of the random fluctuations in the volume fraction signal, (V^2)
 j = total volume flux, (m/s)
 j_g = gas volume flux, (m/s)
 j_p = solids volume flux, (m/s)
 j_{pj} = solids drift flux, (m/s)
 L = vertical separation between pressure taps, (m)
 Δp = hydrostatic pressure difference in a three-component mixture between the pressure taps, relative to that in water, (N/m^2)

$R_{\bar{v}\bar{v}}$ = Auto-correlation Function of the random, fluctuations in the volume fractional signal, (V^2)
 STNR = signal to noise ratio of the volume fraction signal, (m/s)
 v_g = mean gas velocity, (m/s)
 v_l = mean liquid velocity, (m/s)
 v_p = mean solids velocity, (m/s)
 $v_{g(pl)}$ = mean gas velocity relative to the combined solids and liquid volume flux, (m/s)
 \bar{V} = mean value of the volume fraction signal, (V)

\bar{V} = fluctuating component of the volume fraction signal, (V)
 α = volume fraction of gas (%)
 ν = volume fraction of solids, (%)
 ρ_g = gas density, (kg/m^3)
 ρ_l = liquid density, (kg/m^3)
 ρ_p = solids density, (kg/m^3)
 $\tau_{1/2}$ = time at which the ACF has decayed to half of its maximum value, (s)
 ξ = time constant of coherence in the random fluctuations of the volume fraction signal

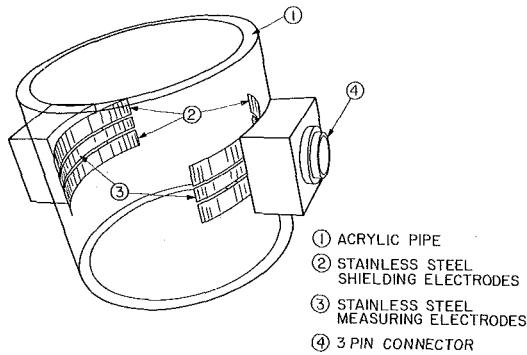


Fig. 2 Isometric view of the shielded Impedance Volume Fraction Meter electrode geometry

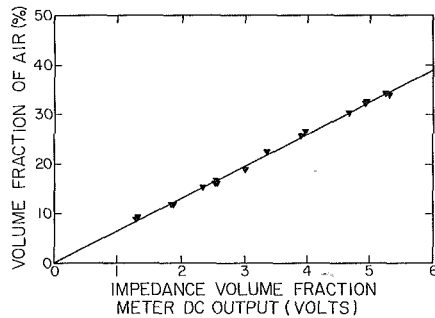


Fig. 3 Steady state calibration of the Impedance Volume Fraction Meter with bubbly flows for zero water volumetric flux. The volume fraction was derived from the hydrostatic pressure gradient measurement.

40 KHz at which the impedance is found to be primarily resistive. The excitation and signal processing equipment is described in more detail by Bernier (1981). The IVFM is calibrated with both bubbly and particulate flows against the volume fraction (α and ν , respectively) obtained from the static pressure gradient measurement. These two plots are shown in Figs. 3 and 4. Equations (1) and (2) are the respective linear regression fits of the shown plots. The corresponding correlation coefficients for these fits are .9992 and .997. The discrepancy between the two fits (up to 4 percent) is attributed to experimental error in the measurement.

$$\alpha(\%) = 6.53 \text{ IVFM(Volts)} - .006 \quad (1)$$

$$\nu(\%) = 6.77 \text{ IVFM(Volts)} - .41 \quad (2)$$

The IVFM is found to have excellent linearity up to the volume fractions of at least 40%. With a sensitivity of .15 Volts per percent of volume fraction, and the passage of individual bubbles (or particles) is readily detectable.

3 Experimental Procedure and Presentation of Results

After initiation of each experiment, data were not taken for 30 seconds in order to permit passage of the initial transient. Then observations of the flow pattern were made. For each run, measurements were made of the air flow rate (using the orifice meter), the liquid flow rate (measured with an electromagnetic flow meter). The total flow rate was constrained by flooding of either the solid or the gas phase and the total flux was restricted to the range of $-.1$ m/s to $.2$ m/s. The IVFM d.c. output and the static pressure transducer output were monitored on a strip chart recorder. In two component flows, ν , the solids volume fraction or α , the air volume fraction is directly obtained from the IVFM. At low flow rates α or ν is also given by the output of the differential pressure transducer since the frictional component of the pressure drop is very small. Indeed this is how the calibration equations (1) and (2) were obtained. In a three-component flow at low flow

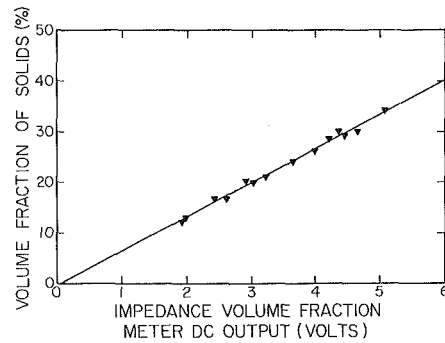


Fig. 4 Steady state calibration of the Impedance Volume Fraction Meter with particulate flows for zero total zero total volumetric flux. The volume fraction was derived from the hydrostatic pressure gradient measurement.

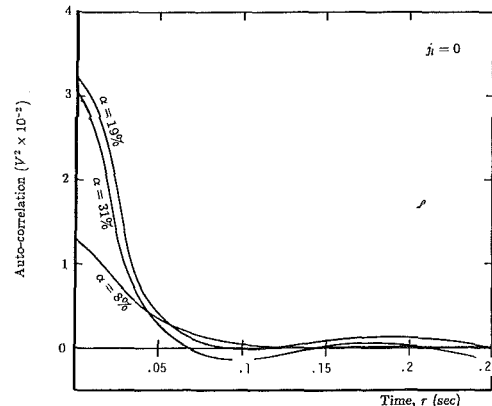


Fig. 5 Typical auto-correlograms of the IVFM output fluctuations in a steady bubbly flow regime obtained from the HP 3562 Digital Signal Processor for a 60 second record

rates, the differential static pressure transducer yields the bulk density which is a function of the individual volume fractions of air and solids. The mean IVFM d.c. output gives the sum of the air and solid volume fractions. Thus we can deduce the concentration of the individual constituents.

The IVFM a.c. component was recorded on magnetic tape through a d.c. blocking amplifier with a 3dB cut off frequency of .032 Hz and a fall off slope at 10 dB per octave. The record length was five minutes whenever possible. The shortest record was of one minute which proved adequate for accurate determination of IVFM output fluctuation statistics.

The size distribution of a multicomponent flowing medium influences the statistical properties of the fluctuating component of volume fraction signals. For example, for two flows of equal volume fraction, the one with large particles will yield less frequent and larger fluctuations in the measurement than the one with very small particles. In this paper we used the properties of the Auto-Correlation Function (ACF) of the IVFM output fluctuations to characterize the flow. Typical ACF records are shown in Fig. 5. The two dominant features of the AFC are a) its amplitude ($R_{\bar{v}\bar{v}}(0)$) which is the mean square magnitude of the fluctuations, and b) the time at which the function has decayed to a certain fraction of its peak value. The latter is interpreted as a measure of the coherent time scale. These two quantities were used to characterize the structure of a variety of two- and three-component flows. The amplitude ($R_{\bar{v}\bar{v}}(0)$) is presented in terms of the dimensionless Signal To Noise Ratio (STNR), and the coherent time scale is presented in terms of the time constant ξ ; these variables are defined below:

$$\text{STNR} = \frac{\bar{V}}{\sqrt{R_{\bar{v}\bar{v}}(0)}}, \quad (3)$$

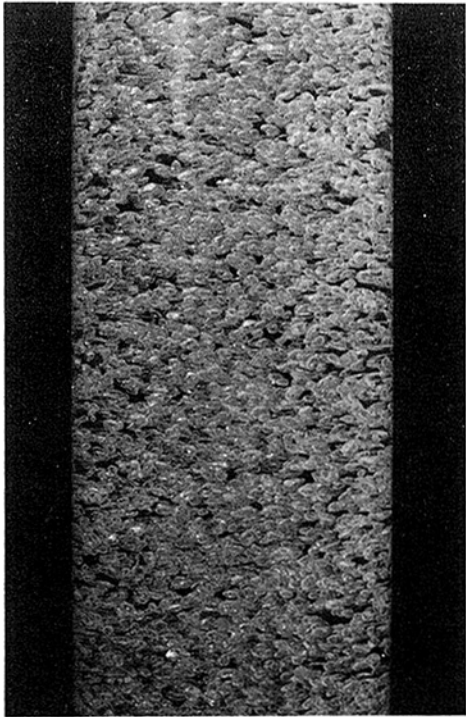


Fig. 6 Bubbly-air water flow of 8 percent volume fraction

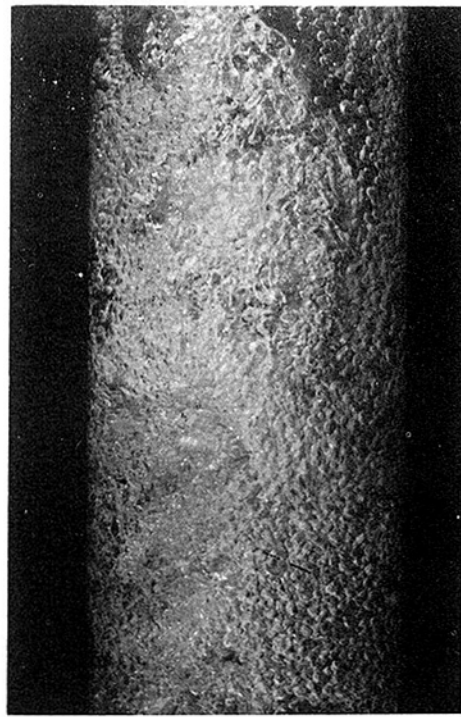


Fig. 7 Churn-turbulent air-water flow of 37 percent volume fraction

where \bar{V} is the mean d.c. IVFM output voltage, and

$$\xi = 1.6783/\tau_{1/2}, \quad (4)$$

where $\tau_{1/2}$ is the time at which the ACF has decayed to half of its maximum value. A Hewlett Packard 3562 spectral analyser was used to obtain the Auto Correlation Functions (ACF) of IVFM output fluctuations. A chosen ensemble length of one second proved to be adequate to give a repeatable ensemble averaged ACF records. Simultaneous visual observations were made of the nature of the flows and the flow pattern. Measurements of time constants ξ and the STNR are related below to the disperse medium volume fraction and mean velocity, and observations of the flows.

4 Air-Water Flows

The air-water flows are created by injecting air bubbles into water. At low air volume fractions, the resulting two-component medium consists of a homogeneous distribution of bubbles with a photographically measured average bubble size of 4 mm and a deviation of up to .5 mm from the mean. The flow remains uniform up to a volume fraction of approximately 42 percent. This type of flow is known as the dispersed bubbly flow, an example of which is shown in Fig. 6. As the flow rate of the injected air is increased, the two-component medium becomes intermittently agitated and the formation of large bubbles becomes visible. This flow is said to be churn-turbulent. A photograph of such a flow (Fig. 7) shows the presence of large bubbles. Transition from bubbly flow to churn-turbulent is observed to happen more suddenly than the change in the opposite direction. An initially churn-turbulent flow takes of the order of minutes to settle down to a bubbly state when the air of the initially agitated medium is decreased. The change in regime has the notable effect of preventing the volume fraction from ever rising above 45.

The structure of these air-water flows is characterized using the statistics of the fluctuations of measured volume fraction signals. Two statistical criteria are used, namely the Signal To Noise Ratio (STNR) which is the ratio of the d.c. IVFM output and the amplitude of the fluctuations, and the time constant, ξ , which is inversely proportional to the coherent time

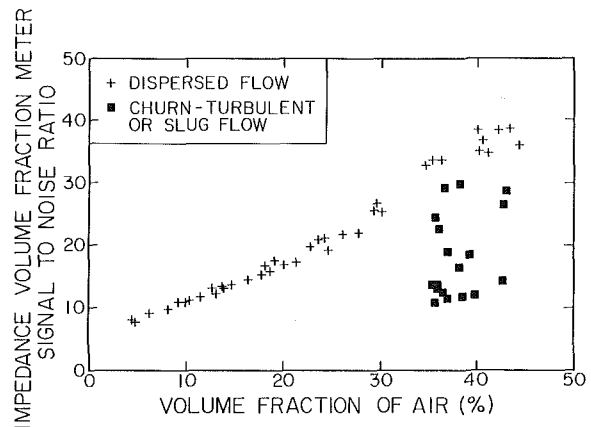


Fig. 8 Signal To Noise ratio of the Impedance Volume Fraction Meter output for bubbly and churn-turbulent flows

scale of the "noise." These variables were derived from experimentally obtained auto-correlation records of the fluctuating signal.

The Signal To Noise Ratio (STNR) of the IVFM was found to behave in two distinct ways depending on whether the flow is bubbly or churn-turbulent. In bubbly air-water flows, the STNR rises monotonically as the volume fraction is increased up to 45 percent. Upon additional air injection, a sudden drop in STNR is experienced along with a slight decrease in volume fraction as shown in Fig. 8. The drop in STNR coincides with the formation of slugs of air present in churn-turbulent flows. The accompanying drop in void fraction is caused by the increase in the mean relative velocity and the preservation of continuity at the air flow rate at which transition occurs. Thus there are two stable values of signal to noise ratio for volume fractions between 35 and 45 percent.

The time constant, ξ , in bubbly flows is found to be linearly proportional to the mean bubble velocity, v_b . This quantity is derived from the measured air flux j_g and its volume fraction, α using the following equation:

$$v_g = \frac{j_g}{\alpha} \quad (5)$$

The results for the time constant, ξ , are shown in Fig. 9 plotted against the mean air velocity. The bubbly flow results are indicated by the encircled points. These all fall on a straight line (slope $\approx 370 \text{ m}^{-1}$ and zero vertical axis intercept). In other words, the coherent time scale of fluctuations caused by the passage of individual bubbles past the IVFM electrodes is found to be linearly proportional to their average residence time in the field of influence of the device (the electric field caused by the electrodes). However, at onset of churn-turbulence, the magnitude of the time constant decreases sharply by an order of magnitude. This decrease is indicative of the formation of large structures in the agitated flow regime. Constant liquid flux curves assume a "C" shape; four such curves are presented. For a constant liquid flux, the lower volume fraction flows exhibit higher values of ξ since bubble interactions cause their terminal velocity to decrease with volume fraction. The marked decrease in ξ caused by the onset of churn-turbulence occurs as the air volume fraction is increased above its critical value of approximately 42 percent. Points on the vertical part of the constant liquid flux curves are considered to be transitional, and points on the rising lower branch of these curves are considered "fully developed." Churn-turbulent data are presented on a separate

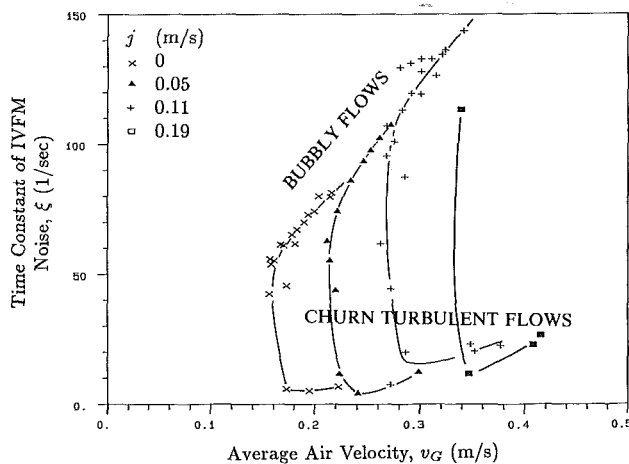


Fig. 9 Time constant ξ (reciprocal of the coherent time scale) of the fluctuating IVFM output signal in bubbly and churn-turbulent flows versus the average air velocity. Note the dramatic drop in ξ on onset of churn-turbulence.

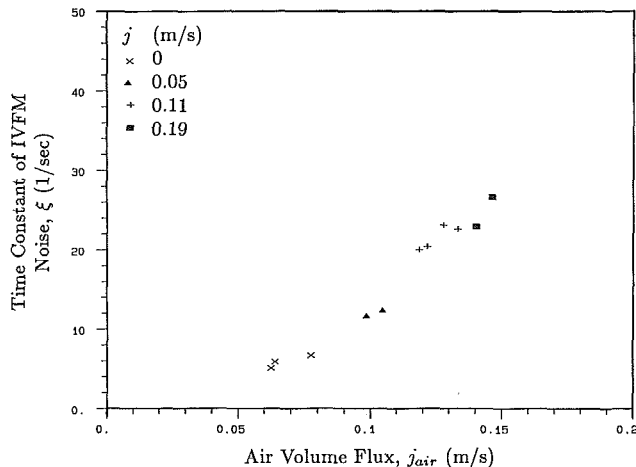


Fig. 10 Time constant ξ of the fluctuating IVFM signal in fully developed churn-turbulent flows versus the air volumetric flux, showing all points on the one curve with little scatter

graph. Values of ξ for fully developed churn-turbulent flows are plotted versus the air flux j_g in Fig. 10. The curve displays a monotonic increase of the time constant with air flux with less scatter than the corresponding points in Fig. 9.

These findings demonstrate the rich information content in the noise of the measured volume fraction signal. The STNR is a dimensionless quantity, and it is independent of the sensitivity (gain) of the measuring device (in our case the IVFM). The consistent relationship between the STNR and volume fraction for bubbly flows indicates a possible method of monitoring volume fraction using the STNR in situations where the

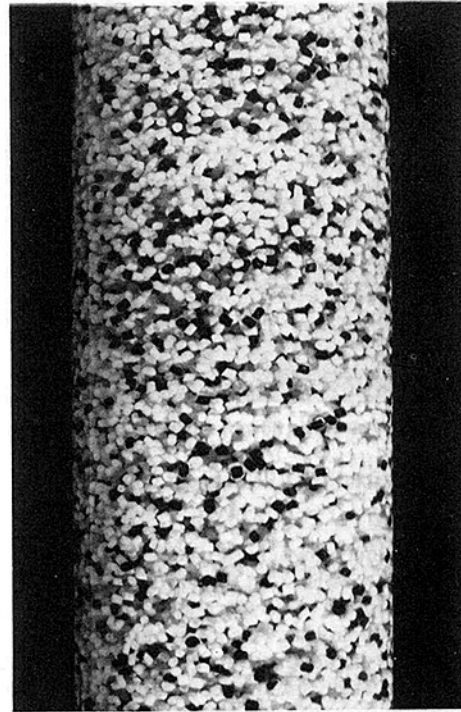


Fig. 11 Dispersed solids-water flow of 12 percent volume fraction

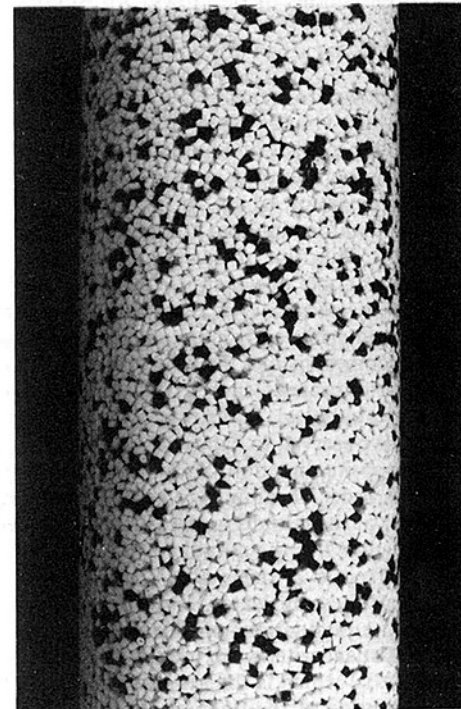


Fig. 12 Solids-water plug flow of 55 percent volume fraction

recalibration of the monitoring device is not convenient or is impossible. The STNR, used in conjunction with the volume fraction provides a flow regime delimiting tool capable of differentiating between bubbly and churn-turbulent flows. The obtained values of the time constant, ξ , suggest that it could be used to determine the mean air velocity and flux of both bubbly and churn-turbulent flows in a non-intrusive fashion. The magnitude of ξ is also found to be sensitive to the flow regime and thus a good indicator of it.

5 Solid-Liquid Flows

The solid-liquid flows studied consist of polyester particles of an average diameter of 3 mm. These flows do not display any distinct change in flow regime and remain disperse for the range of total volume flux considered (0–.24 m/s) and volume fractions of up to 60 percent. Figure 11 shows a disperse solids-water flow of 12 percent volume fraction. At large volume fractions, the particles are no longer able to move relative to one another and they appear to translate as a solid plug inside the pipe. Such a plug flow is shown in Fig. 12.

We take advantage of the absence of instability in solids-water flows to investigate whether the useful results for disperse bubbly flows hold for particulate flows. Namely that the STNR can be used as a measure of total volume fraction and that the time constant ξ is linearly proportional to the average disperse medium velocity.

Particle flow STNR values are shown versus the volume fraction of solids in Fig. 13. All STNR values fall on a single monotonically increasing curve. Remarkably, this curve coincides with the bubbly flow curve (deviations are within the present experimental scatter), despite the difference in diameter between the particles and bubbles. Measured values of ξ are presented versus volume fraction for different total fluxes in Fig. 14. In the solid-liquid flows, ξ behaves linearly with respect to the particle velocity v_p . It gradually decreases with v for constant total flux (the settling velocity decreases with increased volume fraction) and for a given value of v , the higher the total flux the larger the resulting ξ .

In the present experimental facility, we have no direct means of evaluating the particle flow rate or speed. An indirect method was devised for this purpose. We determined the particle Drift Flux Curve from kinematic shock speed measurements, and then used this result to determine the particle velocity for comparison. The estimate of the solids average velocity is given by

$$v_p = \frac{j_{pj}}{\nu} + j, \quad (6)$$

which is derived directly from the definition of the drift flux.

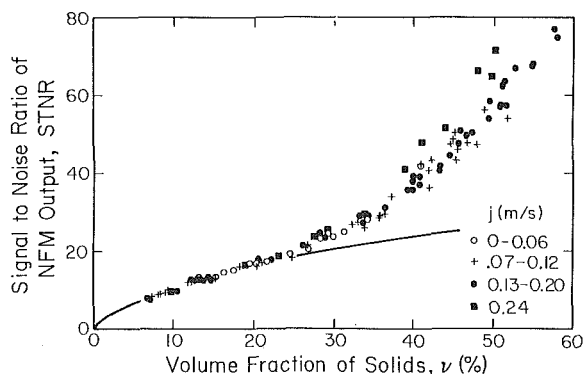


Fig. 13 Signal To Noise ratio of IVFM output for particle flows of different total fluxes plotted against the volume fraction of solids. Also shown is the theoretical half power curve. The results deviate from this at an approximate volume fraction of 25 percent.

The velocity given by equation (6) is not an exact measure since $j_{pj}(v)$ was derived for zero total flux, and it is now applied to non-zero flowrates. However, for the maximum total flux considered (.25 m/s which corresponds to $Re = 25 \times 10^3$) the error in the disperse medium velocity is small. Experiments to measure ξ were carried out for volume fractions ranging from 6 to 55 percent. The results, presented in Fig. 14, show that the time constant, ξ , is indeed linearly proportional to the mean particle velocity, and the constant of proportionality is almost exactly the same as for bubbly flows. Therefore the suggested method based on the determination of the characteristic coherent time scale of the IFVM “noise” can truly be used as a non-intrusive measurement of the disperse medium velocity with the maximum error of ± 25 percent of the measurement for the lower velocities considered.

6 Gas-Solid-Liquid Three-Component Flows

Three component flows consisting of polyester particles (3 mm diameter) and air bubbles (uncoalesced diameter of 4 mm) in a continuous medium of water were investigated for low total fluxes ($j < .06$ m/s), and total volume fractions up to 50 percent.

At the flow rates considered, the pressure gradient in the vertical test section is predominantly hydrostatic. Thus, neglecting the wall effect at these low flow rates, the pressure gradient is linearly proportional to the bulk density which is a function of the volume of the individual constituents. We measure the pressure gradient in the medium using a differential pressure transducer between two taps located a distance $L = 1.694$ m apart. The lines leading to the device are filled with water; therefore the measurement is relative to the hydrostatic pressure difference in water over the same height. Hence, the device output pressure can be presented as a linear combination of the disperse medium volume fractions:

$$\Delta p = \rho_l L [\nu(\rho_p - \rho_l) - \alpha(\rho_l - \rho_g)]. \quad (7)$$

where ν is the volume fraction of solids and α the volume fraction of air. The mean IVFM output gives the sum of the air and solid volume fractions. Since the material constants in (7) are known, the volume fractions can therefore be computed from the two measurements.

6.1 Three-Component Flow Pattern Observations. One of the distinctive characteristics of the three component flows is the dramatic increase in the level of audible noise caused by particle impacts against one another and against the pipe wall. This was found to be true for all volume fractions of air and solids. It is interpreted as a consequence of the increase in the

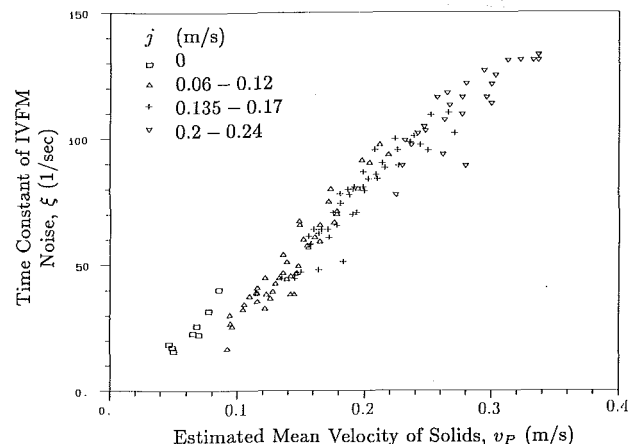


Fig. 14 Time constant ξ of the fluctuating IVFM signal in solids-water flows versus an estimate of the average particle velocity based on the drift flux model

disperse medium pressure caused by bubble-particle interactions. This effect is consistent with the enhanced erosive property of three component flows.

At low volume fractions ($\alpha, \nu < 17$ percent) the flows are dispersed and well behaved. The small scale of the structure is revealed in a time lapse photograph of such a flow in Fig. 15. However, a flow regime transition was observed above a certain combination of volume fraction values. Above this threshold, the homogeneous three-component distribution is observed to become unstable and is replaced by an unsteady flow regime with vortical structure; this is called the agitated vortical regime. Regime transition is observed to take place at solid and air volume fractions of approximately 17 percent. The vortices created have the same typical size as the pipe diameter (4 in.). This is seen in a time lapse photograph in Fig. 16. At high solid fractions the air flow is hardly visible, indicating that the bubbles tend to flow in the central region of the pipe. At larger air flow rates, groupings of air bubbles and slugs do however become visible, typically in the center of vortices. Thus, there exists a segregation effect of the vortices on the dispersed components. A flow regime map is presented in Fig. 17 showing the prevalence of dispersed flows at lower volume fractions of both bubbles and solids, and the onset of agitated flows at higher values.

6.2 Average Air Velocity in a Three-Component Flow. The average air velocity v_g in the three-component flows studied was computed from the total air flux j_g and the calculated air volume fraction α .

$$v_g = \frac{j_g}{\alpha} \quad (8)$$

We now introduce the average air velocity relative to the combined flux of liquid and solids, $v_{g(pl)}$, which is defined by:

$$v_{g(pl)} = v_g - j_p - j_l \quad (9)$$

The velocity $v_{g(pl)}$ indicates the extent of flow interference between the bubbles and the liquid-solid medium. This quantity is plotted in Fig. 18 against the total volume fraction of the

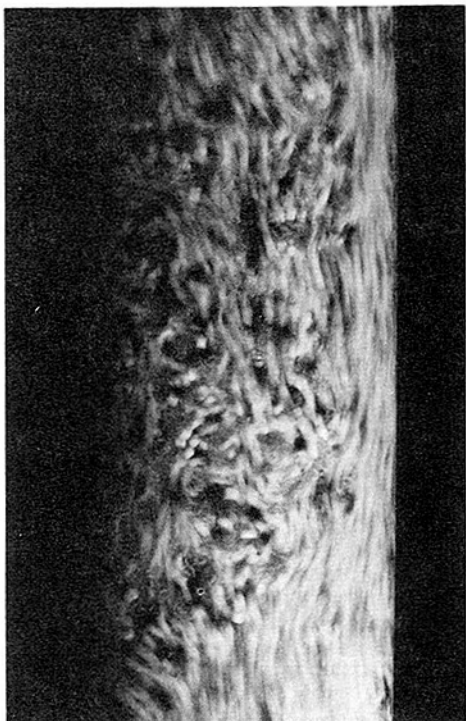


Fig. 15 Three component flow of 12 percent solids volume fraction and 15 percent air volume fraction, showing the small scale structure of disperse flow. 1/30 second exposure was used.

medium ($\alpha + \nu$). It can be seen that flows which do not exhibit large vortical structure have small relative gas velocities, less than .05 m/s at total volume fractions between 15 and 30 percent. After transition, the relative velocity in the agitated flows rises sharply up to about .35 m/s. This sudden increase in the relative velocity is characteristic of a change in regime as was shown by a number of investigators for air-water flows (these results are summarized by Wallis (1969) in his book). In their low Reynolds number work on suspensions, Fessas and Weiland (1981) observed similar behavior in the settling velocity of heavy particles in a bidisperse medium. They present the settling velocity of one species as a function of the concentration of the other, with the concentration of the first as a parameter. The curves display the same initial decrease that we find followed by a sharp increase after a minimum value is reached. Visual observation of their sedimenting flows revealed segregation of species into vertical fingers subsequent to the regime change. This is in contrast to

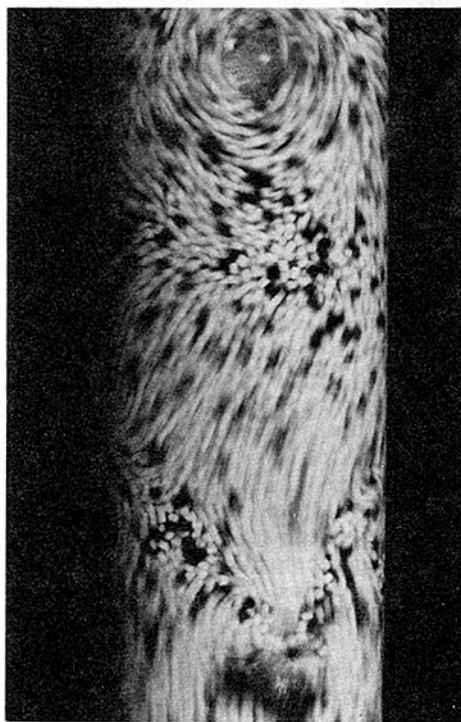


Fig. 16 Three component flow of 30 percent solids volume fraction and 15 percent air volume fraction, showing large vortex structure. 1/30 second exposure was used.

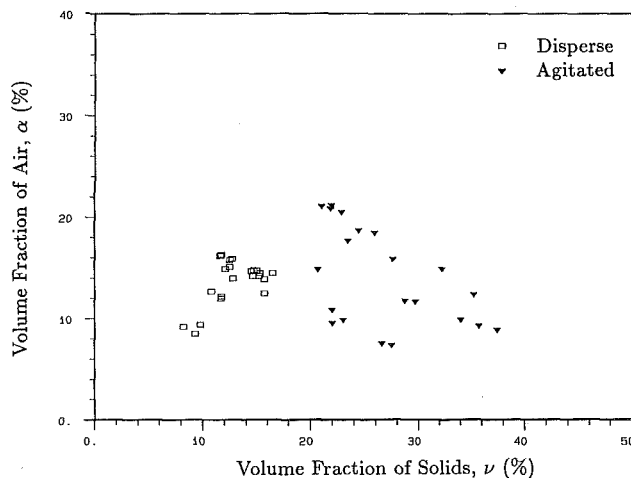


Fig. 17 Flow regime map of three component flows based on visual observation

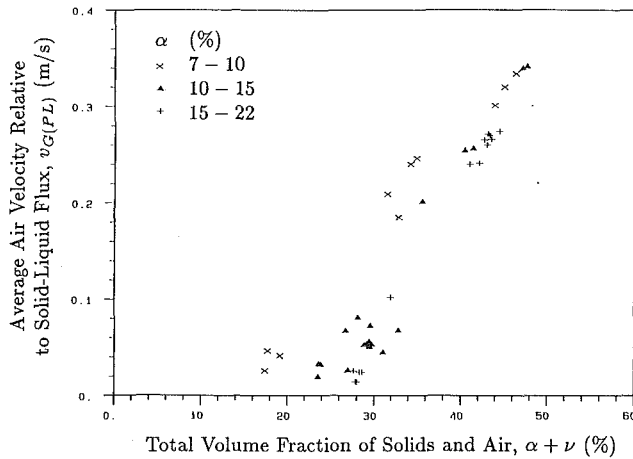


Fig. 18 Average velocity of air relative to the combined flux of liquid and solids versus total volume fraction of disperse material

the present flows, which manifest large vortical structure subsequent to the loss of stability of the disperse regime.

All the relative velocity data falls on the same general curve when presented as a function of the total volume fraction of the disperse medium. This is also true for Fessas and Weiland's data though they do not make note of this fact. This property was assumed in a low Reynolds number bi-disperse model by Lockett and Al-Habbooby (1974) and proved to give good agreement with experimental data. It therefore appears that this property holds not only for flows of small particle Reynolds number but also for the higher Reynolds numbers of about 1000 which pertain to this study.

6.3 Statistical Properties of Volume Fraction Signals in Three-Component Flows. We now turn attention to the statistical properties of the fluctuations in the measured volume fraction signals of three-component flows. In Sections 4 and 5 we showed that the amplitude of the fluctuations presented in the form of the Signal To Noise Ratio and the coherent time scale presented in the form of a time constant ξ both contained valuable information on the nature of two-component flows.

In the three-component flows, the STNR shown in Fig. 19 displays a nearly linear dependence on total volume fraction, with a scatter of ± 5 percent. The STNR of well behaved disperse flows coincide with both bubbly and particle disperse flow values shown on Figs. 8 and 13. The flows which exhibit large vortical structure assume STNR values below the disperse flow curves. The small scatter in the results indicates that this type of measurement has potential as a means of monitoring the total volume fraction. The STNR exhibits the largest deviation from the disperse flow curves for flows of very low solids volume fraction resembling churn-turbulent flows. This is exemplified by the STNR curve for air-water flows, Fig. 8. These are the conditions under which the STNR would be least accurate as a measure of total volume fraction.

The coherent time scale of the noise in the three-component flows is presented in the form of the time constant ξ versus the average air velocity in Fig. 20 for a wide range of gas volume fractions. Surprisingly, all points fall on one common curve with a maximum which coincides with the onset of vortical motion in the flow. The maximum value of ξ is 75 with a corresponding average gas velocity of .14 m/s. All well behaved dispersed flows fall to the left of the maximum and all agitated flows to the right. Note that the behavior of the time constant in churn-turbulent two-component flows (Fig. 9) was markedly different. The right-hand part of the curve which shows a

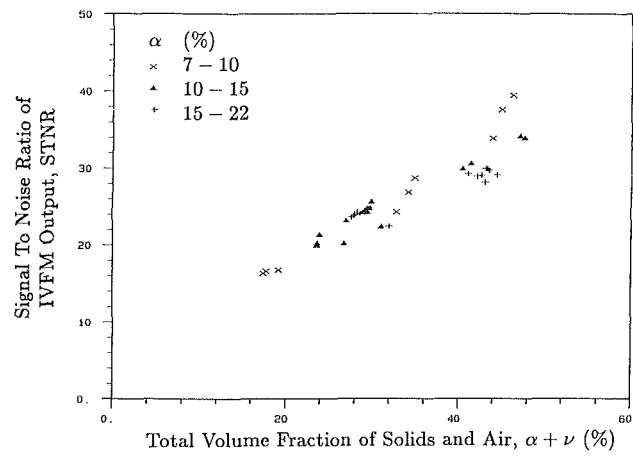


Fig. 19 Signal to noise ratio of the IVFM output in three component flows versus total disperse material volume fraction

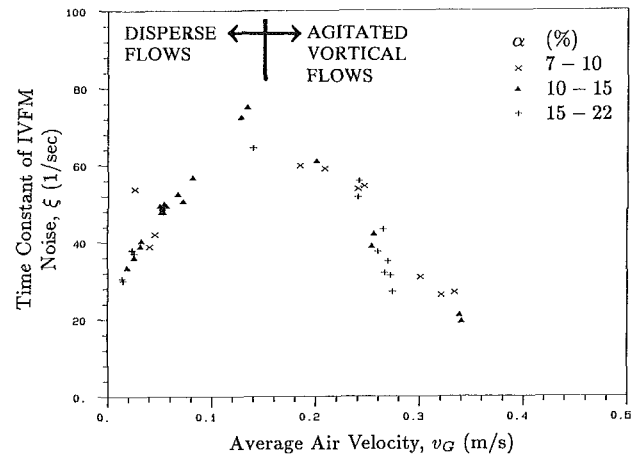


Fig. 20 Time constant ξ of IVFM output fluctuations in three component flows versus the average air velocity

decreasing time constant implies the development of large scale vortical structure in the flow.

7 Conclusion

In this study, the nature of vertical two- and three-component gravity driven flows was studied. Gas-liquid and gas-liquid-solid mixtures were found to undergo a transition from a disperse to an agitated regime. The agitated vortical air-water-solids flows were so named for their distinct eddies of the size of the pipe diameter.

Solid-liquid flows, however, were found to remain quite homogeneously distributed for all volume fractions and flowrates considered. In agitated vortical three-component flows, segregation of species was observed. Air bubbles formed groupings in the center of large vortices, and slugs were occasionally created. This regime exhibited a dramatic increase in the gas flux relative to the solid-liquid mixture. A map of three-component flow regimes is presented in terms of the volume fractions of the individual constituents showing the regions of disperse and agitated vortical flows.

The structure of these flows was quantitatively analyzed by making use of the statistics in the fluctuations of volume fraction measurements. The statistical properties of the fluctuations were presented in terms of two properties of their auto-correlation function, namely its peak value (at $\tau=0$) which represents the fluctuations amplitude and its "fall off" time which is a measure of the characteristic coherent time scale in the "noise." The former is presented in the form of a Signal To Noise Ratio (STNR), and the latter as a time constant of

coherence, ξ . In disperse bubbly and particle flows, the STNR was found to be directly related to the volume fraction of air or solids. Remarkably, the results for bubbles and particles were found to be virtually identical. This consistency of the measurement and the independence of the dimensionless STNR on the IVFM sensitivity (gain) suggests that the STNR may be a useful measure of volume fraction in locations of adverse conditions where recalibration of the IVFM is inconvenient if not impossible. The time constant, ξ , was found to be linearly proportional to the mean particle and bubble velocities in disperse two-component flow conditions. Furthermore, the constant of proportionality was found to be the same for both types of flow. On the basis of this result, ξ could be used as a nonintrusive measure of the mean velocity of the flowing particulate or bubbly material. As the gas-liquid and gas-liquid-solid flows develop large scale structure and become churn-turbulent and vortical respectively, both the STNR and ξ are found to decrease.

The size and propagation speed of large scale structure in churn-turbulent and unsteady three-component flows remains unexplored. Future efforts should be concentrated on applying a combination of auto-correlation and cross-correlation

measuring techniques using more than one transducer to investigate the size, speed and persistence of the observed structures.

References

- 1 Batchelor, G. K., and Janse Van Rensbury, R. W., 1986, "Structure Formation in Bi-Disperse Sedimentation," *J. Fluid Mech.*, Vol. 166, pp. 379-407.
- 2 Bernier, R. N., 1981, "Unsteady Two-Phase Flow Instrumentation and Measurement," Ph.D. thesis, California Institute of Technology.
- 3 Fessas, Y. P., and Weiland, R. H., 1981, "Convective Solids Settling Induced by a Buoyant Phase," *AIChE Journal*, Vol. 27, No. 4.
- 4 Ishagai, S., Yamane, M., and Roko, K., 1965, "Measurement of the Component Flows in a Vertical Two-Phase Flow by Making Use of the Pressure Fluctuations," *Bull. JSME*, Vol. 8, pp. 375-390.
- 5 Jones, O. C., and Zuber, N., 1975, "The Interrelation between Void Fraction Fluctuations and Flow Pattern in Two-Phase Flow," *Int. J. Multiphase Flow*, Vol. 2, pp. 273-306.
- 6 Kytömaa, H. K., 1986, "Stability of the Structure in Multicomponent Flows," Ph.D. thesis, California Institute of Technology.
- 7 Lockett, M. J., and Al-Habbooby, H. M., 1974, "Relative Particle Velocities in Two-Species Settling," *Power Technol.*, Vol. 10, pp. 67-71.
- 8 Wallis, G. B., 1961, *One Dimensional Two-Phase Flow*, McGraw-Hill, New York.

Modelling Collisional Stresses in a Dense Fluid-Solid Mixture

H. H. Shen

Clarkson University,
Potsdam, New York

M. A. Hopkins

Dartmouth College,
Hanover, New Hampshire

N. L. Ackermann

Clarkson University,
Potsdam, New York

An idealized dense mixture of fluid and solid is considered. The mixture consists of identical spheres and a Newtonian fluid. Collisional stresses in a simple shear flow of such a mixture are quantified. These stresses are considered to be generated by binary collisions of spheres which result from the mean shear flow. The fluid is considered to act only as a dissipater of the fluctuating motion of the solids. Fluid stresses are neglected. Unlike previous analyses which make similar assumptions about the effect of the fluid, the present work does not require assumptions about the collision kinematics, except that the kinematics be homogeneous in the entire flow field. This is achieved by replacing analytical integrations with a Monte Carlo procedure. The resulting collisional stresses are found to increase and compare better with experimental data than previously obtained analytical results.

Introduction

Flows of fluid-solid mixtures occur in numerous industrial and natural processes. For design and control purposes the quantitative understanding of such flows is important. Most existing mathematical models of such flows rely on phenomenological parameters. A commonly used rheological model that yields satisfactory results in many slurry pipe flows is the Bingham plastic model. In this model the shear stress is expressed as

$$\tau = \tau_0 + \eta (du_1/dx_3)^n \quad (1)$$

where τ_0 is the yield shear stress, η is the dynamic viscosity, du_1/dx_3 is the shear rate and n is a constant power law index. τ_0 , η and n are determined experimentally.

Difficulties in adopting such a model arise when those phenomenological parameters become flow dependent. The validity of using a set of such parameters becomes questionable for flows outside the range for which those parameters were determined. It is thus desired to understand the rheology of flowing fluid-solid mixtures in a more fundamental way, such that the stress and strain rate relations may be obtained which are free of unknown constants.

Recently there have been many studies that analyzed the detailed mechanics that occur at the particle level to quantify stresses generated by a deforming idealized granular material. These studies have successfully described stresses developed in a simple shear flow of disks or spheres, provided that the stresses in such a flow are generated by the random binary collision among these shearing particles. A common assumption in all of these theories is that the effect of the interstitial fluid is negligible. Such a simplifying assumption was not used in

the granular flow theory developed in [1], where the interstitial fluid acts as an energy dissipater. In that analysis the momentum transfer by the shearing interstitial fluid is not included. Results from that analysis were reasonably well correlated with experimental data obtained in [2, 3], however, the magnitude of the predicted stresses was much lower than measured.

A common problem of the existing analyses for quantifying collisional stresses in a highly concentrated granular flow is the mathematical complexity. Many assumptions are made to facilitate explicit solutions. The most severe among these assumptions is that the magnitude of the random motion of the solid particles is much higher than the mean motion. This assumption has limited the applicability of the resulting stress-strain rate relations to flows of very elastic particles. In a fluid-solid mixture, the same assumption would imply that the fluid density must be orders of magnitude lower than that of the solid. To apply the results to hydraulically transported mixtures is thus out of the question. Relaxation of this assumption requires very involved mathematics which leads to a series of progressively higher order approximations [4, 7].

A Monte Carlo method has recently been developed [5] to replace the tedious analytical procedure. This method requires no restriction on the flow kinematics as long as it is homogeneous in the entire flow field. As a result, it may be used to analyze inelastic as well as elastic solids mixed with fluid of unlike or like densities.

This Monte Carlo method has been successfully adopted to predict stresses in a simple shear flow of disks or spheres without fluid effects. In the present study, it is applied to flows of a fluid-solid mixture. The result is compared with the previous analytical result obtained in [1] and the experimental data reported in [3]. It will be shown that a much better comparison with the experimental data may be obtained with the present results.

Contributed by the Fluids Engineering Division of THE AMERICAN SOCIETY OF MECHANICAL ENGINEERS and presented at the International Symposium on Slurry Flow, ASME Winter Annual Meeting, Anaheim, Calif., December 7-12, 1986. Manuscript received by the Fluids Engineering Division June 17, 1986.

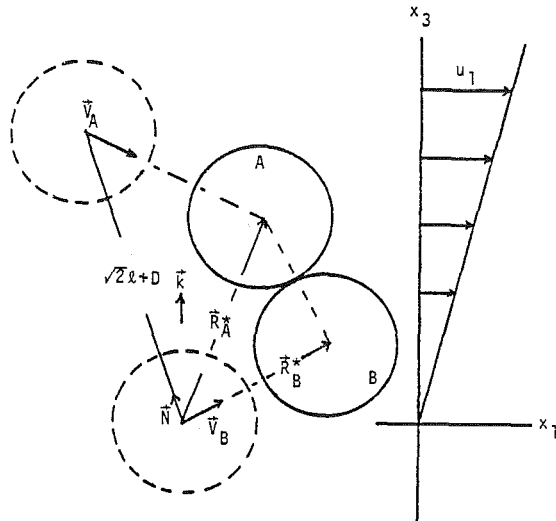


Fig. 1 Collision geometry

Theoretical Development

A flowing fluid-solid mixture has several distinct regimes. The classification of these regimes varies however in different fields of application. Ordinary terminology in the literature on slurry flow denotes these regimes as homogeneous, heterogeneous and bed load. In the field of a more general flow of granular material, they are designated as inertia dominant, macro-viscous and quasistatic. The mechanism of stress generation in a granular material differs a great deal among different flow regimes. We will investigate stresses that are generated mainly due to the collision of solids. In the case of slurry flows, this then restricts our attention to the highly concentrated homogeneous and part of the heterogeneous regimes, of equivalently to the inertia dominant flow of a fluid-solid mixture.

In such a flow, stresses are quantified as the product of the number of solids on a unit surface, the collision frequency of each solid particle and the momentum transfer per collision. Due to the random nature of collisions, this product must be statistically averaged over all possible collision kinematics. The collision kinematics are defined by three components: solid concentration, mean strain rate and magnitude of solid velocity fluctuations. Insisting that the work done by collisional stresses be equated to the energy dissipated by collision and fluid drag, the magnitude of solid velocity fluctuation and collision frequency are quantified. This procedure has been used in [1, 4, 7] to determine analytically the rheology of a fluid-solid mixture. For instance, the resulting stresses for a simple shear flow of spheres obtained in [1] are

$$\tau_{13} = \frac{1}{2} \frac{C_0^{1/2} C^{2/3}}{C_0^{1/3} - C^{1/3}} \left(\frac{(1-\epsilon)^3 0.05}{\frac{3}{2} C_D \frac{\rho_f}{\rho_s} \frac{C^{1/3}}{C_0^{1/3} - C^{1/3}} + \frac{1-\epsilon^2}{8}} \right)^{1/2} \cdot \rho_s D^2 \left(\frac{du_1}{dx_3} \right)^2 \quad (2)$$

$$\tau_{33} = \frac{1}{\pi^2} \frac{C C_0^{1/3}}{C_0^{1/3} - C^{1/3}} \frac{(1-\epsilon)^2 0.05}{\frac{3}{2} C_D \frac{\rho_f}{\rho_s} \frac{C^{1/3}}{C_0^{1/3} - C^{1/3}} + \frac{1-\epsilon^2}{8}} \cdot \rho_s D^2 \left(\frac{du_1}{dx_3} \right)^2 \quad (3)$$

where C is the solid concentration, C_0 is the value of C in the packed state, ϵ is the restitution coefficient of solids, ρ_f and ρ_s are densities of fluid and solid respectively, C_D is the drag coefficient, D is the solid sphere diameter and du_1/dx_3 is the shear rate.

As discussed earlier, due to the assumptions made in deriving the above stresses, the applicability of equations (2) and (3) is limited.

The Monte Carlo simulation procedure which eliminates analytical assumptions is described briefly here, with a focus on including the fluid drag effect. Details of this simulation are reported elsewhere [5]. This simulation may be applied to a general homogeneous deformation field as shown in [5]. A simple shear field, however, is discussed in the following.

Consider the two identical spheres in a simple shear field as shown by the dotted circles shown in Fig. 1. These two spheres are considered to have just experienced a collision with some other particles and now have post-collision velocities

$$\mathbf{V}_A = u_A \mathbf{i} + \mathbf{v}'_A, \quad \mathbf{V}_B = u_B \mathbf{i} + \mathbf{v}'_B \quad (4a,b)$$

where u_A and u_B are the mean velocities appropriate to the locations of those first collision locations and \mathbf{v}'_A and \mathbf{v}'_B are the corresponding fluctuation velocities. These two spheres are then to collide at the point shown in the flow field after each has traveled (on the average) a distance equal to the mean free path l . While traveling through the interstitial fluid a distance l , the kinetic energy of the spheres are reduced by the drag forces acting on them. This drag force is expressed as

$$F_D = C_D \rho_f \frac{\pi D^2}{4} \frac{v^2}{2} \quad (5)$$

Nomenclature

A, B = spheres
 C, C_0 = solid concentrations
 C_D = drag coefficient
 D = sphere diameter
 F_D = drag force
 $\mathbf{i}, \mathbf{k}, \mathbf{N}$ = unit vectors
 K = constant
 l = mean free path
 n = power law index
 NT = number of iterations

P = number of spheres cut by unit surface area
 $\mathbf{R}_A^*, \mathbf{R}_B^*$ = position vectors
 u_A, u_B = mean speed
 u_1 = mean flow component
 $\mathbf{V}_A, \mathbf{V}_B$ = actual velocities
 $\mathbf{V}_A^r, \mathbf{V}_B^r$ = reduced velocities
 $\mathbf{V}_A^*, \mathbf{V}_B^*$ = post-collision velocities
 $\mathbf{v}'_A, \mathbf{v}'_B, \mathbf{v}'$ = fluctuation velocities

v = speed
 v_r = reduced speed
 x_1, x_3 = coordinates
 χ = frequency correction factor
 ϵ = restitution coefficient
 η = viscosity parameter
 ρ_f, ρ_s = fluid and solid densities
 τ, τ_0 = stresses

where C_D , ρ_f and D are defined in equations (2) and (3) and v is the relative velocity between the moving sphere and surrounding fluid. After traveling a mean free path, these two spheres occupy the positions shown by the solid circles in Fig. 1, and collide with reduced velocities \mathbf{V}_{Ar} and \mathbf{V}_{Br} . The new post-collision velocities are computed as

$$\mathbf{V}_A^* = \frac{1-\epsilon}{2}\mathbf{V}_{Ar} + \frac{1+\epsilon}{2}\mathbf{V}_{Br} \quad (6)$$

$$\mathbf{V}_B^* = \frac{1+\epsilon}{2}\mathbf{V}_{Ar} + \frac{1-\epsilon}{2}\mathbf{V}_{Br} \quad (7)$$

The velocities \mathbf{V}_A^* and \mathbf{V}_B^* are obtained from linear momentum conservation and the restitution law determined by the restitution coefficient ϵ . Friction forces between colliding spheres have been included in previous analysis [1, 5] but are neglected here. The stress tensor which resulted from these collisions is obtained from the average of collision events over all possible collision contact points indicated by \mathbf{N} in Fig. 1 and all possible velocity pairs \mathbf{V}_A , \mathbf{V}_B which would produce such collisions. This average may be expressed as [6]

$$\tau = \frac{p}{2} \frac{\rho_s}{\rho_s} \frac{\pi D^3}{6} \frac{\sum_{(\mathbf{V}_A - \mathbf{V}_B) \cdot \mathbf{N} > 0} \sum_{(\mathbf{V}_A - \mathbf{V}_B) \cdot \mathbf{N} > 0} \sum_{(\mathbf{V}_A - \mathbf{V}_B) \cdot \mathbf{N} > 0} (\mathbf{V}_B^* - \mathbf{V}_{Br}) \otimes \mathbf{N} \frac{(\mathbf{V}_A - \mathbf{V}_B) \cdot \mathbf{N}}{l}}{\sum_{(\mathbf{V}_A - \mathbf{V}_B) \cdot \mathbf{N} > 0} \sum_{(\mathbf{V}_A - \mathbf{V}_B) \cdot \mathbf{N} > 0} \sum_{(\mathbf{V}_A - \mathbf{V}_B) \cdot \mathbf{N} > 0} 1} \quad (8)$$

where $p = 6C/\pi D^2$ represents the number of spheres cut by a unit surface area.

Analytical procedures have been developed to approximate the fluctuation component \mathbf{v}' . This is accomplished by assuming a distribution and determining the root-mean-square of this distribution through an energy balance argument (cf. [1, 4, 7]). The Monte Carlo simulation is designed to determine this distribution by emulating the process by which this distribution is created naturally due to the mean flow.

The Monte Carlo simulation is produced as follows. A sample space of dimension n is first designated. This sample space is to eventually contain a precise ensemble of the fluctuation velocities experienced by a sphere, such as sphere B , in the simple shear field. Initially all of these samples are arbitrarily set to zero. As the simulation begins, an initial period therefore exists during which the sample space contains fluctuation velocities that are not representative of what are found in the actual flow field. The procedure starts by picking a random collision point indicated by \mathbf{N} in Fig. 1. Two random samples of the velocity \mathbf{v}' are then chosen from the sample space to represent \mathbf{v}'_A and \mathbf{v}'_B which appeared in equations (4a,b). If the mean free path for any sphere is l , the mean separation between A and B in Fig. 1 is $\sqrt{2}l$ [8]. Therefore, sphere A can be considered to be originally a distance $\sqrt{2}l + D$ away from B at the beginning of its travel to collide with B . The velocities of spheres A and B are thus

$$\mathbf{V}_A = (D + \sqrt{2}l) \frac{du_1}{dx_3} (\mathbf{N} \cdot \mathbf{k}) \mathbf{i} + \mathbf{v}'_A, \quad \mathbf{V}_B = \mathbf{v}'_B \quad (9a,b)$$

where the reference frame, having a mean velocity $u_B \mathbf{i}$, is located at the center of sphere B at the dotted location shown in Fig. 1. This is equivalent to $\mathbf{u}_B = 0$ in equation (4b). After traveling a distance l , fluid drag will reduce the speeds of spheres A and B to

$$\mathbf{V}_{Ar} = e^{-2K} \left(\sqrt{2}l \frac{du_1}{dx_3} (\mathbf{N} \cdot \mathbf{k}) \mathbf{i} + \mathbf{v}'_A \right) + D \frac{du_1}{dx_3} (\mathbf{N} \cdot \mathbf{k}) \mathbf{i},$$

$$\mathbf{V}_{Br} = e^{-2K} \mathbf{v}'_B \quad (10a,b)$$

as described in detail in the appendix where

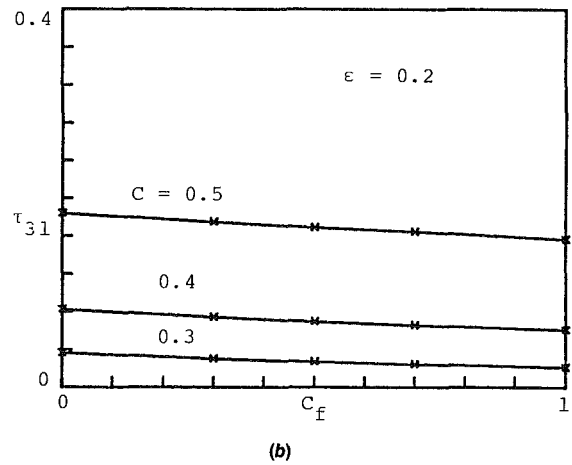
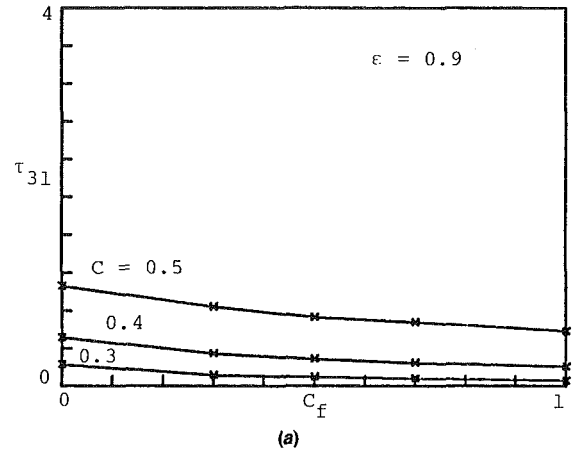


Fig. 2 Shear stress

$$K = \frac{3C_D}{8} \frac{\rho_f}{\rho_s} \frac{l}{D} \quad (11)$$

Utilizing equations (6) and (7), the post-collision velocities \mathbf{V}_A^* , \mathbf{V}_B^* may be obtained. At this location (indicated by the solid spheres in Fig. 1) the new fluctuation velocities are $\mathbf{V}_A^* - (\mathbf{R}_A^* \cdot \mathbf{k}) du_1/dx_3 \mathbf{i}$ and $\mathbf{V}_B^* - (\mathbf{R}_B^* \cdot \mathbf{k}) du_1/dx_3 \mathbf{i}$ where \mathbf{R}_A^* and \mathbf{R}_B^* are the position of vectors A and B at collision in the chosen reference frame. For computational convenience these fluctuation velocities for spheres A and B are approximated as $\mathbf{V}_A^* - (D + \sqrt{2}l)(\mathbf{N} \cdot \mathbf{k}) du_1/dx_3 \mathbf{i}$ and \mathbf{V}_B^* . The same type of approximation has been used to compute \mathbf{V}_{Ar} and \mathbf{V}_{Br} in equations (10a,b).

Since a homogeneous flow field is considered, the fluctuation velocity has an identical distribution at any point in the flow field. Therefore, these new fluctuation velocities are returned to the sample space to replace the values chosen prior to this collision.

After repeating this procedure a large number of times, the sample space will contain statistically stable values of the velocity fluctuation. After this condition is achieved stresses are then computed from equation (12) by performing a large number, NT , of additional interactions

$$\tau = \frac{p}{2NT} \sum_{NT} \rho_s \frac{\pi D^3}{6} (\mathbf{V}_B^* - \mathbf{V}_{Br}) \otimes \mathbf{N} \frac{(\mathbf{V}_{Ar} - \mathbf{V}_{Br}) \cdot \mathbf{N}}{l} \quad (12)$$

In the above simulation, the mean free path is determined from the solid concentration C as

$$l = \frac{D}{6\sqrt{2}C} \quad (13)$$

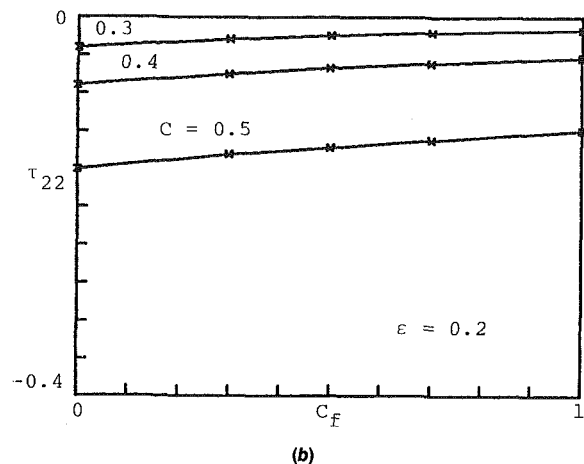
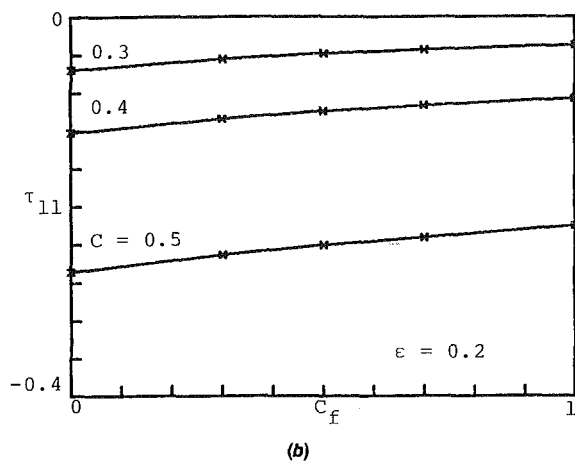
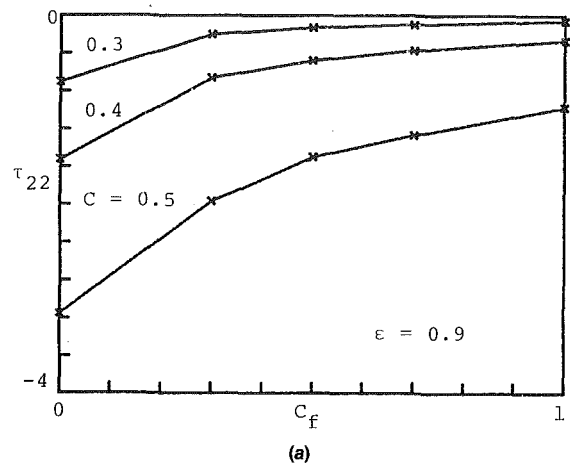
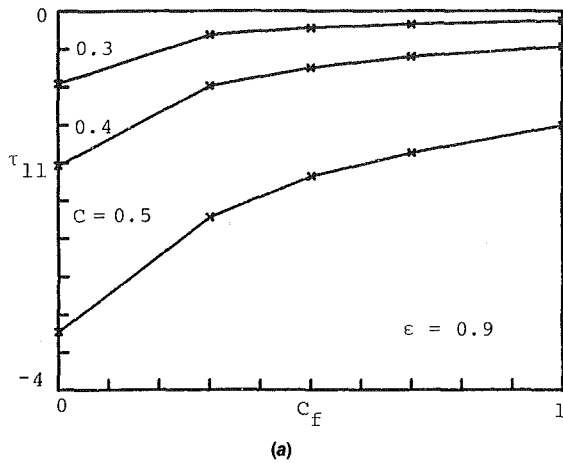


Fig. 3 Normal stress in the x_1 direction

Fig. 4 Normal stress in the x_2 direction

where

$$\chi = \frac{1 - 0.5C}{(C_0 - C)^3} \quad (14)$$

with C_0 indicating the densest solid concentration. Equations (13) and (14) are presented in literature on the kinetic theory for gases [9]. The factor χ accounts for the increase of collision probability in a dense gas. There has been discussion on the form of χ and the appropriate value of C_0 . The results presented in the next section are obtained with $C_0 = 1$. The corresponding formula is called the Carnahan-Starling formula [10].

Results

Since the drag coefficient C_D and the ratio of fluid to solid density appear together as a product the effect of the fluid may be represented by a single parameter

$$C_f = C_D \frac{\rho_f}{\rho_s} \quad (15)$$

Figures 2, 3, 4, and 5 give the behavior of the shear stress and the three normal stresses obtained from the simulation for $\epsilon = 0.2$ and 0.9 , $C = 0.3, 0.4$ and 0.5 and $C_f = 0.0$ to 1.0 . An interesting observation not available from previous analytical results given in [1] is that the normal stresses are not identical. Moreover, the stress magnitudes were consistently in the order $\tau_{11} > \tau_{33} > \tau_{22}$ for all the parameters used in this simulation. All stresses given here are nondimensionalized by dividing with $\rho_s D^2 (du_1/dx_3)^2$. Figure 6 gives the ratio of τ_{31}/τ_{33} which may be called the internal friction coefficient of the fluid-solid mixture. The result of this simulation indicates that when C_f

increases, stresses monotonically approach constant values at large values of C_f .

Figure 7 presents a comparison of the Monte Carlo results and the experimental results obtained in [3]. In [3], the material used was neutrally buoyant polystyrene beads in salt water. The restitution coefficient for the polystyrene used in these experiments was not reported. It was considered, however, that $\epsilon = 0.9$ provided a reasonable estimate. The experimental data from [2] is not used here for comparison because the material property is far more uncertain.

In Fig. 7 calculations based upon $\epsilon = 0.9$ was used to compare the results obtained by the Monte Carlo simulation, and the experimentally determined values for the polystyrene spheres. Questions about the proper interpretation of the experimental results make them something less than a perfect basis for comparison when judging the validity of the Monte Carlo approach.

It was found that the shear stresses generated with the Monte Carlo simulation are approximately twice as large as previous analytical results in [1]. The same trend also appears in the normal stresses.

Discussion

In this analysis, the hydrodynamic force on a moving sphere is very simplistically included as a drag force. In formulating this drag force, the effect of solid concentration, particle Reynolds number, density difference between solid and fluid are all lumped into one single coefficient C_f equal to $C_D \rho_f / \rho_s$.

In [1], this drag coefficient was approximated from experimental results [11] describing a single sphere settling in a

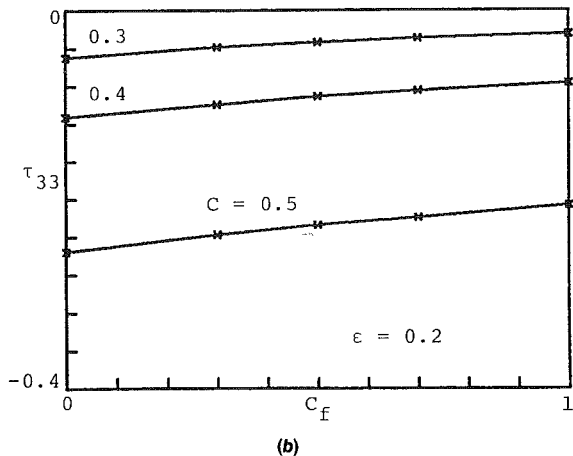
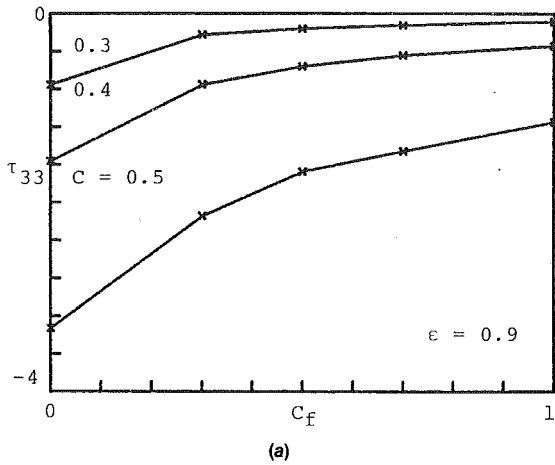


Fig. 5 Normal stress in the x_3 direction

fluid-filled cylinder. It was assumed that the interparticle separation in a dense fluid-solid mixture produced the same hydrodynamic effect as the gap between the cylinder wall and the settling sphere. It was found in [1] that for the range of concentrations possible in rapidly shearing granular flows, C_D could be reasonably approximated as being equal to 1.

However, in the presence of other particles within the flow field, the hydrodynamics may in fact be quite different from that of a single sphere settling in a cylinder. Extensive literature exists on 2-body hydrodynamic forces (e.g. [12], [13], [14], [15]). Little information is available, however, on multibody forces. The 2-body forces have been analyzed in two limiting cases, namely the viscous regime and the inviscid regime. Discussion on the first may be found in [12] and [13] and the second in [14] and [15].

Analysis given in [12] shows that the viscous drag force F_v is

$$F_v = 3\pi\mu Dv' C_v \quad (16)$$

where μ is the absolute fluid viscosity and C_v is a coefficient which depends on the proximity of a sphere with a rigid wall. This wall may represent the plane of symmetry between two identical approached spheres along their line of centers. The coefficient C_v goes to infinity as the gap between the sphere and the wall vanishes. In the present study the concentration $C=0.5$ corresponds to a gap between spheres of about $10^{-1}D$. Considering that Stoke's law applies for this gap size the coefficient C_v , as determined from [12], is about 3. This value reduces rapidly with decreasing C .

By equating equations (5) and (16), the drag coefficient C_D in this viscous regime becomes

$$C_D = 24 C_v / Re \quad (17)$$

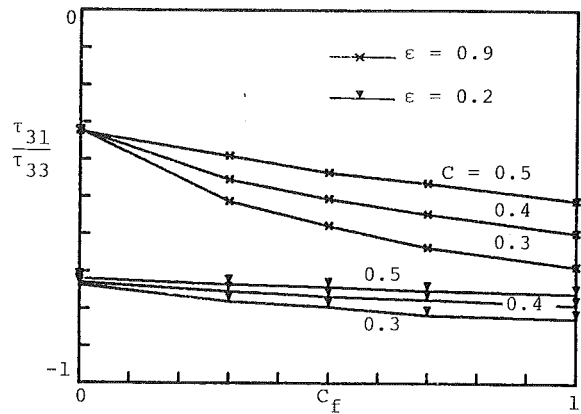


Fig. 6 Internal friction coefficient

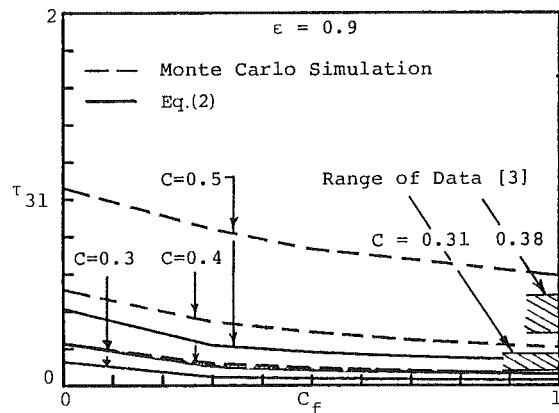


Fig. 7 Comparison of shear stress from theoretical results and experimental data

where $Re = v'D/\nu$ is the particle Reynolds number. As the particle Reynolds number decreases with increasing viscous effects C_D similarly increases with no upper bound.

For the inviscid case, when the particle Reynolds numbers become large, the reduced pressure between the spheres as they make contact, tends to draw the approaching spheres together (see e.g., [15]). There is also a contribution to the added mass coefficient due to the presence of another particle. In the limit of infinite separation, this coefficient reduces to 0.5, which is identical to the single sphere case. When a spherical particle approaches a wall, this added mass coefficient reaches an upper limit of 0.8 as the gap size vanishes. The added mass effect is not included explicitly in the present analysis. However, if one would introduce such an added mass effect, it may be incorporated by letting ρ_f be $(1 + C_M)\rho_f$ in equation (18), where C_M is the added mass coefficient which depends on the proximity of the sphere which is moving towards a neighboring sphere.

A careful study of the 2-body hydrodynamic forces in the present work is missing. It is desirable to modify the fluid-solid interaction force given in equation (18). This modification must include effects from the presence of neighboring particles. We will leave this for future study.

As can be seen, however, from Fig. 7 the effect of fluid viscosity on the collisional stress is limited to a relatively small variation for any fixed particle concentration. For example, for $C=0.4$, the range of τ_{31} is from 0.5 to 0.2 for a variation in C_f from 0 to 1. Simulation results show that τ_{31} approaches 0.045 as $C_f > 100$. As the collisional stress decreases, the mixture would be dominated by fluid stress. If $\rho_f = \rho_s$ as for a neutrally buoyant suspension, $C_f = C_D$ and the value of τ_{31} in

Fig. 7, for $C_D=0$, corresponds to the case in which the interstitial fluid as purely inviscid. At the other extreme, the value of τ_{31} , for a fixed value of C , appears to reach an asymptotic limit as the flow becomes increasingly viscous (e.g., C_D increases). The experimental data from [3] as shown in Fig. 7, appears to lie within these limiting extreme values (e.g., fully viscous and inviscid flow). This provides a good indication that the technique of calculating fluid effects with the Monte Carlo simulation may indeed provide a successful approach.

The challenge remains however to accurately assess a correct value of C_D for a particular granular flow keeping in mind that this value of C_D is a function of the instantaneous particle Reynolds number which continually changes. If an instantaneous value of C_D could be found as a function of particle Reynolds number, the collisional stresses could be readily calculated using the Monte Carlo method.

Conclusion

A Monte Carlo simulation procedure is adopted to analyze the collisional stresses developed in a simple shear flow of fluid-solid mixture. The fluid effect is considered to retard the fluctuation of the solid particles after collisions. The stresses generated within the fluid phase is neglected.

This Monte Carlo procedure does not require assumptions about the particle kinematics as long as it is homogeneous in the flow field. Therefore it models the collision process more accurately than other existing analytical methods. Resulting stresses are found to increase from previously obtained analytical values. Comparison with the experimental data is reasonable.

In reality, stresses developed in a fluid-solid mixture come from both the fluid and solid phases. These two phases interact and alter each other's property. In this analysis only one component of this interaction, namely, the drag due to the fluid acting on the solid is considered. To make the analysis more complete, other aspects need to be included. A few examples of these aspects are, influence of the solids on the turbulent structure of the fluid, determination of drag coefficient, and resitution of collision in fluids.

The present analysis is believed only to provide a reasonable model for stresses in a flow of fairly dense fluid-solid mixture, in which case the interstitial fluid stress may indeed be neglected.

Acknowledgment

This study was partially supported by grant number MSM-8419416 of the National Science Foundation and grant number DACA89-86-K-0015 of the U.S. Army Cold Regions Research and Engineering Laboratory.

References

- Shen, H. H., and Ackermann, N. L., "Constitutive Relationships for Fluid-Solid Mixtures," *ASCE Eng. Mech. Div.*, Vol. 108, No. EM5, Oct. 1982, pp. 748-763.
- Bagnold, R. A., "Experiments on a Gravity-Free Dispersion of Large Solid Spheres in a Newtonian Fluid Under Shear," *Proc. Roy. Soc. London, Ser. A*, Vol. 225, Aug. 1954, pp. 49-63.
- Savage, S. B., "Experiments on Shear Flows of Cohesionless Granular Materials," *Proc. US-Japan Seminar on Continuum Mechanical and Statistical Approaches on the Mechanics of Granular Materials*, June 1978, Sendai, Japan, pp. 216-228.
- Lun, C. K. K., Savage, S. B., Jeffrey, D. J., and Chepurnyi, N., "Kinetic Theories for Granular Flow: Inelastic Particles in Couette Flow and Slightly Inelastic Particles in a General Flowfield," *J. Fluid Mech.*, Vol. 140, Jan. 1984, pp. 223-256.
- Hopkins, M. A., "Collisional Stresses in a Rapidly Deforming Granular Flow," M.S. thesis, Clarkson University, May 1985, 89 p.
- Pasquarell, G., Ackermann, N. L., Shen, H. H., and Hopkins, M. A., "Bagnold Revisited," *ASCE Eng. Mech. Div.*, Vol. 114, No. EMI, Jan. 1988, pp. 49-64.
- Jenkins, J. T., and Richman, M. W., "Grad's 13-Moment System for a Dense Gas of Inelastic Spheres," *Arch. Rat. Mech. and Anal.*, Vol. 87, No. 4, 1985, pp. 355-377.
- Jeans, J., *An Introduction to the Kinetic Theory of Gases*, Cambridge Press, 1948, 311 p.
- Chapman, S., and Cowling, T. G., *The Mathematical Theory of Non-Uniform Gases*, Cambridge Press, 1970, 423 p.
- Carnahan, N. F., and Starling, K. E., "Equations of State for Non-Attracting Rigid Spheres," *J. Chem. Phys.*, Vol. 51, 1969, pp. 635-636.
- McNown, J. S., Lee, H. M., McPherson, M. B., and Engez, S. M., "Influence of Boundary Proximity on the Drag of Spheres," *Proc. 7th Int. Congress Appl. Mech.*, Vol. 2, Part 1, London, England, 1948.
- Brenner, H., "The Slow Motion of a Sphere Through a Viscous Liquid Towards a Plane Surface," *Chem. Eng. Sci.*, Vol. 16, 1961, pp. 242-251.
- Frankel, N. A., and Acrivos, A., "On the Viscosity of a Concentrated Suspension of Solid Spheres," *Chem. Eng. Sci.*, Vol. 22, 1967, pp. 847-853.
- Miloh, T., "Hydrodynamics of Deformable Contiguous Spherical Shapes in an Incompressible Inviscid Fluid," *J. Eng. Math.*, Vol. 11, No. 4, 1977, pp. 349-372.
- Bentwich, M., and Miloh, T., "On the Exact Solution for the Two-Sphere Problem in Axisymmetrical Potential Flow," *ASME Journal of Applied Mechanics*, Vol. 45, 1978, pp. 463-468.

APPENDIX

Consider a sphere which moves relative to the surrounding fluid a distance l . The initial speed of this sphere is v_0 , the speed after traveling a distance l is v_r . The drag force during this motion is represented as

$$F_D = C_D \rho_f \frac{\pi D^2}{4} \frac{v^2}{2} \quad (18)$$

The equation of motion for this sphere is thus

$$\rho_s \frac{\pi D^3}{6} v \frac{dv}{dx} = -C_D \rho_f \frac{\pi D^2}{4} \frac{v^2}{2} \quad (19)$$

Solving v_r from the above, one obtains

$$v_r = v_0 e^{-2K} \quad (20)$$

where

$$K = \frac{3}{8} C_D \frac{\rho_f}{\rho_s} \frac{l}{D} \quad (21)$$

Limitation of Ejector Performance Due to Exit Choking

J. C. Dutton¹ and B. F. Carroll¹

Introduction

Because of their design simplicity, ejectors are widely used in a variety of industrial settings, such as in pumping, mixing, and entrainment applications. In previous publications (Dutton and Carroll, 1983, 1986), the authors have presented techniques for solving a large class of supersonic ejector design optimization problems. Typical results for optimum designs that span the range of applications mentioned above have also been presented. The method is based on a simplified one-dimensional constant area flow model that, when modified with an empirical pressure recovery coefficient, has been found to be in good agreement with experimental measurements over a wide range of geometrical and operational variables. The technique predicts the combination of primary nozzle Mach number and nozzle exit-to-mixing tube area ratio that optimizes the primary-to-secondary stagnation pressure ratio, mass entrainment ratio, or exit-to-secondary compression ratio given the values of the other two parameters, the gas properties, and the stagnation temperatures.

Because of the isolation provided from downstream influences, the ejector is assumed to operate at "breakoff" points where the mass flow ratio just becomes independent of the compression ratio due to choking of the secondary stream at either the inlet or at an aerodynamic throat location near the inlet. However, under certain relatively extreme combinations of gas properties and operating parameters, the one-dimensional model has recently been found to predict that no solution for the mixed exit flow is possible at the inlet choking condition. The objectives of this paper are to describe the extensions to the flow model necessary to analyze this situation and to present typical optimization results for these conditions.

Flow Model Extensions

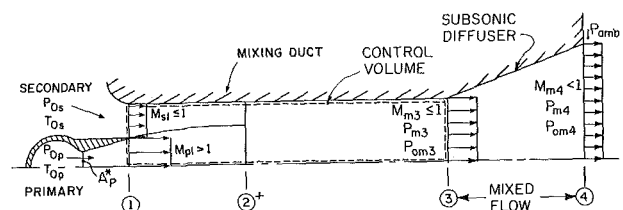
The basic flow model used in the optimization procedure is the one-dimensional constant area model of Addy et al. (1981). A schematic of the ejector system under analysis, along with the relevant nomenclature, is shown in Fig. 1. A high velocity supersonic primary stream entrains a lower velocity secondary stream by means of viscous interaction

¹ Associate Professor and ONR Graduate Fellow, respectively, Department of Mechanical and Industrial Engineering, University of Illinois at Urbana-Champaign, Urbana, Ill. 61801. Professor Dutton is a Mem. ASME.

Contributed by the Fluids Engineering Division of THE AMERICAN SOCIETY OF MECHANICAL ENGINEERS. Manuscript received by the Fluids Engineering Division August 19, 1987.

such that the two streams mix in the constant area duct and are assumed to exit uniformly and subsonically at location 3. As shown in the figure, a subsonic diffuser is also often added to improve the system pressure recovery. Using control volume continuity, momentum, and energy principles, the model predicts the mixed exit flow properties at station 3 given the flow conditions of the primary and secondary streams at inlet location 1. The steady, frictionless, adiabatic flow of perfect gases is assumed, although the streams may have different molecular weights, specific heat ratios, and stagnation temperatures. The well known aerodynamic choking phenomenon (Fabri and Siestrunk, 1958) is analyzed using a second series of control volume relations written between the inlet and the aerodynamic choking station 2 under the assumption that the secondary Mach number is unity at this location. Based on comparison of experimental results to the model predictions, the simplified theory has been modified to include an empirical ejector pressure recovery coefficient defined as the ratio of the actual to the ideal exit static pressure, $R_E \equiv (P_{m3})_A / (P_{m3})_I$. Previous experimental studies (Petric, 1980; Dutton et al., 1982) have shown that this loss coefficient is typically in the range of $R_E = 0.75-0.85$.

In the solution procedure for the mixed exit flow properties at location 3 the key unknown parameter is the Mach number, M_{m3} . It is determined from the solution of a quadratic equation that results from the combination of continuity, momentum, and energy equations written for the control volume shown in Fig. 1. Although the algebraic details are much too lengthy to include herein, the discriminant in this quadratic equation contains the secondary-to-primary stagnation temperature and molecular weight ratios, T_{0s}/T_{0p} and MW_s/MW_p , among other parameters. It has been found that for relatively extreme combinations of these two ratios the discriminant in the quadratic may be negative at the Fabri inlet choking point, thereby predicting complex exit Mach numbers for these cases. This is particularly true when seeking solutions for relatively low P_{m3}/P_{0s} back pressure ratios. Thus, even though it is possible to find the inlet conditions at the Fabri breakoff point, since they are based on separate control volume relations written between locations 1 and 2, no exit flow solution at station 3 is possible for these inlet conditions. However, by lowering the secondary inlet Mach number, M_{s1} , (and, therefore, the mass entrainment ratio W_s/W_p for fixed



+ EXISTS ONLY FOR SUPERSONIC REGIME (SR)

Fig. 1 Schematic and nomenclature for the supersonic ejector system

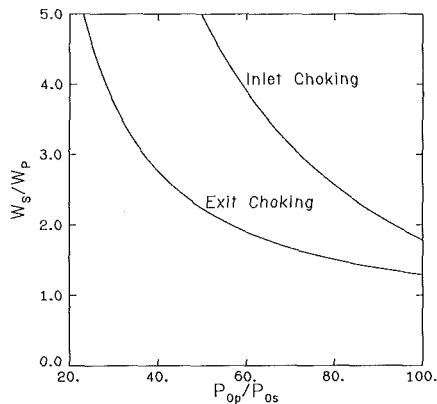


Fig. 2 Comparison of inlet and exit choking constraints for $\gamma_s = \gamma_p = 1.4$, $MW_s/MW_p = 14.5$, $T_{0s}/T_{0p} = 0.25$, $M_{p1} = 3.0$, $A_{p1}/A_{m3} = 0.1$, and $R_E = 0.8$

stagnation pressure ratio P_{0p}/P_{0s}) from the breakoff value, eventually a mixed exit flow solution *can* be found. In addition, at the condition when an exit solution is first possible, M_{m3} is unity. Therefore, the ejector operation is limited for these cases not by the usual Fabri inlet choking phenomenon but rather by mixed flow choking at the *exit*. This result can be argued physically from the standpoint that, say, for a hot primary stream (low T_{0s}/T_{0p}) and low back pressure ratio, thermal choking of the mixed flow can be expected. The same argument can be made for a low molecular weight primary (high MW_s/MW_p), since the stagnation temperature and molecular weight always occur as a quotient in the analysis. Emanuel (1982) has also examined limitations on ejector operation, including the Fabri inlet choking constraint, although not in the context of optimization and by using a more simplified flow model than that presented here.

A quantitative comparison of the inlet and exit choking constraints for a representative case is presented in Fig. 2. The parameter values in this example are: $\gamma_s = \gamma_p = 1.4$, $MW_s/MW_p = 14.5$, $T_{0s}/T_{0p} = 0.25$, $M_{p1} = 3.0$, $A_{p1}/A_{m3} = 0.1$, and $R_E = 0.8$. These values are typical of those encountered when using heated hydrogen as the primary stream and ambient air as the secondary, as might occur in various combustion system applications employing ejectors. This figure is a two-dimensional projection of the three-dimensional operating surface presented in Fig. 2 of Dutton and Carroll (1986) onto the $W_s/W_p - P_{0p}/P_{0s}$ plane; in this case, the solution surface cannot be shown in the third P_{m3}/P_{0s} dimension since mixed exit flow solutions do not exist for mass flow ratios above the exit choking curve. Clearly, over the range of parameters shown, the exit choking criterion acts to significantly reduce the entrained mass flow ratio from what would be expected based on the inlet choking condition alone. Thus, the exit choking criterion is an additional constraint that must be considered in the design and optimization of ejector systems when the applicable range of operating parameters and gas properties warrants.

The three-dimensional operating surface for an ejector constrained by exit choking is qualitatively similar to that for inlet choking except that the breakoff curve between regimes is determined from the condition that $M_{m3} = 1.0$ instead of $M_{s2} = 1.0$ or $M_{s1} = 1.0$ as in the "supersonic" or "saturated supersonic" regimes of the more common inlet choked case. For exit choking, however, there is only one regime for which the mass entrainment ratio is independent of the compression ratio, since the analysis predicts that the mixed flow is always choked at exit location 3 instead of inlet station 1 or aerodynamic throat location 2.

It is to be emphasized that none of the previous analyses or results are invalidated by this finding of the mixed flow choking phenomenon. When exit choking occurs, results cannot

even be presented for operating points above the breakoff curve, since exit flow solutions cannot be found for these cases. The basic flow model must simply be extended, as described here, to be able to analyze ejector operation under these conditions.

Optimization Results

The flow model extensions discussed in the previous section have been incorporated in the previously developed optimization computer program, with the resulting code named CAEOPT3. The solution methodology used by CAEOPT3 is described in detail in Dutton and Carroll (1986). Briefly, given γ_s , γ_p , MW_s/MW_p , T_{0s}/T_{0p} , and R_E , the program generates design curves that determine the primary nozzle Mach number, M_{p1} , and area ratio, A_{p1}/A_{m3} , for optimization of either W_s/W_p , P_{0p}/P_{0s} , or P_{m3}/P_{0s} , knowing the values of the other two ratios. The duct exit stagnation pressure ratio or the diffuser exit static or stagnation pressure ratios, P_{0m3}/P_{0s} , P_{m4}/P_{0s} , or P_{0m4}/P_{0s} , respectively, may also be used as the characteristic compression ratios. However, to avoid making assumptions about the diffuser geometry, all results presented here will be in terms of P_{m3}/P_{0s} .

A series of optimization diagrams is shown in Figs. 3(a)–(c) for the same gas properties, stagnation temperature ratio, and pressure recovery coefficient used in Fig. 2: $\gamma_s = \gamma_p = 1.4$, $MW_s/MW_p = 14.5$, $T_{0s}/T_{0p} = 0.25$, and $R_E = 0.8$. The optimized solutions are presented for compression ratios in the range $0.5 < P_{m3}/P_{0s} < 2$, entrainment ratios in the range $0.5 < W_s/W_p < 4$, and stagnation pressure ratios ranging from $1 < P_{0p}/P_{0s} < 100$. All optimization points in these figures are breakoff points, and for the parameters investigated here all of the points are constrained by exit choking rather than Fabri inlet choking. The key plot in the series is Fig. 3(a) where the performance parameters P_{0p}/P_{0s} , P_{m3}/P_{0s} , and W_s/W_p are presented. Entering this figure with any two of these quantities, the optimized value of the third can be determined. Then with P_{m3}/P_{0s} and W_s/W_p known, the values of M_{p1} and A_{p1}/A_{m3} required to achieve this optimum performance can be found from Figs. 3(b) and (c), respectively.

Comparing these results for exit choking to those for a similar inlet choked case with $MW_s/MW_p = T_{0s}/T_{0p} = 1.0$ and all other parameters the same (Dutton and Carroll, 1986), one apparent conclusion is that the entrainment ratios possible in the present case are higher, $0.5 < W_s/W_p < 4$, than those of the previous results, $0.5 < W_s/W_p < 2.5$, all other factors being equal. However, on a "reduced" mass flow basis, i.e. accounting for the differences in molecular weight and stagnation temperature ratios, the performance of the current exit choking case is actually quite poor. The mass flow ratio range for the exit choked case shown in Fig. 3 corresponds to a reduced flow ratio range of: $0.066 < (W_s/W_p)(T_{0s}/T_{0p})^{1/2}/(MW_s/MW_p)^{1/2} < 0.53$. This degradation of performance on a reduced basis is a direct result of the fact that exit choking lowers the breakoff entrainment ratio below that which is expected on the basis of Fabri inlet choking, as demonstrated in Fig. 2.

The qualitative parametric trends, and even the magnitudes, exhibited in Fig. 3 are quite similar to those of previous optimization cases constrained by inlet choking. One exception is that the shapes of the constant W_s/W_p curves on both the $P_{0p}/P_{0s} - P_{m3}/P_{0s}$ and $M_{p1} - P_{m3}/P_{0s}$ figures for the smaller values of W_s/W_p are concave downward for the present results, Figs. 3(a) and (b), in contrast to the previous cases. In addition, these curves are flatter and even rise slightly for the larger P_{m3}/P_{0s} values for the $A_{p1}/A_{m3} - P_{m3}/P_{0s}$ plot, Fig. 3(c), as compared to inlet choking results. However, these differences in shape are not unexpected since exit choking is the phenomenon governing breakoff for the current case.

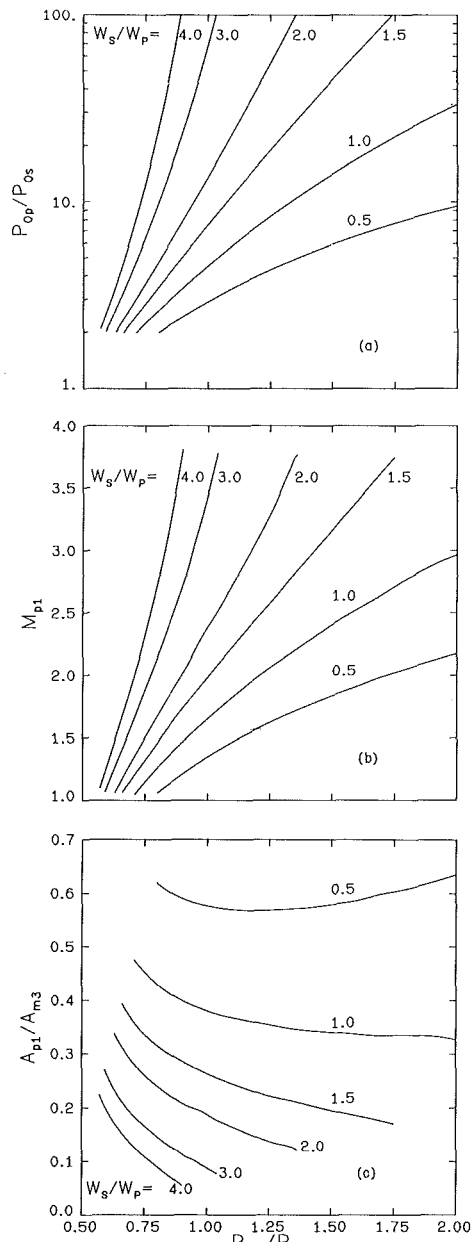


Fig. 3 Optimized ejector design curves for $\gamma_s = \gamma_p = 1.4$, $MW_s/MW_p = 14.5$, $T_{0s}/T_{0p} = 0.25$, and $R_E = 0.8$: (a) performance variables, (b) primary Mach number, (c) area ratio

Another interesting feature of these results, which is not shown in the figures, is the fact that the inlet static pressure ratio for the optimum cases presented is always very nearly unity. In fact, for the entire range of cases considered in Fig. 3, this parameter varies only over the narrow range $0.94 < P_{s1}/P_{p1} < 1.03$. This result was also previously found for ejectors constrained by inlet choking and is fortuitous since ratios far different from unity indicate incipient separation of one of the streams at the inlet with resultant poor performance.

Conclusions

A technique that was previously developed to determine optimized ejector performance and designs for a large class of practical problems has been extended to include the phenomenon of mixed flow exit choking. This phenomenon occurs for relatively extreme combinations of molecular weight and stagnation temperature ratios and acts to reduce

ejector performance over that which is expected based on the well known Fabri inlet choking criterion.

Acknowledgments

This research was supported in part by an Office of Naval Research Graduate Fellowship for B. F. Carroll and by the Department of Mechanical and Industrial Engineering.

References

- Addy, A. L., Dutton, J. C., and Mikkelsen, C. D., 1981, "Supersonic Ejector-Diffuser Theory and Experiments," Report No. UIIU-ENG-82-4001, Department of Mechanical and Industrial Engineering, University of Illinois at Urbana-Champaign, Urbana, Ill.
- Dutton, J. C., and Carroll, B. F., 1983, "Optimized Ejector-Diffuser Design Procedure for Natural Gas Vapor Recovery," *ASME Journal of Energy Resources Technology*, Vol. 105, No. 3, pp. 388-393.
- Dutton, J. C., and Carroll, B. F., 1986, "Optimal Supersonic Ejector Designs," *ASME JOURNAL OF FLUIDS ENGINEERING*, Vol. 108, No. 4, pp. 414-420.
- Dutton, J. C., Mikkelsen, C. D., and Addy, A. L., 1982, "A Theoretical and Experimental Investigation of the Constant Area, Supersonic-Supersonic Ejector," *AIAA Journal*, Vol. 20, No. 10, pp. 1392-1400.
- Emanuel, G., 1982, "Comparison of One-Dimensional Solutions with Fabri Theory for Ejectors," *Acta Mechanica*, Vol. 44, pp. 187-200.
- Fabri, J., and Siestrunk, R., 1958, "Supersonic Air Ejectors," *Advances in Applied Mechanics*, Vol. V, Academic Press, New York, pp. 1-34.
- Petrie, H. L., 1980, "An Experimental and Theoretical Investigation of Multiple Ducted Streams with a Periodic or a Steady Supersonic Driver Flow," M.S. thesis, Department of Mechanical and Industrial Engineering, University of Illinois at Urbana-Champaign, Urbana, Ill.

Incremental Pressure Drop Number in Parallel-Plate Heat Exchangers

T. V. Nguyen¹ and I. L. Maclaine-cross²

Numerical solutions of the Navier-Stokes equations are presented for developing laminar flow in the entrance region of a cascade of parallel horizontal plates with a uniform velocity profile at upstream infinity. Extrapolation to zero mesh size is used. Detailed results on the incremental pressure drop number are presented for Reynolds number ranging from 40 to 2000.

Nomenclature

- D_h = hydraulic diameter
- f = Fanning friction factor
- f_∞ = fully developed Fanning friction factor
- h = mesh size
- H = channel width
- K = incremental pressure drop number
- $K(\infty)$ = fully developed incremental pressure drop number
- L_K = "pressure drop" entrance length
- Re = Reynolds number = $V_\infty D_h / \nu$
- t = time
- u = x component of velocity
- v = y component of velocity
- V_∞ = free stream velocity
- x = coordinate normal to the plates
- y = coordinate along the plates
- y_T = transformed coordinate along the plates
- ψ = stream function
- ζ = vorticity
- ν = kinematic viscosity

¹Senior Research Scientist, Commonwealth Scientific and Industrial Research Organization, Division of Mineral Engineering, Clayton, Victoria 3168, Australia.

²Lecturer, School of Mechanical and Industrial Engineering, University of New South Wales, Kensington, New South Wales 2033, Australia.

Contributed by the Fluids Engineering Division of THE AMERICAN SOCIETY OF MECHANICAL ENGINEERS. Manuscript received by the Fluids Engineering Division June 2, 1986.

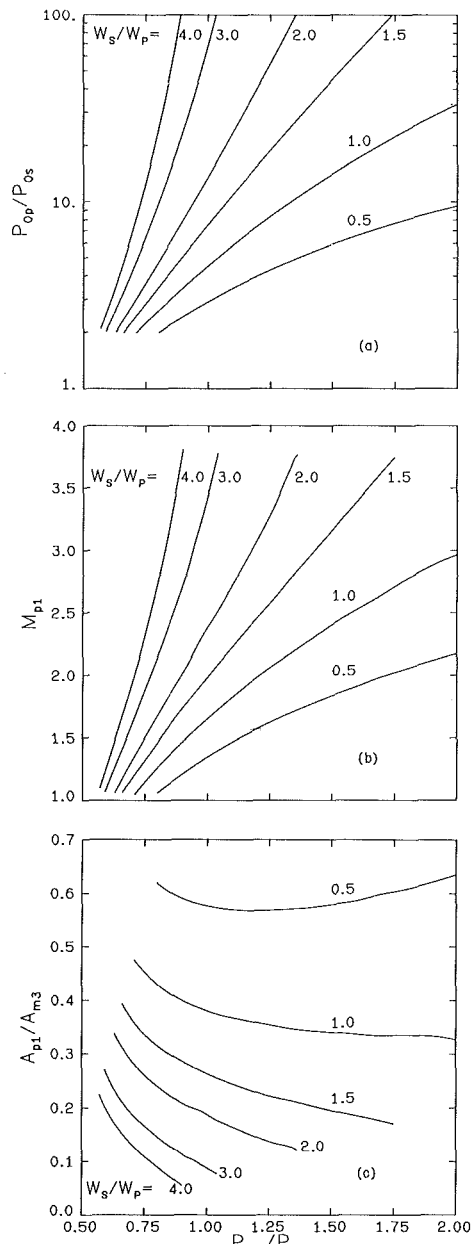


Fig. 3 Optimized ejector design curves for $\gamma_s = \gamma_p = 1.4$, $MW_s/MW_p = 14.5$, $T_{0s}/T_{0p} = 0.25$, and $R_E = 0.8$: (a) performance variables, (b) primary Mach number, (c) area ratio

Another interesting feature of these results, which is not shown in the figures, is the fact that the inlet static pressure ratio for the optimum cases presented is always very nearly unity. In fact, for the entire range of cases considered in Fig. 3, this parameter varies only over the narrow range $0.94 < P_{s1}/P_{p1} < 1.03$. This result was also previously found for ejectors constrained by inlet choking and is fortuitous since ratios far different from unity indicate incipient separation of one of the streams at the inlet with resultant poor performance.

Conclusions

A technique that was previously developed to determine optimized ejector performance and designs for a large class of practical problems has been extended to include the phenomenon of mixed flow exit choking. This phenomenon occurs for relatively extreme combinations of molecular weight and stagnation temperature ratios and acts to reduce

ejector performance over that which is expected based on the well known Fabri inlet choking criterion.

Acknowledgments

This research was supported in part by an Office of Naval Research Graduate Fellowship for B. F. Carroll and by the Department of Mechanical and Industrial Engineering.

References

- Addy, A. L., Dutton, J. C., and Mikkelsen, C. D., 1981, "Supersonic Ejector-Diffuser Theory and Experiments," Report No. UIIU-ENG-82-4001, Department of Mechanical and Industrial Engineering, University of Illinois at Urbana-Champaign, Urbana, Ill.
- Dutton, J. C., and Carroll, B. F., 1983, "Optimized Ejector-Diffuser Design Procedure for Natural Gas Vapor Recovery," *ASME Journal of Energy Resources Technology*, Vol. 105, No. 3, pp. 388-393.
- Dutton, J. C., and Carroll, B. F., 1986, "Optimal Supersonic Ejector Designs," *ASME JOURNAL OF FLUIDS ENGINEERING*, Vol. 108, No. 4, pp. 414-420.
- Dutton, J. C., Mikkelsen, C. D., and Addy, A. L., 1982, "A Theoretical and Experimental Investigation of the Constant Area, Supersonic-Supersonic Ejector," *AIAA Journal*, Vol. 20, No. 10, pp. 1392-1400.
- Emanuel, G., 1982, "Comparison of One-Dimensional Solutions with Fabri Theory for Ejectors," *Acta Mechanica*, Vol. 44, pp. 187-200.
- Fabri, J., and Siestrunk, R., 1958, "Supersonic Air Ejectors," *Advances in Applied Mechanics*, Vol. V, Academic Press, New York, pp. 1-34.
- Petrie, H. L., 1980, "An Experimental and Theoretical Investigation of Multiple Ducted Streams with a Periodic or a Steady Supersonic Driver Flow," M.S. thesis, Department of Mechanical and Industrial Engineering, University of Illinois at Urbana-Champaign, Urbana, Ill.

Incremental Pressure Drop Number in Parallel-Plate Heat Exchangers

T. V. Nguyen¹ and I. L. Maclaine-cross²

Numerical solutions of the Navier-Stokes equations are presented for developing laminar flow in the entrance region of a cascade of parallel horizontal plates with a uniform velocity profile at upstream infinity. Extrapolation to zero mesh size is used. Detailed results on the incremental pressure drop number are presented for Reynolds number ranging from 40 to 2000.

Nomenclature

- D_h = hydraulic diameter
- f = Fanning friction factor
- f_∞ = fully developed Fanning friction factor
- h = mesh size
- H = channel width
- K = incremental pressure drop number
- $K(\infty)$ = fully developed incremental pressure drop number
- L_K = "pressure drop" entrance length
- Re = Reynolds number = $V_\infty D_h / \nu$
- t = time
- u = x component of velocity
- v = y component of velocity
- V_∞ = free stream velocity
- x = coordinate normal to the plates
- y = coordinate along the plates
- y_T = transformed coordinate along the plates
- ψ = stream function
- ζ = vorticity
- ν = kinematic viscosity

¹Senior Research Scientist, Commonwealth Scientific and Industrial Research Organization, Division of Mineral Engineering, Clayton, Victoria 3168, Australia.

²Lecturer, School of Mechanical and Industrial Engineering, University of New South Wales, Kensington, New South Wales 2033, Australia.

Contributed by the Fluids Engineering Division of THE AMERICAN SOCIETY OF MECHANICAL ENGINEERS. Manuscript received by the Fluids Engineering Division June 2, 1986.

1 Introduction

The parallel plate passage geometry [1] is attractive because it offers a high fully developed Nusselt number and high Stanton number friction factor ratio [2]. Compact gas-to-gas exchangers require small Reynolds numbers and laminar flow. Exact solutions are known for the fully developed laminar velocity profile. For most applications [2], more than one transfer unit (length/width) is necessary giving fully developed flow at exit but developing flow over much of the passage.

Three approaches to solving the Navier-Stokes equations for this geometry have been used. Simplify the equations and solve with exact boundary conditions [3], or simplify the boundary conditions and solve the equations numerically [4], or simplify both equations and boundary conditions [5]. In most of these studies, the velocity distribution was considered as uniform at the entrance to the passage. In fact, if the velocity distribution and pressure gradients were required near the entrance region, realistic boundary conditions of uniform velocity distribution far upstream must be used.

In this paper we describe the results of a numerical study of the developing flow in the entrance region of a cascade of parallel horizontal plates. The flow has been assumed to be uniform at upstream infinity. Extrapolation to zero mesh size [6] has been used to reduce the effect of discretization errors. The Fanning friction factor f for this type of compact heat exchanger will be greater than its fully developed value f_∞ by an amount depending on the fully developed incremental pressure drop number $K(\infty)$ [7] and the values of $K(\infty)$ are presented in the present work for a range of Reynolds number.

2 Theory and Method of Solution

Consider the steady laminar, two-dimensional flow through a cascade of parallel horizontal plates of an incompressible Newtonian fluid. As indicated in Fig. 1, the free stream velocity V_∞ is uniform far upstream from the channel entrance and far downstream, the flow becomes fully developed. Dimensionless Cartesian coordinates x, y are chosen which make the plate spacing unity. This system of axes is convenient in setting up the solution field and marching the iterative procedure.

The stream function ψ and vorticity ζ are defined by

$$u = \frac{\partial \psi}{\partial y}; \quad v = -\frac{\partial \psi}{\partial x} \quad \text{and} \quad \zeta = \frac{\partial v}{\partial x} - \frac{\partial u}{\partial y} \quad (1)$$

where u, v are velocity components in the x, y directions.

The nondimensional governing equations for vorticity and stream function derived from the Navier-Stokes equations are

$$\frac{\partial \zeta}{\partial t} = -\frac{\partial}{\partial x}(u\zeta) - \frac{\partial}{\partial y}(v\zeta) + \frac{1}{\text{Re}} \left(\frac{\partial^2 \zeta}{\partial x^2} + \frac{\partial^2 \zeta}{\partial y^2} \right) \quad (2)$$

and

$$\frac{\partial^2 \psi}{\partial x^2} + \frac{\partial^2 \psi}{\partial y^2} = -\zeta \quad (3)$$

Figure 1 shows the region ABCDE within which these equations were solved. The solution region is extended to infinity in both upstream and downstream directions from the entrance

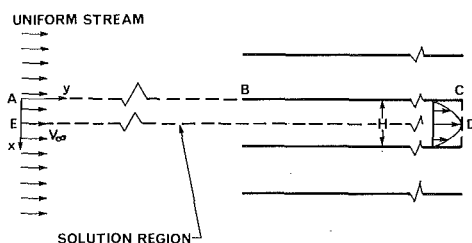


Fig. 1 Boundary conditions and solution region for parallel plate cascade

of the channels. On section AE, uniform flow was imposed: $u=0; v=1; \zeta=0$. Since the solution region represents the upper half of a channel formed by two parallel horizontal plates, the boundary conditions on sections AB and DE are: $u=0; \partial v/\partial x=0; \zeta=0$. The velocities are zero on section BC, the stream function is constant, and the vorticity is determined by the second-order formula [8]:

$$\zeta_p = 3(\psi_p - \psi_1)/h^2 - \zeta_1/2 \quad (4)$$

where 1 denotes the mesh point next to the plates and h is the mesh size.

Stretched coordinates were used both upstream and downstream of the entrance to provide a more suitable distribution of computational grid points and to take into account points at infinity. The following dimensionless downstream transformation function was chosen as it closely represents the downstream decay [9]. It was also used with appropriate sign changes upstream.

$$y_T = \frac{\text{Re}}{8} \ln \left(\frac{1}{1-y} \right) \quad (5)$$

A number of changes were introduced into the governing equations: (i) the elliptic equation (3) is converted into a parabolic one which can be solved by a marching technique; and (ii) different coefficients are inserted into the time derivatives of the equations so that the time rates of change of ζ and ψ can be controlled separately [10], [11]. The equations were then discretized with finite differences and solved by the ADI method. The "QUICK" scheme [12] was used to provide a more accurate and stable approximation to the streamwise advection term in the momentum equation. Forward differences were used for the time derivatives and central differences for other space derivatives.

3 Results and Discussion

Computations were carried out for Reynolds number ranging from 40 to 2000 on three mesh systems: 6×41 ; 11×81 ; and 21×161 . For a 21×161 mesh, the solution takes about 4 hours to converge starting from rest on a Pyramid 90x. The incremental pressure drop number K was obtained by the Richardson's extrapolation to zero mesh size using the solution of the finite difference equations for three mesh sizes. The following extrapolation formula was derived from [6]

$$K = K_3 - \frac{(K_3 - K_1) - 12(K_3 - K_2)}{21} \quad (6)$$

where K_3 is the value of K at the smallest mesh size, etc... It should be noted that the above formula is valid only for grids formed by successive mesh doubling, only for numerical methods which are uniformly second-order accurate, and for very tight iterative convergence. Flow fields, heat transfer results and effects of the plate thickness can be found in [10] and [11].

In Fig. 2, the fully developed incremental pressure drop number $K(\infty)$ is plotted against h^2 for the whole range of Reynolds numbers, with the extrapolated values shown on the vertical axis. It is seen that $K(\infty)$ drops quickly as Re increases and the curves tend to collapse into one at high Re. The dependence of $K(\infty)$ on the mesh size is quite apparent from the curvature of these constant Re lines. Extrapolation to zero mesh size, therefore, eliminates this dependence and offers far more accurate results.

Figure 3 shows the variation of $K(y)$ with y , the distance from the entrance, for Re of 40, 100 and 2000. The "pressure drop" entrance length L_K , defined as the channel length at which $K(y)$ reaches 99 percent of its fully-developed value, can be calculated from $L_K/D_h = 0.01378 \text{ Re}$ to within 1 percent of the results presented here.

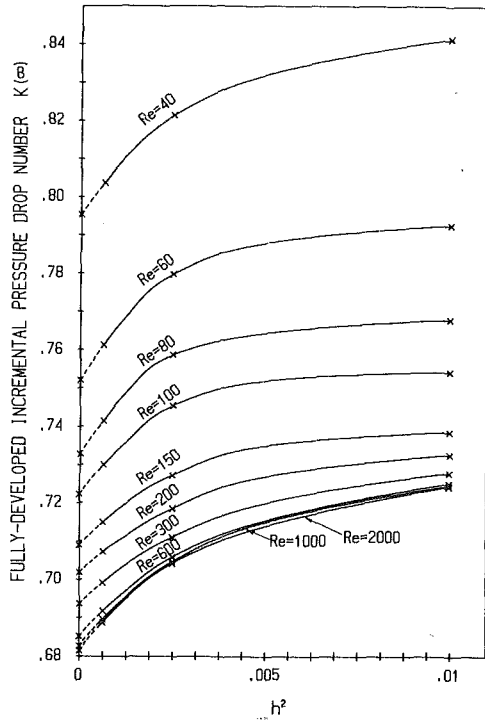


Fig. 2 Extrapolation of fully developed incremental pressure drop number $K(\infty)$ to zero mesh size, h

Numerically determined values of the fully developed incremental pressure drop number $K(\infty)$ are tabulated to four significant figures in Table 1 for various Re and mesh sizes. The extrapolated values of $K(\infty)$ are also presented graphically against $1/Re$ in Fig. 4 and the following correlation approximates the data to within 1 percent.

$$K(\infty) = 0.6779 + 4.5914 \frac{1}{Re} \quad (7)$$

It should be noted that Re is based on the hydraulic diameter $D_h = 2H$.

The three point extrapolation to zero mesh size in Table 1 reduces but does not eliminate discretization error. An indication of the remaining discretization error may be had by comparing two point and three point extrapolation [6]. Two point extrapolation using the smallest meshes gave values between 1.4×10^{-3} and 2.9×10^{-3} greater than three points. The largest difference for $Re = 60$ was 0.39 percent. It is believed that the residual discretization error in $K(\infty)$ is less than 0.39 percent.

Shah and London [7] after detailed consideration of a large number of approximate solutions, recommended 0.674 for $K(\infty)$ at large Reynolds numbers. This is only 0.58 percent less than the value given by the above correlating equation. The Lundgren et al. [13] value of 0.686, recommended in [1], is a useful approximation to the correlation for the practical range of Re from 100 to 1000. In practical parallel plate exchangers, finite plate thickness [10] will give higher values of $K(\infty)$.

4 Concluding Remarks

We have used a numerical model based on the ADI and QUICK methods to obtain values of the incremental pressure drop number in the entrance region of parallel-plate heat exchangers. A uniform velocity profile was assumed at upstream infinity and a fully developed flow downstream infinity. Numerical predictions of K were obtained and extrapolated to zero mesh size for Reynolds number in the range 40–2000. Values of K , to four decimal digits, were presented in both

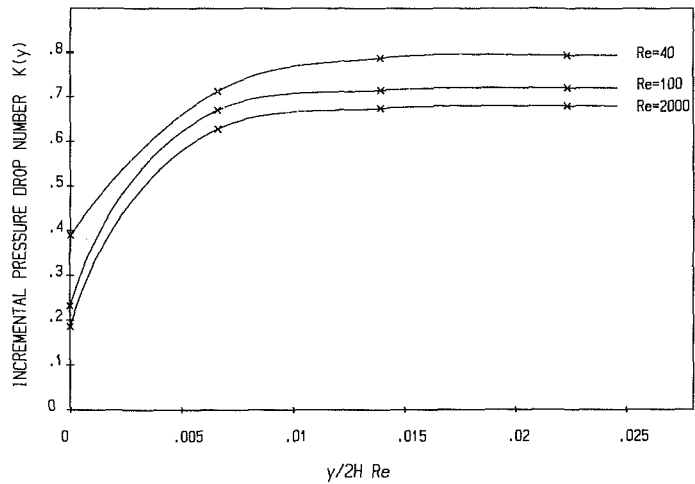


Fig. 3 Dependence of incremental pressure drop number for the wall $K(y)$ on dimensionless distance from the passage entrance $y/(2H Re)$

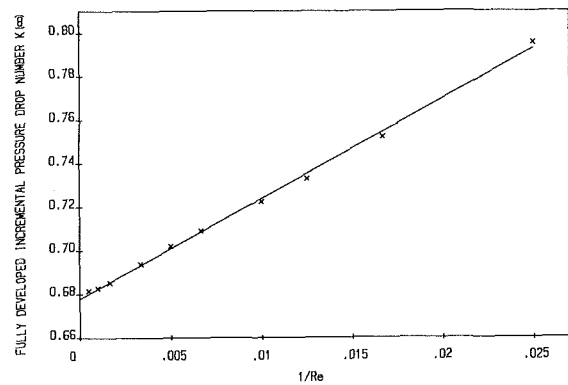


Fig. 4 Linear least squares fit of fully developed incremental pressure drop number $K(\infty)$ to reciprocal of Reynolds number $1/Re$

Table 1 Incremental pressure drop number $K(\infty)$

Re	6×41	11×81	21×161	Extrapolated
40	0.8414	0.8213	0.8037	0.7954
60	0.7927	0.7798	0.7613	0.7522
80	0.7681	0.7587	0.7415	0.7329
100	0.7544	0.7454	0.7300	0.7224
150	0.7387	0.7273	0.7150	0.7091
200	0.7327	0.7186	0.7073	0.7020
300	0.7280	0.7111	0.6992	0.6938
600	0.7252	0.7059	0.6918	0.6853
1000	0.7246	0.7047	0.6897	0.6828
2000	0.7244	0.7042	0.6888	0.6817

graphical and tabular forms. Correlations for $K(\infty) v/s 1/Re$ and the pressure drop entrance length $L_K/D_h v/s Re$ are also presented with errors of less than 1 percent of the predicted results.

Acknowledgments

This work was supported in part by the Australian National Research, Development and Demonstration Council. The authors wish to thank Associate Professor G. de Vahl Davis and Dr J. A. Reizes of the University of New South Wales, Australia, for their help and interest during the course of this project.

References

- 1 MacLaine-cross, I. L., and Ambrose, C. W., "Predicted and Measured Pressure Drop in Parallel Plate Rotary Regenerators," ASME JOURNAL OF FLUIDS ENGINEERING, Vol. 102, No. 1, Mar. 1980, pp. 59–63.

2 Dunkle, R. V., Banks, P. J., and Maclaine-cross, I. L., "Wound Parallel Plate Exchangers for Air-Conditioning Applications," *Compact Heat Exchangers*, ed. R. K. Shah et al., ASME HTD-10, 1980, pp. 65-71.

3 Sparrow, E. M., "Analysis of Laminar Forced-Convection Heat Transfer in Entrance Region of Flat Rectangular Ducts," NASA TN3331, 1955.

4 Hwang, C. I., and Fan, F. T., "Finite Difference Analysis of Forced-Convection Heat Transfer in Entrance Region of a Flat Rectangular Duct," *Appl. Sci. Res.*, Section A, Vol. 13, 1963, p. 401.

5 Mercer, W. E., Pearce, W. M., and Hitchcock, J. E., "Laminar Forced Convection in the Entrance Region Between Parallel Flat Plates," *ASME Journal of Heat Transfer*, 1967, p. 251.

6 Maclaine-cross, I. L., "A Theory of Combined Heat and Mass Transfer in Regenerators," Ph.D. thesis, Department of Mechanical Engineering, Monash University, Australia, 1974.

7 Shah, R. K., and London, A. L., "Laminar Flow Forced Convection in Ducts," *Advances in Heat Transfer*, Ed. by T. F. Irvine and J. P. Harnett, Academic Press, 1978.

8 Woods, L. C., "A Note on the Numerical Solution of Fourth Order Differential Equations," *Aeronautical Quarterly*, Vol. 5, Part 3, 1954, p. 176.

9 Wilson, B., "The Development of Poiseuille Flow," *J. Fluid Mech.*, Vol. 38, Part 4, 1969, pp. 793-806.

10 Nguyen, T. V., "Parallel Plate Heat Exchangers," Ph.D. thesis, School of Mechanical and Industrial Engineering, University of New South Wales, 1980.

11 Nguyen, T. V., Maclaine-cross, I. L., and de Vahl Davis, G., *Numerical Methods in Heat Transfer*, Ed. R. W. Lewis, K. Morgan and O. C. Zienkiewicz, Wiley, 1981, pp. 349-372.

12 Leonard, B. P., "A Stable and Accurate Convective Modelling Procedure Based on Quadratic Upstream Interpolation," *Comp. Meth. in Applied Mech. and Eng.*, Vol. 19, 1979, pp. 59-98.

13 Lundgren, T. S., Sparrow, E. M., and Starr, J. B., "Pressure Drop Due to the Entrance Region in Ducts of Arbitrary Cross Section," *ASME Journal of Basic Engineering*, Vol. 86, No. 3, Sept. 1964, pp. 620-626.

Theoretical Calculations of the Flow Around a Rotating Circular Cylinder Placed in a Uniform Flow

Taha K. Aldoss¹ and Awad Mansour²

The rotation of a circular cylinder placed in a uniform flow is assumed to add a circulation to the flow around the cylinder proportional to the product of the angular velocity of the cylinder and the front area between upper and lower separation points. Adding the velocity due to this induced circulation to the base velocity distribution of the non-rotating cylinder the new velocity distribution on the rotating cylinder is formed. Thwaites' method is then used to calculate the laminar boundary layer on the upper and on the lower sides of the cylinder. The stagnation point, and the upper and lower separation points are also calculated at different values of rotational speed. The calculated lift and drag coefficients using a linear pressure distribution on the wake part of the cylinder with the calculated pressure distribution on the front part between the two separation points show the same trend as the measured values. The torque coefficient is also calculated to estimate the necessary power required to rotate the cylinder to produce the needed lift.

Nomenclature

- C_D = dimensionless drag coefficients, $2F_D/\rho V_\infty^2 D$.1
 C_L = dimensionless lift coefficient, $2F_L/\rho V_\infty^2 D$.1
 CP = dimensionless pressure coefficient, $P/1/2\rho V_\infty^2$
 C_T = dimensionless torque coefficient, $2T/\rho V_\infty^2 D^2$
 D = cylinder diameter
 F_D = drag force
 F_L = lift force

¹ Assistant Professor, Mechanical Engineering Department, Jordan University of Science & Technology.

² Associate Professor, Chemical Engineering Department, Jordan University of Science & Technology, Irbid-Jordan.

Contributed by the Fluids Engineering Division of THE AMERICAN SOCIETY OF MECHANICAL ENGINEERS. Manuscript received by the Fluids Engineering Division June 25, 1987.

- P = static pressure
 R = cylinder radius
 S = distance along the cylinder contour
 T = torque
 V_R = rotational speed ratio, $\Omega.R/V_\infty$
 V = velocity distribution on the cylinder
 V_b = base velocity distribution of non-rotating cylinder
 V_∞ = free stream velocity
 ϕ = dimensionless arc distance S/R
 ω = angular velocity of the cylinder
 ν = kinematic viscosity of fluid
 Γ = Induced circulation

Subscripts

- l = on the lower attached side of the cylinder
 $S1$ = at the upper separation point
 $S2$ = at the lower separation point
 ST = at the stagnation point
 u = on the upper attached side of the cylinder
 w = on the wake side of the cylinder

Introduction

In addition to its academic interest, the flow around a rotating cylinder placed in a uniform stream has found many engineering and industrial applications, e.g., Flettner rotors [1]. One of the most important applications is moving surfaces used to control the boundary layer flows [2].

Although there are some experimental measurements of lift and drag on a rotating cylinder available in the literature [3-6] no theoretical investigations seem to have been done on this subject.

The purpose of this paper is to present a new theory to theoretically calculate the lift, drag and torque coefficient as a function of the rotational speed ratio of the rotating circular cylinder.

Mathematical Modeling and Analysis

The flow around a circular cylinder which is placed in a uniform flow will stay attached to the cylinder surface until a certain point at which the flow will separate from the surface of the cylinder. These points are called the separation points. If the cylinder is rotated the velocity of the flow around the cylinder will be altered and it increases in the region where the flow is in the same direction of the rotation and decreases in the regions where the flow is in the opposite direction of the rotation. This will create asymmetry in the velocity distribution around the rotating cylinder which will lead to asymmetry in the pressure distribution too, which results in a side force called lift. This phenomena is called the Magnus effect. The stagnation point and the two separation points are also expected to move from their original positions of the non-rotating case.

The new velocity distribution around the rotating cylinder is thus because of the cylinder rotation. The no-slip condition between the front part of the cylinder i.e., the area between the two separation points, and the fluid attached to it is believed to be responsible for transferring the rotational motion of the cylinder surface to the fluid. This rotational motion transferred to the fluid is what is called the circulation, Γ , and it is assumed to be proportional to the product of the angular velocity and the front area of the cylinder, between the two separation points as described in the following equation:

$$\Gamma = (\phi_{s1} + \phi_{s2}) \times R \times \Omega.R \quad (1)$$

where ϕ_{s1} , and ϕ_{s2} , are the upper and lower separation points, respectively, and $\Omega.R$ is the speed of the cylinder surface.

To check the validity of the above assumption, the lift produced by this amount of circulation is calculated using the formula ($L = \rho \Gamma V_\infty$), and compared with the one measured by

2 Dunkle, R. V., Banks, P. J., and Maclaine-cross, I. L., "Wound Parallel Plate Exchangers for Air-Conditioning Applications," *Compact Heat Exchangers*, ed. R. K. Shah et al., ASME HTD-10, 1980, pp. 65-71.

3 Sparrow, E. M., "Analysis of Laminar Forced-Convection Heat Transfer in Entrance Region of Flat Rectangular Ducts," NASA TN3331, 1955.

4 Hwang, C. I., and Fan, F. T., "Finite Difference Analysis of Forced-Convection Heat Transfer in Entrance Region of a Flat Rectangular Duct," *Appl. Sci. Res.*, Section A, Vol. 13, 1963, p. 401.

5 Mercer, W. E., Pearce, W. M., and Hitchcock, J. E., "Laminar Forced Convection in the Entrance Region Between Parallel Flat Plates," *ASME Journal of Heat Transfer*, 1967, p. 251.

6 Maclaine-cross, I. L., "A Theory of Combined Heat and Mass Transfer in Regenerators," Ph.D. thesis, Department of Mechanical Engineering, Monash University, Australia, 1974.

7 Shah, R. K., and London, A. L., "Laminar Flow Forced Convection in Ducts," *Advances in Heat Transfer*, Ed. by T. F. Irvine and J. P. Harnett, Academic Press, 1978.

8 Woods, L. C., "A Note on the Numerical Solution of Fourth Order Differential Equations," *Aeronautical Quarterly*, Vol. 5, Part 3, 1954, p. 176.

9 Wilson, B., "The Development of Poiseuille Flow," *J. Fluid Mech.*, Vol. 38, Part 4, 1969, pp. 793-806.

10 Nguyen, T. V., "Parallel Plate Heat Exchangers," Ph.D. thesis, School of Mechanical and Industrial Engineering, University of New South Wales, 1980.

11 Nguyen, T. V., Maclaine-cross, I. L., and de Vahl Davis, G., *Numerical Methods in Heat Transfer*, Ed. R. W. Lewis, K. Morgan and O. C. Zienkiewicz, Wiley, 1981, pp. 349-372.

12 Leonard, B. P., "A Stable and Accurate Convective Modelling Procedure Based on Quadratic Upstream Interpolation," *Comp. Meth. in Applied Mech. and Eng.*, Vol. 19, 1979, pp. 59-98.

13 Lundgren, T. S., Sparrow, E. M., and Starr, J. B., "Pressure Drop Due to the Entrance Region in Ducts of Arbitrary Cross Section," *ASME Journal of Basic Engineering*, Vol. 86, No. 3, Sept. 1964, pp. 620-626.

Theoretical Calculations of the Flow Around a Rotating Circular Cylinder Placed in a Uniform Flow

Taha K. Aldoss¹ and Awad Mansour²

The rotation of a circular cylinder placed in a uniform flow is assumed to add a circulation to the flow around the cylinder proportional to the product of the angular velocity of the cylinder and the front area between upper and lower separation points. Adding the velocity due to this induced circulation to the base velocity distribution of the non-rotating cylinder the new velocity distribution on the rotating cylinder is formed. Thwaites' method is then used to calculate the laminar boundary layer on the upper and on the lower sides of the cylinder. The stagnation point, and the upper and lower separation points are also calculated at different values of rotational speed. The calculated lift and drag coefficients using a linear pressure distribution on the wake part of the cylinder with the calculated pressure distribution on the front part between the two separation points show the same trend as the measured values. The torque coefficient is also calculated to estimate the necessary power required to rotate the cylinder to produce the needed lift.

Nomenclature

- C_D = dimensionless drag coefficients, $2F_D/\rho V_\infty^2 D$.1
 C_L = dimensionless lift coefficient, $2F_L/\rho V_\infty^2 D$.1
 CP = dimensionless pressure coefficient, $P/1/2\rho V_\infty^2$
 C_T = dimensionless torque coefficient, $2T/\rho V_\infty^2 D^2$
 D = cylinder diameter
 F_D = drag force
 F_L = lift force

¹ Assistant Professor, Mechanical Engineering Department, Jordan University of Science & Technology.

² Associate Professor, Chemical Engineering Department, Jordan University of Science & Technology, Irbid-Jordan.

Contributed by the Fluids Engineering Division of THE AMERICAN SOCIETY OF MECHANICAL ENGINEERS. Manuscript received by the Fluids Engineering Division June 25, 1987.

- P = static pressure
 R = cylinder radius
 S = distance along the cylinder contour
 T = torque
 V_R = rotational speed ratio, $\Omega.R/V_\infty$
 V = velocity distribution on the cylinder
 V_b = base velocity distribution of non-rotating cylinder
 V_∞ = free stream velocity
 ϕ = dimensionless arc distance S/R
 ω = angular velocity of the cylinder
 ν = kinematic viscosity of fluid
 Γ = Induced circulation

Subscripts

- l = on the lower attached side of the cylinder
 $S1$ = at the upper separation point
 $S2$ = at the lower separation point
 ST = at the stagnation point
 u = on the upper attached side of the cylinder
 w = on the wake side of the cylinder

Introduction

In addition to its academic interest, the flow around a rotating cylinder placed in a uniform stream has found many engineering and industrial applications, e.g., Flettner rotors [1]. One of the most important applications is moving surfaces used to control the boundary layer flows [2].

Although there are some experimental measurements of lift and drag on a rotating cylinder available in the literature [3-6] no theoretical investigations seem to have been done on this subject.

The purpose of this paper is to present a new theory to theoretically calculate the lift, drag and torque coefficient as a function of the rotational speed ratio of the rotating circular cylinder.

Mathematical Modeling and Analysis

The flow around a circular cylinder which is placed in a uniform flow will stay attached to the cylinder surface until a certain point at which the flow will separate from the surface of the cylinder. These points are called the separation points. If the cylinder is rotated the velocity of the flow around the cylinder will be altered and it increases in the region where the flow is in the same direction of the rotation and decreases in the regions where the flow is in the opposite direction of the rotation. This will create asymmetry in the velocity distribution around the rotating cylinder which will lead to asymmetry in the pressure distribution too, which results in a side force called lift. This phenomena is called the Magnus effect. The stagnation point and the two separation points are also expected to move from their original positions of the non-rotating case.

The new velocity distribution around the rotating cylinder is thus because of the cylinder rotation. The no-slip condition between the front part of the cylinder i.e., the area between the two separation points, and the fluid attached to it is believed to be responsible for transferring the rotational motion of the cylinder surface to the fluid. This rotational motion transferred to the fluid is what is called the circulation, Γ , and it is assumed to be proportional to the product of the angular velocity and the front area of the cylinder, between the two separation points as described in the following equation:

$$\Gamma = (\phi_{s1} + \phi_{s2}) \times R \times \Omega.R \quad (1)$$

where ϕ_{s1} , and ϕ_{s2} , are the upper and lower separation points, respectively, and $\Omega.R$ is the speed of the cylinder surface.

To check the validity of the above assumption, the lift produced by this amount of circulation is calculated using the formula ($L = \rho \Gamma V_\infty$), and compared with the one measured by

Rouse [5] and Prandtl [4]. The calculated result is found to be comparable with the measurements. The maximum lift coefficient due to the above assumed circulation using the above equation ($L = \rho \Gamma V_\infty$) was 10.0 compared with 9.0 by Rouse experiment and 10.0 by Prandtl experiment, where a pair of end disks were made to rotate with the cylinder.

Now, part of this induced circulation (equation (1)) will work to alter the base velocity distribution of the fluid on the front part of the circular cylinder in proportion to the ratio of the area between the separation points and the total area of the cylinder. The remainder part of the circulation will contribute to the shed vortices behind the cylinder. Thus the velocity distribution at the upper side i.e., from the stagnation point until the upper separation point and at the lower side i.e., from the stagnation point until the lower separation point, of the rotating circular cylinder V_u and V_L , respectively, can be calculated in dimensionless form as follows

$$V_u/V_\infty = V_b/V_\infty + V_R(\phi_{s1} + \phi_{s2})/2\pi \quad (2a)$$

and

$$V_l/V_\infty = V_b/V_\infty - V_R(\phi_{s1} + \phi_{s2})/2\pi \quad (2b)$$

where V_b is the base velocity distribution on a nonrotating cylinder and V_R is the rotational speed ratio, $\Omega R/V_\infty$. The stagnation point at different values of V_R is calculated by setting any of the above velocities equal to zero. Once the stagnation point is determined, each side, the upper side from the stagnation point ϕ_{sT} to the upper separation point ϕ_{s1} , and the lower side from the stagnation point to the lower separation point ϕ_{s2} (see Fig. 1) is treated separately. Knowing the velocity distribution and its derivative at each side, Thwaites' approximate method (see Schlichting [2]), is used to calculate the laminar boundary layer developed on these sides of the cylinder. A two dimensional incompressible flow is assumed.

The separation points are determined where shear stress vanishes. The calculated separation points are used to determine the new velocity distributions for the next V_R step using equations (2a) and (2b). The known ϕ_{s1} and ϕ_{s2} of the nonrotating cylinder were used for the first step of calculation. Also the actual velocity distribution measured by Hiemenz [7] was used as the base velocity distribution of the non-rotating cylinder as follows:

$$V_b/V_\infty = 1.814\phi - 0.271\phi^3 - 0.0471\phi^5 \quad (3)$$

where $\phi = \frac{S}{R}$, the dimensionless arc length along the surface of the cylinder, measured from the stagnation point.

The pressure distribution on the front parts of the cylinder is calculated from Bernoulli equation as follows:

$$CP_u = 1 - (V_u/V_\infty)^2, \quad CP_l = 1 - (V_l/V_\infty)^2 \quad (4)$$

The values of the pressure coefficient at the separated values CP_{s1} and CP_{s2} are calculated from equation (4) evaluated at $\phi = \phi_{s1}$ and at $\phi = \phi_{s2}$, respectively.

To calculate the forces on the rotating circular cylinder, the pressure distribution in the wake part of the cylinder is still to be known. No measurements, or calculations of the pressure in the wake region of a rotating circular cylinder placed in a uniform flow exist up to the knowledge of the authors. However, the wake pressure distribution of the non-rotating cylinder is well known at different Reynolds numbers, Achenbach [8], where the pressure distribution at the wake region is found to be constant and it has the value of the pressure at the separation points. Since in the rotating circular cylinder the pressures at the upper and at the lower separation points take different values, the most appropriate assumption of the pressure in the wake region could be the linear distribution between the two values at the separation points as follows:

$$CP_w = \frac{CP_{s2} - CP_{s1}}{\phi_{s2} - \phi_{s1}}(\phi - \phi_{s1}) + CP_{s1} \quad (5)$$

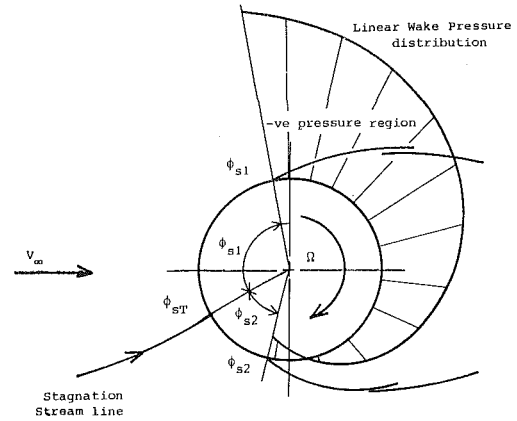


Fig. 1 Schematic diagram of a rotating cylinder in a uniform flow with the assumed wake linear pressure distribution

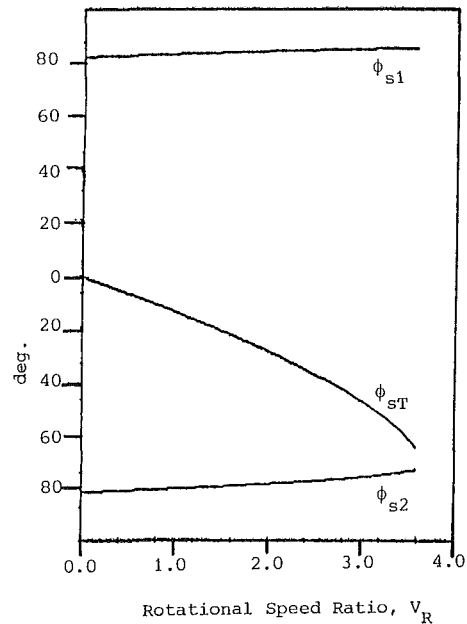


Fig. 2 The variation of the stagnation point, ϕ_{sT} , the upper separation point, ϕ_{s1} , and the lower separation point, ϕ_{s2} with rotational speed ratio, V_R

where CP_w is the pressure coefficient on the wake part of the cylinder, (see Fig. 1).

Knowing the pressure distribution around the whole surface of the cylinder, the lift, drag and torque coefficients can be calculated and compared with the experimental findings.

Results and Discussion

A computer program has been constructed to perform the necessary calculations to determine the locations of the stagnation point, upper and lower separation points at each rotational speed ratio. An increment of 0.05 in V_R is used starting from the known solution of the nonrotating circular cylinder. The calculation proceeds till the lower stagnation point detachment from the circular cylinder surface occurs i.e., when the location of the lower separation point coincides with the stagnation point. This occurs at $V_R \approx 3.8$. The forces on the cylinder is calculated from the calculated pressure distribution around the cylinder surface, where the assumed linear pressure distribution in the wake region is used each time. The lift, drag and torque coefficients are then calculated and compared with the available experimental results. In Fig. 2 the variation of the location of the stagnation point, the upper separation point and the lower separation point is plotted

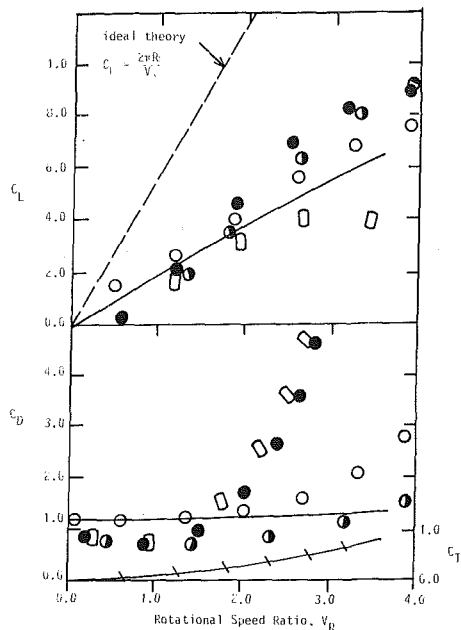


Fig. 3 The lift, drag and torque coefficients versus the rotational speed ratio, present theory and the other experiments • Betz: with end disks [4], ○ Reid: without end disks [3], □ Betz: without end disks [4], — present theory, C_L, C_D , ++ present theory, C_T .

against the rotational speed ratio. The upper separation point moves downstream and the lower separation point moves upstream with increasing rotational speed. The rate of change in the location of the lower separation point with V_R is larger than that of the upper separation point, however both vary at low rate. On the other hand the stagnation point moves downstream with increasing rotational speed but at higher rate compared with the upper and lower separation points. It reaches its minimum value at $\phi = 71.2$ degrees where it meets the lower stagnation point, after which the stagnation point deattached from the cylinder surface and the present theoretical model breaks down. The value of the rotational speed ratio where the deattachment occurs was ≈ 3.8 . At this velocity the upper separation point reaches the value of 84 deg.

Figure 3 shows a comparison between the present calculations and the experimental results of the variation of the lift and drag coefficients with the rotational speed ratio. A lot of discrepancies between the available experimental results are found because the experiments were executed at different conditions, some with and some without end disks and at different aspect ratios. Anyhow the present calculations seem to predict the general behavior of the C_L and C_D variation with V_R and at the same time they are not that far from the experimental findings. More adequate experiments are needed for better comparison.

To complete the information the torque coefficient variation with the rotational speed ratio is presented in Fig. 3. The torque required to rotate a circular cylinder increases with increasing angular velocity of the cylinder.

Conclusions

A simple theory by which the lift coefficient, drag coefficient and torque coefficient of a rotating circular cylinder placed in a uniform flow is suggested. It is assumed that the flow velocity in the front side of the cylinder, i.e., the area between the two separation points, is equal to the base velocity of nonrotating circular cylinder and the part contributed from the circulation introduced because of the cylinder rotation. It is also assumed that the pressure in the wake side of the

cylinder assumes a linear distribution between the two values of the pressure at the two separation points. The calculated results using the present theory show the same trend as the available experiments. The calculated values are found to lie between the experimental results.

Acknowledgments

The authors gratefully acknowledge Yarmouk University for permitting them to carry out this investigation on their VAX computer.

References

- 1 Fleming, P. D., and Probert, S. D., "The Evolution of Wind-Turbines: A Historical Review," *Applied Energy*, Vol. 18, 1984, pp. 163-170.
- 2 Schlichting, H., *Boundary-Layer Theory*, McGraw-Hill, 1979.
- 3 Reid, N. A. C. A., Technical Note No. 209, 1924.
- 4 Betz., *Zeitschr. des Vereines deutscher Ingenieure*, Vol. 69, 1925, pp. 11-14.
- 5 Prandtl and Tietjens, *Die Naturwissenschaften*, Vol. 13, 1925, pp. 93-108.
- 6 Rouse, H., *Elementary Mechanics of Fluids*, Wiley, New York, 1946.
- 7 Hiemenz, *Dinglers Polytech. J.*, Vol. 326, 1911, p. 321.
- 8 Achenbach, E., "Distribution of Local Pressure and Skin Friction Around a Circular Cylinder in Cross-Flow up to $Re = 5 \times 10^6$," *J. Fluid Mech.*, Vol. 34, Part 4, 1968, pp. 625-639.

Eddy Viscosity Distributions Through the Transition of an Incompressible Free Jet

S. Emami¹, G. Morrison¹, and G. Tatterson¹

Nomenclature

- A = constant
- a = virtual origin of the jet
- E = reduced kinematic eddy viscosity, defined by equation (2)
- D = jet diameter at exit, nozzle diameter at exit
- R = radial distance across the jet from the centerline
- r = radial component
- U = jet exit velocity
- U_x = axial velocity
- U_{xc} = centerline axial velocity
- U_r = radial velocity
- $u_r u_x$ = Reynolds stress component
- X = axial distance downstream along the jet centerline
- x = axial component
- ϵ_T = turbulent kinematic eddy viscosity
- ν = thermodynamic kinematic eddy viscosity

Introduction

Most theoretical analyses of the transition from laminar to turbulent flow in a free jet are based on instability theory. The theory hypothesizes that a small disturbance causes an instability in laminar boundary layers. Once the transition Reynolds number is met or exceeded, the transition from laminar to turbulent flow begins. Initially, the transitional jet is laminar with a potential core. As the flow proceeds, a shear layer develops around the jet and the onset of turbulence occurs. Normally, once the transition begins, it continues until the jet becomes fully turbulent.

¹Mechanical Engineering Department, Texas A & M University, College Station, Texas 77843-3123.

Contributed by the Fluids Engineering Division of THE AMERICAN SOCIETY OF MECHANICAL ENGINEERS. Manuscript received by the Fluids Engineering Division May 5, 1987.

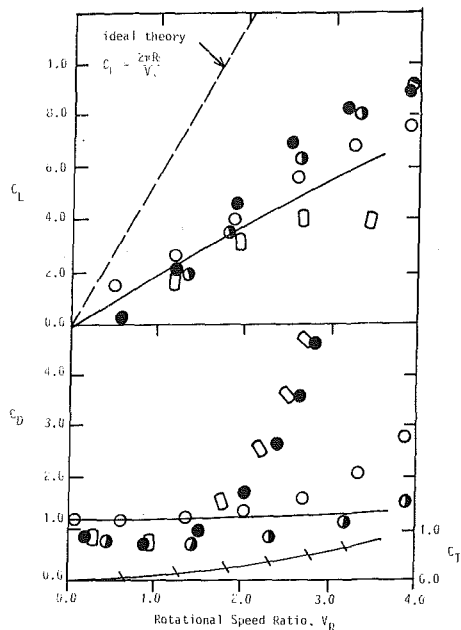


Fig. 3 The lift, drag and torque coefficients versus the rotational speed ratio, present theory and the other experiments • Betz: with end disks [4], ○ Reid: without end disks [3], ○ Rouse (6), □ Betz: without end disks [4], — present theory, C_L, C_D , ++ present theory, C_T .

against the rotational speed ratio. The upper separation point moves downstream and the lower separation point moves upstream with increasing rotational speed. The rate of change in the location of the lower separation point with V_R is larger than that of the upper separation point, however both vary at low rate. On the other hand the stagnation point moves downstream with increasing rotational speed but at higher rate compared with the upper and lower separation points. It reaches its minimum value at $\phi = 71.2$ degrees where it meets the lower stagnation point, after which the stagnation point deattached from the cylinder surface and the present theoretical model breaks down. The value of the rotational speed ratio where the deattachment occurs was ≈ 3.8 . At this velocity the upper separation point reaches the value of 84 deg.

Figure 3 shows a comparison between the present calculations and the experimental results of the variation of the lift and drag coefficients with the rotational speed ratio. A lot of discrepancies between the available experimental results are found because the experiments were executed at different conditions, some with and some without end disks and at different aspect ratios. Anyhow the present calculations seem to predict the general behavior of the C_L and C_D variation with V_R and at the same time they are not that far from the experimental findings. More adequate experiments are needed for better comparison.

To complete the information the torque coefficient variation with the rotational speed ratio is presented in Fig. 3. The torque required to rotate a circular cylinder increases with increasing angular velocity of the cylinder.

Conclusions

A simple theory by which the lift coefficient, drag coefficient and torque coefficient of a rotating circular cylinder placed in a uniform flow is suggested. It is assumed that the flow velocity in the front side of the cylinder, i.e., the area between the two separation points, is equal to the base velocity of nonrotating circular cylinder and the part contributed from the circulation introduced because of the cylinder rotation. It is also assumed that the pressure in the wake side of the

cylinder assumes a linear distribution between the two values of the pressure at the two separation points. The calculated results using the present theory show the same trend as the available experiments. The calculated values are found to lie between the experimental results.

Acknowledgments

The authors gratefully acknowledge Yarmouk University for permitting them to carry out this investigation on their VAX computer.

References

- 1 Fleming, P. D., and Probert, S. D., "The Evolution of Wind-Turbines: A Historical Review," *Applied Energy*, Vol. 18, 1984, pp. 163-170.
- 2 Schlichting, H., *Boundary-Layer Theory*, McGraw-Hill, 1979.
- 3 Reid, N. A. C. A., Technical Note No. 209, 1924.
- 4 Betz., *Zeitschr. des Vereines deutscher Ingenieure*, Vol. 69, 1925, pp. 11-14.
- 5 Prandtl and Tietjens, *Die Naturwissenschaften*, Vol. 13, 1925, pp. 93-108.
- 6 Rouse, H., *Elementary Mechanics of Fluids*, Wiley, New York, 1946.
- 7 Hiemenz, *Dinglers Polytech. J.*, Vol. 326, 1911, p. 321.
- 8 Achenbach, E., "Distribution of Local Pressure and Skin Friction Around a Circular Cylinder in Cross-Flow up to $Re = 5 \times 10^6$," *J. Fluid Mech.*, Vol. 34, Part 4, 1968, pp. 625-639.

Eddy Viscosity Distributions Through the Transition of an Incompressible Free Jet

S. Emami¹, G. Morrison¹, and G. Tatterson¹

Nomenclature

- A = constant
- a = virtual origin of the jet
- E = reduced kinematic eddy viscosity, defined by equation (2)
- D = jet diameter at exit, nozzle diameter at exit
- R = radial distance across the jet from the centerline
- r = radial component
- U = jet exit velocity
- U_x = axial velocity
- U_{xc} = centerline axial velocity
- U_r = radial velocity
- $u_r u_x$ = Reynolds stress component
- X = axial distance downstream along the jet centerline
- x = axial component
- ϵ_T = turbulent kinematic eddy viscosity
- ν = thermodynamic kinematic eddy viscosity

Introduction

Most theoretical analyses of the transition from laminar to turbulent flow in a free jet are based on instability theory. The theory hypothesizes that a small disturbance causes an instability in laminar boundary layers. Once the transition Reynolds number is met or exceeded, the transition from laminar to turbulent flow begins. Initially, the transitional jet is laminar with a potential core. As the flow proceeds, a shear layer develops around the jet and the onset of turbulence occurs. Normally, once the transition begins, it continues until the jet becomes fully turbulent.

¹Mechanical Engineering Department, Texas A & M University, College Station, Texas 77843-3123.

Contributed by the Fluids Engineering Division of THE AMERICAN SOCIETY OF MECHANICAL ENGINEERS. Manuscript received by the Fluids Engineering Division May 5, 1987.

There are many ways to study and describe the transition of a free jet. One description is based on the use of eddy viscosity. Previous work is available for comparison. Page and Hill [1], for example, report eddy viscosities.

There are several Reynolds numbers which can be defined. One is the jet Reynolds number, UD/ν , which is based on the jet exit velocity, U , and diameter, D . For this work, this Reynolds number was 45,000 at a Mach number of 0.15. Another Reynolds number, $U_{xc}X/\nu$, is based on the jet local centerline velocity, U_{xc} , and the axial distance, X , from the jet exit. This Reynolds number is called the length Reynolds number.

Objectives

The first objective of this study was to obtain eddy viscosity distributions as a function of radial and axial positions in the jet. Such data are helpful in understanding the mechanism of transition. The second objective was to obtain radially averaged eddy viscosity as a function of length Reynolds number, $U_{xc}X/\nu$, and compare the results to that of Page and Hill [1].

Experimental Procedures and Facility

The experiments were performed in a free jet test facility in which a round, axisymmetric jet of air, 12.5 mm diameter, was exhausted at atmospheric pressure into a large anechoic chamber. The Mach number for the jet was 0.15. To form the jet, the flow was accelerated through a nozzle whose contour was described by a third order polynomial. The contraction ratio for the nozzle was 100 to 1. The hot-wire probes were operated by a four channel TSI model 1050 anemometer system. A four degree of freedom probe drive (three linear traverses and one rotational mode) was used to position the probe. The rotational degree of freedom was for yawing the crossed hot-wire probe for calibration.

Detailed measurements in the mixing layer of the flow field were made using a crossed hot wire. The local mean jet velocity and two instantaneous signals, proportional to the axial and radial velocity fluctuations, respectively, were obtained. These two fluctuation signals were decomposed using techniques by Horstman and Rose [2] and Johnson and Rose [3]. The resulting signals were correlated and time averaged to obtain the local Reynolds stresses throughout the flow field. The uncertainty in all the measurements was ± 7 percent. From the Reynolds stresses and the mean velocity gradients, eddy viscosity distributions were obtained throughout the flow as well, as shown in Fig. 1.

In this work, kinematic eddy viscosity was defined in the traditional way as:

$$-\overline{u_r u_x} = \epsilon_T \left(\frac{\partial U_r}{\partial x} + \frac{\partial U_x}{\partial r} \right) \quad (1)$$

and was calculated using equation (1). Since the eddy viscosity distributions were obtained, it was possible to average over the

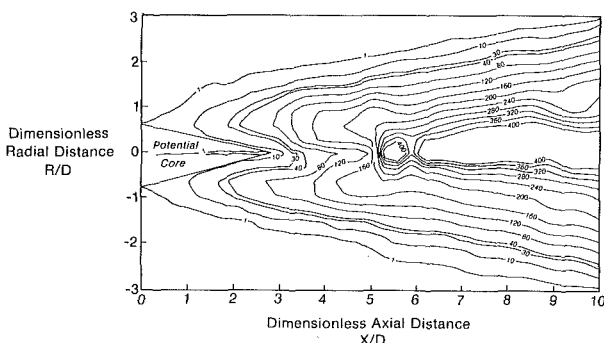


Fig. 1 Contours of the ratio of eddy viscosity to the molecular viscosity, ϵ_T/ν , at $M = 0.15$ and a jet Reynolds number of $(UD/\nu) = 45,000$ at 25°C

jet radius to obtain an average radial eddy viscosity. These eddy viscosities were divided by the jet local centerline velocity, U_{xc} , and the distance from the origin of the jet to obtain a dimensionless viscosity, E .

$$E = (\int \epsilon_T dr / \int dr) / U_{xc} X \quad (2)$$

The averages for the dimensionless eddy viscosity were obtained for every $0.25X/D$ position starting at the jet exit up to about $X/D = 5$ then every $0.50X/D$ up to $X/D = 10$. This dimensionless viscosity was a function of the length Reynolds number and the jet exit Reynolds number (Fig. 2). The uncertainty in E was estimated to be ± 10 percent. This value was relatively difficult to determine since integration in equation (2) tended to average out random errors. Furthermore, the turbulent nature of the jet caused spread in the data because of the turbulence which can be larger than the uncertainty in the measurements.

Results and Conclusions

Centerline Velocity. The centerline velocity data for the fully turbulent portion of the jet in this experiment can be modeled as:

$$U_{xc}/U = AD/(X+a) \quad (3)$$

where the constant, A , is a function of the jet strength and turbulent kinematic eddy viscosity and the ratio, a/D , is a function of spread rate of the jet. The constant, A , was evaluated at the centerline of the jet at the beginning of the fully turbulent region where $\epsilon_T/\nu = 400$ and was found to be 10.27 in this work. The ratio a/D was found to be equal to 1.98. In equation (3), the jet nozzle diameter is D and a is the virtual origin of the jet.

Eddy Viscosity Distributions. An example is shown in Fig. 1 of the eddy viscosity contours in which D is the exit diameter of the jet, R is the radial distance from the jet centerline and X is the axial direction along the centerline. The jet exit Reynolds number, UD/ν , for this jet was 45,000. As the contours indicate, from $X/D = 0.0$ to 1.0, the jet is laminar, so the molecular viscosity dominates the flow. As the shear layers grow downstream, the turbulent mixing increases. From $X/D = 1.0$ to 4.5, the eddy viscosity increases radially from the edge of the jet toward the shear layer, where it reaches a local maximum, and then decreases as the potential core is reached. In incompressible and high speed, subsonic jets, the potential core is present from $X/D = 0$ to approximately 5. As the flow progresses downstream from $X/D = 3$ to 5, the end of the potential core is encountered. The eddy viscosity starts to increase from $\epsilon_T/\nu = 10$ to 400 along the centerline of the jet. From the end of the potential core, the eddy viscosity reaches a maximum and remains constant along the centerline of the jet. The sudden increase in the eddy viscosity is due to the presence of a fully turbulent region beyond the end of the potential core. From $X/D = 5$ to 10, the eddy viscosity increases from the edge of the jet toward the center. The mean

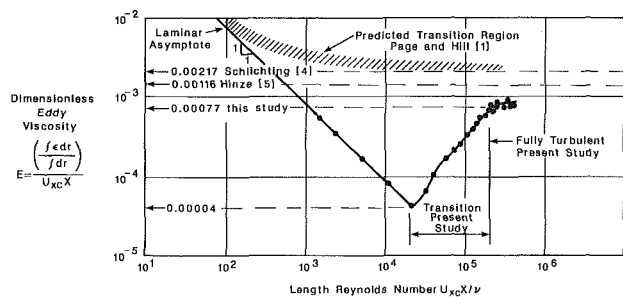


Fig. 2 Dimensionless eddy viscosity versus length Reynolds number, $U_{xc}X/\nu$, at a jet Reynolds number, UD/ν , of 45,000

local velocity gradients decrease and the Reynolds' stress increases toward the centerline.

Eddy Viscosity as a Function of Length Reynolds Number. Experimental data (Fig. 2) show that the jet in the present study is laminar up to a length Reynolds number of 30,000, and the dimensionless eddy viscosity varies inversely with length Reynolds number. The molecular viscosity dominated the flow under these conditions. Above a length Reynolds number of 30,000, the transition to a turbulent jet begins to occur where the dimensionless viscosity, E , is characterized by a large dependence on length Reynolds number. When the jet becomes fully turbulent, E appears to become independent of length Reynolds number. Unfortunately, very high length Reynolds numbers were not obtained in our facility. The highest dimensionless eddy viscosity obtained was 0.00095 at a Reynolds number of 300,000.

Several comparisons can be made concerning these data and those reported by Page and Hill [1], Schlichting [4], and Hinze [5]. Page and Hill [1] hypothesized a gradual asymptotic transition from laminar to turbulent flow in the jet, beginning at a length Reynolds number of about 100 from their figure. However, the present study found that the jet remained laminar up to a length Reynolds number of 30,000 and then transitioned abruptly to a turbulent flow with the dimensionless eddy viscosity increasing exponentially with length Reynolds number. The same type of transition was observed

by Nikuradse (6) for pipe flows where the transition was found dependent upon the roughness of the pipe. Although the transitions in pipes and jets are based on different mechanisms, the flow behavior is analogous. The exact value of transition Reynolds number for a free jet should be dependent upon the surface roughness and turbulence level present in the jet at the nozzle exit.

Schlichting [4] and Hinze [5] indicated asymptotic limits of 0.00214 and 0.00116 for E at high length Reynolds numbers, respectively. Although further work is needed at higher Reynolds numbers, this study showed that the rate of growth in E decreased rapidly at 0.00077 with a very gradual rate of increase in E thereafter. More data are needed to firmly establish the asymptotic limit.

References

- 1 Page, R. H., and Hill, W. G., "Location of Transition in a Free Jet Region," *AIAA J.*, Vol. 4, No. 5, 1966, p. 944.
- 2 Horstman, C. C., and Rose, W. C., "Hot-Wire Anemometry in Transonic Flow," *AIAA J.*, Vol. 15, No. 3, 1977, pp. 395-401.
- 3 Johnson, D. A., and Rose, W. C., "Laser Velocimeter and Hot-Wire Anemometer Comparison in a Supersonic Boundary Layer," *AIAA J.*, Vol. 13, No. 4, 1975, pp. 512-515.
- 4 Schlichting, H., *Boundary Layer Theory*, McGraw-Hill, New York, 6th ed., 1969, p. 699.
- 5 Hinze, J. O., *Turbulence*, McGraw-Hill, New York, 2 ed., 1975, p. 539.
- 6 Nikuradse, J., "Laws of Flow in Rough Pipe", NACA Tech. Memo 1292, 1950.

Noise and Erosion of Self-Resonating Cavitation Jets¹

F. G. Hammitt.² The paper is a very interesting and valuable study of methods for understanding and predicting cavitation erosion in given flow situations. In my opinion, as already expressed in the past literature [13–15], such progress is most likely through the use of cavitation noise, particularly in the form of bubble-collapse pressure pulses and observed erosion in the same flow regime. We (Univ. of Michigan) did many such tests [13, 15], e.g., Ph.D. thesis of M. K. De) at Michigan a few years ago, in a relatively conventional venturi. The present authors did relatively similar work in a much more intensely cavitating venturi. It seems best in my discussion to compare our own general conclusions with those of present paper. Our tests were limited mostly to soft aluminum (1100-0) specimens inserted through the venturi-wall, while theirs involved other materials, including aluminum, and the venturi itself was test material.

In any case, we would agree strongly with their conclusions (a)–(c). In my opinion (c) may be most important. Conclusion (d) is interesting, but I have no observations concerning the frequency contents of damaging and nondamaging signals. Conclusions (e) and (f) are also interesting, but I have no related information.

Authors' Closure

We would like to thank Professor Hammitt for his interest and commendation of our paper. His contributions and those of his co-workers to the subject matter played a leading role in the comparative study of the erosion and noise of cavitation. Our erosion studies using the self-resonating cavitating jets had the advantage of achieving observable results in a short period of time due to the intensive and controllable cavitation generated by our jets. We agree with Professor Hammitt that our conclusion (c) is most important. The time variations of the total volume of eroded material removed appeared in our tests to be directly correlated with the time variations of the RMS sound pressures detected. Our results, if confirmed by further observations, provide a simple acoustic qualitative technique to assess material volume removal when visual observation is not possible.

¹By G. L. Chahine and P. Courbiere, published in the December 1987 issue of the JOURNAL OF FLUIDS ENGINEERING, Vol. 109, pp. 429–435.

²ME/AM Department, University of Michigan, Ann Arbor, Mich.

Erosion Due to Impingement of Cavitating Jet¹

A. F. Conn.² The authors are to be congratulated for exerting considerable effort, which has greatly added to the body of data on cavitation effects. In particular, they warn the reader to be concerned about those as-yet-not-understood parameters such as nozzle sizes and shapes, and the size of test specimens and test chambers. The reader should, however, be aware that this present paper shares with the work of Kleinbreuer several systematic errors which flaw any detailed interpretation of the results. By ignoring, during their testing, the scaling afforded by using the cavitation number (roughly ambient pressure divided by the pressure drop across the nozzle), much of their data cannot be internally compared. This, and the following error, have probably caused their disagreement with previous investigators, as shown in Fig. 15, when at last cavitation number is introduced.

A second mistake was the use, arbitrarily, of the mass loss at a single, fixed increment of testing time (for each of the two apparatus sizes) for characterizing the highly nonlinear erosion-vs-time curve (see Fig. 7). Although this testing philosophy saves much time (by avoiding the periodic removal, weighing and reinsertion of test specimens) it is well known that only comparisons among erosion *rate* curves, at some characteristic point, e.g., peak rate of erosion, have validity.

Despite these flaws, the *trends* reported by varying parameters such as testing time, standoff distance, ambient pressure and pressure drop across the nozzle are useful, even though precise conclusions cannot be drawn because of the reasons cited.

Authors' Closure

The authors would like to express their gratitude to Dr. Conn for his discussions and comments to this paper.

The cavitation number is one of important scaling parameters. The definition of the cavitation number σ used in this paper is

$$\sigma = P_d / P_u \quad (\text{A-1})$$

On the other hand, strictly defined cavitation number σ_{st} is given by

$$\sigma_{st} = (P_d - P_v) / (\rho u^2 / 2) \quad (\text{A-2})$$

where P_v and u are vapor pressure of the liquid and jet exit

¹By A. Yamaguchi and S. Shimizu published in the December 1987 issue of the JOURNAL OF FLUIDS ENGINEERING, Vol. 109, pp. 442–447.

²Tracor Hydraulics, Inc., Laurel, MD 20207.